

**DYNAMICS OF FLUIDS, HEAT AND SOLUTES
ALONG SEDIMENT-WATER INTERFACES:
A MULTIPHYSICS MODELING STUDY**

By

Meinhard Bayani Ramos Cardenas

Submitted in Partial Fulfillment
of the Requirements for the

Doctorate of Philosophy in Earth and Environmental Science
With Dissertation in Hydrology

The New Mexico Institute of Mining and Technology
Socorro, New Mexico

August 2006

To my parents, Marlito and Maria Lydia,
to my brothers, Marnilo and Manfred,
to my wife and son, Tracy and Makisig,
to the rest of my family,
and to the Filipino people.

*Para sa aking mga magulang, mga kapatid,
asawa at anak, at iba ko pang kamag-anak,
at para sa mga kababayan ko sa Pilipinas*

Abstract

The water cycle includes many reservoirs wherein water is stored and is characterized by many pathways through which water is conveyed. Humans have relied on two major reservoirs in the hydrosphere, surface water bodies, e.g., rivers and lakes, and groundwater stored in aquifers. In many cases, surface water and groundwater interact through exchange across the groundwater-surface water interface. Groundwater-surface water exchange mediates ecological and biogeochemical processes as water is also a transporting agent for chemical and thermal energy. The proper management of both groundwater and surface water therefore requires a basic understanding of the dynamics of not only fluid flow but also of other fluid-borne entities.

I study the dynamics of fluids, heat and solutes along the sediment-water interface (SWI). Above the interface is a water column, usually with a flowing fluid. Below the interface is a sediment. The SWI represents one of the smallest spatial scales (cm's to m's) where groundwater and surface water interactions can be studied and observed. The mechanisms, internal and external, which drive fluid, solute and energy transport across the SWI are investigated using numerical simulation models.

Fluid flow within sediments is controlled locally by the internal permeability structure of the sediment and also by external forcing due to pressure gradients. A major external forcing is fluid flow in the water column. Water-column flow over sediments with non-flat topography, which is typically due to the presence of bedforms such as ripples and dunes, generates a spatially variable pressure distribution along the SWI. This pressure distribution, characterized by high and low pressure areas, drives water into and then out of the sediments. The zone defined by water infiltrating into the sediments from

the water column, flowing through the sediments, and then returning to the water column is referred to here as the *interfacial exchange zone* (IEZ). An analogous term is the *hyporheic zone* commonly applied in fluvial settings. In addition to current-bedform driven exchange, fluid flow through sediments and interfacial exchange may be driven by larger forcing such as head gradients due to stream channel morphology, e.g., sinuosity, or regional hydraulic head gradients.

The relative contributions to interfacial exchange of (1) the internal heterogeneous permeability structure of streambed sediments, (2) head gradients due to channel bends, and (3) an irregular pressure distribution along the SWI, are analyzed using numerical simulation of three-dimensional groundwater flow via the popular finite-difference code MODFLOW. The effects of current-bedform interactions are simplified and represented by a sinusoidal pressure distribution imposed on a flat sediment surface. The importance of local scale control groundwater flow by permeability diminishes as the amplitude and frequency of the sinusoidal pressure distribution, the external forcing, increases. The major effect of channel curvature is to drive hyporheic flow towards the pointbar due to a lateral pressure gradient. I present dimensionless numbers which quantify the relative importance of permeability, channel curvature, and current-bedform-driven SWI pressure distribution.

The dynamics of current-bedform-driven interfacial exchange is explicitly investigated by numerically modeling coupled, two-dimensional fluid flow both above and below an SWI characterized by bedforms. The coupling is sequential, modeling first the water column, and then using bottom pressures, at the SWI, as the boundary condition for porous flow in the sediments. In my first model, the flow in the water

column is assumed laminar and governed by the steady-state Navier-Stokes equations, while pore water flow in the sandy sediments follows Darcy's Law. Finite element numerical analysis is conducted via the code FEMLAB (now Comsol Multiphysics). Multiple dynamical scenarios are represented by varying the Reynolds number (Re) of the laminar flow, and geometric configurations of the bedform, achieved by changing the bedform height, length and asymmetry. Simulations show that the configuration of and flux through the IEZ are driven by a pressure minimum at the bedform crest, where an eddy detaches, and a pressure maximum at the stoss side, where the eddy reattaches. The distance between eddy detachment and reattachment points increases with Re , with the eddy length ultimately confined to the bedform length. Under neutral conditions, when the water column has no net gain or loss of water, the IEZ depth is dependent on Re via a function of Michaelis-Menten type, suggesting that the IEZ depth will never be greater than the length of the bedform. This behavior is ultimately driven by the dynamical relationship between the eddy length and the Re . Under gaining conditions, IEZs extend to shallower depths, compared to equivalent neutral conditions, and may be absent when the ambient upwards flow of groundwater overpowers interfacial exchange. For a given magnitude of groundwater gain I quantify threshold Res , below which there is no IEZ. Above the threshold, flux through the IEZ is related to Re via a power function.

My second model of interfacial exchange dynamics considers turbulent flow conditions in the water column. A finite-volume solution of turbulent flow, governed by the Reynolds-averaged Navier-Stokes equations (implemented with the code CFD-ACE+), is sequentially coupled with the finite-element model for groundwater flow. The formulation for the hydrodynamic model is validated with previously published

laboratory flume experiments, including successful simulation of dye tracer experiments by a solute transport model. Neutral, gaining and losing water columns are considered. Under fully-developed turbulent conditions, water-column eddies are insensitive to Re and are smaller than under laminar conditions. Since the pressure distribution associated with an eddy drives interfacial exchange, the turbulent flow IEZ is shallower, relative to laminar flow IEZs, and like the eddy is insensitive to Re . Turbulent flow simulations under gaining and losing conditions show that IEZs develop if the water-column current is strong enough to drive flow into the sediments. If the Re is below a threshold interfacial exchange is overpowered by ambient groundwater discharge (AGD). This dynamical behavior, controlled by thresholds, is similar to the gaining conditions for laminar flow. Flux through the IEZ depends on Re via a power function, as for laminar flow. I develop simple predictive equations for IEZ depth and flux that consider dynamical and geometric conditions.

Heat transport through the IEZ is simulated by numerically solving the advection-conduction-dispersion equation. The transport simulations are based on the flow fields defined by the turbulent hydrodynamic models. Diurnal water column temperature changes are imposed on the SWI. Interfacial exchange results in an irregular temperature distribution, both through space and time, within the IEZ, as well as deeper parts of sediments not subjected to interfacial exchange. When AGD is present, whether towards or away from the SWI, the influence of current-bedform induced heat advection becomes subdued until, at high AGD, fluid flow and heat transport become essentially vertically one-dimensional and the IEZ is absent. Zones within the sediments experiencing strong diurnal temperature variations may be found horizontally adjacent to zones lacking any

substantial temperature variations. These zones with weak temperature variations are found close to crests of dunes where pore water is upwelling from deeper areas of the sediments, while strong temperature variations are observed underneath areas where water is infiltrating into the sediments from the water column.

Acknowledgments

This dissertation is the fruit of the many forms of support I received from institutions, mentors, colleagues, friends, and family.

I have been primarily supported throughout my four years at New Mexico Tech by the New Mexico Bureau of Geology and Mineral Resources' Frank E. Kottowski Fellowship. Being the first recipient of the Kottowski Fellowship has been a tremendous honor, privilege, and challenge. It allowed me to pursue a project of my own design. My research during the last couple of years was funded by a New Mexico Water Resources Research Institute Student Grant and an American Geophysical Union Horton Research Grant. I also acknowledge the patience of and support by technicians from COMSOL and ESI-Group, vendors and developers of the codes that I used for my research. Travel grants from the NMT Graduate Student Association allowed me to attend and present at conferences because of which I was able to develop ideas for my research.

I thank my mentors who mold me as a scientist, hydrologist and educator. Early in my career as a graduate student, Dr. Vitaly Zlotnik and Dr. Stefan Kollet, colleagues from my days in Nebraska, were, and continue to be, role models and a source of good memories. Stefan taught me that expensive beer is worth the money. I thank my dissertation committee at New Mexico Tech for the guidance and support. Dr. Dan Stephens, despite his busy schedule running several offices of his consulting company, agreed to be part my dissertation committee and even drove down to Socorro for my oral

candidacy exam even though it would have been easier for him to do it through teleconferencing. I am glad I do not have to pay for his time. Dr. Glenn Spinelli has been very helpful in the latter part of this dissertation and is always available for advice. I thank Dr. Dave Love for his guidance and accompaniment in excursions for choosing potential field sites for other related studies and for sharing his expertise in Quaternary geology, geomorphology and sedimentology of the region. I am grateful to Dr. Fred Phillips for his constant encouragement to push the scientific envelope through his own example, by imposing unwavering standards, and through critique of my ideas. Early on when Dr. Rob Bowman was my adviser during my first year at Tech, he suggested that I consider having Dr. John Wilson as my primary research adviser, which I eventually followed, since my interests are more parallel with John's expertise. Rob will continue to be a model of unselfishness and putting the welfare of the student at the forefront. Lastly, I thank my adviser, Dr. John Wilson, for giving me this opportunity to work with him, for the guidance in the past and present as well as in my future career, and most importantly for being a wonderful illustration of a scientist who makes a difference through leadership and active engagement of the community, through the breadth and depth of his own work, and through altruistic and committed mentoring of aspiring scientists like me. I regret that I never took him up on his offer to baby sit our son for us.

Other professors and fellow graduate students at Tech have helped me along the way. Dr. Penelope Boston graciously shared the cost of the license for FEMLAB. Dr. Enrique Vivoni, although he is not officially part of my dissertation committee, has been an important source of career advice and has supported me by writing recommendation letters. I am privileged to have been surrounded by and share offices with outstanding

fellow graduate students and friends at Tech. Guys, there is light at the end of the tunnel. Thanks for the good times and conversations.

I thank Al and Diane Nelson (and their flock of cockatiels), formerly of Lincoln, Nebraska, for their generosity in helping Tracy and me soon after we moved to the United States until we could stand on our own feet.

I thank my relatives both here and in the Philippines. All my accomplishments would not have materialized if not for the sacrifices and the love and support of my parents, Marlito and Maria Lydia. *Papi at Mutti, natapos din ako.* My brothers, Marnilo and Manfred, have always influenced me. Finally, finishing graduate school and overcoming its challenges as well as what lie ahead will not have any meaning if I did not have the love of my life, Tracy, and our beautiful son, Makisig, to share it with.

Maraming salamat sa inyong lahat!

Table of Contents

Title Page	i
Abstract	
Acknowledgements	ii
Table of Contents	v
List of Tables	viii
List of Figures	ix
List of Appendices	xvii
CHAPTER 1: INTRODUCTION	1
1.1. Introduction and Research Questions	1
1.2. Organization of the Dissertation.	3
1.3. Chapter Descriptions	4
References	8
CHAPTER 2: IMPACT OF HETEROGENEITY, BEDFORMS AND STREAM CURVATURE ON SUBCHANNEL HYPORHEIC EXCHANGE.	9
2.1 Introduction	9
2.1.1 Relevance and previous work	9
2.1.2. Purpose of this study	14
2.2. Methodology	14
2.2.1. Background and model hydraulic properties.	14
2.2.2. Flow and transport modeling.	16
2.3. Results and Discussion	20
2.3.1. Hyporheic zone morphology.	20
3.3.2. Implications on short-term hyporheic zone dynamics	27

3.3.3. Flux calculations.	28
3.3.4. Mean residence times of particles.	30
2.4. Summary	34
References.	37

CHAPTER 3: HYDRODYNAMICS OF COUPLED FLOW ABOVE AND BELOW A SEDIMENT-WATER INTERFACE WITH TRIANGULAR BEDFORMS (LAMINAR CASE)	41
3.1. Introduction	41
3.1.1. Relevance and previous work	41
3.1.2. Purpose of this study	45
3.2. Methodology.	46
3.3. Results and Discussion	51
3.3.1. Eddy geometry and bottom pressure distribution	51
3.3.2. Interfacial exchange zone configuration and flux	55
3.3.3 IEZ Sensitivity to current and Reynolds Number in the water column	60
3.3.4. IEZ Sensitivity to bedform geometry	63
3.4. Limitations and Comparison to Experiments	65
3.5. Summary	69
References	72

CHAPTER 4: THE INFLUENCE OF AMBIENT GROUNDWATER DISCHARGE ON EXCHANGE ZONES INDUCED BY CURRENT-BEDFORM INTERACTIONS (LAMINAR CASE)	76
4.1 Introduction	76
4.2. Methodology	77
4.3. Results and Discussion	81
4.3.1. Eddies and pore-water flow divides	82
4.3.2. Effect of Reynolds Number	83
4.3.3. Residence times through the exchange zones	87
4.4. Summary.	89
References	91

CHAPTER 5: DUNES, TURBULENT EDDIES, AND INTERFACIAL EXCHANGE WITH POROUS MEDIA	93
5.1. Introduction	93
5.2. Methodology and Validation	96
5.2.1.1. General formulation for turbulent flow over dunes	96
5.2.1.2. Validation for turbulent flow	100
5.2.2. Linking the two-domains: pressure along the interface	101
5.2.3.1. Sequentially coupled simulation for porous media flow	104
5.2.3.2. Sequentially coupled simulation validation	105
5.3. Dynamical relationships between turbulent flow and porous media flow, and its effects on interfacial exchange	108

5.3.1. Eddy and dune geometry, bottom pressure distribution and the interfacial exchange zone	109
5.3.2. Fluxes and mean residence times	117
5.3.3. Predictive relationships	119
5.3.4. Towards fully coupled models and determining the nature of coupling	122
5.4. Summary	125
References	128
CHAPTER 6: EXCHANGE ACROSS A SEDIMENT-WATER INTERFACE WITH AMBIENT GROUNDWATER DISCHARGE (TURBULENT CASE)	132
6.1. Introduction	132
6.2. Methodology	134
6.3. Results and Discussion	136
6.3.1. IEZ spatial configuration and fluxes: gaining conditions	139
6.3.2. IEZ spatial configuration and fluxes: losing conditions	143
6.3.3. Exchange zone areas and residence times for both cases	145
6.3.4. On the similarity of gaining and losing IEZ metrics	147
6.3.5. Predicting the presence of an IEZ	151
6.3.6. Implications for biogeochemical and thermal processes	152
6.4. Summary	153
References	156
CHAPTER 7: THE EFFECTS OF CURRENT- BEDFORM INDUCED FLUID FLOW ON THE THERMAL REGIME OF SEDIMENTS	158
7.1. Introduction	158
7.2. Methodology	160
7.3. Results	167
7.3.1. The impact of dunes and comparison to pure conduction case	167
7.3.2. Effect of temperature dependent viscosity on interfacial flux and effect of dispersion on temperature distribution. . .	171
7.3.3. Gaining and losing conditions	175
7.4. Ecological and biogeochemical implications	180
7.5. Summary	182
References	185
CHAPTER 8: CONCLUSIONS AND RECOMMENDATIONS	189
8.1. Epilogue	189
8.2. Synthesis	189
8.3. Recommendations for Future Work	194
BIBLIOGRAPHY	196
APPENDICES	209

List of Tables

Table 2.1. Top boundary prescribed-head conditions and corresponding steady-state fluxes.	19
Table 2.2. Statistics of residence time distributions (natural log transformed and standard times).	32
Table 3.1. Results of regression of simulated d_z/L with Re (see Figure 3.7 and equations (3.7) and (3.8)).	63
Table 4.1. Fitting parameters corresponding to the curves in Figure 4.3.	86
Table 4.2. Fitted MMF models to Figure 4.4.	86
Table 7.1. Parameters used in the simulations	164

List of Figures

- Figure 2.1.** Topographic map of the Prairie Creek test site, Nebraska (elevation in m; contour interval = 0.2 m). Enlarged rectangular block is the model domain. . . . 15
- Figure 2.2.** Model domain with three-dimensional hydraulic conductivity field. 16
- Figure 2.3.** Longitudinal cross-sections taken at $x=10$ m: (a) and (b) show pathlines (gray) and isoconcentration lines (black) for a homogeneous and heterogeneous domain, respectively. Top prescribed-head boundary in (a) and (b) is described by the same sinusoidal function. 21
- Figure 2.4.** Steady-state simulations results (see Table 1 for model conditions). The gray surfaces are the 50 mg/L isosurfaces and represent the extent of the advective subchannel hyporheic zones. Model conditions and letter designations in Table 2.1 are shown beside the images. 22
- Figure 2.5.** Simulation results showing increasing influence of heterogeneity from (a) to (e). Dimensionless N (see explanation in text) and letter designations in Table 1 are shown beside the images. 24
- Figure 2.6.** Comparison of steady-state fluxes and mean residence times: (a and b) homogeneous vs. heterogeneous cases with similar (sinusoidal) head boundaries; (c and d) no transverse gradient vs. with transverse gradient top boundary condition under similar K setting; (e and f) linear vs. sinusoidal head top boundary condition under similar K setting. “ xX ” in the x -axis means that values were scaled X times to fit in the graph. Positive percentages in the graphs correspond to increases. Conditions for simulations as well as flux and residence time values are in Tables 1 and 2. 29
- Figure 2.7.** Histograms of natural logarithm of residence times plus fitted normal curves. Chart labels correspond to simulations in Tables 2.1 and 2.2. 31
- Figure 3.1.** (a) Schematic of model domain and system formulation. (b) Representative finite element mesh illustrating normal flux (small white arrows) through the bed surface, q_{int} , and average horizontal velocity in the water column (large white arrow), U_{ave} . (c) Typical solution for flow directions (arrows are of equal lengths and do not indicate magnitude); dashed line in the porous bed is a dividing streamline which separates the interfacial exchange zone from deeper zones

dominated by ambient underflow, the vertical distance from the trough of the bedform to the deepest section of this streamline defines the depth of the exchange zone, d_z . (d) Close up view of the eddy. (Simulation for larger $H/L=0.143$ and smaller $L_c/L=0.74$ to make eddy more prominent.) 49

Figure 3.2. Typical solutions for normalized pressure (indicated by color spectrum) and flow directions (arrows are of equal lengths and do not indicate magnitude) over and through a dune. Shown are flow fields (a-f) for six Reynolds numbers ($Re=6, 59, 174, 569, 1124, 2221$) depicting the development of the eddy, and the collocation of eddy reattachment points and pore-water flow divides. Dashed lines are streamlines that divide the porous bed into distinct flow cells. ($H =0.05$ m, $L=1.0$ m, $H/L=0.05$, $L_c/L=0.9$, $d_b = 2.0$ m, $d_{wat} =0.45$ m, $k= 1 \times 10^{-10}$ m/s.)53

Figure 3.3. (a) Relationship of eddy length, L_e (squares), and interfacial exchange zone depth, d_z , (x's) with Re . The horizontal length of the eddy is measured from the detachment to reattachment points, across the trough. (b) Relationship between IEZ depth and area, A_z . (c) Interfacial exchange flux density, q_{int}^* as a function of (c) Re and (d) pressure drop between points of maximum and minimum bottom pressure (where the pressure drop is written in terms of head, $h=p/\rho g$). Conditions used in simulations are the same as in Figure 3.2. The six simulations in Figure 3.2 are indicated by encircled x's and corresponding letter labels in (b). 54

Figure 3.4. Simulated pressure (normalized p^*) profiles for different Re taken along the bed surface for the conditions of Figure 3.2 (letter scheme is same as in Figure 3.2). Location x is measured downstream from the trough. Gray area illustrates the corresponding bedform geometry. 55

Figure 3.5. Depth profiles of normalized magnitudes of pore-water velocities (q is Darcy velocity and q_{max} is maximum velocity just below the interface at the crest) taken below the crest (hollow symbols) and below the trough (solid symbols) for different Res . Depths are taken from the crest. Conditions are the same as in Figures 3.2d ($Re=569$).58

Figure 3.6. Plot of interfacial exchange zone vertical extent, d_z , versus d_z/d_b with underflow in the sediments. When the depth of the impermeable boundary, d_b , is sufficiently large ($d_z/d_b <0.7$), the simulated extent d_z approximates that for an infinite bed. Conditions are the same as in Figure 3.2 except for variable d_b ($Re=1000$). 59

Figure 3.7. Dependence on Re of dimensionless exchange depth d_z/L (a) and dimensionless bed-surface exchange flux density q_{int}^* (b). ($L_c/L=0.9$, $H=0.05$ m, $k= 1 \times 10^{-10}$ m².) 61

Figure 3.8. Effect of bedform asymmetry, L_c/L , on IEZ depth, d_z/L (a) and on IEZ flux density, q_{int}^* (b); in all cases flow is from left to right. ($L=1.0$ m, $H/L=0.05$, $H =0.05$ m, $k= 1 \times 10^{-10}$ m².)65

Figure 3.9. Simulated pressure (normalized p^{**} , where p^{**} is normalized similar to p^* except that the ambient gradient is removed) profiles for different Re taken along the bed surface for a ripple bedform [Elliott and Brooks, 1997a]; gray line corresponds to normalized pressure distribution based on measurements by Fehlman [1985] over a similar bedform, as presented in Elliott and Brooks [1997a]. ($L=0.178$ m, $L_c=0.132$ m, $H=0.0254$ m, $H/L=0.143$, $d_b = 0.135$ m, $d_{wat} = 0.0645$ m., $k= 2 \times 10^{-10}$ m².) 68

Figure 4.1. (a) Schematic of model domain and system formulation. (b) Representative finite element mesh illustrating exchange flux through the bed surface, q_{int} , prescribed basal flux, q_{bas} , and average horizontal velocity in the water column, U_{ave} . In all simulations $L_c/L= 0.9$, $H=0.05$ m and $d_{wat}=0.45$ m. 79

Figure 4.2. Plots of water column flow streamlines (white lines) and vorticity (color contours), porous bed velocity magnitude (color contours, $Q^*=Q/Q_{max}$, where Q and Q_{max} are the velocity magnitude and the maximum based on all simulations, respectively) and direction (small black arrows), and exchange zone boundaries for different dimensionless ambient basal fluxes, $q_{bas}^*= 0, 5.5e-6, 1.8e-6, 1.8e-5$ and $1.8e-4$ for a-e, respectively. The dashed black line is a dividing streamline which separates the interfacial exchange zone from deeper zones dominated by ambient underflow or upwelling groundwater flow; the vertical distance (see (a)) from the trough to the deepest section of this streamline defines the depth of the exchange zone, d_z . Also illustrated are the normal flux through the SWI (large gray arrow in b) induced by current-bedform interactions, q_{int} . $Re=1500$ for all simulations. $H= 0.05$ m, $L=1.0$ m, and $d_b= 2$ m. 80

Figure 4.3. Dependence on Re of normalized exchange zone depth d_z/L (a, b) and dimensionless interfacial flux q_{int}^* (c, d). Shown are results for different bedform aspect ratios (H/L ; $H=0.05$ m for all cases) and dimensionless basal fluxes q_{bas}^* . The curves in (b) and (d) are fitted for different q_{bas}^* (see Table 4.1 for fitting parameters); MMF fits are shown in (b) and linear fits are shown in (d). Flow in the water column may be transitional or turbulent at higher Res . No additional considerations were made to correct for turbulent flow. Thus, the simulation results at high Res may be inconsistent with real scenarios but are still presented because thresholds for the different bedform shapes are not yet well established. d_b varies from 2 m to 2.5 m where cases with larger L corresponding to larger d_b 84

Figure 4.4. Relationship between Re_{crit} and q_{bas}^* including fitted MMF models (see Table 4.2). 87

Figure 4.5. Relationship of t^* , q_{int}^* and A^* with q_{bas}^* . $Re=500$ for all simulations; $H=0.05$ m, and $L=1$ m. 88

Figure 5.1. Modeling formulation, numerical grids (a,c) and typical results (b,d) for

turbulent flow in the water column (a,b) and porous media flow (c,d). Mean flow is from left to right. The color scale for the two outputs, representing pressure, are similar but not exactly the same; warmer colors: higher pressure, cooler colors: lower pressure. The top right figure shows streamlines while the bottom right figure shows flow directions. Dune length $L=1.0$ m. The streamlines in (d) define the interfacial exchange zone (IEZ) with area A_z ; this streamline separates all the streamlines originating from and returning to the interface from the deeper part of the porous media that is dominated by the mean flow from left to right (i.e., underflow). The depth of the IEZ, d_z , is the vertical distance between the trough and the deepest portion of the streamline delineating the IEZ. 97

Figure 5.2. Comparison of experimental dimensionless water-column velocity profiles from *van Mierlo and de Ruiter* [1988] to simulated velocity profiles. Flow is from left to right. Profile numbers in the top locate the velocity profiles shown below. Note that both axes of the velocity profiles are nondimensional. The inlet average velocity is $U_o=0.63$ m/s and the inlet depth is $d_o=0.29$ m; these values are used for normalization.102

Figure 5.3. Comparison of measured pressure profiles along an impermeable dune surface (hollow squares) with simulated pressure profiles (gray and black curves). Flow in the water column is from left to right. The Run numbers correspond to original numbering scheme in *Fehlman* [1985]. Two simulated curves are presented. *Fehlman* defines the pressure change (ΔP) as the difference between the interpolated pressure at the crest and the pressure at other measurement points. The black curve corresponds to ΔP 's calculated based on the original definition. The gray curve corresponds to the simulated pressure difference referenced to a point just upstream of and not exactly at the crest. The geometry of the experimental dune is illustrated. Calculated average velocities taken at the crest are 0.43 m/s and 0.86 m/s, for Runs 4 and 10 respectively. Flow depth at the crest is 0.15 m for both runs. 103

Figure 5.4. a) Comparison of dye streaks (black curves) from *Elliott's* [1990] Run 9 with simulated streamlines (dashed gray curves); b) comparison of dye penetration fronts (black lines) mapped at 75, 150, 320, and 650 minutes to simulated advective solute fronts (dashed gray curves) for the same run. Flow in the overlying water column (not shown) is from left to right.107

Figure 5.5. Dimensionless eddy length (L_e/S or L_e/H , S =back-step height) as a function of Reynolds Number (Re). The data in (a) are from experiments for flow past a backward-facing step by *Armaly et al.* [1983], while those in (b) and (c) are from our numerical simulations for dunes. Note that dimensionless eddy lengths and Re 's are computed differently in *Armaly et al.* [1983]. *Armaly et al.* [1983], based on the behavior of the eddy length, suggest that their experiments covered the three flow domains labeled in (a) and indicated by different shades. Data shown in (b) include results from laminar flow simulations (hollow squares) and turbulent flow simulations (solid circles). Results in (c) are from turbulent flow

simulations representing different dune steepness (H/L); $L=1.0$ m and $L_c/L=0.9$ in all cases. 111

Figure 5.6. Part a) shows dimensionless interfacial exchange zone depth (d_z/L) as a function of Reynolds Number (Re) for laminar and turbulent flow simulations; $H/L=0.05$, $L_c/L=0.9$. Part b) shows simulated d_z/L for turbulent flow over different dune steepnesses (H/L ; $L=1.0$ m and $L_c/L=0.9$ in all cases). Also presented in (b) is the dimensionless area of the IEZ (A_z/L^2) for the case where $H/L=0.05$, indicated by gray-filled triangles. Shown in (c) are the dimensionless interfacial fluxes (q_{int}^*) corresponding to the same cases in (b). Gray-filled triangles in (c) correspond to the dimensionless residence times (t_r^*) for $H/L=0.05$. Curves in (c) are all fitted power models with $R^2>0.99$ in all cases. ... 114

Figure 5.7. Flow and pressure fields for simulations with different H/L 's and $L_c/L=0.9$ (a) and different L_c/L 's with $H/L=0.05$ (b). Gray lines delineate the interfacial exchange zone and two flow cells within it. Pressure is normalized as $p^*=(p-p_{min}) / (p_{max} - p_{min})$, where p is the pressure, and p_{min} and p_{max} are, respectively, the minimum and maximum for each simulation. p_{min} and p_{max} are located near where the streamlines originate from at the top boundary. Illustrated in both panels are streamlines in the water column which delineate the eddy. 116

Figure 5.8. (a) and (c) are dimensionless pressure profiles taken along the sediment-water interface for the different-dune-shape simulations presented in Figure 7a and 7b, respectively. Pressure is normalized as $p^{**}=(p-p_{mid}) / (p_{max} - p_{min})$, where p_{mid} is the midpoint between the maximum and minimum pressures, p_{max} and p_{min} . The ambient pressure gradient has been removed in these profiles. (b) and (d) show the x -locations of the critical pressure points and eddy detachment and reattachment points for the same simulations in (a) and (c). The troughs are located at $x=0$ and 1 m for all figures. In (b) the crest is at $x=0.9$ m for all 5 cases; in (d) the crest location increases from $x=0.5$ to 0.9 m in increments of 0.1 m (consistent with the depicted range in L_c/L). 117

Figure 5.9. Normalized interfacial exchange zone flux density as a function of the head gradient along the sediment-water interface due to current-dune interactions, $L_c/L=0.9$ 118

Figure 5.10. (a) Dimensionless exchange zone depths scaled by H/L raised to a power $c=0.218$. (b) Dimensionless flux similarly scaled with $(H/L)^c$ with $c=2.18$. The lone fitting parameter for the power-function in (b) is $a=1.53 \times 10^{-12}$; b is fixed as 2.18 and is equal to c . $L_c/L=0.9$ in all simulations. 121

Figure 6.1. Schematic representation of the periodic flow domain, depicting geometric parameters- height (H) and length (L)- and fluxes- basal (q_{bas}) and interfacial (q_{int}). The depth of the interfacial exchange zone (IEZ), d_z , is the vertical distance from the trough to the deepest portion of the streamline enveloping the region

wherein water flows from and then back into the water column. Small arrows correspond to flow directions. 135

Figure 6.2. The top row shows pressure fields (color) and flow directions (arrows) for gaining conditions ($q_{bas}^*= 9.8 \times 10^{-2}$) at different Reynolds number (Re). The bottom row shows the same for losing conditions ($q_{bas}^*= -9.8 \times 10^{-2}$). Pressure is normalized as follows: $p^*=(p-p_{min})/(p_{max}-p_{min})$ where p^* is normalized pressure, p is pressure, p_{max} and p_{min} are the maximum and minimum pressures for each simulation. The gray streamlines delineate the IEZs. $H/L=0.05$ and $L=1.0$ m for all cases. 138

Figure 6.3. Gaining conditions. Dimensionless IEZ depths (d_z/L) and interfacial fluxes (q_{int}^*) for bedforms with different bedform steepness (H/L) and subjected to different upward AGD. The horizontal gray lines in the left column indicate the IEZ depth for the base case without AGD [Cardenas and Wilson, 2006c]. The solid curves in this column are MMF (6.3) fits to the simulation data. 140

Figure 6.4. Critical Reynolds numbers, Re_{crit} , for bedforms with different bedform steepness (H/L) and subjected to different AGD (q_{bas}^*). (a) shows results for gaining conditions and (b) shows results for losing conditions. 142

Figure 6.5. Losing conditions. Dimensionless IEZ depths (d_z/L) and interfacial fluxes (q_{int}^*) for bedforms with different bedform steepness (H/L) and subjected to different downward AGD. The horizontal gray lines in the left column indicate the IEZ depth for the base case without AGD [Cardenas and Wilson, 2006c]. The solid curves in this column are MMF (6.3) fits to the simulation data. 144

Figure 6.6. The left and right columns show results for gaining and losing conditions, respectively, with AGD magnitude $|q_{bas}^*|= 9.8 \times 10^{-2}$. In all cases $H/L=0.5$, $L=1.0$ m. (a) and (b) illustrate the extent of the IEZs for different Re s (labels). (c) and (d) show the power relationships (solid lines) between dimensionless IEZ area (A_z/L^2) and depth (d_z/L) for the gaining and losing cases in (a) and (b). The coefficients for the power models in (c) are $a=1.046$ and $b=1.377$, while in (d) they are $a=1.029$ and $b=1.358$; $R^2>0.99$ in both cases. (e) and (f) show the dimensionless IEZ areas (hollow triangles) and residence times (t_r^* ; solid triangles, $q_{bas}^*=9.8 \times 10^{-2}$; solid circles, $q_{bas}^*=0$) as a function of Re . MMF models (6.3) (solid lines) are fitted to the $A_z/L^2(Re)$ data; $R^2>0.99$ for both cases. The dashed line in (e) and (f) represent A_z/L^2 for the base case without AGD ($q_{bas}^*=0$) [Cardenas and Wilson, 2006c]. 146

Figure 6.7. Superposed plot of pressure gradients, as a function of Re , along the SWI (dP_{swi}), between the lateral spatially periodic boundaries which drives underflow (dP_{und}) and the current in the water column, and the vertical gradient (dP_{bas}) along the bottom of the sediments due to the prescribed basal flux. Results plotted correspond to the simulations in Figure 6.2 (gaining conditions only, but with a

sign change for dP_{bas} the pressure gradients for losing conditions are exactly the same). 150

Figure 6.8. Pressure gradient along the SWI, dP_{swi} , as a function of Re scaled by bedform steepness, H/L . The fitted power model ($R^2 > 0.99$) has coefficients $a = 1.028 \times 10^{-12}$ and $b = 2.423$ 152

Figure 7.1. Numerical modeling formulation and sample grids. The gray lines bounding the domains illustrate boundary conditions for the fluid flow (turbulent and Darcy) models while the black lines and bold labels represent boundaries for the heat transport model. q_{bas} , the prescribed basal flux represented by arrows at the bottom of the sediment domain suggesting upward flux, is zero and downwards in some simulations. The governing equations are usually solved sequentially in the following order: 1) RANS- $k-\omega$, 2) groundwater flow equation, and 3) heat advection-conduction-dispersion. $L = 1.0$ m, $H = 0.05$ m, $d_{wat} = 0.5$ m and the crest is at $0.9L$ in all simulations. 161

Figure 7.2. Typical prescribed temperature, $T(t)$, as described by equation (7.8), used as a Dirichlet top boundary for the sediment domain and representing the sediment-water interface. The timing is similar for all simulations, i.e., no phase shift, but the temperature amplitude (T_{amp}) and average (T_{ave}) vary in some simulations. The circles correspond to the timing of the simulation results presented in Figures 7.3, 7.7, and 7.8. 165

Figure 7.3. Temperature fields through time for cases where the water column is neither gaining nor losing net water, i.e., the bottom boundary is a no-flow boundary and $q_{bas} = 0$. Results are shown for simulations with different permeability values (second to fourth rows) as well as a reference simulation where fluid advection due to current-bedform effects is ignored (the pure conduction case). The rightmost column shows plots of normalized temperature amplitude, T^* , described by equation (7.11). Small arrows indicate flow directions and not magnitude. 168

Figure 7.4. T^* , normalized temperature amplitude variation (7.11), plots for cases with varying permeability k_p and boundary amplitude T_{amp} 170

Figure 7.5. Fitted polynomial function, equation (7.13), to define the viscosity-temperature relationship used in simulations for testing sensitivity of flux through the interfacial exchange zone to viscosity (a). The shaded and hatched areas indicate the ranges in temperature, and the dashed line indicates the average temperature, used in the sensitivity simulations. Relative change in interfacial exchange zone flux through a diurnal period for three scenarios (b) whose temperature range correspond to the similarly colored temperature regions in (a); the dashed line corresponds to the hatched region (a). 172

Figure 7.6. T^* , normalized temperature amplitude variation (7.11), plots for cases considering viscosity effects but ignoring mechanical dispersion (a), ignoring both

viscosity effects and mechanical dispersion (b), and ignoring viscosity effects while considering mechanical dispersion (c). $k_p=5 \times 10^{-10} \text{ m}^2$, $T_{ave} = 20^\circ\text{C}$, and $T_{amp} = 3^\circ\text{C}$ for all cases.174

Figure 7.7. Temperature fields through time for ambient groundwater discharge where the water column is losing net water, i.e., the bottom boundary is prescribed a normal downward flux, q_{bas}^* (7.13). Results are shown for simulations with different basal flux values (first to third rows). The rightmost column shows plots of normalized temperature amplitude, T^* (7.11). The two bottom rows have similar q_{bas}^* . Like the rows above, the third row considers current-bedform effects (i.e., the pressure at the top is taken from the turbulent flow model) while the bottom row is based on a top boundary with a uniform pressure distribution. $k_p=5 \times 10^{-10} \text{ m}^2$ in all simulations. Small arrows indicate flow directions and not magnitude.176

Figure 7.8. Temperature fields through time for ambient groundwater discharge where the water column is gaining net water, i.e., the bottom boundary is prescribed a normal upward flux, q_{bas}^* (7.13). Results are shown for simulations with different basal flux values. The rightmost column shows plots of normalized temperature amplitude, T^* (7.11). The top two rows have similar q_{bas}^* . The second row (and rows below) considers current-bedform effects (i.e., the pressure at the top is taken from the turbulent flow model) while the top row is based on a top boundary with a uniform pressure distribution. $k_p=5 \times 10^{-10} \text{ m}^2$ in all simulations. Small arrows indicate flow directions and not magnitude. 178

List of Appendices

Appendix I Tabulation of Results from Chapter 3	210
Appendix II Tabulation of Results from Chapter 4	212
Appendix III Discussion of CFD-ACE+ k- ω model and Tabulation of Results from Chapter 5	216
Appendix IV Tabulation of Results from Chapter 6	231
Appendix V Results of SF ₆ Tracer Tests Conducted in the Rio Grande.....	254
Appendix VI Comment on “Flow resistance and bed form geometry in a wide alluvial channel” by S-Q Yang, S-K Tan and S-Y Lim	259

This dissertation is accepted on behalf of the
Faculty of the Institute by the following committee:

Adviser

Date

I release this document to the New Mexico Institute of Mining and Technology.

Student's Signature

Date

CHAPTER 1

INTRODUCTION

1.1. Introduction and Research Questions

Interfaces are ubiquitous in hydrologic systems. Interfaces are present from the micro-scale (e.g., biofilms around a single grain surrounded by water), up to the global scale (e.g., the land-atmosphere or land-ocean boundary). The physico-chemical nature of interfaces regulates the connectivity of different reservoirs of the water, nutrient and carbon cycles, and in turn affects the physical, chemical and biological processes occurring within discrete reservoirs. Across a range of spatial scales, thermal and chemical energy is advected across interfaces with the movement of fluids. When exchange and transport is dominated by advection, understanding of ecological and biogeochemical processes necessarily begins with knowledge of the underlying hydrodynamic processes. The hydrodynamics *within* hydrologic reservoirs has been studied for many decades, if not centuries, although some fundamental questions remain unanswered. There is much less knowledge concerning the hydrodynamic processes occurring at or *across* interfaces between reservoirs, about which most fundamental questions have not even been asked.

In recent years several government agencies and scientific organizations have posed their research questions or agenda around interfaces and the interaction between components of the water cycle across interfaces. The National Science Foundation's

Advisory Committee for Environmental Research and Education [2005] recommended that "... the National Science Foundation focus on water as a unifying theme for Complex Environmental Systems research...Water related research requires enhanced understanding of processes along interfaces,..., and improved coupling of biological and physical processes." The Department of Energy and the National Science Foundation sponsored a workshop entitled *Water: Challenges at the Intersection of Human and Natural Systems*. The workshop report [Smyth and Gephart, 2005] emphasizes similar research directions by identifying "Coupling of cycles and process, with emphasis on the role of interfaces" as one of three scientific themes for interdisciplinary water research. The National Research Council's Committee on Hydrologic Science [2004] earlier recognized the importance of characterizing and quantifying fluxes across interfaces in a report entitled *Groundwater Fluxes Across Interfaces* [NRC Committee on Hydrologic Science, 2004]. In the Statement of Task it mentions that "Fluxes to and from groundwater systems are critical to most aspects of hydrologic sciences, and therefore to its related sister sciences, but these fluxes are traditionally neglected or estimated using simple and unverified assumptions." More specific research questions were posed in the report *Emerging Research Questions for Limnology- The Study of Inland Waters* [Wurtsbaugh et al., 2003] released by the American Society of Limnology and Oceanography. "Hydrodynamic Controls of Biogeochemical and Ecosystem Activity Across Space and Time" was one of four themes that was discussed under which they posed the three following questions:

1. "How do hydrodynamic processes control formation and persistence of chemical and biotic patches within lakes and sediments?"

2. “What are the dominant hydrodynamic processes occurring at interfaces and how do they regulate biogeochemical fluxes across interfaces?”
3. “What are the implications of the spatial and temporal heterogeneity created by turbulent events and coherent flows for spatial and temporal patterns in biogeochemical processes?”

This dissertation is centered on and addresses the research themes and questions above, focusing on the interface between a water column –a stream, river, lake, estuary or ocean – and an underlying porous media. More specifically, this dissertation is a detailed investigation of the dynamics of fluids, heat and solutes along sediment-water interfaces (SWIs) dominated by current-topography driven advective exchange (see §1.3), at scales of centimeters to several meters. The dynamics along SWIs are first investigated through groundwater flow models based on extensive field information and then through virtual experiments based on high-fidelity multiphysics numerical simulations of coupled hydrodynamic (both laminar and turbulent flow in the water column and Darcy flow in the sediments), energy and solute transport models.

1.2. Organization of the Dissertation

Each succeeding chapter within this dissertation is written (submitted or published) as an individual manuscript for journal publication, with each chapter having its own Introduction (and brief literature review), Methodology, Results, Summary and References sections. This introductory chapter presents a general description of the succeeding chapters and highlights important results. A detailed introduction of the entire dissertation is not presented here. Equations and variables are defined and sometimes re-introduced in each chapter. Pertinent data in each chapter are presented in a corresponding Appendix. An unpublished report on a field tracer test and a commentary

paper that has been accepted for publication are also included as Appendices. All the references cited within each chapter are collected in a single Bibliography.

1.3. Chapter Descriptions

The chapters are arranged in a manner such that the questions addressed and techniques employed to answer them increase in complexity, with each chapter more or less building on concepts from previous chapters. First, I define important terms. The *hyporheic zone* (HZ) refers to the area adjacent to and below a stream that receives water from and transmits it back to the stream. In essence, the hyporheic zone is the groundwater-surface water interface. We introduce and apply a more general term- *interfacial exchange zone* (IEZ)- to include areas in sediments, whether underneath rivers, lakes, estuaries, or oceans, that receive and transmit water from their overlying surface water bodies. Fluid flow through these zones is referred to as *interfacial exchange* and is a generalization for *hyporheic exchange*. These terms are used interchangeably in this manuscript.

In Chapter 2 (Impact of Heterogeneity, Bedforms and Stream Curvature on Subchannel Hyporheic Exchange), the relative impacts on hyporheic exchange of a streambed with a heterogeneous permeability field, in the presence of irregular pressures along the interface representing the impact of bedforms, and in the presence of bends along rivers, are illustrated and quantified. This part of the study takes the “groundwater” perspective and is based on numerical modeling using the popular MODFLOW code for simulating groundwater flow in the streambed. The stream, in this case, is only represented by defining simple boundary conditions on the top of the streambed. The major result of this study is the illustration that, indeed, the permeability structure of the

streambed exerts an important effect on the exchange between groundwater and surface water, but that its effects can be overpowered by external forcing mechanisms of groundwater flow such as the presence of bedforms and stream curvature. Dimensionless numbers summarizing the relative impacts of these factors on groundwater-surface water exchange are presented.

In Chapter 3 (Hydrodynamics of Coupled Flow above and below a Sediment-Water Interface with Triangular Bedforms), more sophisticated modeling approaches are used in order to investigate the fundamental physics of coupled fluid flow above and below the SWI. Fluid flow above dunes is simulated with a laminar flow model of the water column. The results of these simulations are sequentially coupled to a groundwater flow model for the sediments. This allows for investigation of the coupling of the dynamics of flow in the water column and the underlying sediments. It is well known that the presence of topography along the SWI results in an irregular pressure distribution which drives fluid circulation, or interfacial exchange, within the sediments. A highlight of this study is the direct illustration that the irregular pressure distribution along a triangular bedform surface is due to both a Bernoulli effect caused by the expansion and contraction of the channel and by flow separation or formation of an eddy above the bedforms. Simulation results show that infiltration into the sediments is centered around a pressure maximum located at the eddy reattachment point, on the stoss face of the dune, and exfiltration back to the water column, which is focused at the pressure minimum along the crest where the eddy detaches. Simulation of multiple dynamic and geometric configurations allowed for the derivation of equations for predicting the spatial extent of interfacial exchange within the sediments and the flux of water through this interfacial

exchange zone. These equations show that the IEZ depth is dependent on the Reynolds number (Re) in the water column via a function similar to the Michaelis-Menten model, while flux through the IEZ is dependent on the Re via a power function.

Chapter 4 (The Influence of Ambient Groundwater Discharge on Exchange Zones Induced by Current-Bedform Interactions) is an extension of Chapter 3, where it was assumed that the water column is neither gaining nor losing net water. The influence of ambient groundwater discharge (AGD) on interfacial exchange is investigated and discussed here, for the case where the water column is gaining net water. The methodology follows that in Chapter 3 with a minor modification in the lower porous media boundary condition to represent AGD. The highlight of this chapter is the illustration that IEZs can be present under gaining surface water bodies. Criteria are presented for thresholds where IEZs collapse, due to being overpowered by AGD. They encompass the competition between AGD and the driving forces for interfacial exchange. Once again, multiple dynamic and geometric settings are investigated.

Most natural flows in water columns are turbulent. Chapters 3 and 4 assume laminar flow in the water column; laminar flow in this context is rare in nature. The lessons learned from laminar-flow Chapters 3 and 4, and the recognition of their limitations, are used in constructing modeling studies considering turbulent flow above bedforms. The results of the turbulent flow studies are presented in Chapter 5 (Dune, Turbulent Eddies, and Interfacial Exchange with Porous Media) and Chapter 6 (Exchange Across a Sediment-Water Interface with Ambient Groundwater Discharge). Chapter 5, which is basically the turbulent flow counterpart of Chapter 3, discusses similar issues in Chapter 3. The major result in Chapter 5 is that the presence of smaller

eddies in the turbulent water column, compared to the larger eddies in laminar flows, results in a shallower IEZ that is insensitive to Re . IEZ flux is also dependent on Re via a power function under turbulent conditions, similar to the laminar flow conditions, but with much larger flux rates. Chapter 6, the turbulent flow counterpart of Chapter 4, shows similar competition between AGD and interfacial exchange but now under turbulent flow conditions in the channel. Thresholds, where an IEZ does not form due to overpowering by AGD, are quantified. Predictive functional relationships between IEZ flux and IEZ depth with Re are developed.

Chapter 7 (The Effects of Current-Bedform Induced Fluid Flow on the Thermal Regime of Sediments) examines heat transport within sediments through sequential numerical simulation of turbulent flow, groundwater flow, and heat transport. The simulations account for the effects of the hydrodynamic processes explored in Chapters 5 and 6. The thermal forcing is a diurnally varying temperature in the water column. The simulations show that two-dimensional current-bedform induced fluid flow results in a complicated but predictable transient temperature distribution within the sediments. When AGD is present, whether towards or away from the SWI, the influence of current-bedform induced heat advection becomes subdued until, at high AGD, fluid flow and heat transport become essentially vertically one-dimensional. Zones within the sediments that experience strong diurnal temperature variations are found horizontally adjacent to zones lacking any substantial temperature variations. The zones with weak temperature variations are found close to crests of dunes where pore water is upwelling from deeper areas of the sediments, while strong temperature variations are observed underneath areas where water is infiltrating into the sediments from the water column.

Conclusions and Recommendations are presented in Chapter 8.

References

- Advisory Committee for Environmental Research and Education, *Complex Environmental Systems: Pathways to the Future*, National Science Foundation, Washington, DC, 12 pp., 2005.
- Committee on Hydrologic Sciences, *Groundwater Fluxes Across Interfaces*, National Research Council, National Academies Press, Washington DC, 85 pp., 2004.
- Smyth, R. L, and J. M. Gephart (eds), *Water: Challenges at the Intersection of Human and Natural Systems*, US Department of Energy, 50 pp., 2005.
- Wurtsbaugh, W., J. Cole, D. McKnight, P. Brezonik, S. MacIntyre, and K. Potter (eds), *Report on the Workshop on Emerging Research Questions for Limnology: The Study of Inland Waters*, American Society of Limnology and Oceanography, Waco, Texas, 50 pp., 2003.

CHAPTER 2

IMPACT OF HETEROGENEITY, BED FORMS AND STREAM CURVATURE ON SUBCHANNEL HYPORHEIC EXCHANGE

(This chapter is published as: Cardenas, M. B., J. L. Wilson, and V. A. Zlotnik, Impacts of heterogeneity, bed forms, and stream curvature on subchannel hyporheic exchange, *Water Resources Research*, 40, W08307, doi: 10.1029/2004WR003008, 2004.)

2.1 Introduction

2.1.1 Relevance and previous work

A “hyporheic zone” (or HZ for brevity) is an area where water infiltrates from streams then flows through streambed sediments and stream banks and returns to the surface after relatively short pathways. These zones are important for two major reasons. They provide hyporheic and riparian organisms critical solutes, including nutrients, and dissolved gases [Triska *et al.*, 1989; Triska *et al.*, 1993; Findlay, 1995; Harvey and Fuller, 1998; Doyle *et al.*, 2003]; they also control the distribution of solutes and colloids from bedform to watershed scales [Elliot and Brooks, 1997a; Woessner, 2000; Packman and Brooks, 2001; Sophocleous, 2002; Kasahara and Wondzell, 2003]. Understanding of HZ exchange improves through integrated modeling and field observations, supported by laboratory experiments.

Several methods have been proposed for modeling hyporheic exchange, and are reviewed by *Packman and Bencala* [2000]. Among the simplest of models are those that describe the exchange of solutes between rivers and adjacent transient storage zones as linear first-order mass transfer processes with lumped exchange coefficients, such as those by *Bencala and Walters* [1983] or *Young and Wallis* [1986]. Exchange models based on one-dimensional diffusive processes, transverse to the channel, are slightly more sophisticated [*Worman*, 1998; *Jonsson et al.*, 2003]. Other models consider the effects of early non-Fickian transport of solutes from the substratum to the stream [*Richardson and Parr*, 1988]. Parameters in these models are determined by empirically matching model output to actual solute breakthrough curves in laboratory experiments [*Marion et al.*, 2002] and detailed field experiments [*Harvey et al.*, 1996; *Choi et al.*, 2000; *Jonsson et al.*, 2003]. In certain settings, empirical determination of these parameters is not straightforward, and sometimes not possible, suggesting that these models are conceptually inconsistent with some environments [*Harvey and Fuller*, 1998; *Harvey and Wagner*, 2000]. A major source of discrepancy is that these simple models do not completely and realistically represent the hydrodynamics involved in hyporheic exchange.

In some cases, exchange processes between streams and aquifers are dominated by advection rather than diffusion. Two important mechanisms for this type of hyporheic exchange have been proposed. The first is driven by advective flow induced by head gradients which are in turn generated by streambed topography due to bed forms or other irregularities such as logs and boulders and/ or water surface topography. The second is due to the dynamic behavior of bed forms which temporarily trap and release water as

they migrate. These two mechanisms are referred to as “pumping” and “turnover” [Elliot and Brooks, 1997a; Packman and Brooks, 2001].

Several studies have investigated the mechanics of pumping from a theoretical perspective, often supported by experiments. *Ho and Gelhar* [1973] present results of analytical and experimental studies on turbulent flow with wavy permeable boundaries. *Thibodeaux and Boyle* [1987] propose a simple physically-based model supported by laboratory observations. *Shum* [1992] examines the effects of the passage of progressive gravity waves on advective transport in a porous bed. *Savant et al.* [1987], applying the boundary element numerical method, replicate flume observations of flow along a vertical plane induced by head fluctuations. More sophisticated analytical models, supported by flume experiments and numerical modeling, consider the transfer of solutes and colloids through mobile bed forms [Elliot and Brooks, 1997a; Elliot and Brooks, 1997b; Packman and Brooks, 2001]. *Worman et al.* [2002] present a model that couples longitudinal solute transport in streams with solute advection along a continuous distribution of hyporheic flow paths. All of these theoretical, experimental and numerical studies are confined to two-dimensional (2D) vertical domains, taken longitudinally along the channel, either due to their experimental setup or to enable simpler theoretical or numerical analyses.

There has also been considerable work on 2D essentially horizontal flow models. Examples of reach scale 2D numerical modeling of hyporheic exchange can be found in *Harvey and Bencala* [1993], *Wondzell and Swanson* [1996] and *Wroblicky et al.* [1998]. The first example conceptually studies the impact of stepped-channels on surface-subsurface exchange. The last two examples are based on extensive data sets that allowed

calibration of the flow models. All three cases demonstrate the viability of using numerical models to simulate horizontal flow into, through and out of channel banks while neglecting vertical exchange.

There are a few fully three-dimensional (3D) simulations of hyporheic exchange. For example there are channel scale (hundreds of meters) studies by *Storey et al.* [2003], who investigate key factors controlling hyporheic exchange, and by *Kasahara and Wondzell* [2003], who examine the impacts of morphologic features. *Storey et al.* [2003] demonstrate that the homogeneous hydraulic conductivity (K) of the alluvial deposits controls the rate and extent of hyporheic exchange; no hyporheic exchange will occur if the K of the streambed is below a certain threshold.

Some of the models mentioned above consider heterogeneity at larger spatial scales. For instance, *Kasahara and Wondzell* [2003] interpolated slug test data by assigning K values to regions around wells using the Thiessen Polygon method. *Storey et al.* [2003] employed spatially variable aquifer and streambed hydraulic properties that varied at a scale on the order of tens of meters. However, owing to their scales and resolution, all of these models ignore the finer scale heterogeneity typical of streambeds [*Bridge*, 2003]. This limitation is widely recognized by investigators of hyporheic processes, and is best summarized by *Packman and Bencala* [2000]. “Some additional complexities typically found in the natural environment, such as heterogeneity in the bed sediment, have also been omitted from the current models. Thus, even though these models are useful because they include process-level understanding, their application has been limited.” Even earlier *Harvey and Bencala* [1993] stated “...the influence of heterogeneous hydraulic properties of the alluvium on surface-subsurface water exchange

is a high priority to be considered in future research”. Is there field evidence to confirm this speculation on the importance of heterogeneity? *White's* [1993] observed temperature distributions at a site in the Maple River, northern Michigan, from which he inferred HZ geometry, appear to confirm this importance. Stronger confirmation comes from field tracer tests by *Wagner and Bretschko* [2002], which suggest that bed scale variability of K results in a complex 3D network of flow paths, and from which they deduce that heterogeneity is responsible for the patchy distribution of benthic invertebrates at their study site in Austria. What modeling has been done to test the importance of heterogeneity? A recent compilation of research on modeling of HZ processes listed no efforts addressing issues relating to streambed heterogeneity [*Runkel et al.*, 2003]. However, there are a few on-going investigations that tackle these issues [*Matos et al.*, 2003; *Salehin et al.*, 2003].

Conceptual understanding of hyporheic processes can only be further broadened if multidimensional analyses including heterogeneity are pursued [*Sophocleous*, 2002]. Numerical modeling of hyporheic flow is a viable solution to this impasse since it allows flexibility in the parameters and processes that can be investigated [*Packman and Bencala*, 2000]. Previous modeling efforts by *Woessner* [2000] elucidated this. He introduced high K rectangles set in a matrix of lower K . A linear head gradient was then imposed on the top boundary of the two-dimensional vertical section. A no-flow boundary was set at the downstream end of the domain in order to generate return flow to the river. This resulted in flow lines that are similar to field observations (see figures 5 and 6 of *Woessner* [2000]) although the model conditions, i.e., no flow at the downstream end and a binary K field, are only a crude approximation of natural conditions.

2.1.2 Purpose of this study

Previous studies have not exploited the capability of groundwater flow models to explicitly consider bed-scale 3D spatial variability in hydraulic properties of the sub-channel HZ. Partly, this owes to the extensive fieldwork necessary for the data intensive sedimentological models necessary to represent realistic spatial heterogeneity of streambed hydraulic conductivity. Thus, several fundamental questions remain unanswered. Under what conditions does heterogeneity induce substantial hyporheic exchange? Is the influence of heterogeneity on hyporheic flow comparable to the control exerted by bed or water surface topography, including the effects of bed forms and channel curvature? How are HZ geometry, streambed flux, and the HZ residence time of surface water controlled by each of these influences? In particular, when can we neglect and when should we consider heterogeneity, and channel curvature, in models of hyporheic processes? How do these answers change during the dynamic events of a flood with its evolving boundary condition at the streambed? The purpose of this paper is to provide some tentative answers to these questions based on modeling efforts using previously published field observations of heterogeneous streambed conductivity.

2.2. Methodology

2.2.1. Background and model hydraulic properties

We used a heterogeneous 3D reconstruction of modern channel bend deposits developed by *Cardenas and Zlotnik* [2003a] for the flow and transport simulations. Their reconstruction is based on numerous constant-head injection tests [*Cardenas and Zlotnik*, 2003b] and ground-penetrating radar surveys of Prairie Creek in Central Nebraska, USA (Figure 2.1). The interpolated hydraulic conductivity data compared favorably with data

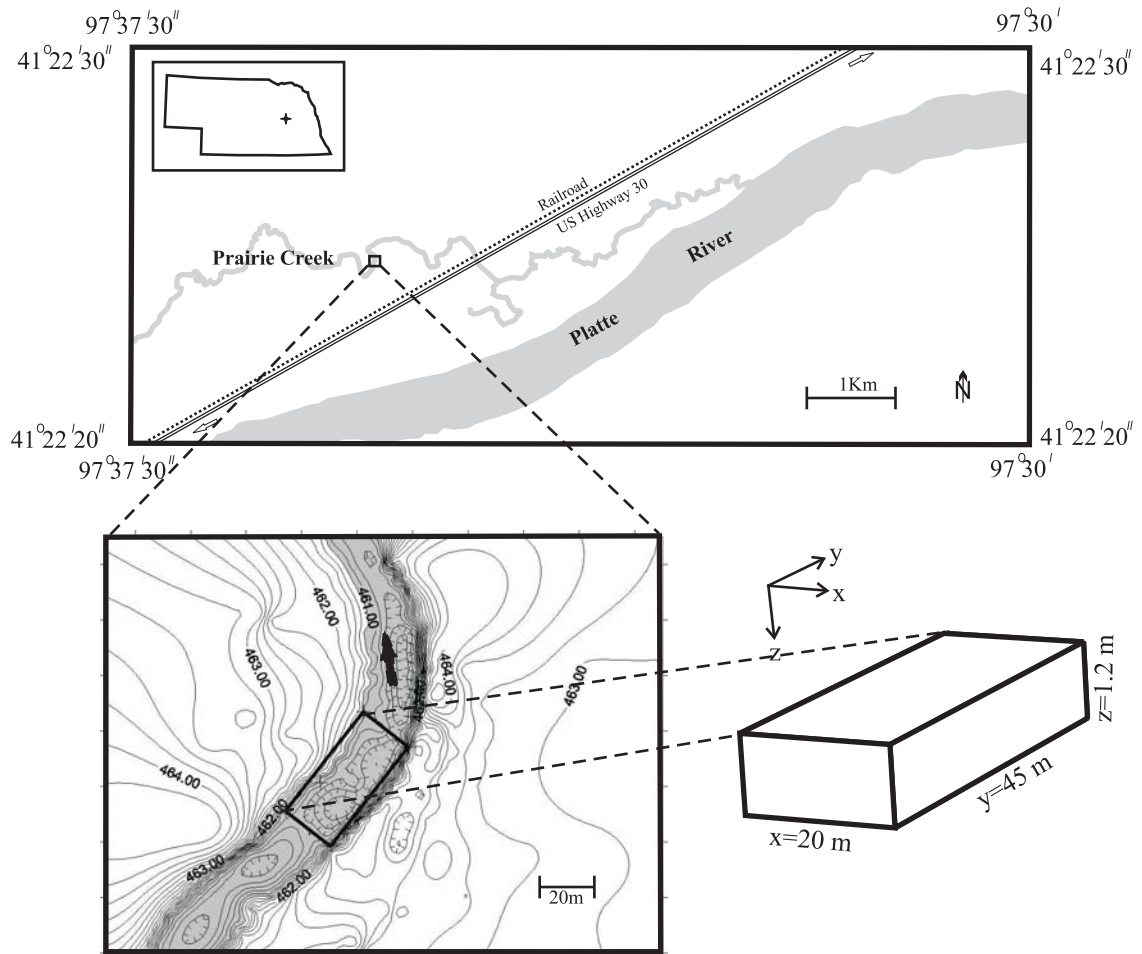


Figure 2.1. Topographic map of the Prairie Creek test site, Nebraska (elevation in m; contour interval = 0.2 m). Enlarged rectangular block is the model domain.

collected from surficial deposits in similar environments. The Prairie Creek's streambed is dominantly sand with some gravel and is typical of the small low-gradient streams traversing the mid-Western United States in contrast with the steep gravel-bedded headwater streams where most field experiments on hyporheic exchange had been conducted. Its discharge varies from dry conditions during the summer irrigation season to $50 \text{ m}^3/\text{s}$ when large storms pass through its 250 km^2 drainage area.

We subdivided the reconstruction into 11 K values (Figure 2.2), which range from 2.5 m/d to 52.5 m/d , in our domain. An equivalent homogeneous medium, with a K of 18

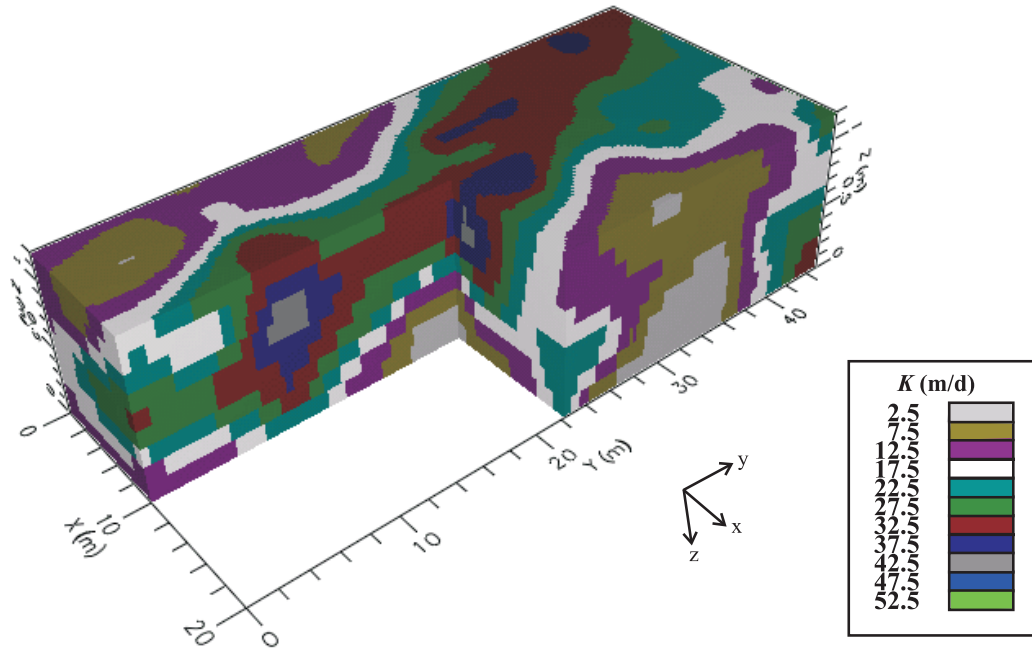


Figure 2.2. Model domain with three-dimensional hydraulic conductivity field.

m/d assigned throughout the domain, was used as a control. Equivalence of the heterogeneous medium was accomplished through both volumetric averaging and numerical Darcian approaches [Cardenas and Zlotnik, 2003a]. All K values were locally isotropic as justified by the measurement scale of the instruments for hydraulic testing and the results of upscaling calculations. Effective porosity was 0.3 throughout the domain.

2.2.2. Flow and Transport Modeling

We used the finite-difference code MODFLOW [McDonald and Harbaugh, 1996] for flow modeling, MT3D99 [Zheng, 1999] for transport simulation, ZONEBUDGET [Harbaugh, 1990] for calculation of fluxes, and MODPATH [Pollock, 1994] for forward particle tracking. Solute transport in MT3D99 was simulated with a

third order total-variation-diminishing (TVD) scheme. Data processing and code execution were handled through the Visual MODFLOW user interface [*Waterloo Hydrogeologic Inc.*, 2000].

The model domain is 45 m x 20 m x 1.2 m (Figure 2.2). Each block is 25 cm x 25 cm x 4 cm (Δx , Δy , and Δz). These blocks are smaller (finer resolution) than the horizontal and vertical block sizes of 0.5 m and 0.13 m, respectively, used by *Cardenas and Zlotnik* [2003a] for their upscaling work. We refined the horizontal grid resolution so that sinusoidal prescribed head boundaries at the streambed interface would not become filtered. Vertical grid resolution was refined to limit solute numerical dispersion. We imposed a no-flow boundary at the bottom and prescribed heads at the remaining external faces of the domain. Varying the top boundary between simulations allowed us to represent various streambed interface conditions. Although somewhat arbitrary, the four external vertical faces were assigned the same heads as in the corresponding grid block in the top boundary.

Simulations were designed to allow us to identify the effects of varying individual features including spatial heterogeneity, bed form configuration, and channel curvature. The initial simulations considered a top head boundary characterized by an along-stream or mean longitudinal gradient $J_y = -\partial h / \partial y$. We arbitrarily imposed a gradient of 0.011 (head is 3 m at $y=0$ m and 2.5 m at $y=45$ m). Although this gradient is high, it is about half of the gradient that *Woessner* [2000] used in his simulations, and in any event the results of this linear system simulation can be normalized by the gradient. We then superposed an across-stream or transverse gradient $J_x = -\partial h / \partial x$ to the previous top boundary in the second simulation. In streams, such a boundary will be generated due to

the elevation of the water surface along the outer bank of a meander [*Bridge, 1992*]. In most simulations, we arbitrarily imposed a J_x of -0.01 (a change of 20 cm along the 20 m width), similar to the longitudinal gradient. We also ran low gradient simulations. In these cases, the longitudinal and transverse gradients, respectively, were 0.0011 and -0.001 (a head change of 5 cm along the 45-m length and a head change of 2 cm along the 20-m width), an order of magnitude smaller than most of our simulations, but identical once normalized.

Based on the models for advective flow through stream bottoms, as well as actual observations, head fluctuations due to irregularities of the bed or water surface pump water into and out of HZs. These head fluctuations are commonly idealized in theoretical models and represented as a harmonic function imposed on a flat surface [*Ho and Gelhar, 1973; Shum, 1992; Elliot and Brooks, 1997a; Packman and Brooks, 2001*]. A larger scale analogue of this technique of approximating topographic variations by imposing sinusoidal head fluctuations on a flat boundary can be traced back to *Toth* [1963]. We similarly represented this effect by superimposing a sinusoidal head boundary to the linear gradient as described by the following equation:

$$h=b - J_y y + A \sin(\omega y) \quad (2.1)$$

where h is the head at longitudinal location y , b is the head at the upstream boundary, and A is the amplitude of the fluctuations. The angular frequency is defined by $\omega=2\pi/\lambda$ where λ is the wavelength. Conditions for the various simulations are given in Table 2.1. While we have used a reconstructed streambed from the Prairie Creek, there were no

quantitative field observations of stream flow, bed topography, and porous media head distributions. The simulation boundary conditions and results are hypothetical and do not reproduce field conditions.

Table 2.1. Top boundary prescribed-head conditions and corresponding steady-state fluxes.

Model ¹	Figure ²	K field	J_x	J_y (-)	A (m)	λ (m)	Flux ³ (m ³ /d)	N_E	z_{HZ} (m)	N_H	N
A	2.4a,2.5e	het	-	0.011	-	-	12.40	0.00	0	∞	∞
B	2.4b	het	0.01	0.011	-	-	18.06	0.00	0	∞	∞
C	2.4c, 2.5d	het	-	0.011	0.01	12.5	33.99	0.29	0.68	0.54	1.87
D	2.4d	hom	-	0.011	0.01	12.5	27.41	0.29	0.68	0.00	0.00
E		het	-	0.011	0.01	12.5 ⁴	29.34	0.29	0.68	0.54	1.87
F		hom	-	0.011	0.01	12.5 ⁴	24.74	0.29	0.68	0.00	0.00
G	2.4e	het	0.01	0.011	0.01	12.5	32.67	0.29	0.68	0.54	1.87
H	2.4f	hom	0.01	0.011	0.01	12.5	24.74	0.29	0.68	0.00	0.00
I	2.5a	het	-	0.011	0.02	2	709.45	3.64	1.04	0.36	0.10
J		hom	-	0.011	0.02	2	563.75	3.64	1.04	0.00	0.00
K	2.5b	het	-	0.011	0.01	2	356.06	1.82	0.88	0.42	0.23
L		hom	-	0.011	0.01	2	282.86	1.82	0.88	0.00	0.00
M		het	0.01	0.011	0.01	2	356.23	1.82	0.84	0.44	0.24
N		hom	0.01	0.011	0.01	2	282.98	1.82	0.84	0.00	0.00
O	2.5c	het	-	0.011	0.01	6.2	91.72	0.59	0.88	0.42	0.72
P		hom	-	0.011	0.01	6.2	78.13	0.59	0.88	0.00	0.00
Q		het	0.01	0.011	0.01	6.2	92.78	0.59	0.88	0.42	0.72
R		hom	0.01	0.011	0.01	6.2	78.44	0.59	0.88	0.00	0.00
S		het	-	0.0011	-	-	1.27	0.00	0	∞	∞
T		het	0.001	0.0011	-	-	1.94	0.00	0	∞	∞
U		hom	0.001	0.0011	0.005	6.2	39.04	2.93	1.2	0.00	0.00
V		het	0.001	0.0011	0.005	6.2	45.55	2.93	1.2	0.31	0.11

¹Same designation in Figures 2.6 and 2.7

²Designations in Figures 2.4 and 2.5

³flux=inflow \equiv outflow

⁴shifted by half a wavelength

We followed *Woessner's* [2000] approach to illustrate the 3D morphology of the HZ with a constant-concentration (Dirichlet) boundary of 100 mg/L at top of the domain to represent stream water and a background concentration of 0 mg/L (pure groundwater) throughout the rest of the domain at the start of each run. Dispersivity was set to zero

since we want to study advective hyporheic exchange. Inflow and outflow boundaries, i. e., the side vertical boundaries, were considered as Cauchy type boundaries where the dispersive flux is ignored as this is customary in MT3D [Zheng, 1999]. The bottom was a no-flux boundary. Numerical dispersion was analyzed by comparing isoconcentration lines with pathlines (see discussion below). All flow and transport simulations were executed to steady-state. Flux calculations through the streambed were determined by assigning the top boundary as a “zone” in ZONEBUDGET.

Residence time of water originating from the surface was determined through forward tracking of 1215 particles initially distributed uniformly on the top horizontal layer. The reported residence time was the total tracking time or the time it takes for the particle to exit the domain, which does not necessarily occur through the top boundary. Some particles continue traveling in the subsurface. Thus, the tracking times are minimum residence times and some of the resulting distributions are biased.

2.3. Results and Discussion

2.3.1. Hyporheic zone morphology

Longitudinal cross-sections along $x=10$ m in Figure 2.3 shows that the 50 mg/L isoline mimics pathlines originating from the top boundary, i. e., the stream, and coincides with the deepest pathlines. We conclude that the 50 mg/L isoline/ isosurface is an accurate representation of the area influenced by advection from the stream, i. e., the advective HZ. Minor discrepancies between the deepest pathline and the 50 mg/L isoline in Figure 2.3b (heterogeneous case) arise from the projection of the pathlines to the cross-sectional surface. Figures 2.4 and 2.5 show the results of our steady-state simulations (the letter designations in the figures correspond to those in the second

column of Table 2.1). The gray surfaces are the 50 mg/L isosurfaces and represent the extent of the advective subchannel HZs.

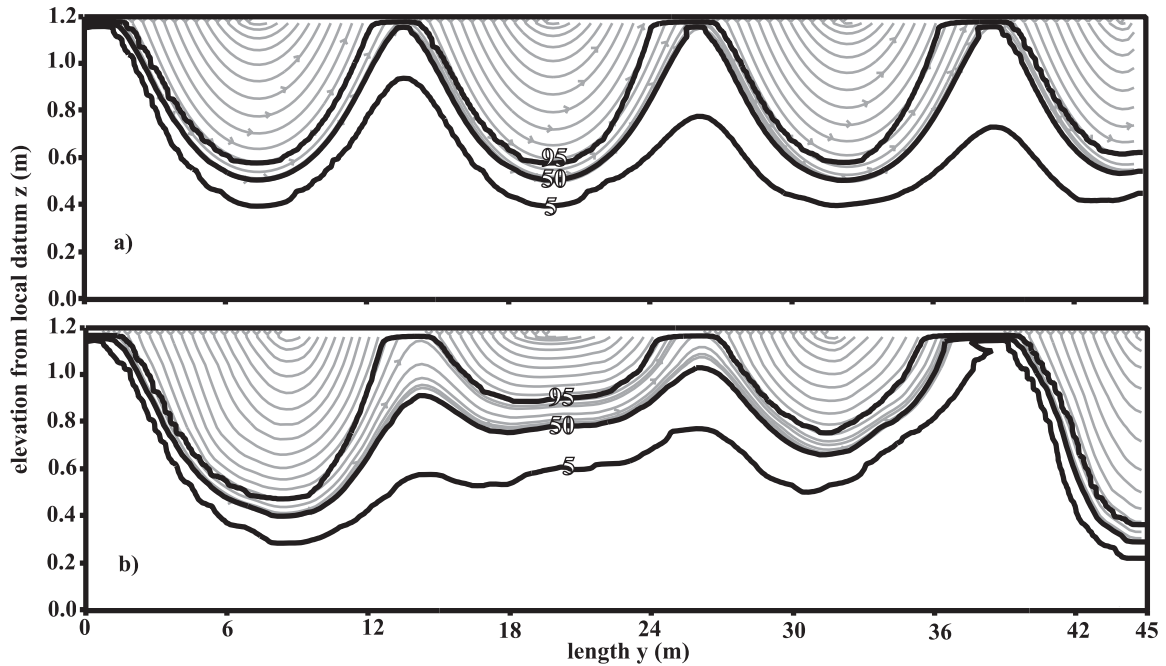


Figure 2.3. Longitudinal cross-sections taken at $x=10$ m: (a) and (b) show pathlines (gray) and isoconcentration lines (black) for a homogeneous and heterogeneous domain, respectively. Top prescribed-head boundary in (a) and (b) is described by the same sinusoidal function.

Imposing only a linear longitudinal head gradient on the top boundary of a homogeneous K field does not produce an advective HZ since the “stream water” in the first layer (top boundary) flows only horizontally. In this case subchannel HZs would only be produced by considering transverse diffusion and dispersion, processes which we ignore. However, inclusion of heterogeneity under the same boundary conditions does produce an advective HZ (Figure 2.4a). The geometry of this zone is reminiscent of *White’s* [1993] 3D representation of the HZ based on temperature distribution. Clearly, heterogeneity determines the location of upwelling and downwelling areas. Figure 2.4b is

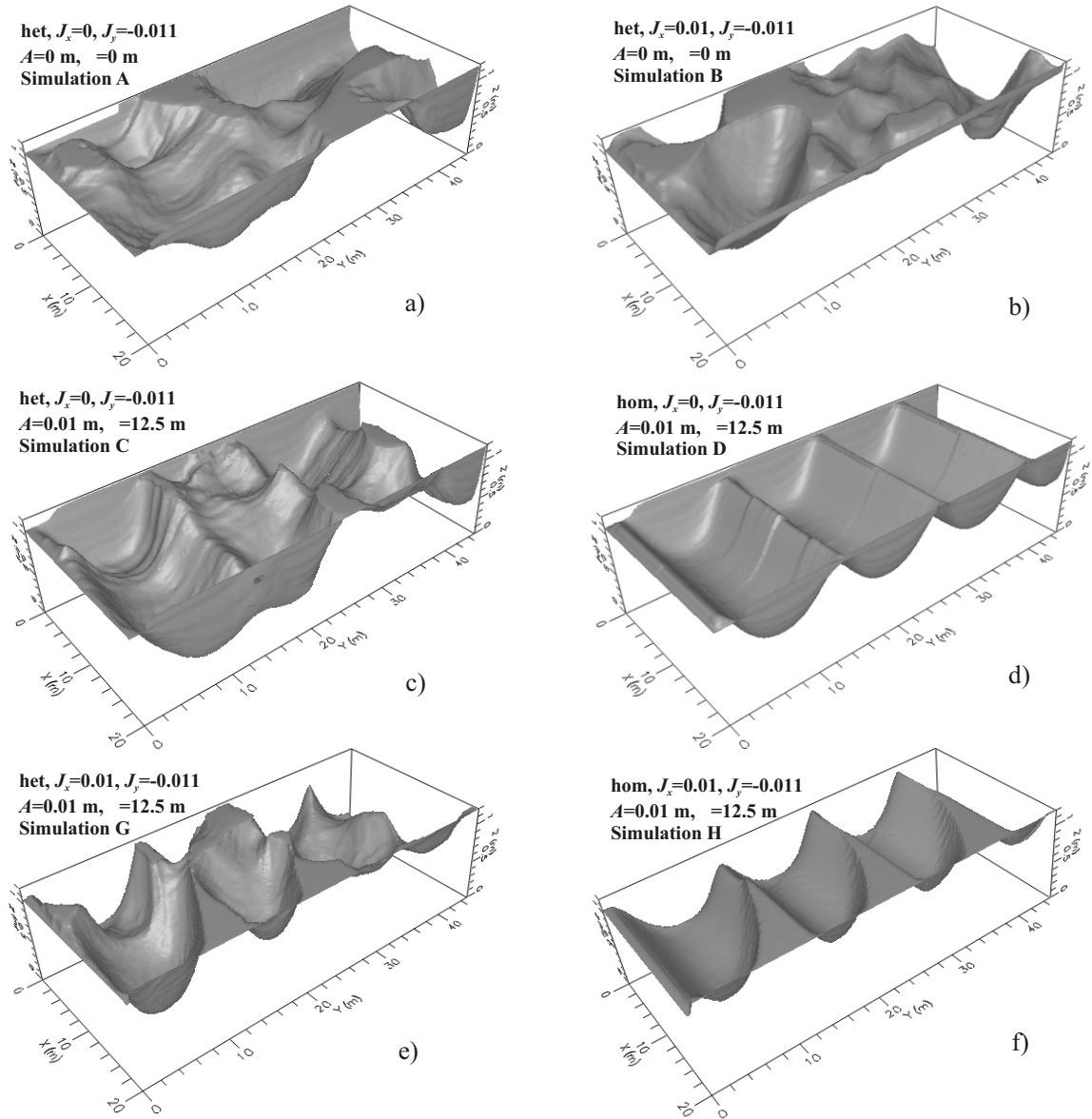


Figure 2.4. Steady-state simulations results (see Table 1 for model conditions). The gray surfaces are the 50 mg/L isosurfaces and represent the extent of the advective subchannel hyporheic zones. Model conditions and letter designations in Table 2.1 are shown beside the images.

based on similar conditions as in Figure 2.4a except that we add the effects of a raised surface water level (J_x) on one side of the channel due to channel curvature. Expectedly, the HZ deflects towards the pointbar (see Figure 1 for orientation of domain along the channel) where the resulting gradient is directed. *Harvey and Bencala* [1993] and *Wroblicky et al.* [1998] observe and model flow through pointbars. They show that hyporheic exchange is driven by the confluent effects of river geomorphology and the ambient down-valley gradient of groundwater (see *Larkin and Sharp* [1992] for more examples). Our results illustrate that the water surface topography along meanders also contributes to this exchange. Furthermore, the spatial pattern of K works in tandem with this effect since high- K areas, the locations of which are controlled by surface water dynamics, are aligned with the prevailing gradients caused by the stream's curvature.

The effects of heterogeneity on HZ geometry are less prevalent when there is a sinusoidal head boundary representing the effects of bed forms and water surface topography (Figure 2.5). Increasing the frequency or amplitude of the sinusoidal fluctuations further reduces the influence of a heterogeneous K field. These relationships can be analyzed by introducing two dimensionless numbers that represent external forcing terms and internal spatial variability separately. The first number:

$$N_E = \frac{2A/(\lambda/2)}{|J_y|} = \frac{4A}{\lambda|J_y|} \quad (2.2)$$

relates the local-scale forcing mechanism (gradient within half a wavelength of the sinusoidal head fluctuations) to the larger scale forcing term (mean longitudinal gradient). The second number, N_H assesses effects of heterogeneity on the geometry of

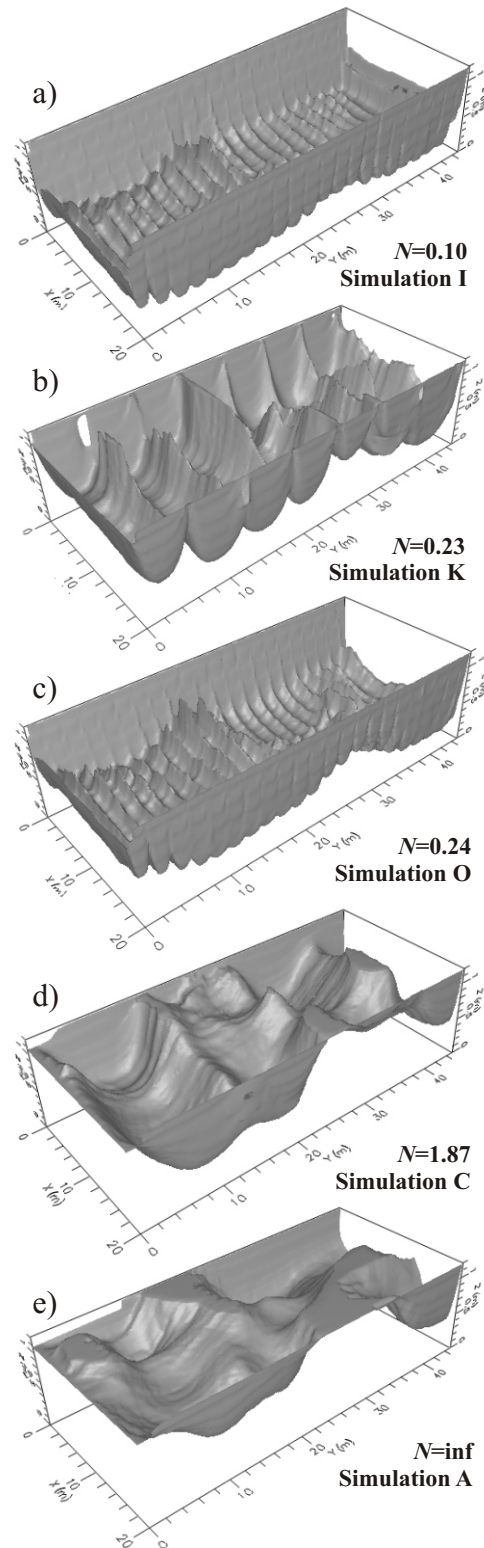


Figure 2.5. Simulation results showing increasing influence of heterogeneity from (a) to (e). Dimensionless N (see explanation in text) and letter designations in Table 1 are shown beside the images.

the HZ by comparing the effects of vertical advection in the HZ due to bed forms with statistics summarizing the spatial variability of K :

$$N_H = \frac{\sigma_{\ln K}^2 l_z}{z_{HZ}} \quad (2.3)$$

using two spatial scales, namely the HZ vertical extent z_{HZ} due to bed forms and the product of the variance, $\sigma_{\ln K}^2$, and vertical correlation length, l_z , of $\ln(K)$. For each particle tracking simulation, z_{HZ} was estimated as the location of the deepest point of all streamlines emanating from the streambed. z_{HZ} was determined for each homogeneous case and applied to its heterogeneous counterpart, to avoid double counting the influence of heterogeneity which is already represented in the numerator of equation (3). Finally, equations (2) and (3) can be combined as:

$$N = \frac{N_H}{N_E} = \frac{|J_y| \sigma_{\ln K}^2 l_z \lambda}{4A z_{HZ}} \quad (2.4)$$

Larger values of this dimensionless number indicate a significant heterogeneity induced HZ, which occurs when the variability of $\ln(K)$ is large and spatially correlated, and the frequency and amplitude of the sinusoidal head fluctuations are small. Missing from (4) is any consideration of the horizontal correlation lengths of $\ln(K)$.

Based on *Cardenas and Zlotnik [2003a]*, $\sigma_{\ln K} = 0.86$ and $l_z = 0.5$ m for the Prairie Creek streambed. $N_H = 0$ for the homogeneous cases. Likewise, $N_E = 0$ for cases where we don't consider a sinusoidal head distribution (no local gradients). Computations for N are

presented in Table 2.1 and simulation examples are in Figure 2.5. The dimensionless numbers partly verify and summarize our observations. When $N=0$, heterogeneity is clearly not a factor. As N increases, the influence of heterogeneity increases. When N is ∞ , such as in cases (A) and (B) of Table 2.1, and Figure 2.5e, the advective HZ is driven completely by heterogeneity. Additional theoretical analysis or simulations considering various values for $\sigma_{\ln K}$ and l_z , and accounting for heterogeneity correlation in other directions (l_y and l_x), are needed to confirm the definition, significance and critical values of N .

The usefulness of dimensionless N comes into play when the external driving mechanisms and internal variability can be readily constrained, estimated, or are actually known *a priori*. For example estimation of N can help in the appropriate design of field experiments such as tracer tests. If estimated N is small the experimental design should put more weight on the configuration of the bed forms or other factors that cause head fluctuations. If estimated N is large any field campaign should take heterogeneity into consideration. N estimates could also be applied in the cross-comparison of streams or stream reaches, and perhaps in biological diversity studies.

Simulations (A) to (R) (Table 2.1, and Figures 2.4 and 2.5) illustrate the effects of some of the controlling factors on hyporheic flow in high gradient streams. In the last series of simulations (S-V in Table 2.1) we attempted to simulate conditions that are more typical of lower gradient streams. Hyporheic zone geometry for simulations (S) and (T) are similar to Figures 2.4a and 2.4b since they are linearly scaled, thus confirming that heterogeneity is important in this setting. This further evinces that the HZ distribution is more sensitive to a heterogeneous K field if a linear gradient dominates

over the local sinusoidal head field at the top boundary.

3.3.2. Implications on short-term hyporheic zone dynamics

Wondzell and Swanson [1999] observed changes in HZs due to dynamic geomorphic readjustments of cobble-bedded streams as a result of flooding. Other studies show that HZs can dynamically change even without the channel-floodplain scale geomorphic changes that accompany most major floods. *Marion et al.* [2002] demonstrated through flume experiments that different bed form shapes and sizes produce different rates of stream-subsurface exchange, thus resulting in different HZ geometry. Since bed forms are in dynamic equilibrium with flow conditions [*Allen*, 1982; *Southard and Boguchwal*, 1990], HZs can then be expected to evolve along with the bed forms as they respond to dynamic surface flow regimes. Our simulations suggest the possible dynamics between HZ geometry, streambed heterogeneity, and varying surface water conditions.

Periodic pressure distributions in the streambed are set-up by topographic irregularities such as dunes and other typical bed forms. These pressure distributions are not exactly sinusoidal although it is not uncommon to idealize them as such. Examples of pressure distributions over triangular shaped obstructions, i. e., ripples and dunes, are found in *Vittal et al.* [1977] and *Shen et al.* [1990]. The wavelengths and heights of dunes are determined by flow parameters such as depth and velocity [*Yalin*, 1977; *Allen*, 1982]. Thus, the sinusoidal head distributions that we consider can be thought of as a proxy for varying stream discharges. Although we did not monitor nor model flooding explicitly, we show indirectly a connection of flood and hyporheic zone dynamics through specifying various head boundaries representative of different bed form heights and

lengths. Simulations that include a simple planar head boundary (pure longitudinal gradient with or without a transverse gradient) are representative of conditions that favor the formation of lower-stage and upper-stage plane beds. Models that consider a sinusoidal head distribution are a proxy for flow conditions that generate dunes and antidunes. Unfortunately, our grid resolution prevented us from including fluctuations with cm-scale wavelengths, i. e., ripples. Nonetheless, we have shown that different surface flow conditions, represented by the different top boundaries, result in distinct HZ shapes. Such flow conditions may be present in different stages of a single flood. For example, a sequence of bed form states with increasing flow velocity is lower-stage plane beds to dunes to upper-stage plane beds or antidunes [*Bridge, 2003*]. Therefore, the influence of heterogeneity on HZ configuration (and the value of dimensionless N) may vary through extremely short cycles.

3.3.3. Flux calculations

Steady-state fluxes through the top boundary are given in Table 2.1 and illustrated in Figure 2.6 (since total flux “in” is approximately equal to total flux “out” through this boundary, the term “flux” herein refers only to influx). Comparison of cases with similar boundary conditions but different K fields (heterogeneous vs. an equivalent homogenous medium, Figure 2.6a) shows that heterogeneity increases flux across the streambed. Flux enhancement ranges from 17%, for simulation (V) and its homogeneous equivalent (U), to 32%, for simulations (H) and (G). As discussed previously, there is no flux under the conditions of a purely linear longitudinal gradient at the top boundary imposed on a homogenous K field. Consideration of heterogeneity under the same boundary conditions generates a flux of $12.4 \text{ m}^3/\text{d}$.

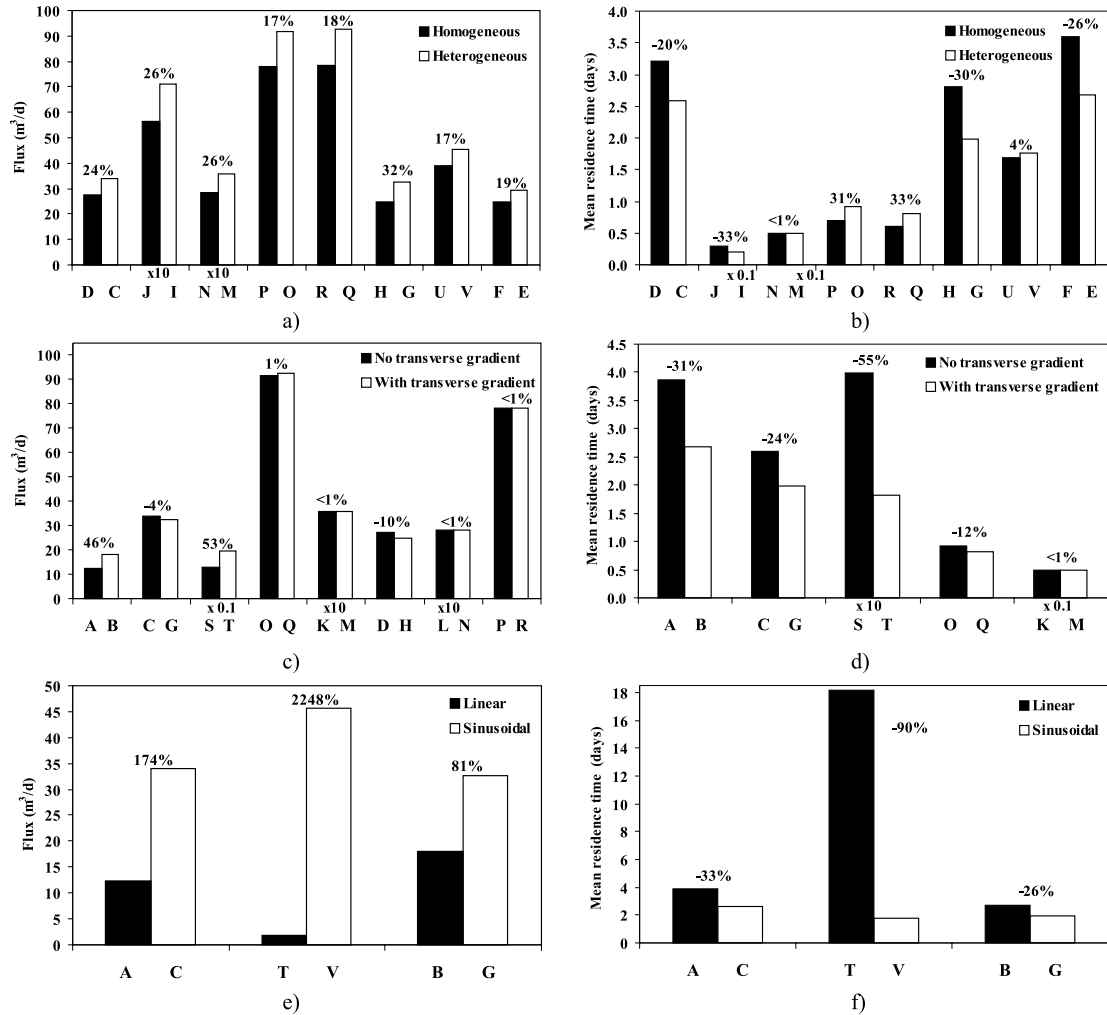


Figure 2.6. Comparison of steady-state fluxes and mean residence times: (a and b) homogeneous vs. heterogeneous cases with similar (sinusoidal) head boundaries; (c and d) no transverse gradient vs. with transverse gradient top boundary condition under similar K setting; (e and f) linear vs. sinusoidal head top boundary condition under similar K setting. “ xX ” in the x -axis means that values were scaled X times to fit in the graph. Positive percentages in the graphs correspond to increases. Conditions for simulations as well as flux and residence time values are in Tables 2.1 and 2.2.

The effects of an across-stream gradient depend on the presence of head fluctuations (Figure 2.6c). The flux changes only slightly for cases where the top constant-head boundary is sinusoidal but it increases approximately 50% for cases where

the top constant-head boundary is linear (both A vs. B and S vs. T). The large increase in flux for the “linear” cases can be explained by the fact that the velocities are aligned along the direction of a high- K area in the domain (see Figure 1 and Figure 7 in *Cardenas and Zlotnik [2003a]*) when J_x is considered. The high- K area, whose deposition is determined by the superelevated surface water flow regime, acts as a preferential pathway. Since water surface topography and sediment distribution are strongly coupled along bends [*Bridge, 1992*], fluxes should be higher along similar portions of other river channels.

Including a sinusoidal head boundary results in larger gradients and significant increases of flux (Figure 2.6e). Superposition of even subtle sinusoidal head fluctuations on a small longitudinal gradient can result in a many fold increase in flux (T vs. V in Table 2.1 and Figure 2.6e).

3.3.4. Mean residence times of particles

The HZ residence times, t_r , of water packets originating from the river were determined by computing total tracking times for 1215 regularly distributed particles originating from the top boundary. The residence time distributions are shown in Figure 2.7 and their statistics are summarized in Table 2.2. The distributions and statistics are biased. Particles with a total tracking time of zero (particles that are in upwelling or effluent areas) are excluded from the calculations. The residence times for the remaining particles are biased low. They are minimum values since some particles exit through the vertical faces of the domain and would move further in the HZ that is external to our modeled area (second column of Table 2.2). This is especially true in cases where we impose a transverse gradient (e.g., simulations B, G, H shown in Figure 2.4b, e, f), where

as many as half of the particles exit through the sides of the domain.

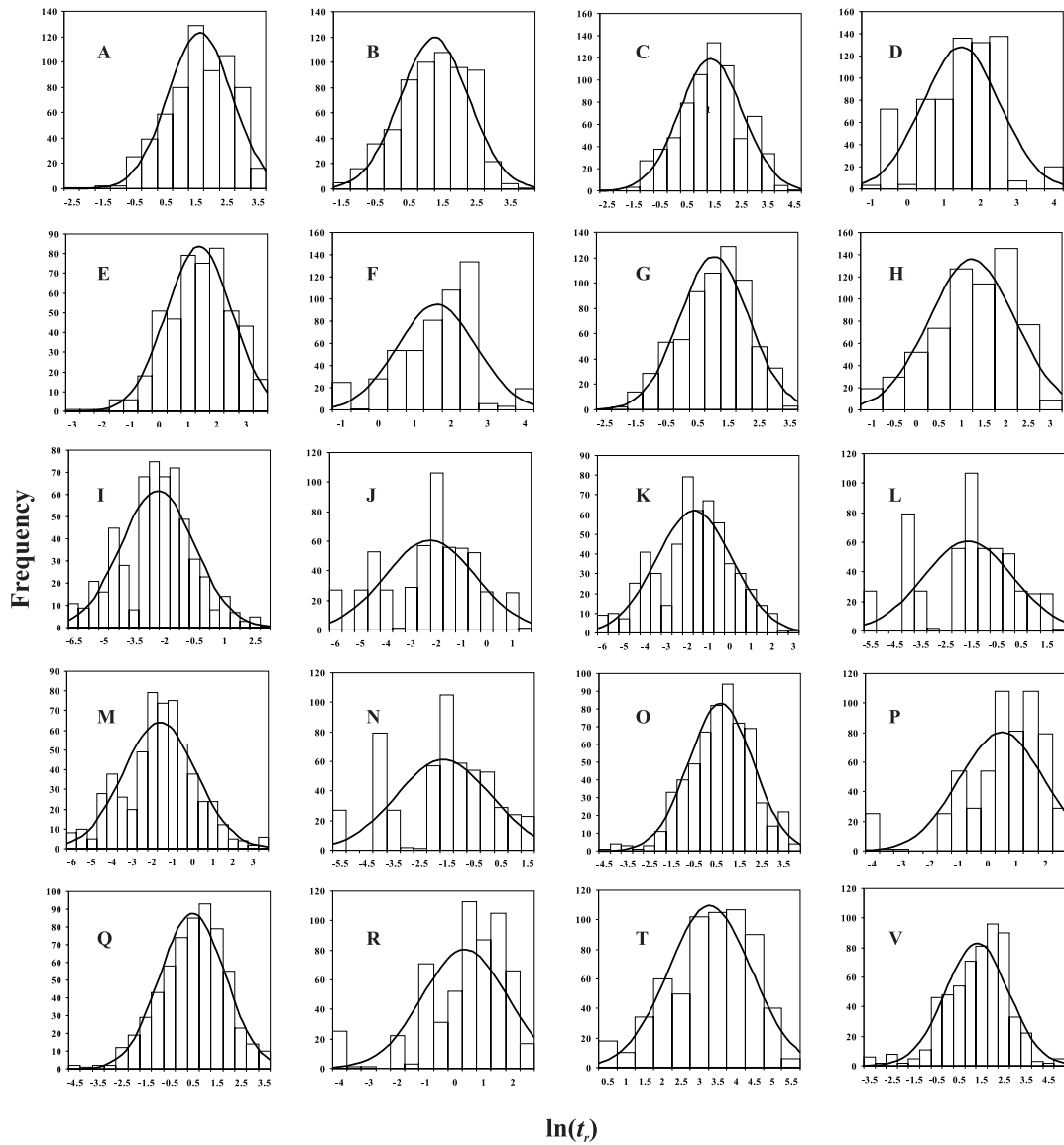


Figure 2.7. Histograms of natural logarithm of residence times (t_r , in days) plus fitted normal curves. Chart labels correspond to simulations in Tables 2.1 and 2.2.

The residence time distributions are closely approximated by lognormal distributions (Figure 2.7). Lognormal curves describe the data better than exponential or normal curves, as is apparent in the Kolmogorov-Smirnov statistic D for the \ln -transformed

Table 2.2. Statistics of residence time distributions (natural log transformed and standard times) and fluxes.

Model ¹	Flux [m ³ /d]	% ²	$\overline{\ln(t_r)}$ [-]	$\sigma_{\ln(t_r)}$ [-]	D	D_{crit} ³	$\overline{t_r}$ [days]	σ_{t_r} [days]
A	12.4	58	1.87	1.02	0.054	0.065	3.87	8.84
B	18.1	65	1.51	1.03	0.052	0.066	2.67	6.20
C	33.4	68	1.64	1.17	0.033	0.062	2.59	8.87
D	27.4	77	1.72	1.05	0.089	0.063	3.22	7.89
E	29.3	84	1.63	1.14	0.037	0.075	2.67	8.34
F	24.7	100	1.85	1.07	0.103	0.072	3.59	9.40
G	32.7	53	1.30	1.11	0.059	0.063	1.98	5.70
H	24.7	53	1.49	0.95	0.096	0.064	2.81	5.35
I	709.4	100	-2.08	1.82	0.071	0.069	0.02	0.63
J	563.7	100	-2.01	1.78	0.132	0.07	0.03	0.64
K	356.1	100	-1.43	1.79	0.059	0.069	0.05	1.16
L	282.9	100	-1.36	1.77	0.115	0.07	0.05	1.21
M	356.2	93	-1.39	1.81	0.064	0.068	0.05	1.25
N	283.0	97	-1.37	1.76	0.118	0.07	0.05	1.17
O	91.7	96	0.94	1.43	0.036	0.067	0.92	6.64
P	78.1	100	0.73	1.48	0.139	0.067	0.70	5.81
Q	92.8	78	0.73	1.37	0.043	0.066	0.81	4.85
R	78.4	86	0.59	1.47	0.137	0.067	0.61	5.01
S	1.3	58	4.19	1.00	0.056	0.066	39.87	87.17
T	1.9	64	3.54	1.13	0.063	0.065	18.15	55.45
U	39.0	68	1.58	1.45	0.135	0.067	1.69	13.02
V	45.6	77	1.55	1.40	0.069	0.067	1.76	11.73

¹Same as Table 2.1

²% of total number of particles tracked that exit through the streambed, the rest exit through the sides

³Critical value of Kolmogorov-Smirnov test statistic D for 2-tailed test at $\alpha=0.01$

distributions (Table 2.2). One motivation of hyporheic exchange modeling is to replicate field observations of residence time distributions as well as the tailing in breakthrough curves of tracer pulses injected into the HZ. In previous studies, several probability density functions (PDFs) have been applied including lognormal, exponential, uniform, and Dirac delta distributions. These PDFs correspond to different site-specific scenarios and different exchange processes. However, it has been shown that exchange models based on advection are best represented by lognormal residence times PDFs [Worman et al., 2002]. Our direct modeling of purely advective hyporheic exchange, as characterized by particle tracking, further illustrates this point. A lognormal PDF for residence times is

typically attributed to a sinusoidal head distribution along the streambed [Worman et al., 2002]. The residence time distribution of simulations (A) and (B) (Figure 2.7) are lognormally distributed, despite the absence of a sinusoidal head boundary (see Tables 2.1 and 2.2), showing that heterogeneity in K alone can result in lognormal residence time PDFs. However, it should be noted that only 58% and 65% of the particles used in determining residence times PDFs for (A) and (B) exit through the top (see Table 2.2). It is difficult to discern how long (and what path) that the particles, that exit along domain sides, would have taken to return to the stream. These particles might remain in the subsurface until they encounter some heterogeneous inclusion, most likely a low-permeability zone, which will deflect them back toward the stream. Therefore, our residence time distributions are biased towards shorter residence times corresponding to paths confined within the model domain. The actual distributions would presumably have longer tails.

One would think that adding heterogeneity would increase residence time, t_r , especially under simple linear gradients, since the particles take a more tortuous path. However, Figure 2.6b shows that this is not always the case when the head distribution at the upper boundary is sinusoidal. Changes varied from a decrease of 33% to an increase of 33%. The lack of any noticeable trend in changes in t_r distributions owes to the complex interaction between the three-dimensionally variable head and hydraulic property distributions.

The general effect of inclusion of a transverse gradient due to channel curvature is to decrease t_r (Figure 2.6d). Several particles exit the domain during early times through the left face (towards the point bar). Thus, these times are biased and do not accurately

represent residence times in the HZ since these particles, although outside the modeled domain, remain in the HZ. Decreases in t_r , which range from less than 1% to 55%, are observed in all comparative cases. These particles traverse longer paths in the longitudinal direction (Figures 2.4a and 2.4b illustrate this) when the transverse gradient is excluded.

A sinusoidal top constant-head boundary decreases t_r (Figure 2.6f). The river water packets/ particles follow shorter routes (see Figure 2.3a, b) as a result of increased gradients per wavelength. As discussed in the previous section, these elevated gradients result in increased fluxes. The short residence times and large fluxes characteristic of this setting are ideal for circulating stream water more efficiently through the HZ. This has implications on the transport of ecologically important solutes and dissolved gases.

2.4. Summary

We simulated hyporheic flow and transport through reconstructed heterogeneous streambed sediments and an equivalent homogeneous streambed. In addition to examining the impact of heterogeneity on hyporheic exchange, we investigated the effects of boundary head sinusoidal fluctuations caused by surface water flow over bed forms and the effects of surface water topography resulting from channel curvature. The simulations show that the configuration of sub-channel hyporheic zones is determined by both the pattern of heterogeneous streambed hydraulic conductivity and the space-periodic head fluctuations at the top of the streambed. The relative importance of heterogeneity versus space-periodic boundary head distributions are summarized by a dimensionless number that considers external forcing mechanisms (global and local head gradients) and internal control by heterogeneity. The results not only show that

heterogeneity is more important when boundary head fluctuations are subdued but also has implications on the dynamic influence of heterogeneity on the hyporheic zone. The various head boundaries employed in our modeling efforts are proxies for different surface water conditions and bed form states that may occur during a single flood. We also found that an across-stream gradient, caused by flow along meander bends, deflects the hyporheic zone towards the cutbank. This deflection is magnified by the natural alignment of high permeability areas in the streambed along the direction of maximum gradient.

Flux calculations through the modeled streambed show that inclusion of heterogeneity can generate an increase in flux of 17 to 32% in the presence of bed forms represented by a space-periodic head boundary. When the head distribution is approximately linear, such as when lower-stage and upper-stage plane beds are the dominant bed forms, flux into the hyporheic zone is entirely driven by heterogeneity. The effects of cross-stream gradients along meanders vary from miniscule additions in cases where the head boundary is space-periodic to 46-53% increase in flux where the top boundary is planar. The larger increase under planar boundary head distributions is due to alignment of velocities with a geomorphologically controlled high-hydraulic conductivity lens. Superposition of a sinusoidally varying head boundary on a linear longitudinal gradient, over a heterogeneous streambed, increases flux by a factor of two to more than an order of magnitude.

Residence times determined through forward tracking of particles originating from the stream bottom (top boundary) are closely approximated by a lognormal distribution. Mean residence times both increase and decrease when heterogeneity is considered and

decrease when a space-periodic head boundary is taken into consideration. Thus, cycling of nutrient rich water is more effective in settings where sinusoidal head distributions are dominant because of the increased fluxes and decreased residence times. Mean residence times in subchannel HZs are smaller when the stream is flowing through a bend. Some of our residence time empirical distributions are biased by particles exiting through the sides of the domain, but remaining in the subsurface. A more accurate and systematic assessment of trends in residence time distributions will require a different approach.

We explicitly show that heterogeneity, bed form configuration, and river bends have significant influence on subchannel hyporheic processes, in particular on hyporheic zone geometry, fluxes, and residence times. The relative importance of heterogeneity, bed form configuration and channel curvature is dynamic. The contribution of heterogeneity, relative to bed form configuration, can change from most to least dominant. This dominance is related to bed form amplitude and frequency which normally change through a single flood cycle. Hyporheic zone dynamics are better understood when heterogeneity, bed form configuration, and stream curvature are each included in models and field and laboratory observational programs.

References

- Allen, J. R. L., *Sedimentary Structures: Their Character and Physical Basis*, Volume I. Developments in Sedimentology 30, Elsevier Science Publishers, Amsterdam, 1982.
- Bencala, K. E., and R. A. Walters, Simulation of solute transport in a mountain pool-and-riffle stream: a transient storage model, *Water Resour. Res.*, 19(3), 718-724, 1983.
- Bridge, J. S., *Rivers and Floodplains: Forms, Processes, and Sedimentary Record*, Blackwell Publishing, UK, 491 pp., 2003.
- Bridge, J. S., A revised model for water flow, sediment transport, bed topography and grain size sorting in natural river bends, *Water Resour. Res.*, 28(4), 999-1013, 1992.
- Cardenas, M. B., and V. A. Zlotnik, Three-dimensional model of modern channel bend deposits, *Water Resour. Res.*, 39(6), 1441, doi:10.1029/2002WR001383, 2003a.
- Cardenas, M. B., and V. A. Zlotnik, A simple constant-head injection test for streambed hydraulic conductivity estimation, *Ground Water*, 41(6), 867-871, 2003b.
- Choi, J., J. W. Harvey, and M. H. Conklin, Characterizing multiple scales of stream and storage zone interaction that affect solute fate and transport in streams, *Water Resour. Res.*, 36(6), 1511-1518, 2000.
- Doyle, M. W., E. H. Stanley, and J. M. Harbor, Hydrogeomorphic controls on phosphorus retention in streams, *Water Resour. Res.*, 39(6), 1147, doi:10.1029/2003WR002038, 2003.
- Elliot, A. H., and N. H. Brooks, Transfer of nonsorbing solutes to a streambed with bed forms: Theory, *Water Resour. Res.*, 33(1), 123-136, 1997a.
- Elliot, A. H., and N. H. Brooks, Transfer of nonsorbing solutes to a streambed with bed forms: Laboratory experiments, *Water Resour. Res.*, 33(1), 137-151, 1997b.
- Findlay, S., Importance of surface-subsurface exchange in stream ecosystems: The hyporheic zone, *Limnol. Oceanogr.*, 40(1), 159-164, 1995.
- Harbaugh, A. W., *A Program for Calculating Subregional Water Budgets using Results from the U. S. Geological Survey's Modular Three-dimensional Finite-difference Ground-water Flow Model*, USGS Open File Report 90-392, Reston, VA, 27 pp., 1990.
- Harvey, J. W., and K. E. Bencala, The effect of streambed topography on surface-subsurface water exchange in mountain catchments, *Water Resour. Res.*, 29(1), 89-98, 1993.

- Harvey, J. W., and C. W. Fuller, Effect of enhanced manganese oxidation in the hyporheic zone on basin-scale geochemical mass balance, *Water Resour. Res.*, 34(4), 623-636, 1998.
- Harvey, J. W., and B. J. Wagner, Quantifying hydrologic interactions between streams and their subsurface hyporheic zones, in *Streams and Ground Waters*, edited by J. B. Jones and P. J. Mulholland, Academic Press, San Diego CA, 3-44, 2000.
- Harvey, J. W., B. J. Wagner, and K. E. Bencala, Evaluating the reliability of the stream tracer approach to characterize stream-subsurface water exchange, *Water Resour. Res.*, 32(8), 2441-2451, 1996.
- Ho, R. T., and L. W. Gelhar, Turbulent flow with wavy permeable boundaries, *J. Fluid Mech.*, 58(2), 403-414, 1973.
- Jonsson, K., H. Johansson, and A. Worman, Hyporheic exchange of reactive and conservative solutes in streams- tracer methodology and model interpretation, *J. Hydrology*, 278(1-4), 153-171, 2003.
- Kasahara, T., and S. M. Wondzell, Geomorphic controls on hyporheic exchange flow in mountain streams, *Water Resour. Res.*, 39(1), 1005, doi:10.1029/2002WR001386, 2003.
- Larkin, R. G., and J. M. Sharp, Jr., On the relationship between river-basin geomorphology, aquifer hydraulics, and ground-water flow direction in alluvial aquifers, *Geol. Soc. America. Bull.*, 104, 1608-1620, 1992.
- Marion, A., M. Bellinello, I. Guymer, and A. Packman, Effect of bed form geometry on the penetration of nonreactive solutes into a streambed, *Water Resour. Res.*, 38(10), 1209, doi:10.1029/2001WR000264, 2002.
- Matos, J.E.R., Welty, C., and Packman, A.I., Stream-groundwater interactions: The influence of aquifer heterogeneity and stream meandering on 2-D and 3-D hyporheic exchange flows, Proceedings of MODFLOW and More 2003: Understanding through Modeling, Golden, Colorado, Sept. 17-19, 2003.
- McDonald, M. G., and A. W. Harbaugh, *Programmer's Documentation for MODFLOW-96, an update to the U.S. Geological Survey Modular Finite-Difference Ground-Water Flow Model*, U.S. Geol. Surv. Open File Rep. 96-486, 220 pp., 1996.
- Packman, A. I., and K. E. Bencala, Modeling surface-subsurface hydrological interactions, in *Streams and Ground Waters*, edited by J. B. Jones and P. J. Mulholland, Academic Press, San Diego CA, 45-80, 2000.
- Packman, A. I., and N. H. Brooks, Hyporheic exchange of solutes and colloids with

- moving bed forms, *Water Resour. Res.*, 37(10), 2591-2605, 2001.
- Pollock, D. W., *User's Guide for MODPATH/ MODPATH-PLOT, Version 3: A particle tracking post-processing package for MODFLOW, the U. S. Geological Survey finite-difference ground-water flow model, U.S. Geol. Surv. Open File Rep. 94-464*, 234 pp., 1994.
- Richardson, C. P., and A. D. Parr, Modified Fickian model for solute uptake by runoff, *J. Environ. Eng.*, 114(4), 792-809, 1988.
- Runkel, R. L., D. M. McKnight, and H. Rajaram, Modeling hyporheic zone processes, *Adv. Water Resour.*, 26(9), 901-905, 2003.
- Salehin, M., A. I. Packman, and M. Paradis, Hyporheic exchange with heterogeneous streambeds: laboratory experiments and modeling, *Eos Trans. AGU*, 84(46), Fall Meet. Suppl., 2003.
- Savant, S. A., D. D. Reible, and L. J. Thibodeaux, Convective transport within stable river sediments, *Water Resour. Res.*, 23(9), 1763-1768, 1987.
- Shen, H. W., H. M. Fehlmán, and C. Mendoza, Bedform resistances in open channel flows, *J. Hydraul. Eng.*, 116(6), 799-815, 1990.
- Shum, K. T., Wave-induced advective transport below a rippled water-sediment interface, *J. Geophys. Res.*, 97(C1), 798-808, 1992.
- Sophocleous, M., Interactions between groundwater and surface water: the state of the science, *Hydrogeol. J.*, 10(1), 52-67. doi:10.1007/s10040-001-0170-8, 2002.
- Southard, J. B., and L. A. Boguchwal, Bed configurations in steady unidirectional flows. Part 2. Synthesis of flume data. *J. Sed. Pet.*, 60(5), 658-679, 1990.
- Storey, R. G., K. W. F. Howard, and D. D. Williams, Factors controlling riffle-scale hyporheic exchange and their seasonal changes in a gaining stream: A three-dimensional groundwater flow model, *Water Resour. Res.*, 39(2), 1034, doi:10.1029/2002WR001367, 2003.
- Thibodeaux, L. J., and J. D. Boyle, Bed form-generated convective-transport in bottom sediments, *Nature*, 325, 341-343, 1987.
- Tóth, J., A theoretical analysis of groundwater flow in small drainage basins, *Jour. Geophys. Res.*, 68(10), 4795-4812, 1963.
- Triska, F. J., V. C. Kennedy, R. J. Avanzino, G. W. Zellweger, and K. E. Bencala, Retention and transport of nutrients in third-order stream in Northwestern California: Hyporheic processes, *Ecology*, 70(6), 1893-1905, 1989.

- Triska, F. J., J. H. Duff, and R. J. Avanzino, The role of water exchange between a stream channel and its hyporheic zone in nitrogen cycling at the terrestrial-aquatic interface, *Hydrobiologia*, 251(1-3), 167-184, 1993.
- Vittal, N. K., K. G. Rangu Raju, and R. J. Garde, Resistance of two-dimensional triangular roughness, *J. Hydraul. Res.*, 15(1), 19-36, 1977.
- Wagner, F. H., and G. Bretschko, Interstitial flow through preferential flow paths in the hyporheic zone of the Oberer Seebach, Austria, *Aquat. Sci.*, 64(3), 307-316, 2002.
- Waterloo Hydrogeologic, Inc., *Visual MODFLOW v2.8.2 User's Manual*, 311 pp., 2000.
- White, D. S., Perspectives on defining and delineating hyporheic zones, *J. N. Am. Benthol. Soc.*, 12(1), 61-69, 1993.
- Woessner, W. W., Stream and fluvial plain ground water interactions: rescaling hydrogeologic thought, *Ground Water*, 38(3), 423-429, 2000.
- Wondzell, S. M., and F. J. Swanson, Floods, channel change, and the hyporheic zone, *Water Resour. Res.*, 35(2), 555-567, 1999.
- Wondzell, S. M., and F. J. Swanson, Seasonal and storm dynamics of the hyporheic zone of a 4th-order mountain stream. 1. Hydrologic processes, *J. N. Am. Benthol. Soc.*, 15(1), 3-19, 1996.
- Worman, A., Analytical solution and timescale for transport of reactive solutes in rivers and streams, *Water Resour. Res.*, 34(10), 2703-2716, 1998.
- Worman, A., A. I. Packman, H. Johansson, and K. Jonsson, Effect of flow-induced exchange in hyporheic zones on longitudinal transport of solutes in streams and rivers, *Water Resour. Res.*, 38(1), doi:10.1029/2001WR000769, 2002.
- Wroblicky, G. J., M. E. Campana, H. M. Valett, and C. N. Dahm, Seasonal variation in surface-subsurface water exchange and lateral hyporheic area of two stream-aquifer systems, *Water Resour. Res.*, 34(3), 317-328, 1998.
- Yalin, M. S., *Mechanics of Sediment Transport*, Oxford, Pergamon Press, 1977.
- Young, P. C., and S. G. Wallis, The aggregated dead zone (ADZ) model for dispersion in rivers, paper presented at International Conference on Water Quality Modeling in the Inland Natural Environment, Bournemouth, England, June 10-13, 1986.
- Zheng, C., MT3DMS, A modular three-dimensional multi-species transport model for simulation of advection, dispersion and chemical reactions of contaminants in groundwater systems; documentation and user's guide, U.S. Army Engineer Research and Development Center Contract Report SERDP-99-1, 202 p., 1999.

CHAPTER 3

HYDRODYNAMICS OF COUPLED FLOW ABOVE AND BELOW A SEDIMENT-WATER INTERFACE WITH TRIANGULAR BEDFORMS

(This chapter has been submitted as: Cardenas, M. B., and J. L. Wilson, Hydrodynamics of coupled flow above and below a sediment-water interface with triangular bed forms: underflow case, *Advances in Water Resources*.)

3.1. Introduction

3.1.1. Relevance and previous work

The physical and biogeochemical complexity of the sediment-water interface (SWI) or transition zone between benthic water and pore water, sometimes referred to as the "hyporheic zone" in freshwater aquatic systems, has not been investigated in detail. However, we know that ecologically and environmentally significant processes occurring in these zones control the distribution of solutes, colloids, dissolved gases and biogeochemical reactions from ripple to global scales [Riedl *et al.*, 1972; Rutherford *et al.*, 1995; Elliott and Brooks, 1997a; Huettel *et al.*, 1998; Packman and Brooks, 2001; Worman *et al.*, 2002; Burnett *et al.*, 2003; Kasahara and Wondzell, 2003; Huettel *et al.*, 2003; Precht and Huettel, 2003;], and thus affect the distribution of benthic flora and

fauna in lakes, oceans, bays and estuaries [*Riedl et al.*, 1972; *Huettel et al.*, 2003; *Choe et al.*, 2004], as well as hyporheic and riparian organisms in fluvial systems [*Triska et al.*, 1989; *Findlay*, 1995; *Harvey and Fuller*, 1998].

While field and laboratory observations are necessary for a comprehensive understanding of interfacial exchange processes, fundamental advancements are made when these empirical data are verified or reproduced through mathematical modeling based on the conservation laws of mass, momentum, and energy. Many studies have presented both modeled and observed results on fluid flow and solute transport for benthic-pore water exchange. These are reviewed in *Boudreau* [2001], *Jorgensen and Boudreau* [2001] and *Huettel and Webster* [2001] for marine settings and by *Packman and Bencala* [2000] for fluvial hyporheic zones. There is no specific marine counterpart for the freshwater ‘hyporheic zone’, thus we generalize the nomenclature and refer instead to the interfacial exchange zone (IEZ) as the area within the permeable sediments that is physically influenced by fluid exchange across the sediment-water interface.

A holistic view of the dynamics of the IEZ necessarily begins with a comprehensive knowledge of the fluid physics as mass flux is usually governed by advection rather than molecular diffusion or dispersion [*Savant et al.*, 1987; *Huettel et al.*, 2003]. Advective exchange between the water column and the underlying porous sediments occurs mainly due to pressure gradients. These pressure gradients are typically generated by currents above any bed-surface topography or by oscillatory flow due to waves and tidal fluctuations [*Webb and Theodor*, 1968; *Shum*, 1992; *Huettel and Webster*, 2001]. Some benthic organisms also generate flow across the sediment-water interface and mixing of sediments; these phenomena are referred to as bioirrigation and

bioturbation. Aside from the advective process, which has been referred to as “pumping”, the movement of bedforms also results in the trapping and release of solutes and is termed “turnover” [Elliott and Brooks, 1997a]. A thorough investigation of the mechanics of pumping is necessary if we are to understand the fluid physics of IEZs.

Several studies, often supported by experiments, have investigated the mechanics of pumping but within a limited context. *Thibodeaux and Boyle* [1987] present results of flume experiments with gravel beds and apply Darcy’s Law combined with pressure distributions measured over triangular roughness from *Vittal et al.* [1977] to estimate pore-water velocities along the SWI for one scenario. This study illustrated the presence of interfacial exchange but did not thoroughly investigate the fundamental hydrodynamics of the system both in the water column and within the sediments. *Savant et al.* [1987], applying the boundary element numerical method, replicate flume observations of flow through a single dune induced by pressure gradients also calculated following *Vittal et al.* [1977]. *Elliott and Brooks* [1997a] followed the same procedure of taking pressure profiles from previous experiments, this time from *Fehlman* [1985], and imposed it as a boundary for a numerical model of Darcy flow within the sediments. Moreover, they approximated the pressure profile along the SWI with a sine function to derive an exact solution for potential flow in the sediments, while assuming that the interface is flat [Elliott and Brooks, 1997a]. Observed tracer trajectories within permeable sediments were modeled successfully by *Huettel and Gust* [1992] who applied a sink-source potential flow model. Although early numerical simulations of flow within the sediments considered bedforms explicitly [Elliott, 1990; Savant et al., 1987], several recent approaches involve imposing a functional pressure distribution on the flat upper

boundary of pore-water flow models which consider homogeneous [Shum, 1992; Huettel *et al.*, 1998; Packman and Brooks, 2001] as well as heterogeneous permeability fields [Cardenas *et al.*, 2004]. The spatially periodic, and approximately sinusoidal, pressure distributions represent the impact of bed topography. Despite elucidating processes operating in the sediments, models that ignore the geometry of bedforms miss a substantial part of the IEZ and provide an incomplete picture. Marion *et al.* [2002] have shown that pore-water flow models of pumping induced exchange with flat upper boundaries cannot accurately predict results of experiments when bedforms protrude significantly into the water column, i.e., bedform height is comparable to water column depth. They attribute this to inadequate representation of the parts of dunes located higher than the mean bed elevation. Moreover, flume studies using gravel and sand beds show that pore-water flow velocities decelerate nonlinearly away from the interface [Thibodeaux and Doyle, 1987; Huettel *et al.*, 1996; Packman *et al.*, 2004] supporting the emphasis on processes occurring along and adjacent to the bed surface.

The studies cited in the previous paragraph illustrated or emphasized processes within the sediments. There have also been investigations that simultaneously analyze flow above and below the interface. Ho and Gelhar [1973] present results of analytical and experimental studies on turbulent flow in pipes with permeable walls characterized by wavy periodic topography. They assumed potential flow both outside of and above the permeable media. Shum [1992] examines the effects of the passage of progressive gravity waves on advective transport in a porous rippled bed. Once again, potential flow was assumed for the oscillatory flow in the water column. This allowed for an exact representation of the pressure along the surface of the sinusoidal ripples and the

derivation of an analytic solution for potential flow within the ripples. Furthermore, *Shum* [1992] numerically solved the Navier-Stokes equations for laminar oscillatory flow above the ripples and similarly imposed the pressure solution from the Navier-Stokes as a boundary for the flow model of the sediments. This allowed, for the first time, an investigation of the underlying and fundamental dynamics of advective exchange between rippled sediments and the water column driven by gravity waves. However, only a handful of cases were presented by *Shum* [1992] and the study was limited to sinusoidal ripples under oscillatory flow. To our knowledge no similar study has been done for triangular bedforms under unidirectional flow. We address this through sequentially coupled numerical modeling of fluid flow both above and below a SWI with triangular bedform topography.

3.1.2. Purpose of this study

The goal of this paper is to use two-dimensional coupled flow simulations to elucidate the basic hydrodynamic interactions between mean unidirectional laminar flow in the water column above triangular bedforms, with porous flow in the underlying permeable sediments. In this study the effects of oscillatory flow, turbulence, bioirrigation, and bioturbation are assumed negligible. We address the following questions. How do bedforms affect water column eddy geometry and the pressure distribution at the SWI? How do eddy geometry and the bottom pressure distribution affect interfacial exchange and flow through the underlying sediments? How do these effects change with flow conditions in the overlying water column and with bedform shape? These questions can also be posed for different scenarios of ambient groundwater discharge- ‘neutral’, ‘gaining’ or ‘losing’ conditions. The gaining scenario refers to cases

where the water column is gaining net water, e.g., gaining rivers or lakes and coastal zones subjected to submarine groundwater discharge. The gaining case is addressed in another paper [*Cardenas and Wilson*, submitted]. The reference case, where the water column is ‘neutral’ - neither gaining nor losing net water, is addressed here.

Among our assumptions the weakest is laminar flow in the water column; in most natural systems this flow is turbulent. What the laminar flow results lack in predictive ability they more than make up in explanatory power and, in any event, help guide the design of studies to address turbulence as well as other issues. *Shum’s* study [1992] discussed above is an example where a laminar flow based investigation provided much needed fundamental insight. Throughout the development of fluid mechanics laminar-flow studies have played this pioneering role. A recent special issue of *Advances in Water Resources* highlighted papers dealing with modeling of hyporheic zone processes [*Runkel et al.*, 2003] but included none that tackle the coupled hydrodynamics of the water column and porous sediments, not even for laminar flow settings. Consideration for turbulent conditions (e.g., direct numerical solution of transient Navier-Stokes equations) is left for future studies as this is currently beyond the capability of most typical computational resources.

3.2. Methodology

In order to answer these questions, we used FEMLAB (now called COMSOL Multiphysics), a multiphysics finite element analysis software, to numerically model the coupled flow in two-dimensions and at steady-state. The code solves the Navier-Stokes (NS) and continuity equations for incompressible flow for the water column:

$$\rho \frac{\partial \mathbf{u}}{\partial t} - \mu \nabla^2 \mathbf{u} + \rho (\mathbf{u} \cdot \nabla) \mathbf{u} + \nabla p = 0 \quad (3.1)$$

$$\nabla \cdot \mathbf{u} = 0 \quad (3.2)$$

where ρ is fluid density, \mathbf{u} is the velocity vector, μ is dynamic viscosity, and p is pressure. The porous bed domain is governed by the combination of Darcy's Law and the continuity equation for incompressible flow in a non-deformable media, i. e., the groundwater flow equation:

$$\nabla \cdot \mathbf{q} = 0 \quad (3.3)$$

$$\mathbf{q} = -\frac{k}{\mu} \nabla p \quad (3.4)$$

where \mathbf{q} is the specific discharge (i.e. Darcy "velocity") and k is intrinsic permeability. Direct solvers from the UMFPACK algorithm [Davis, 2004] are implemented in FEMLAB. Sequential coupling is implemented via imposing the NS-continuity derived pressure distribution along the bed surface as a Dirichlet boundary for the groundwater flow equation. The top of the water column is treated as a no-flow symmetry boundary and not as a free surface (Figure 3.1a). The water column's bottom boundary, the sediment-water interface (SWI), assumes the no-slip/ no-flow condition:

$$\mathbf{u} = 0 \quad (3.5)$$

The lower boundary of the porous domain is considered impermeable. As just mentioned, the top boundary of the porous domain is a prescribed pressure boundary derived from solving the NS equations in the water column domain. Thus, by definition pressure is continuous across the two domains. However, although the NS velocity is zero at the SWI, the porous bed Darcy velocity is finite resulting in a discontinuous velocity distribution across the interface. Velocity jumps are common in porous systems with sharp contrasts in permeability, such as along the transition from clay to gravel. However, our sequential formulation results in a slight mass imbalance as fluxes into and out of the SWI are not accounted for in the water column. Our coupling is only one-way and not iterative. This imbalance is negligible for the water column as fluid fluxes through the SWI are miniscule compared to other fluxes (less than 0.01% of flux through the water column). It is a somewhat awkward yet convenient approximation for the coupled interface (more on this later). Although formulations that ensure mass balance are possible (e.g., Brinkman-type or Beavers-Joseph-type equations), they are currently difficult to implement as they require *a priori* knowledge of additional parameters (effective viscosity in Brinkman-type equations and a slip-velocity in the Beavers-Joseph-type equations) and have been shown to be valid in porous media whose porosities are of the order of 0.9 or greater [Nield, 1991]. For interfaces with lower porosity media, a no-slip condition for the water column is a valid approximation [Tachie *et al.*, 2003]. In fact, most studies of interfacial exchange processes that focus on fluid flow within the sediments impose a known-pressure boundary along the SWI [Shum, 1992; Huettel *et al.*, 1998; Packman and Brooks, 2001; Cardenas *et al.*, 2004]. The effect

of consideration for a slip-condition along the SWI is to change the pressure distribution. But considering the extremely small slip velocities along the SWI compared to the rest of the flow field in the water column, the pressure distribution will hardly change and its effects on interfacial exchange is similarly minor, if any.

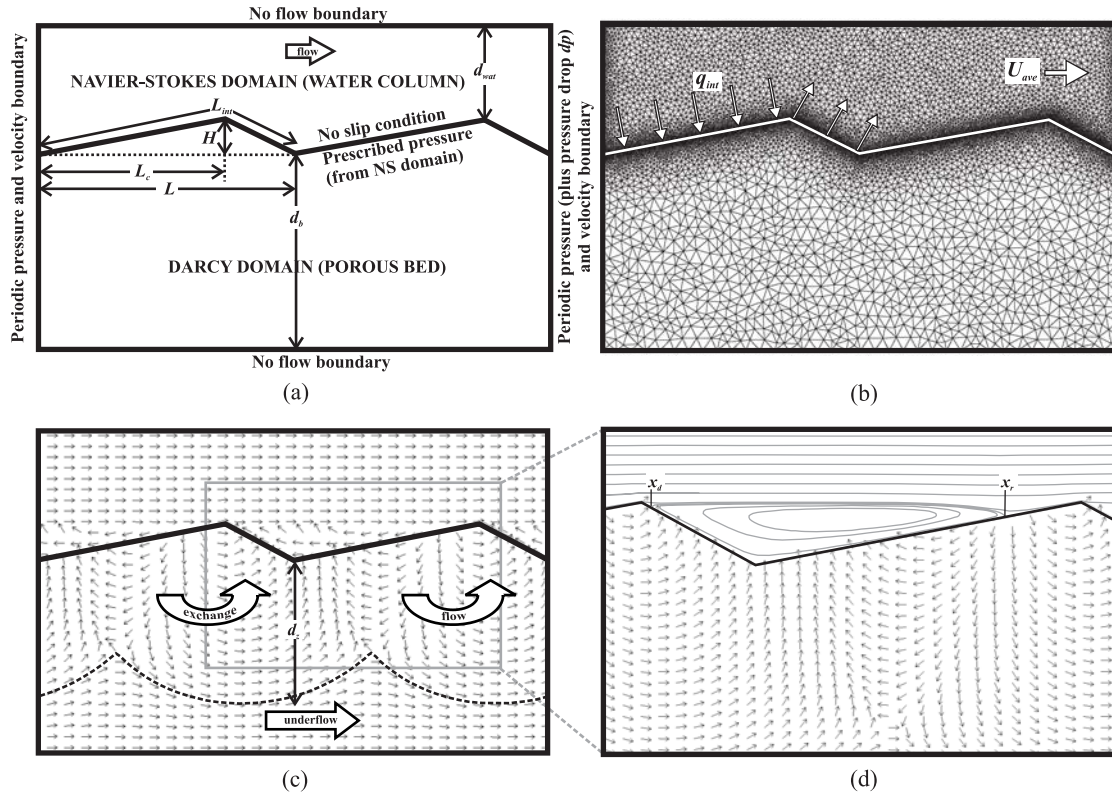


Figure 3.1. (a) Schematic of model domain and system formulation. (b) Representative finite element mesh illustrating normal flux (small white arrows) through the bed surface, q_{int} , and average horizontal velocity in the water column (large white arrow), U_{ave} . (c) Typical solution for flow directions (arrows are of equal lengths and do not indicate magnitude); dashed line in the porous bed is a dividing streamline which separates the interfacial exchange zone from deeper zones dominated by ambient underflow, the vertical distance from the trough of the bedform to the deepest section of this streamline defines the depth of the exchange zone, d_z . (d) Close up view of the eddy. (Simulation for larger $H/L=0.143$ and smaller $L_c/L=0.74$ to make eddy more prominent.)

In order to approximate an infinite horizontal domain solution, we impose spatially periodic pressure and velocity boundaries along the vertical sides for both the

water column and the sediments (Figure 3.1a). The same mean pressure drop, dp , is prescribed between the two vertical boundaries for both domains. Pressure is also specified at the upper right or lower right corner of the NS domain in order to facilitate the periodic boundaries and achieve a unique solution. Ambient flow is always from left to right. Stability and accuracy of the NS solution is ensured via using Lagrange p2-p1 elements (second order Lagrange elements for velocity and linear for pressure). Similarly, we use second order Lagrange elements for the Darcy domain. The number of triangular elements range from about ~ 18000 to near 43000 depending on dune geometry and hydrodynamic conditions (Figure 3.1b). Element distribution is densest at the SWI; and denser in the water column than in the porous bed. Sensitivity to grid spacing was conducted and the solutions presented here are converged with respect to the grid.

In order to answer the questions posed in §3.1.2, we ran multiple simulations with different parameters. We varied the bedform length (L), bed crossover length (L_c , the x -location of the crest relative to the entire bedform), bedform height (H), and the depth of the impermeable boundary of the bed (d_b). These parameters are illustrated in Figure 3.1a. Several ambient or mean pressure drops (dp) were used to effectively vary the average velocity (U_{ave}) in the water column as well as the Reynolds number (Re). We define Re in terms of the bedform height as:

$$Re = \frac{U_{ave} H}{\nu} \quad (3.6)$$

where ν is the kinematic viscosity of water at standard conditions (20°C), and U_{ave} is the characteristic velocity defined as the average velocity along a vertical-section in the

water column, taken from the crest of the bedform to the top boundary. Steady-state numerical solution of the Navier-Stokes equations was possible for Re up to $\sim 15,000$ but we limit our analysis to lower Re where turbulence is less likely to occur. Froude numbers (with the water column depth as the characteristic length) for the water column are $\ll 1$ in all simulations.

Our answers to the questions in §3.1.2 focus on dunes. These ubiquitous larger scale features are expected to have a more profound effect on interfacial exchange than smaller bedforms. Dunes typically, though not strictly, have bedform length (L) greater than 0.6 m and bedform height (H) larger than 0.04 m [Yalin, 1977] and are formed under broad hydrodynamic and sedimentological conditions. Fortunately, empirical studies such as by Yalin [1977] have delimited stability fields for different bedforms including dunes. These were used as the basis for fixing bedform height ($H=0.05$ m), and selecting ranges of bedform length (L), steepness (H/L), and asymmetry (L_c/L) for the sensitivity analyses. We chose as the base case for these simulations $H=0.05$ m, $H/L=0.05$ and $L_c/L=0.9$; this is similar to the base case in Cardenas and Wilson [submitted]. Furthermore, Southard and Boguchwal [1990] demonstrated that dunes do not form in fine sediments ($d_{10} < 0.15$ mm); thus we arbitrarily assigned the sediments for both ripples and dunes an intrinsic permeability value of $k=1 \times 10^{-10}$ m², which is within the range for well-sorted coarse sand. At the end of the paper we also examine a smaller bedform, i.e. ripples, but consider only one bedform geometry (i.e. H , L , H/L , L_c/L , etc. are fixed) and compare to experiments.

3.3. Results and Discussion

3.3.1. Eddy geometry and bottom pressure distribution

We first study the influence of triangular bedforms on the geometry and size of the water-column eddy that forms downstream of the bedform crest, and the resulting bottom pressures (that drive the flow through the sediments). A typical simulation result is portrayed in Figure 3.1c (for a larger dune steepness and smaller asymmetry in order to highlight features). The flow in the water column accelerates on the stoss side and decelerates on the lee side of the bedform. An eddy is visible in the water column downstream of the bedform crest, as indicated by the arrows which show flow direction (not magnitude). A close up view of the eddy is shown in Figure 3.1d, with streamlines instead of velocities in the water column. Figure 3.2 provides a view of the pressures and flow fields for the dune base case, over a range of Reynolds numbers (where increasing dp is used to increase U_{ave} and Re). At the lowest Re , which is of no practical importance, the water column flow is creeping and there is no eddy. Above a threshold Re , which depends on the bedform geometry, separation occurs and an eddy forms around the trough. The eddy gets larger as Re increases further. The eddy detachment point (x_d) migrates upstream and up the lee face towards the crest, while the reattachment point (x_r) migrates downstream and up the stoss face (Figure 3.2). The eddy size, measured by length $L_e = x_r - x_d$, is particularly sensitive to the current at low Re (Figure 3.3a).

Well above the channel bottom, the mean pressure gradient in the water column dominates over local pressure gradients generated by the current-bedform interaction (Figure 3.2). At the bottom, the pressure is continuous across the sediment water interface. The eddy detaches from the SWI near the point of minimum local pressure (p_{min}), which is located close to the bedform crest when $Re > 200$, and re-attaches near the point of maximum pressure (p_{max}), on the stoss face. Normalized bottom pressures

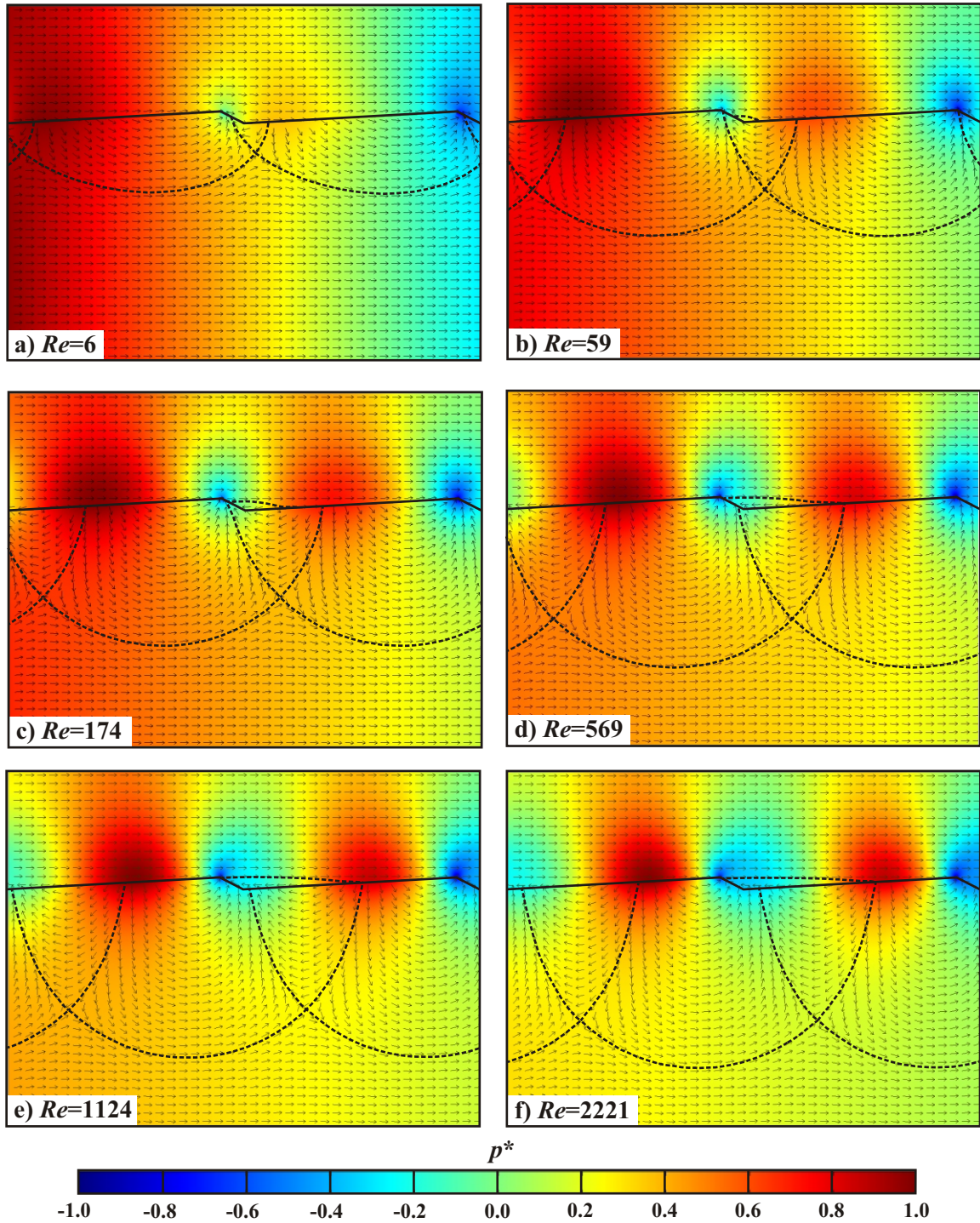


Figure 3.2. Typical solutions for normalized pressure (indicated by color spectrum) and flow directions (arrows are of equal lengths and do not indicate magnitude) over and through a dune. Shown are flow fields (a-f) for six Reynolds numbers ($Re=6, 59, 174, 569, 1124, 2221$) depicting the development of the eddy, and the co-location of eddy reattachment points and pore-water flow divides. Dashed lines are streamlines that divide the porous bed into distinct flow cells. ($H=0.05$ m, $L=1.0$ m, $H/L=0.05$, $L_c/L=0.9$, $d_b=2.0$ m, $d_{wat}=0.45$ m, $k=1 \times 10^{-10}$ m/s.)

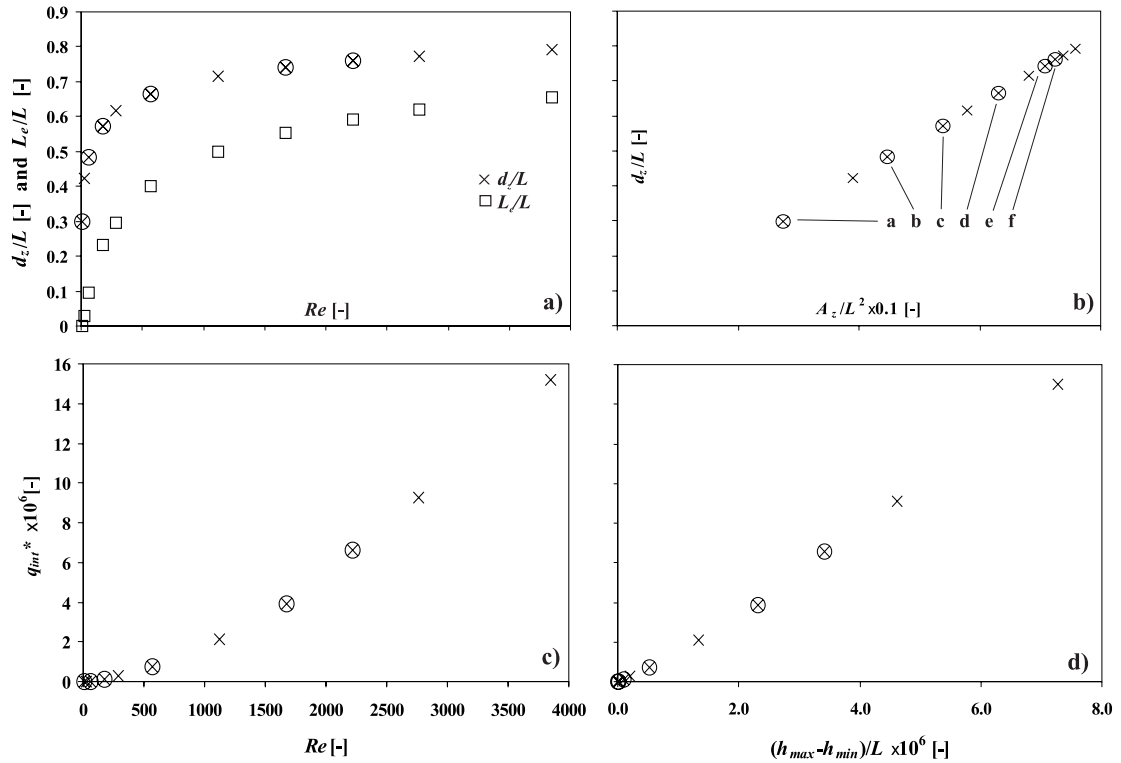


Figure 3.3. (a) Relationship of eddy length, L_e (squares), and interfacial exchange zone depth, d_z , (x's) with Re . The horizontal length of the eddy is measured from the detachment to reattachment points, across the trough. (b) Relationship between IEZ depth and area, A_z . (c) Interfacial exchange flux density, q_{int}^* as a function of (c) Re and (d) pressure drop between points of maximum and minimum bottom pressure (where the pressure drop is written in terms of head, $h=p/\rho g$). Conditions used in simulations are the same as in Figure 3.2. The six simulations in Figure 3.2 are indicated by encircled x's and corresponding letter labels in (b).

(p^*) are plotted in Figure 3.4 for the same Reynolds numbers found in Figure 3.2. The bottom pressures for any one bedform wavelength are normalized by calculating the midpoint pressure (one half of the sum of p_{max} and p_{min}) and pressure “amplitude” (one half of the difference of p_{max} and p_{min}), then subtracting the midpoint value from the bottom pressure and dividing by the amplitude. For creeping flow the maximum pressure, p_{max}^* , is located near the trough, as one would expect from continuity and the Bernoulli equation. As Re increases, an eddy forms and the location of maximum pressure, which

is almost co-located with the reattachment point, migrates downstream. The minimum value of the normalized pressure, p^*_{min} , is located at the crest for creeping flow, and at or just downstream of the crest for higher Re s (where it is essentially co-located with the eddy detachment point for higher Re s). Approaching this minimum from upstream, there is a significant dip in pressure at or near the crest of the bedform. The pressure then gradually recovers over the bedform lee face and trough.

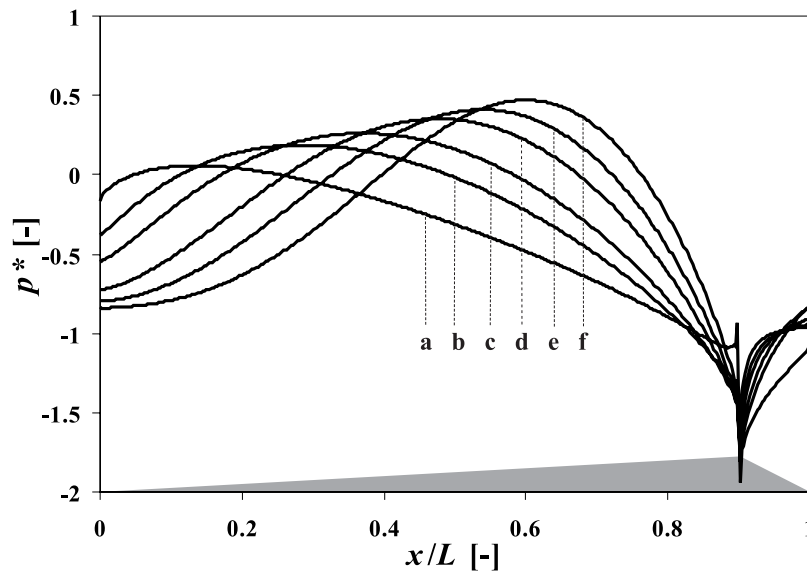


Figure 3.4. Simulated pressure (normalized p^*) profiles for different Re taken along the bed surface for the conditions of Figure 3.2 (letter scheme is same as in Figure 3.2). Location x is measured downstream from the trough. Gray area illustrates the corresponding bedform geometry.

3.3.2. Interfacial exchange zone configuration and flux

Figures 3.1 and 3.2 visually display the relationship between flow conditions above and below the sediment water interface. Below the SWI, the pore-water flow is controlled by the pressure distribution at the bottom of the water column, which at higher

Re_s is related to eddy size. The pattern of pore-water flow directions in Figure 3.2 is indicated by the arrows. Pore-water flow is into the bed on the upper part of the bedform's stoss face, and back up into the water column on the lee face and the lower part of the stoss face. Further away from the SWI, in the porous bed below, the mean pressure gradient dominates over local gradients generated due to the current-bedform interactions. This results in "underflow", or ambient flow, within the sediments and is present in all our simulations. The sediments are subjected to the same mean pressure gradient as that in the water column. Also depicted on Figure 3.1c is a pore-water streamline (dashed line) which separates the sediments affected by advective interfacial exchange flow (the interfacial exchange zone, IEZ), from the unaffected area dominated by underflow. This streamline is visually picked based on a high-density plot of streamlines. The maximum vertical extent of the IEZ (d_z) is delineated by the deepest portion of this streamline, as defined by the vertical distance between the trough of the bedform to the trough of the dashed blue line (see also Figure 3.2). We use this as a metric for IEZ size, and it increases with Re towards some asymptotic limit (Figure 3.3a), and is particularly sensitive to low Re_s . Another metric is the area (A_z) of the IEZ, which is the area swept by all water entering the (upper part of the) stoss face of a single bedform. That d_z is a good metric for the IEZ is confirmed by the almost linear relationship between d_z and A_z (Figure 3.3b).

The eddy, and related bottom pressures, determines the flow field in the sediments and the size of the interfacial exchange zone. We demonstrate this first by examining the dependence of the exchange zone depth (d_z) on Re . As shown in Figure 3.3a, it is functionally similar to that for the eddy length (L_e). Second, we observe that the

flow divides within the sediments, which separate the flow cells into one where flow is dominantly upstream and towards the stoss face and one where flow is dominantly downstream and towards the lee face (Figure 3.2), essentially coincide with eddy reattachment points for $Re > 200$. These observations demonstrate a direct relationship between flow conditions above and below the SWI. The flow fields also show that flow cells within the bed are not confined to a single bedform, i.e., there is cross-bedform flow. Although we'll see below that the bedform length (L) can be applied as a basic unit for scaling the IEZ, this does not necessarily mean that one bedform is a closed hydrodynamic system where divides coincide with natural boundaries such as crests or troughs.

Another measure of interfacial exchange is the IEZ effective flux density. We compute this as follows: i) first, we integrate the magnitude of the normal flux over a bedform's surface, L_{int} (Figure 3.1b), to get total volumetric flux, and then divide it by the wavelength of the bedform (L) which results in an effective flux density; ii) then, we divide the effective flux density by 2 since the integration does not discriminate between flux going in and out of the bed which are approximately equal. The final quantity, q_{int} , is an effective flux density based on the bedform length. We non-dimensionalize q_{int} by dividing by hydraulic conductivity of the sediments, $q_{int}^* = q_{int}/K$ ($K = k\rho g/\mu$, where g is the gravitational constant). Figures 3.3c and 3.3d show that the IEZ flux grows with Re and with the difference between maximum and minimum bottom pressures, both without limit. This we expected. As the current increases the bottom pressure variation induced by current-bedform interactions should increase. What is interesting is that that these relationships becomes linear for $Re > 1000$. Of course we would expect a linear

relationship between pressure drop and IEZ flux by Darcy's law, if the flow area were not changing. But, as suggested by Figures 3.2, 3.3a, and 3.3b, the area is still changing (for $Re > 1000$) and slightly increasing even while the flux appears to have already reached this linear behavior.

Figure 3.5 shows two velocity magnitude-depth profiles, one taken vertically through the bed from the crest, and the other from the trough, down to four bedform heights below. Velocity drops exponentially below the bed surface. At the elevation of the bottom of the bedform trough, the velocity below the crest has dropped by about 93%. Vertical profiles taken from the troughs show a similar but not as drastic decrease in velocity. Moreover, the maximum velocity magnitude for the "trough" profile, which like the "crest" profile also occurs along the SWI, is about 5% of the maximum velocity magnitude of the "crest" profile. This relationship, which is observed over a range of Re 's, suggests that fast flow and therefore efficient materials cycling is expected to be

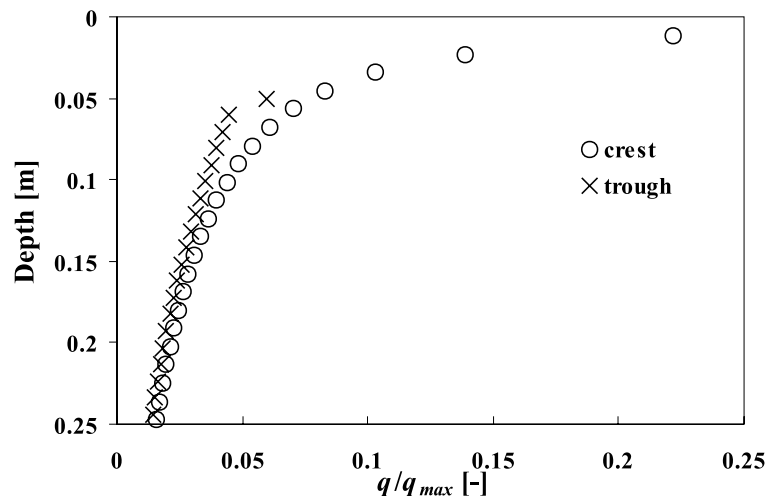


Figure 3.5. Depth profiles of normalized magnitudes of pore-water velocities (q is Darcy velocity and q_{max} is maximum velocity just below the interface at the crest) taken below the crest (hollow symbols) and below the trough (solid symbols) for different Re s. Depths are taken from the crest. Conditions are the same as in Figures 3.2d ($Re=569$).

concentrated within the bedforms. Models that approximate advective exchange through imposing spatially variable pressure on a flat bed surface may be able to correctly simulate deeper portions of the pore-flow field (e.g., *Rutherford et al.* [1995]), but miss this important aspect.

Before beginning the sensitivity exercise in the next section, we need to know that each simulated domain is deep enough to ensure that the IEZ not disturbed by the arbitrary location of the porous domain's bottom boundary. We know that if there were no underflow, IEZ depth d_z would be equal to the depth of the lower impermeable boundary, d_b . When underflow is present, such as in our case, d_z is less than d_b , as long as d_b is deep enough. This is illustrated in Figure 3.6 for $Re=1000$. When d_z/d_b is less than about 0.7, the IEZ is essentially independent of d_b . In order to approximate a solution for a vertically infinite bed in the sensitivity simulations, we ensured that $d_z/d_b < 0.7$. (The results in Figure 3.6 can also be used as a guide for designing flume

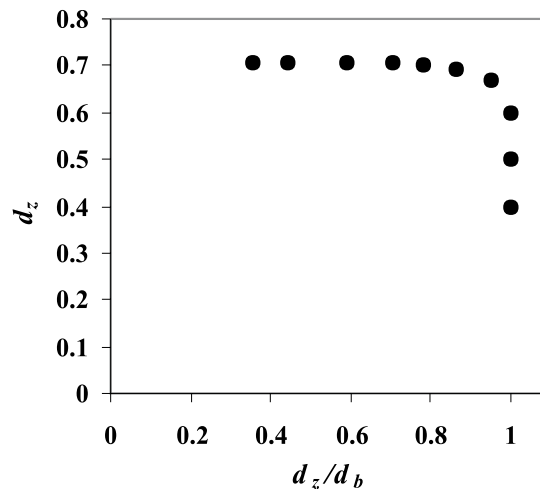


Figure 3.6. Plot of interfacial exchange zone vertical extent, d_z , versus d_z/d_b with underflow in the sediments. When the depth of the impermeable boundary, d_b , is sufficiently large ($d_z/d_b < 0.7$), the simulated extent d_z approximates that for an infinite bed. Conditions are the same as in Figure 3.2 except for variable d_b ($Re=1000$).

experiments and to ensure that boundary effects are minimized. In the next section we'll see that d_z never exceeds L in value; for design purposes this deep-bed criteria can then be conservatively rewritten as $L < 0.7d_b$. This criterion would be even more conservative for ripples, which have a larger H/L .)

3.3.3. IEZ Sensitivity to current and Reynolds Number in the water column

Let's more closely examine how Re affects d_z , the interfacial exchange zone depth, and also q_{int} , the normal flux through the surface of one bedform. This is done by looking at dunes of various geometries found in nature. Our definition of the Reynolds number (3.6) is convenient since it can be directly tied to IEZ dynamics. For instance, if there is no current, $U_{ave}=0$, $Re=0$, and the IEZ will not form. Simply put, there is no pressure gradient along the bed surface set-up by the current-bed topography interactions, such as depicted in Figure 3.2, if there is no current. Likewise, we get the same result when $H=0$ and there is no obstacle or topography. The current induced pressure distribution along the flat surface drops uniformly and linearly, and streamlines in the porous bed are horizontal and parallel to the now flat interface.

We analyzed the impact of Re for different bedform steepnesses or aspect ratios (H/L). Bedform steepness was varied from 0.0385 to 0.0555 following the observations by *Yalin* [1977] that this range for steepness is common for dunes, although there are dunes observed in nature and in lab experiments outside this range. For all the dune bedforms considered, we found that IEZ depth, d_z , increases abruptly when Re is low and eventually becomes asymptotic (as in Figure 3.3a). More notable is that when d_z is nondimensionalized by dividing it by L , the simulation results fall on one curve (Figure 3.7a). Dunes or other bedforms such as ripples with aspect ratios outside of the range we

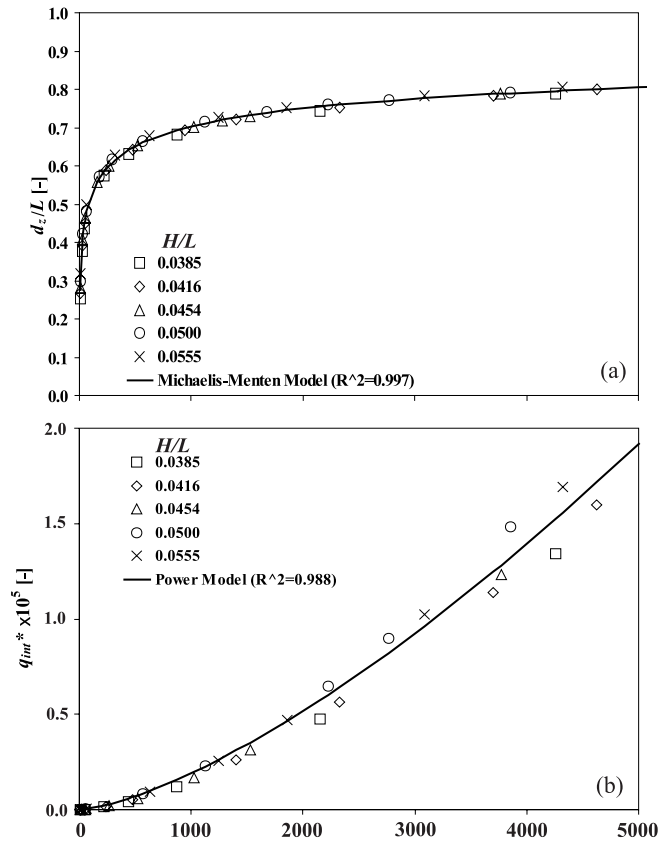


Figure 3.7. Dependence on Re of dimensionless exchange depth d_z/L (a) and dimensionless bed-surface exchange flux density q_{int}^* (b). ($L_c/L=0.9$, $H=0.05$ m, $k=1 \times 10^{-10}$ m².)

investigated may fall outside this curve. We fit the following functional model to the dimensionless data in Figure 3.7a:

Morgan-Mercer-Flodin (MMF) Model:

$$(d_z / L) = \frac{(ab + cRe^d)}{(b + Re^d)} \quad (3.7)$$

The MMF model [Morgan *et al.*, 1975], which was originally developed to describe the

unrelated problem of resource-limited growth rate of higher organisms, fits well. This function behaves such that the dependent variable (d_z/L) is equal to fitting parameter a at the y-intercept and that the asymptotic limit of the dependent variable approaches c as the independent variable (Re) approaches infinity. In our case, a is approximately 0 and c is approximately 1 (see Table 3.1). In fact, we expect that the curve should pass through the origin ($Re = 0, d_z/L = 0 = a$). Thus, we can constrain the MMF model and reduce it to

Michaelis-Menten (MM) Model:

$$(d_z / L) = \frac{Re^d}{b + Re^d} \quad (3.8)$$

which was originally used to describe the kinetics of enzymatically catalyzed reactions [*Michaelis and Menten*, 1913]. The MM model provides a slightly inferior, yet still excellent, fit than the less constrained MMF model (Figure 3.7a; Table 3.1). In both models we find that dune d_z is less than L at all Re 's. Since d_z is tied to and behaves similarly as eddy length, L_e , with respect to changes (see previous discussion) in Re , this limitation in d_z/L is primarily controlled by the natural limitation on the eddy length which can never be greater than the bedform length. Fitted parameters in equations (3.7) and (3.8) are listed in Table 3.1.

Plotting normalized flux density, q_{int}^* , as a function of Re (Figure 3.7b) also results in points essentially lying along one curve, which in this case is described by the power function:

$$q_{int}^* = aRe^b \quad (3.9)$$

where $a=9.78 \times 10^{-11} \text{ ms}^{-1}$ and $b=1.43$. Unlike IEZ depth, which follows a saturation growth type model, the IEZ flux constantly increases with Re (Figure 3.7b).

Table 3.1. Results of regression of simulated d_z/L with Re (see Figure 3.7 and equations (3.7) and (3.8)).

Parameter	MMF	MM
a	-0.0405	---
b	3.9274	4.5158
c	1.0065	---
d	0.3277	0.3429
R^2	0.9970	0.9969

3.3.4. IEZ Sensitivity to bedform geometry

Relationships between bedform steepness, H/L , and IEZ depth, d_z/L , and flux, q_{int}^* , are illustrated in Figure 3.7. Consider the case where U_{ave} and L are constant; an increase in bedform height (H) increases Re and therefore results in an increase in d_z/L and q_{int}^* . Since L is fixed, the interfacial exchange zone depth and total flux increases with bedform height. Now consider water column flows with similar Re and therefore similar d_z/L . Assuming U_{ave} and H are constant, the bedform with smaller length (L) will result in a shallower IEZ, as d_z has to be smaller to offset the decrease in L , and a smaller IEZ flux ($=LK q_{int}^*$). Consideration of these relationships, as well as the limiting behavior of L to d_z , suggests that L is an appropriate bedform dimension for scaling of IEZ spatial extent. This has direct implications for exchange models that include the area of transient storage zones as a parameter (see *Runkel* [2003], for example). Portions of

these areas correspond to “dead zones” in the water column and the rest correspond to IEZs. Knowing a representative value for L could potentially help in the parameterization of this term. Note that this is only valid for cases where the water column is not experiencing a net gain or loss of water through the bed.

We also examined the asymmetry of bedforms as indicated by the ratio of bed crossover length, L_c (see Figure 3.1a for illustration), with respect to the entire bedform length, L . Ripples and dunes are typically formed in unidirectional flow and usually have an asymmetry ratio, L_c/L , of 0.7-0.9. Bedforms with an L_c/L that is less than this range are more typical of areas where flow is not dominantly unidirectional (but not necessarily oscillatory), i.e., estuaries or tidal flats. However, such bedforms are also present in rivers. For example, antidunes have an L_c/L less than 0.5. Our results show that at low Re , IEZ depth, d_z , is not very sensitive to L_c/L (Figure 3.8a). The sensitivity of d_z to L_c/L increases with rising Re . As Re rises, d_z is smallest at $L_c/L = 0.6-0.7$ and largest at $L_c/L = 0.1-0.3$, for low and intermediate Re , and at $L_c/L = 0.9$, for higher Re . The interfacial-exchange flux density, q_{int}^* , decreases slightly with an increase in L_c/L (Figure 3.8b). However, for $L_c/L \geq 0.6$, q_{int}^* appears to stabilize. Equilibrium unidirectional bedforms have L_c/L 's that are in this range because of drag minimization, with the result that these equilibrium bedforms also minimize advective interfacial exchange.

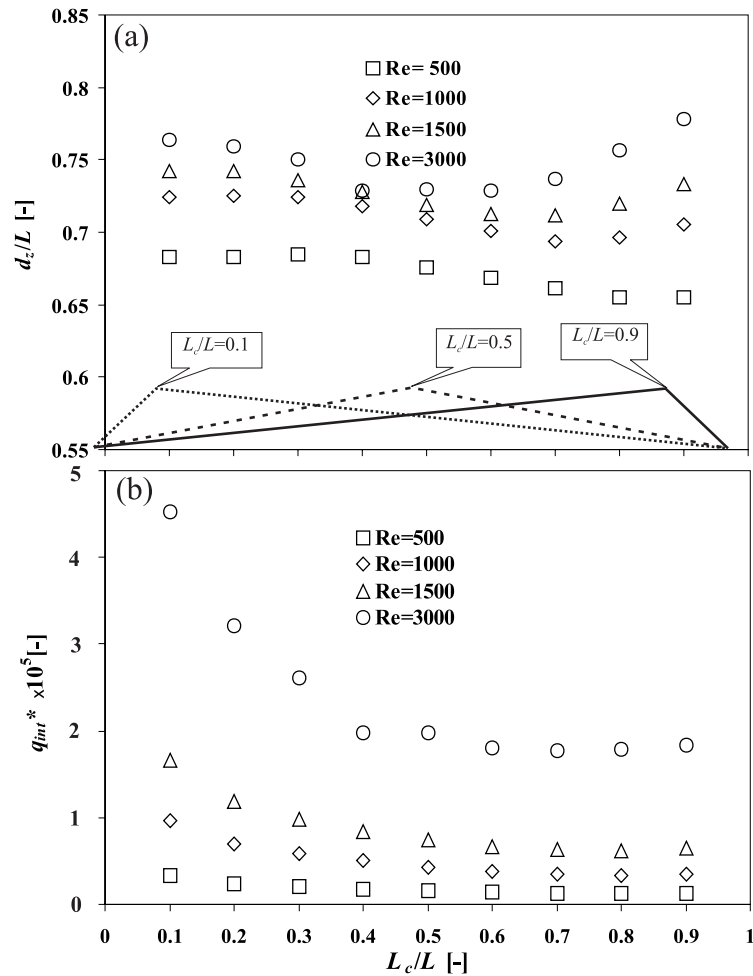


Figure 3.8. Effect of bedform asymmetry, L_c/L , on IEZ depth, d_z/L (a) and on IEZ flux density, q_{int}^* (b); in all cases flow is from left to right. ($L=1.0$ m, $H/L=0.05$, $H=0.05$ m, $k=1 \times 10^{-10}$ m².)

3.4. Limitations and Comparison to Experiments

The major assumption underlying these simulations is laminar flow in the water column. Where natural flows are characterized by small currents and laminar flow such as in quiescent lakes, wetlands or even in coupled flows in fractured rock, our results can be used predictively, but for stronger currents their main power is explanatory. We believe that this power is significant, as demonstrated by the discussion in §3.3.

However, most interesting natural flows, and most laboratory experiments, are turbulent. We compare our simulation results to various laboratory flume experiments (e.g., *Armaly et al.* [1983], *Shen et al.* [1990], and *Cheong and Xue* [1997]), most of which involve turbulent flow. While some differences between the simulations and experiments can be attributed to non-ideal conditions in the experiments (several of which we will mention), the major differences are due to the presence of turbulence.

Eddy geometry. The sharp increase in eddy size with Re , which we demonstrate in Figure 3.3a, is well known for laminar flow past a backward-facing step. *Armaly et al.* [1983] found this behavior for Re 's of 0 to 600, where we've converted their result to a more compatible Re (defined by the mean velocity over the step and the step height). The eddy zone behind the backward-facing step then starts to shrink (in a step-wise fashion) as the flow becomes transitional, at Re 's of 600 to 3300. After the eddy achieves a minimal size, it slightly grows again with even higher Re s up to a stable size for fully-turbulent flow at $Re > 3300$. The turbulent eddy is smaller than the maximum achieved under laminar flow conditions (in *Armaly et al.* [1983] it is less than half the size of the size of the largest laminar eddy). We ran additional triangular bedform simulations for higher Re 's than shown in Figures 3.2, 3.3, and 3.7, but it becomes apparent that, without explicit consideration for turbulence, the simulated eddy attains a maximum size and never decreases. Experiments (e.g., *Nelson and Smith* [1989], *Cheong and Xue* [1997], and *Elliott and Brooks* [1997b]) for fully-turbulent flow over two-dimensional triangular bedforms (there are no published results for laminar or transitional flows) result in smaller eddies that reattach at points closer to the trough than the laminar flow results presented here, consistent with *Armaly et al.*'s [1983] results for the backward-facing

step. Extrapolating from the backward-facing step results, we suggest that the point at which the rate of increase in eddy size with Re starts to decrease significantly (Figure 3.3a) can be loosely interpreted as the limit at which the flow becomes transitional from laminar. In the case of the simulations in Figures 3.3 or 3.7, this limit is roughly in the Re range of 600~900. It might be on the high side of this range, as we expect the eddy growth rate to decrease earlier in our case compared to a back-step, due to the finite amount of space that the eddy can occupy with periodic bedforms. A universal threshold Re between laminar-transitional- turbulent flow regimes for triangular bedforms is not well-documented. Defining a threshold becomes more difficult when multiple geometries (e.g., several H/L and L_c/L values) are considered, such as our case. In this paper we present results at higher Re 's (e.g., Figures 3.7) for these reasons as well as for completeness. Additionally, presenting results through the transitional regime facilitates comparison with similar future multiphysics studies that consider transitional and/ or turbulent flows in the water column.

Bottom pressure. Because of its typically smaller eddy size, turbulent flow in the water column will have a somewhat different pressure distribution along the SWI compared to our laminar flow solution of the NS equations. The differences are elucidated in Figure 3.9 where normalized bottom pressures are plotted for a bedform conforming to the geometry of ripples, both in size (H and L), steepness (H/L) and asymmetry (L_c/L), and are taken from a published flume experiment ('Run 9' of *Elliott and Brooks* [1997b] and *Elliott* [1990]). The normalization is similar to that in Figure 3.4, except that the mean pressure gradient is also removed [*Elliott and Brooks*, 1997a]. The plot includes *Elliott and Brooks*' [1997a] fit of fully-turbulent flow pressure

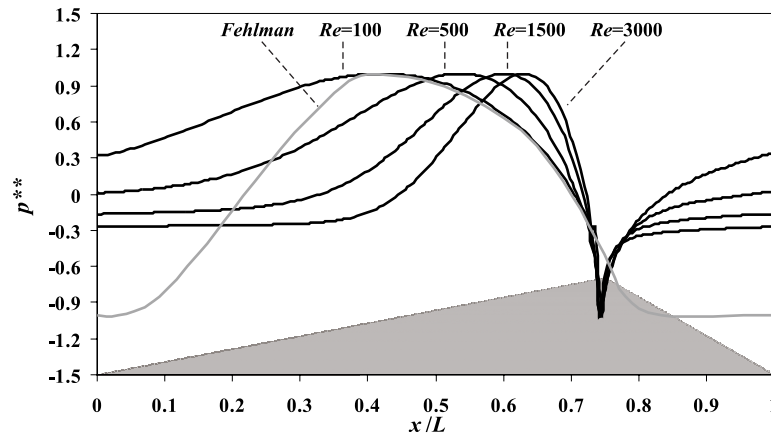


Figure 3.9. Simulated pressure (normalized p^{**} , where p^{**} is normalized similar to p^* except that the ambient gradient is removed) profiles for different Re taken along the bed surface for a ripple bedform [Elliott and Brooks, 1997a]; gray line corresponds to normalized pressure distribution based on measurements by Fehلمان [1985] over a similar bedform, as presented in Elliott and Brooks [1997a]. ($L=0.178$ m, $L_c=0.132$ m, $H=0.0254$ m, $H/L=0.143$, $d_b = 0.135$ m, $d_{wat} = 0.0645$ m., $k= 2 \times 10^{-10}$ m².)

measurements that were taken on similar experimental impermeable triangular ripple bedforms by Fehلمان [1985]. The Fehلمان pressure profile (gray line) has a maximum that is closer to the trough than the ($Re > 200$) laminar flow results (Figure 3.9), consistent with a smaller eddy for turbulent flow. Unlike the simulations, the gray line does not have a dip in pressure at or near the crest of the bedform. Instead, the low pressure zone corresponds to a broad area encompassing the trough of the bedform. This is an experimental artifact, as a pressure dip or adverse pressure gradient is necessary for flow to separate and reverse; it is difficult or impossible to resolve the dip in flume experiments. (Pressure probes need to be accurately placed where the reattachment point is located but this is not known *a priori*. Even if probe placement were optimal, the time-averaging needs to be carefully considered [Chun *et al.*, 2004]). Other studies show disparate results. For example, Raudkivi [1963] found that pressure dips near the crest

then increases through the lee face of the triangular bedform; *Yoon and Patel* [1996], using a Reynolds-averaged NS model of the water column, also found a similar upward trend in pressure on the lee face. A large gradient in pressure at the lee face of a triangular mound was observed by *Huettel and Gust* [1992]. On the other hand, the observations and calculations in *Vanoni and Hwang* [1967] and *Mendoza and Shen* [1990] have more or less similar trends with those of the gray curve in Figure 3.9. Nonetheless, our results, as well as those of the studies mentioned, consistently show the location of the lowest pressure at or near the crest. In some it is a dominant trough and in others a broad area. The differences are due to experimental design and flow conditions, i.e., laminar to transitional to turbulent. The Re s for the references we cite vary from about 3000 to as high as 50000, higher than in the simulations presented here. While the simulations show that for laminar flow the normalized pressure profiles are sensitive to Re (Figures 3.4 and 3.9), sensitivity to Re is expected to be much less for turbulent flow conditions (e.g., *Vanoni and Hwang* [1967], *Fehlman* [1985], and *Shen et al.* [1990]).

The limitations of our formulation, especially the assumption of water-column flow that is laminar, should be considered when interpreting our findings. Despite this, our results help us understand how IEZs develop in these systems and provide a foretaste for future studies that explicitly account for turbulence.

3.5. Summary

We modeled coupled flow above and below a sediment-water interface with two-dimensional bedforms using a sequential numerical formulation. The water column is governed by the Navier-Stokes and continuity equations while the porous bed follows the

groundwater flow equation. FEMLAB (now called COMSOL Multiphysics), a multiphysics finite element analysis software, was used to solve the governing equations. We show, for laminar flow in the water column, how the relationship between driving forces and resulting flow fields and fluxes change across evolving dynamical settings.

Coupling between water column and exchange zone flow is mainly controlled by the behavior of the eddy in the water column. In fact, the deepening of the exchange zone with increasing Reynolds number mirrors the growth of the eddy. The eddy detaches near where the minimum pressure is located along the interface and reattaches close to the location of maximum pressure. These two critical pressures, which determine maximum pressure gradient, dominantly control the exchange zone flow field. The simulations show that the water-column eddy size and reattachment point position controls the location of flow divides within the porous bed. Since eddy size increases with an increase in Reynolds number, the same dynamic behavior is observed in the geometry and flow field of the interfacial exchange zone. Flow divides within the bed do not necessarily correspond to natural breaks such as bedform troughs and crests. Some flow cells cross bedforms illustrating that a bedform is not necessarily a closed hydrodynamic system. Lastly, pore-water velocities drop significantly with depth from the bed surface. Pore-water velocities near the trough are lower than those near the crest. These results support the importance of and the need for hydrodynamic models that explicitly consider the geometry of bedforms.

The plot of interfacial exchange zone depth and the water column Reynolds number is described by a simple function, the Michaelis-Menten model, with a single curve for a range of common dune steepnesses. That the depth is a good metric of the

interfacial exchange zone is shown by the linear relationship between exchange zone area and depth. The interfacial exchange zone is very sensitive to lower Reynolds numbers, but at higher Reynolds numbers stabilizes at a depth that is equivalent to the length of the bedform. This information is potentially useful in the parameterization of the interfacial exchange zone area which is commonly included in transient storage models. The relationship between bed-surface flux and Reynolds number is described by a non-asymptotic power function. Flux is mainly controlled by the pressure gradient set-up along the bed surface due to current-bedform interactions, especially at higher Reynolds numbers. For these conditions the exchange zone depth and area are less sensitive to the pressure gradient, and the exchange zone flux is linearly related to Reynolds number owing to Darcy's Law.

Aside from demonstrating the effects of bedform height and length, the results show that both interfacial exchange zone depth and bed fluxes may change with the relative location of the bedform crest. At low Reynolds number, the interfacial exchange zone depth is not affected much by the relative location of the crest but it becomes more sensitive to the crest location as the Reynolds number increases. Fluxes are higher when the crest is further upstream from the downstream-located trough. Changes to flux are minimized and appear to stabilize as the crest gets closer to the downstream trough.

References

- Armaly B. F., F. Durst, J. C. F. Pereira, and B. Schonung, Experimental and theoretical investigation of backward-facing step flow, *J. Fluid Mech.*, 127, 473-496, 1983.
- Boudreau, B. P., Solute transport above the sediment-water interface, in *The Benthic Boundary Layer: Transport Processes and Biogeochemistry*, edited by B. P. Boudreau and B. B. Jorgensen, New York: Oxford University Press, 2001.
- Burnett W. C., H. Bokuniewicz, M. Huettel, W. S. Moore, and M. Taniguchi M., Groundwater and pore water inputs to the coastal zone, *Biogeochemistry*, 66, 3-33, 2003.
- Cardenas, M. B. , J. L. Wilson, and V. A. Zlotnik, Impact of heterogeneity, bed form configuration, and channel curvature on hyporheic exchange, *Water Resour. Res.*, 40, W08307. doi:10.1029/2004WR003008, 2004.
- Cardenas, M. B., and J. L. Wilson, The influence of ambient groundwater discharge on hyporheic zones induced by current-bedform interactions, submitted to *J. Hydrol.*
- Cheong, H. F., and H. Xue, Turbulence model for water flow over two-dimensional bed forms, *J. Hydraul. Eng.*, 123(5), 402-409, 1997.
- Choe, K. Y., G. A. Gill, R. D. Lehman, S. Han, W. A. Heim, and K. H. Coale, Sediment-water exchange of total mercury in the San Francisco Bay-Delta, *Limnol. Oceanogr.*, 49(5), 1512-1527, 2004.
- Chun, S., Y. Z. Liu, and H. J. Sung, Wall pressure fluctuations of a turbulent and reattaching flow affected by an unsteady wake, *Exp. Fluids*, 37, 531-546, 2004.
- Davis, T. A., A column pre-ordering strategy for the unsymmetric-pattern multifrontal method, *ACM Trans. Math. Software*, 30(2), 165-195, 2004.
- Elliott, A. H., Transfer of solutes into and out of streambeds, Ph.D. thesis, Rep KH-R-52, WM Keck Lab of Hydraul and Water Resour, Calif Inst of Technol, Pasadena, 1990.
- Elliott, A. H., and N. H. Brooks, Transfer of nonsorbing solutes to a streambed with bed forms: Theory, *Water Resour. Res.*, 33(1), 123-136, 1997a.
- Elliott, A. H., and N. H. Brooks, Transfer of nonsorbing solutes to a streambed with bed forms: Laboratory experiments, *Water Resour. Res.*, 33(1), 137-1151, 1997b.
- Fehlman, H. M., Resistance components and velocity distributions of open channel flows over bedforms, M. S. Thesis, Colo State Univ, Fort Collins, CO, 1985.

- Findlay, S., Importance of surface-subsurface exchange in stream ecosystems: The hyporheic zone, *Limnol. Oceanogr.*, 40(1), 159-164, 1995.
- Harvey, J. W., and C. W. Fuller, Effect of enhanced manganese oxidation in the hyporheic zone on basin-scale geochemical mass balance, *Water Resour. Res.*, 34(4), 623-636, 1998.
- Ho, R. T., and L. W. Gelhar, Turbulent flow with wavy permeable boundaries, *J. Fluid Mech.*, 58(2), 403-414, 1973.
- Huettel, M., H. Roy, E. Precht, and S. Ehrenhauss, Hydrodynamical impact of biogeochemical processes in aquatic sediments, *Hydrobiologia*, 494, 231-236, 2003.
- Huettel, M., W. Ziebis, S. Forster, and G. W. Luther III, Advective transport affecting metal and nutrient distributions and interfacial fluxes in permeable sediments, *Geochim. Cosmochim. Acta* 1998;62(4): 613-631.
- Huettel, M., and I. T. Webster, Porewater flow in permeable sediments, in *The Benthic Boundary Layer: Transport Processes and Biogeochemistry*, edited by BP Boudreau and BB Jorgensen, New York: Oxford University Press, 2001.
- Huettel, M., W. Ziebis, and S. Forster, Flow-induced uptake of particulate matter in permeable sediments, *Limnol. Oceanogr.*, 41(2), 309-322, 1996.
- Huettel, M., and G. Gust, Impact of bioroughness on interfacial solute exchange in permeable sediments, *Mar. Ecol. Prog. Ser.*, 89, 253-267, 1992.
- Jorgensen, B. B., and B. P. Boudreau, Diagenesis and sediment-water exchange, in *The Benthic Boundary Layer: Transport Processes and Biogeochemistry*, edited by BP Boudreau and B B Jorgensen, New York: Oxford University Press, 2001.
- Kasahara, T., and S. M. Wondzell, Geomorphic controls on hyporheic exchange flow in mountain streams, *Water Resour. Res.*, 39(1), 1005, doi:10.1029/2002WR001386, 2003.
- Marion, A., M. Bellinello, I. Guymer, and A. Packman, Effect of bed form geometry on the penetration of nonreactive solutes into a streambed, *Water Resour. Res.*, 38(10): 1209, doi:10.1029/2001WR000264, 2002.
- Mendoza, C., and H. W. Shen, Investigation of turbulent flow over dunes, *J. Hydr. Eng. ASCE*, 116(4), 459-477, 1990.
- Michaelis, L., and M. L. Menten, Die kinetik der invertinwirkung (The kinetics of invertase activity), *Biochem. Z.*, 49, 333-369, 1913.

- Morgan, P. H., L. P. Mercer, and N. W. Flodin, General model for nutritional responses of higher order mechanisms, *Proc. Nat. Acad. Sci. USA*, 72(11), 4327-4331, 1975.
- Nelson, J. M., and J. D. Smith, Mechanics of flow over ripples and dunes, *J. Geophys. Res.*, 94(C6), 8146-8162, 1989
- Nield, D. A., The limitations of the Brinkman-Forcheimer equation in modeling flow in a saturated porous medium and at an interface, *Int. J. Heat and Fluid Flow*, 12(3), 269-272, 1991.
- Packman, A. I., M. Salehin, and M. Zaramella, Hyporheic exchange with gravel beds: basic hydrodynamic interactions and bedform-induced advective flows, *J. Hydraul. Eng.*, 130(7): 647-656, 2004.
- Packman, A. I., and N. H., Hyporheic exchange of solutes and colloids with moving bed forms, *Water Resour. Res.*, 37(10): 2591-2605, 2001.
- Packman, A. I., and K. E. Bencala, Modeling surface-subsurface hydrological interactions, in *Streams and Ground Waters*, edited by JB Jones and PJ Mulholland, San Diego: Academic Press, 2000.
- Precht, E., and M. Huettel, Advective pore-water exchange driven by surface gravity waves and its ecological implications, *Limnol. Oceanogr.*, 48(4), 1674-1684, 2003.
- Raudkivi, A. J., Study of sediment ripple formation, *J. Hydr. Div. ASCE*, 89(6): 15-33, 1963.
- Riedl, R. J., H. Huang, and R. Machan, The subtidal pump: A mechanism of interstitial water exchange by wave action, *Mar. Biol.*, 13, 210-221, 1972.
- Runkel, R. L., One dimensional transport with inflow and storage (OTIS): A solute transport model for streams and rivers, U.S. Geological Survey Water-Resources Investigation Report 98-4018, Denver: USGS, 1998.
- Runkel, R. L., D. M. McKnight, and H. Rajaram, Preface: Modeling hyporheic zone processes, *Adv. Water Resour.*, 26(9), 901-905, 2003.
- Rutherford, J. C., J. D. Boyle, A. H. Elliott, T. V. J. Hatherell, and T. W. Chiu, Modeling benthic oxygen uptake by pumping, *J. Environ. Eng.*, 121(1), 84-95, 1995.
- Salehin, M., A. I. Packman, and M. Paradis, Hyporheic exchange with heterogeneous streambeds: Laboratory experiments and modeling, *Water Resour. Res.*, 40: W11504, doi:10.1029/2003WR002567, 2004.
- Savant, S. A., D. D. Reible, and L. J. Thibodeaux, Convective transport within stable river sediments, *Water Resour. Res.*, 23(9), 1763-1768, 1987.

- Shen, H. W., H. M. Fehleman, and C. Mendoza, Bedform resistances in open channel flows, *J. Hydraul. Eng. ASCE*, 116(6), 799-815, 1990.
- Shum, K. T., Wave-induced advective transport below a rippled water-sediment interface, *J. Geophys. Res.*, 97(C1), 798-808, 1992.
- Southard, J. B., and L. A. Boguchwal, Bed configurations in steady unidirectional flows. Part 2. Synthesis of flume data, *J. Sed. Pet.*, 60(5), 658-679, 1990.
- Tachie, M. F., D. F. James, and I. G. Currie, Velocity measurements of a shear flow penetrating a porous medium, *J. Fluid Mech.*, 493,319-343, 2003.
- Thibodeaux, L. J., and J. D. Boyle, Bed form-generated convective-transport in bottom sediments, *Nature*, 325, 341-343, 1987.
- Triska, F. J., V. C. Kennedy, R. J. Avanzino, G. W. Zellweger, and K. E. Bencala, Retention and transport of nutrients in third-order stream in Northwestern California: Hyporheic processes, *Ecology*, 70(6), 1893-1905, 1989.
- Vanoni, V. A., and L. S. Hwang, Relation between bed forms and friction in streams, *J. Hydr. Div. ASCE*, 93(3), 121-144, 1967.
- Vittal, N., K. G. Rangu Raju, and R. J. Garde, Resistance of two-dimensional triangular roughness, *J. Hydraul. Res.*, 15(1), 19-36, 1977.
- Webb, J. E., and J. Theodor, Irrigation of submerged marine sands through wave action, *Nature*, 220, 682-685, 1968.
- Worman, A., A. I. Packman AI, H. Johansson, and K. Jonsson, Effect of flow-induced exchange in hyporheic zones on longitudinal transport of solutes in streams and rivers, *Water Resour. Res.*, 38(1), doi:10.1029/2001WR000769, 2002.
- Yalin, M. S., *Mechanics of Sediment Transport*, 2nd edn.. Oxford: Pergamon Press, 1977.
- Yoon, J. Y., and V. C. Patel, Numerical model of turbulent flow over sand dune, *J. Hydr. Eng. ASCE*, 122(1), 10-18, 1996.

CHAPTER 4

THE INFLUENCE OF AMBIENT GROUNDWATER DISCHARGE ON EXCHANGE ZONES INDUCED BY CURRENT-BEDFORM INTERACTIONS

(This paper has been accepted as: Cardenas, M. B., and J. L. Wilson, Hydrodynamics of coupled flow above and below a sediment-water interface with triangular bed forms and ambient groundwater discharge, *Journal of Hydrology*.)

4.1 Introduction

The biogeochemical processes occurring along sediment-water interfaces (SWIs) have measurable impacts on the distribution of ecologically and environmentally important substances up to the watershed scale in the case of rivers [Harvey and Fuller, 1998] and lakes, and up to the global scale in the case of estuaries [Webster *et al.*, 1996] and oceans [Riedl *et al.*, 1972]. Transport of biogeochemically important solutes along and across these interfaces can either be diffusive or advective. Fluid flow through the permeable sediments is generated by several mechanisms including wave and tidal pumping [Riedl *et al.*, 1972; Shum, 1993], flushing due to flow over irregular surfaces such as bedforms and obstacles [Thibodeaux and Boyle, 1987; Huettel and Gust, 1992; Huettel *et al.*, 2003], and biogenic processes. In this paper, we only consider flushing due

to current-bedform interactions. When the sediments are sufficiently permeable advective transport becomes more important than diffusion. Thus, in permeable sediments, biogeochemical processes are strongly governed by or coupled to hydrodynamical processes [Huettel *et al.*, 2003]. Unfortunately, much remains to be understood regarding the fluid physics along and across SWIs. Discharging groundwater influences and further complicates the physics and biogeochemistry of both pore-water and benthic-water [Burnett *et al.*, 2003]. However, groundwater discharges into most continental and intra-island surface water bodies [Winter *et al.*, 1998], and it is widely accepted that groundwater from coastal confined and unconfined aquifers can be discharged along beaches and even deeper parts of the continental shelf up to as much as 80 km away from the coast [Moore, 1996; Moore and Shaw, 1998; Burnett *et al.*, 2003]. Our already restricted understanding of coupled fluid flow in the water column and underlying sediments is further limited for systems with ambient groundwater discharge (AGD). To our knowledge, the impact of AGD on the hydrodynamics of SWIs has not been investigated either in experimental (field and laboratory) or theoretical studies although Woessner [2000] presented some conceptual models. Our aim is to examine the fluid dynamics along SWIs where there is discharging groundwater.

4.2. Methodology

We address this goal through numerically modeling the steady-state two-dimensional flow along SWIs. We assume laminar flow in the water column and porous media Darcy flow in the underlying sediments. The modeling is implemented in FEMLAB, a multiphysics finite element analysis software. The code solves the Navier-Stokes (NS) and continuity equations for incompressible, viscous flow for the water

column:

$$\rho \frac{\partial \mathbf{u}}{\partial t} - \mu \nabla^2 \mathbf{u} + \rho (\mathbf{u} \cdot \nabla) \mathbf{u} + \nabla p = 0 \quad (4.1)$$

$$\nabla \cdot \mathbf{u} = 0 \quad (4.2)$$

where ρ is fluid density, \mathbf{u} is the velocity vector, μ is dynamic viscosity, and p is pressure. The porous bed domain is governed by the combination of Darcy's Law and the continuity equation for incompressible flow in a non-deformable media, i. e., the groundwater flow equation:

$$\nabla \cdot \mathbf{q} = 0 \quad (4.3)$$

$$\mathbf{q} = -\frac{k}{\mu} \nabla p \quad (4.4)$$

where \mathbf{q} is the specific discharge (i.e. Darcy "velocity") and k is intrinsic permeability. Direct solvers from the UMFPACK algorithm [Davis, 2004] are implemented in FEMLAB. Sequential coupling is implemented via imposing the NS-continuity derived pressure distribution from the bottom of the water column as a Dirichlet boundary at the top of the bed surface, for the groundwater flow equation.

The top of the water column is treated as a no-flow symmetry boundary and not as a free surface (Figure 4.1), while its bottom boundary, the sediment-water interface

(SWI), assumes the no-slip/ no-flow condition. Because the top boundary of the porous domain is a prescribed pressure boundary, derived from solving the NS equations in the water column, the pressure is continuous across the two domains. The lower boundary of the porous domain is a prescribed-flux boundary, thereby representing ambient groundwater discharge upward to the water column. Periodic boundaries are used on the left and right (Figure 4.1) of both domains. Fluid properties are those of fresh water at standard and isothermal conditions (20°C). The sediment is assigned a permeability (k) of 10^{-10} m^2 . Examples of simulated flow fields are shown in Figure 4.2.

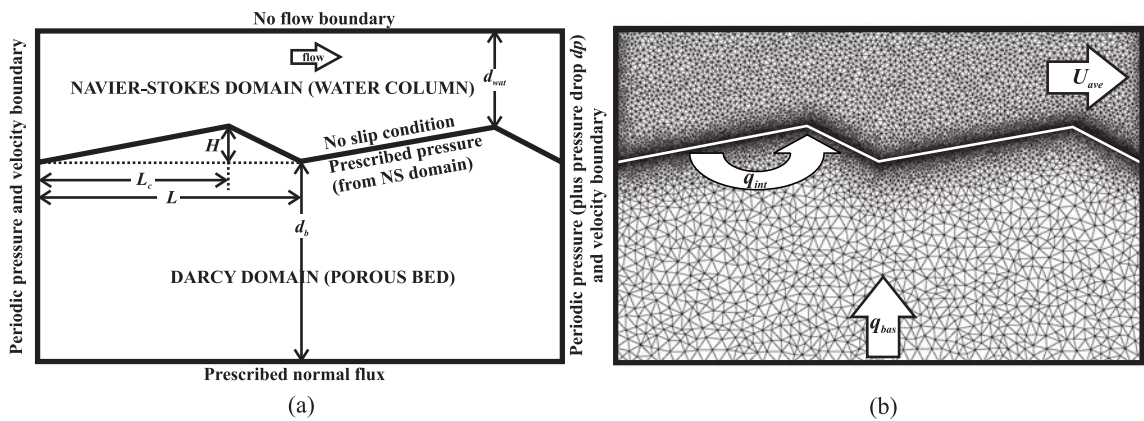


Figure 4.1. (a) Schematic of model domain and system formulation. (b) Representative finite element mesh illustrating exchange flux through the bed surface, q_{int} , prescribed basal flux, q_{bas} , and average horizontal velocity in the water column, U_{ave} . In all simulations $L_c/L=0.9$, $H=0.05$ m and $d_{wat}=0.45$ m.

Multiple simulations with varying parameters were conducted. We varied the bedform length (L), and therefore the height/length ratios or steepness (H/L), in the range of observed fluvial dune geometries, and the prescribed ambient groundwater flux density at the base, q_{bas} , which we refer to as “basal flux”. The average velocity in the water column, U_{ave} , was varied via changing prescribed pressure gradients between the

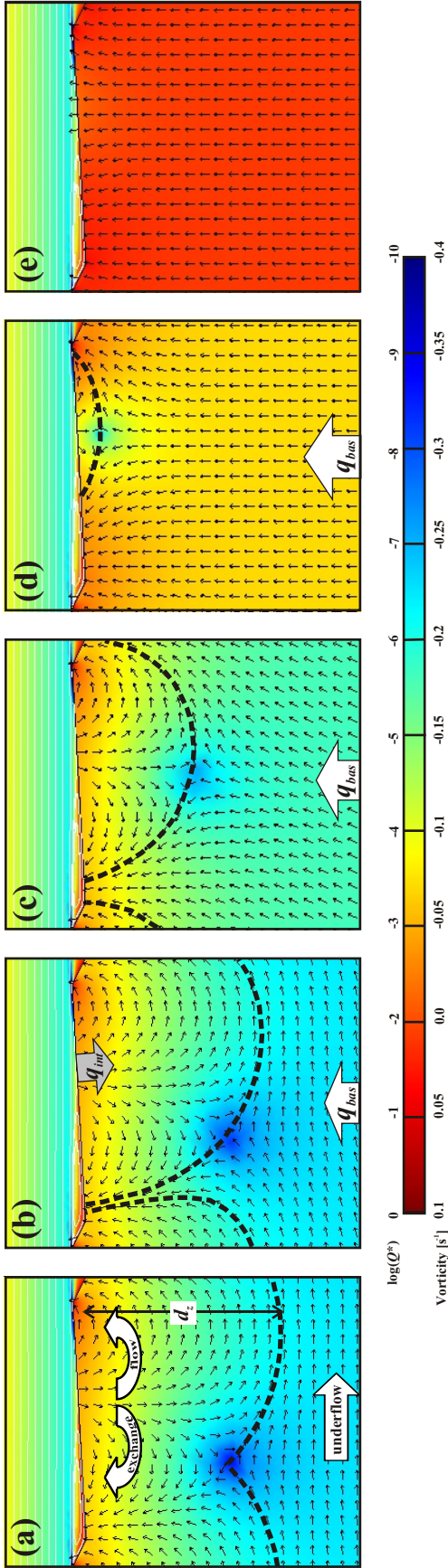


Figure 4.2. Plots of water column flow streamlines (white lines) and vorticity (color contours), porous bed velocity magnitude (color contours, $Q^*=Q/Q_{max}$, where Q and Q_{max} are the velocity magnitude and the maximum based on all simulations, respectively) and direction (small black arrows), and exchange zone boundaries for different dimensionless ambient basal fluxes, $q_{bas}^*=0, 5.5e-6, 1.8e-6, 1.8e-5$ and $1.8e-4$ for a-e, respectively. The dashed black line is a dividing streamline which separates the interfacial exchange zone from deeper zones dominated by ambient underflow or upwelling groundwater flow; the vertical distance (see (a)) from the trough to the deepest section of this streamline defines the depth of the exchange zone, d_z . Also illustrated are the normal flux through the SWI (large gray arrow in b) induced by current-bedform interactions, q_{int} . $Re=1500$ for all simulations. $H=0.05$ m, $L=1.0$ m, and $d_b=2$ m.

two periodic side boundaries. Flow is typically turbulent in rivers, estuaries, and oceans, but we only model laminar conditions in the water column, across the entire range of U_{ave} values.

4.3. Results and Discussion

We refer to the volume within the permeable sediments that is physically influenced by fluid exchange across the SWI as the interfacial exchange zone (IEZ). The IEZ is analogous to the “hyporheic zone” in fluvial settings. The maximum depth of the IEZ, d_z , is taken as the distance between the deepest portion of the streamline which envelopes all streamlines originating from the SWI, and the trough of the bedform (Figure 4.2a). The IEZ flux density through the SWI is computed as follows: i) first, total volumetric flux through the SWI per bedform is computed by integration of the magnitude of the normal flux along the bedform surface; ii) then, we subtract from this total volumetric flux the prescribed volumetric basal flux (basal flux multiplied by the bedform length) resulting in the total volumetric interfacial flux that is induced solely by current-bedform interactions; iii) the resulting quantity is divided by the twice the length of the bedform because the integration does not discriminate between induced flux going in and out of the bed, which are approximately equal. The final value, q_{int} , is an effective flux density based on bedform length; the total IEZ flux is given by the product $q_{int} L$ and takes place only for that portion of the SWI subjected to current-induced flushing (bounded by the dividing streamline discussed above and shown in Figure 4.2). The basal and interfacial flux densities, which are schematically represented in Figure 4.1b, are nondimensionalized as follows:

$$q^*=q/K \quad (4.5)$$

where q^* is the dimensionless flux density and $K=k\rho/\mu$ is the hydraulic conductivity of the sediments.

4.3.1. Eddies and pore-water flow divides

The simulated flow fields illustrate the relationship between flow conditions above and below the SWI (Figure 4.2). We implement sequential and not simultaneous coupling which prevents any feedback effects of discharging groundwater to the water column flow field. The water column dynamics therefore follows the same behavior that is described in detail by Cardenas and Wilson (submitted manuscript and Chapter 3). Note in particular the eddy downstream of the bedform. The pore-water circulating through the IEZ can be divided into two cells, one discharging towards the crest and the other towards the trough. The dividing streamline separating the two cells starts at the eddy reattachment point on the SWI. As the dimensionless basal flux q_{bas}^* increases, the volume of the IEZ diminishes but remains more or less centered around the eddy reattachment point. The Darcy velocity magnitude within the IEZ also decreases. This decrease is small when q_{bas}^* is also small (compare Figures 4.2a-4.2c for example). Thus, although the spatial extent of the IEZ is diminished significantly by discharging groundwater, the amount of material cycled through these smaller zones stays about the same as for the case with no AGD (more on this later). The preferential discharging of ambient groundwater along the troughs may have biogeochemical consequences. We therefore expect the discharge areas close to the troughs, where two different waters mix, to be a biogeochemical or ecological “hotspot”. When groundwater discharge becomes

large enough, the flow field within the sediments is eventually reduced to an upward (more or less) uniform flow field typical of homogeneous porous media subjected to a uniform flux or pressure gradient (Figure 4.2e).

4.3.2. Effect of Reynolds Number

We examined how the water column Reynolds number (Re) affects exchange zone depth, d_z , and dimensionless interfacial flux, q_{int}^* . Re is defined as follows:

$$Re = \frac{U_{ave} H}{\nu} \quad (4.6)$$

where U_{ave} is the average velocity along a vertical-section in the water column taken from the crest of the bedform to the top boundary, H , the height of the bedform, is the characteristic length scale and ν is kinematic viscosity of water. The impact of varying Re was analyzed for different bedform steepnesses or aspect ratios (H/L ; $H=0.05$ m for all cases), but when plotted dimensionlessly the results are the same (Figure 4.3a); the data corresponding to different steepnesses falls on one curve when d_z is normalized by L . A universal threshold Re between laminar-transitional- turbulent flow regimes for triangular bedforms is not well-documented. Defining a threshold becomes more difficult when multiple geometries are considered, such as our case. In this paper we present results at higher Re 's where actual flow may no longer be laminar for these reasons as well as for completeness. Additionally, presenting results through the transitional regime facilitates comparison with similar future multiphysics studies that explicitly consider transitional and/ or turbulent flows in the water column.

For a given groundwater discharge rate, the d_z increases with Re , sharply at low

Re as the eddy grows, and then starts to become asymptotic at higher Re (Figure 4.3a) as the eddy reaches its maximum size. When q_{bas}^* is present, the sharp growth in d_z/L is subdued (Figure 4.3a), and there is a threshold or critical Reynolds number, Re_{crit} , below which there is no IEZ, and the sediments are completely filled with discharging basal groundwater (Figure 4.2e).

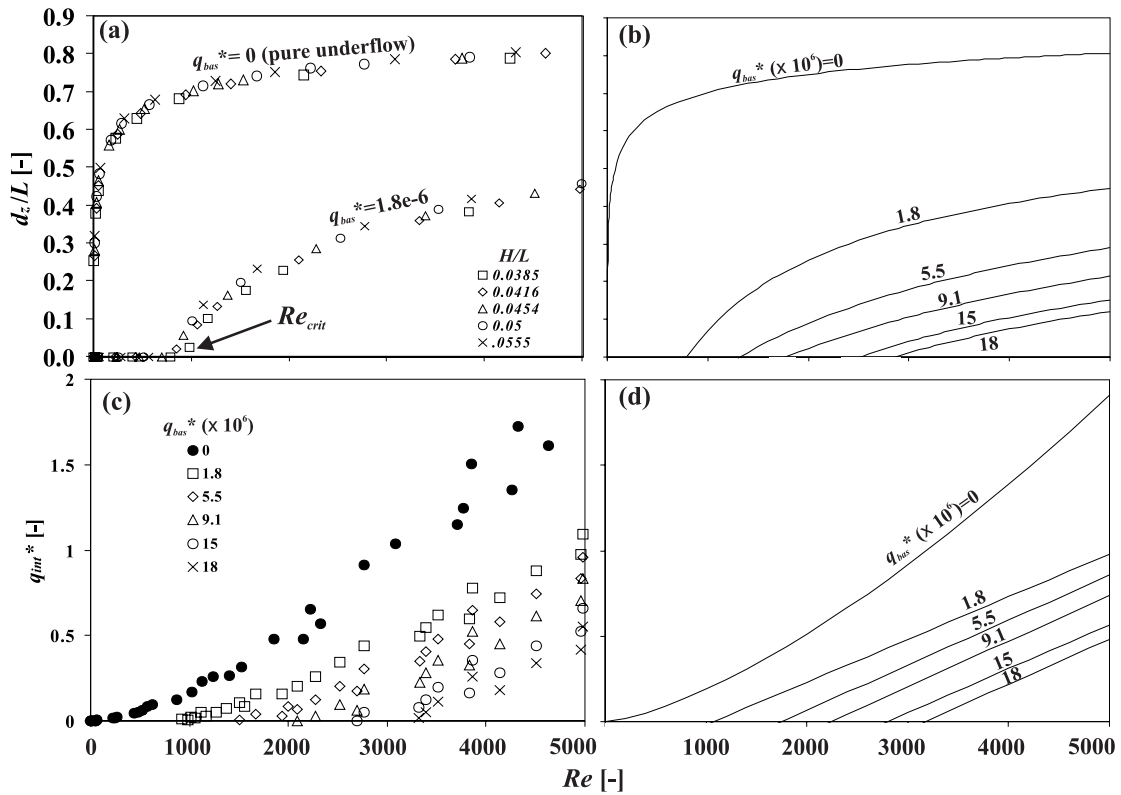


Figure 4.3. Dependence on Re of normalized exchange zone depth d_z/L (a, b) and dimensionless interfacial flux q_{int}^* (c, d). Shown are results for different bedform aspect ratios (H/L ; $H=0.05$ m for all cases) and dimensionless basal fluxes q_{bas}^* . The curves in (b) and (d) are fitted for different q_{bas}^* (see Table 4.1 for fitting parameters); MMF fits are shown in (b) and linear fits are shown in (d). Flow in the water column may be transitional or turbulent at higher Re s. No additional considerations were made to correct for turbulent flow. Thus, the simulation results at high Re s may be inconsistent with real scenarios but are still presented because thresholds for the different bedform shapes are not yet well established. d_b varies from 2 m to 2.5 m where cases with larger L corresponding to larger d_b .

In the absence of AGD, the relationship between Re and d_z (or d_z/L) can be described (Cardenas and Wilson, submitted) by a Michaelis-Menten (MM) functional model [*Michaelis and Menten*, 1913]. This function passes through the origin when there is no basal flux. However, Figure 4.3a shows that when AGD is present, the MM model is no longer appropriate because of the threshold effects and a more general form is warranted. We therefore fit the Morgan-Mercer-Flodin (MMF) model [*Morgan et al.*, 1975] to the simulation results in Figure 4.3a and for four other basal flux scenarios (Figure 4.3b and Table 4.1). The MMF model was originally developed to describe the nutritional response of higher organisms and is defined as:

$$(d_z / L) = \frac{(ab + cRe^d)}{(b + Re^d)} \quad (4.7)$$

The x -intercept of the fitted MMF models represents the critical Reynolds number. The limit of d_z/L , the coefficient c , approaches 1 when there is no AGD [*Cardenas and Wilson*, submitted]. Figure 4.3b, which depicts fitted MMF curves ($R > 0.99$ for all cases), shows that the maximum d_z/L is less than 1 when $q_{bas} > 0$ and decreases with increasing q_{bas}^* , illustrating the expected competing roles of AGD and current-bedform interactions. Figure 4.3b also illustrates how Re_{crit} increases with q_{bas}^* . The relationship between Re_{crit} and q_{bas}^* is also described by a MMF model (Figure 4.4 and Table 4.2). As the magnitude of AGD increases (increasing q_{bas}^*), the current in the water column needs to generate larger pressure gradients along the bedform surface if it is to force water into the sediments to form an IEZ.

Table 4.1. Fitting parameters corresponding to the curves in Figure 4.3.

MMF Fits (equation 7) in Figure 3b: $d_z L(Re)$					
q_{bas} ($\times 10^6$)	1.8	5.5	9.1	15	18
A	-1.18	-0.3	-0.51	-1.04	-0.85
B	46.3	91.2	138.1	81.9	107.6
C	0.78	0.91	1.04	0.58	0.62
D	0.64	0.58	0.57	0.64	0.64
R²	0.988	0.977	0.929	0.910	0.856
Linear Fits in Figure 3d: $q_{int}^* \times 10^6(Re)$					
a (-)	0.268	0.459	0.603	0.718	0.841
b ($\times 10^4$)	2.50	2.63	2.69	2.57	2.65
R²	0.981	0.965	0.949	0.907	0.911
Quadratic Fits based on Figure 3c: $q_{int}^* \times 10^6(Re)$					
a (-)	0.145	0.210	0.249	-0.04	0.650
b ($\times 10^4$)	1.347	0.901	0.554	-0.15	1.708
c ($\times 10^8$)	2.049	2.668	3.00	5.245	1.131
R²	0.988	0.974	0.958	0.921	0.911

Table 4.2. Fitted MMF models to Figure 4.4.

Data	R²	a	b	c	d
d_z/L	0.998	20.2	0.02	62553	0.638
q_{int}^*	0.999	218.6	-136	-1.3e-8	0.531

Unlike d_z which follows a saturation growth curve-type model, the IEZ flux induced by water-column flow continually increases with Re (Figure 4.3c). Recall that the total IEZ flux is given by the product LKq_{int}^* . The relationship between Re and q_{int}^* simulation results can be fit with either a quadratic or a linear model (Table 4.1). Figure 4.3d shows fitted linear models for the cases where basal flux, q_{bas}^* , is non-zero. As q_{bas}^* approaches 0, a quadratic model is more appropriate, as shown for the case where $q_{bas}^*=0$ (solid line in Figure 4.3d). A second estimate of a critical Reynolds number can be defined based on the q_{int}^* information (Figure 4.3d and Table 4.2). The values for Re_{crit} based on linear regression of the $q_{int}^*(Re)$ values is systematically higher than those based on MMF regression of the $d_z L(Re)$ values (partly due to the linear fit missing the

curvature at lower Re values) . However, the MMF-behavior of $Re_{crit}(q_{bas}^*)$ is alike for both cases (Figure 4.4).

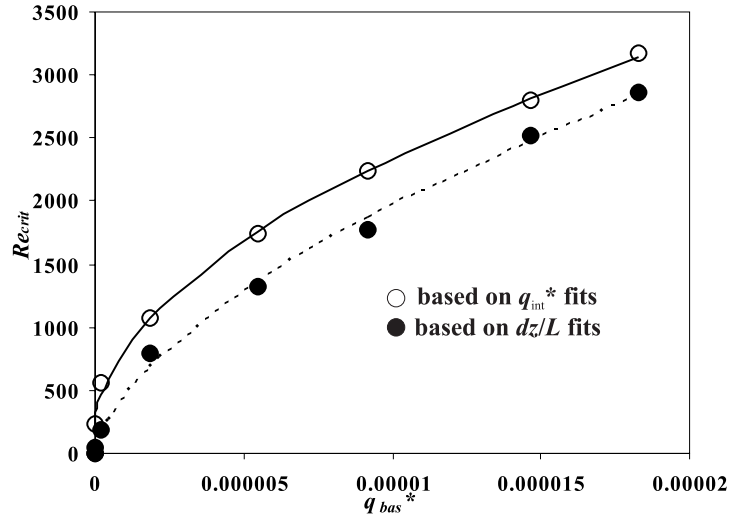


Figure 4.4. Relationship between Re_{crit} and q_{bas}^* including fitted MMF models (see Table 4.2).

4.3.3. Residence times through the exchange zones

The characteristic (mean) residence time through a system can be estimated by dividing the volume of the domain through which the fluid is flowing, by the steady volumetric flux, and multiplying by porosity, n . In our case, the total flux through the IEZ is represented by the product LKq_{int}^* . In our two-dimensional model the volume of the IEZ becomes an area, A , defined by dashed lines in Figure 4.2 and the sediment-water interface. The mean residence time is then estimated as nA/LKq_{int}^* . Defining a dimensionless area, $A^*=A/A_{max}$, where A_{max} is the maximum IEZ area which corresponds to the area of the IEZ when $q_{bas} = 0$ (e.g., Figure 4.2a), the dimensionless mean residence time is defined as:

$$t^* = \frac{A^*}{q_{int}^*} \quad (4.8)$$

Some t^* values are presented in Figure 4.5a. The characteristic residence times decrease with increasing basal flux with a smaller rate of decrease at larger basal fluxes. This behavior is consistent with the qualitative aspects of the flow field shown in Figure 4.2, and quantitative measures in Figure 4.5b. The velocities near the interface (Figures 4.2a to 4.2c) and the interfacial fluxes (Figure 4.5b) decrease only slightly, while the IEZ area

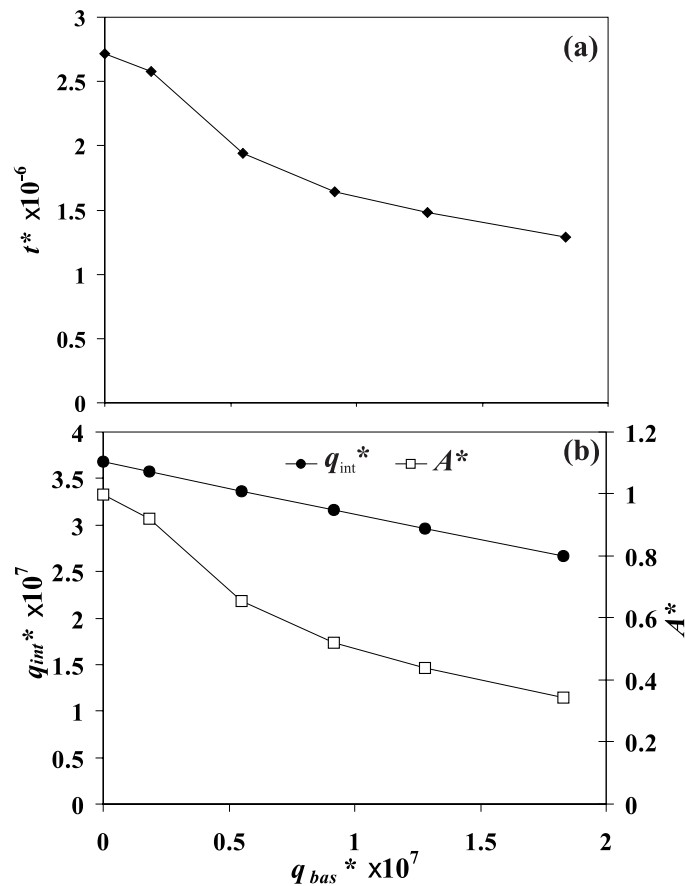


Figure 4.5. Relationship of t^* , q_{int}^* and A^* with q_{bas}^* . $Re=500$ for all simulations; $H=0.05$ m, and $L=1$ m.

decreases much more. The amount of fluid pumped through the IEZ ($=LKq_{int}^*$) stays about the same over the range of AGD, despite the smaller size of the IEZ.

4.4. Summary

We investigated the flow dynamics along and across an irregular sediment-water interface subjected to ambient groundwater discharge (AGD) via sequentially-coupled numerical flow modeling. The governing equations are the Navier-Stokes equations for laminar flow in the water column and the groundwater flow equation for the porous bed; they are solved using the multi-physics finite-element software FEMLAB. To our knowledge, coupled systems with AGD have not been studied in detail theoretically, experimentally, or in natural settings.

Numerical experiments were designed to investigate the competing roles of flow through the sediment-water interface induced by current-bedform topography interactions and by AGD, and to see how the bedform geometry and the conditions in the water column affect the size of and fluxes through the interfacial exchange zone (IEZ) in the porous bed. Water column eddy reattachment points coincide with flow divides within the bed. The cases with no AGD are studied in detail in Cardenas and Wilson (submitted manuscript and Chapter 3). As the AGD increases, the IEZ gets significantly smaller yet remains approximately centered around the eddy reattachment points. The AGD tends to focus near the bedform troughs suggesting that there might be localized biogeochemical hotspots where the two waters mix.

We found that the IEZ develops only when a current threshold is overcome. This threshold is quantified by a critical Reynolds number, below which groundwater discharging to the water column overpowers any interfacial exchange driven by current-

bedform interactions. Above this current threshold, the IEZ deepens sharply with further increase in the Reynolds number and then stabilizes at an asymptotic depth that is less than the length of the bedform. The sharp deepening of the IEZ becomes more gradual, and the asymptotic IEZ depth smaller, with an increase in AGD.

When AGD is absent, the functional relationship between the Reynolds number and the IEZ depth is described by the Michaelis-Menten type model. However, it is modified to the more general Morgan-Mercer-Flodin model, whose x -intercept is no longer at the origin, when the system is influenced by AGD. The x -intercept (representing the critical or threshold Reynolds number) increases with and is related to the ambient groundwater flux also via a Morgan-Mercer-Flodin functional model.

The non-asymptotic relationship between interfacial flux, induced by current-bedform interactions, and Reynolds number is described by quadratic or linear regression models. An increase in AGD results in relatively small changes in induced interfacial flux, especially when compared to the reductions in the IEZ spatial extent. Thus, AGD, while reducing the extent of IEZs, does not substantially impact the amount of fluid and materials transported through these zones (except when the zones are of very limited extent or non-existent), suggesting reduced residence times.

Our results have implications for the biogeochemistry of sediment-water interfaces where material transport is primarily advective. However, because our approach assumes laminar flow conditions in the water column, the results should be taken as explanatory of the hydrodynamic processes rather than predictive, for most natural flows are turbulent.

References

- Burnett, W.C., H. Bokuniewicz, M. Huettel, W. S. Moore, and M. Taniguchi, Groundwater and pore water inputs to the coastal zone, *Biogeochemistry*, 66, 3-33, 2003.
- Cardenas, M.B., and J. L. Wilson, Hydrodynamics of coupled flow above and below a sediment-water interface with triangular bedforms. submitted to *Adv. Water Resour.*
- Davis T.A., A column pre-ordering strategy for the unsymmetric-pattern multifrontal method, *ACM T. Math. Software*, 30(2), 165-195, 2004.
- Harvey, J.W., and C. W. Fuller, Effect of enhanced manganese oxidation in the hyporheic zone on basin-scale geochemical mass balance, *Water Resour. Res.*, 34(4), 623-636, 1998.
- Huettel, M., and G. Gust, Impact of bioroughness on interfacial solute exchange in permeable sediments, *Mar. Ecol. Prog. Ser.*, 89, 253-267, 1992.
- Huettel, M., H. Roy, E. Precht, and S. Ehrenhauss, Hydrodynamical impact of biogeochemical processes in aquatic sediments, *Hydrobiologia*, 494, 231-236, 2003.
- Michaelis L., and M. L. Menten, Die kinetik der invertinwirkung (The kinetics of invertase activity), *Biochem. Z.*, 49, 333-369, 1913.
- Moore, W.S., Large groundwater inputs to coastal waters revealed by ^{226}Ra enrichments. *Nature*, 380, 612-614, 1996.
- Moore, W.S., and T. J. Shaw, Chemical signals from submarine fluid advection onto the continental shelf, *J. Geophys. Res.*, 103(C10), 543-552, 1998.
- Morgan, P.H., L. P. Mercer, and N. W. Flodin, General model for nutritional responses of higher order mechanisms, *P. Natl. Acad. Sci. USA*, 72(11), 4327-4331, 1975.
- Riedl, R.J., N. Huang, R. Machan, The subtidal pump: A mechanism of interstitial water exchange by wave action, *Mar. Biol.*, 3, 210-221, 1972.
- Shum, K.T., The effects of wave-induced pore water circulation on the transport of reactive solutes below a rippled water-sediment interface, *J. Geophys. Res.*, 98C, 10289-10301, 1993.
- Thibodeaux, L.J., and J. D. Boyle, Bedform-generated convective-transport in bottom sediments, *Nature*, 325, 341-343, 1987.
- Webster, I.T., S. J. Norquay, F. C. Ross, and R. A. Wooding, Solute exchange by

convection within estuarine sediments, *Estuar. Coast. Shelf S.*, 42, 171-183, 1996.

Winter, T.C., J. W. Harvey, O. L. Franke, and W. M. Alley, *Ground Water and Surface Water: A Single Resource*, United States Geological Survey Circular 1139, Denver: USGS, 1998.

Woessner, W.W., Stream and fluvial plain ground water interactions: rescaling hydrogeologic thought, *Ground Water*, 38, 423-429, 2000.

CHAPTER 5

DUNES, TURBULENT EDDIES, AND INTERFACIAL EXCHANGE WITH POROUS MEDIA

5.1. Introduction

Interfaces between free-flowing fluids and underlying porous media are ubiquitous in nature. The movement of fluids across these interfaces exerts a strong control on physical, biogeochemical and thermal processes. Field, experimental and modeling experiments have shown that the flow field above an interface strongly interacts with interface topography to generate an irregular pressure distribution along the interface causing fluid circulation within the underlying porous media [*Webb and Theodor, 1968; Thibodeaux and Boyle, 1987; Elliott and Brooks, 1997a; Huettel and Webster, 2001*]. The overlying fluid is in general water or air and the underlying porous media is typically permeable sediments (especially sand) or snow. The interface typically has spatially periodic triangular topography, with wavelengths ranging from centimeters to kilometers. The flow fields above and within porous dunes, for both subaerial and subaqueous conditions, are geometrically and dynamically similar. In this paper the process, especially the porous flow portion, is referred to as current-topography driven fluid flow.

Thibodeaux and Doyle [1987] demonstrated water column-sediment exchange for fluvial systems where current-topography interactions generated flow through a gravel

bed. Similar processes occur in sandy sediments found in rivers [*Elliott and Brooks*, 1997] and in lacustrine, estuarine and marine settings [*Webb and Theodor*, 1968; *Huettel and Webster*, 2001]. These processes affect the ecology and biogeochemistry of hyporheic and riparian zones in fluvial systems up to the watershed scale [*Triska et al.*, 1989; *Findlay*, 1995; *Rutherford et al.*, 1995; *Harvey and Fuller*, 1996; *Worman et al.*, 2002]. Similar impacts are observed for processes in marine settings including early diagenesis [*Huettel and Gust*, 1992; *Huettel et al.*, 1996; *Huettel et al.*, 1998; *Jahnke et al.*, 2000; *Huettel and Webster*, 2001; *Jorgensen and Boudreau*, 2001]. Air circulation, or ventilation, in snow dunes has been attributed to wind-snow dune interactions [*Colbeck*, 1989; *Cunningham and Waddington*, 1993; *Albert and Hawley*, 2002]. Snow ventilation affects snow-atmosphere exchange of both heat and mass thereby influencing internal processes within snowpacks [*Cunningham and Waddington*, 1993; *Albert and Schultz*, 2002]. Similar processes are occurring in other settings including aeolian sand dunes [*Severinghaus et al.*, 1997], bare soil [*Massmann and Farrier*, 1992], and even mountains [*Thorstenson et al.*, 1998]. These processes may also be affecting fluid and heat transport in larger topographic features in the seafloor such as seamounts (e.g., *Goto et al.* [2005]) and may be a possible explanation why fluid and heat transport models for oceanic materials that do not consider current-topography driven fluid flow are not able to completely replicate observed temperature patterns (e.g., *Harris et al.* [2000]). In all of these cases, a complete understanding of most if not all thermal, chemical and biological processes occurring near the interface and within the porous media begins with the physical template– the fluid dynamics.

There have been several advances describing current-topography driven fluid

flow in porous media. However, previous modeling studies have decoupled the two systems. For example, instead of explicitly accounting for fluid flow in the water or air column, it has become customary to consider only the lower half of the domain (the underlying porous media). Most of these studies represent the impacts of water currents or wind on the porous media via a sinusoidal pressure distribution imposed on an interface that is assumed to be flat [Colbeck, 1989; Cunningham and Waddington, 1993; Elliott and Brooks, 1997b; Cardenas *et al.*, 2004]. The few porous media modeling studies that explicitly consider topography of the interface use pressure distributions measured from flume experiments [Savant *et al.*, 1987; Salehin *et al.*, 2004]. But no one has attempted to simultaneously reproduce and investigate the conditions both above and below the interface. Although published studies demonstrate the importance of interfacial exchange processes, they do not provide fundamental predictive, mechanistic relationships that can be applied to a broad spectrum of dynamical settings. This has been overcome recently by multiphysics numerical modeling studies by the authors that consider coupled flow in a water column and its underlying porous media [Cardenas and Wilson, submitted manuscript a; Cardenas and Wilson, submitted manuscript b]. However, these recent studies by the authors considered only laminar flow for the water column. Most natural systems are turbulent.

This paper focuses on fluvial settings represented by a turbulent river flowing over a sand bed with two-dimensional immobile, subaqueous, porous dunes. The results are directly transferable to other settings maintaining geometric and dynamic similitude such as estuarine and marine dunes, wind-snow dunes, and wind-eolian sand dunes. Numerical simulations of turbulent water flow are sequentially coupled to Darcian

porous media flow in the underlying sediments. The coupled simulations explicitly show how the two systems are interrelated. Simulations for different dune geometry (steepness and asymmetry) and current Reynolds Number allow us to investigate and compare multiple dynamical scenarios. We define an interfacial exchange zone (IEZ) as the zone within the porous media and near the fluid column-porous media interface that is influenced by current-topography driven advection. The spatial configuration of and fluxes through the IEZ are determined for the various scenarios. These results are synthesized into simple predictive relationships that describe fluid column-porous media exchange.

5.2. Methodology and Validation

This section presents the modeling scheme and governing equations, focusing first on turbulent river flow and model validation using flume experiment results. The discussion of the coupling scheme and its validity follows. The sequentially-solved porous media flow formulation is presented last, along with another flume validation experiment that considers both turbulent flow in the water column and Darcy flow in the underlying sediments.

5.2.1.1. General formulation for turbulent flow over dunes

We simulate steady-state two-dimensional turbulent water flow over triangular dunes (Figure 5.1a, b) by numerically solving a finite-volume formulation of the Reynolds-averaged Navier-Stokes (RANS) equations for an incompressible, homogeneous fluid:

$$\frac{\partial U_i}{\partial x_i} = 0 \quad (5.1)$$

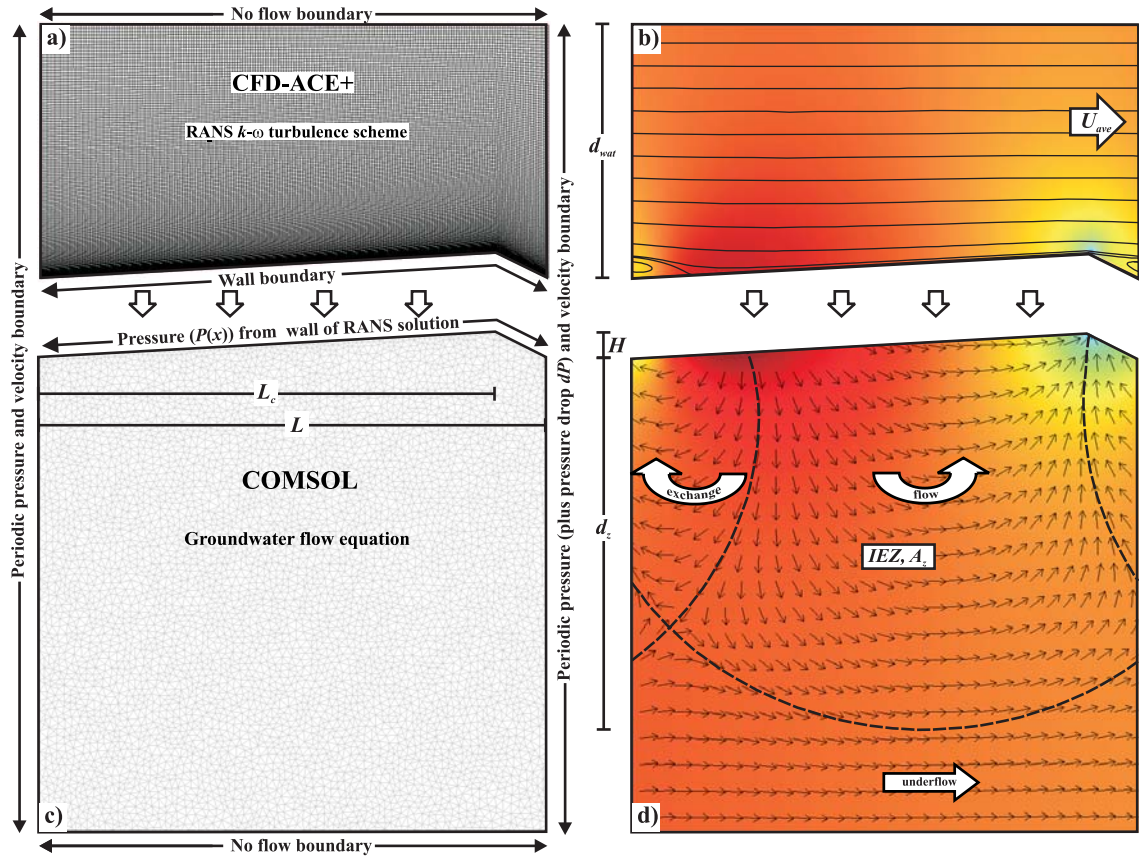


Figure 5.1. Modeling formulation, numerical grids (a,c) and typical results (b,d) for turbulent flow in the water column (a,b) and porous media flow (c,d). Mean flow is from left to right. The color scale for the two outputs, representing pressure, are similar but not exactly the same; warmer colors: higher pressure, cooler colors: lower pressure. The top right figure shows streamlines while the bottom right figure shows flow directions. Dune length $L=1.0$ m. The streamlines in (d) define the interfacial exchange zone (IEZ) with area A_z ; this streamline separates all the streamlines originating from and returning to the interface from the deeper part of the porous media that is dominated by the mean flow from left to right (i.e., underflow). The depth of the IEZ, d_z , is the vertical distance between the trough and the deepest portion of the streamline delineating the IEZ.

$$\rho U_j \frac{\partial U_i}{\partial x_j} = -\frac{\partial P}{\partial x_i} + \frac{\partial}{\partial x_j} (2\mu S_{ij} - \rho \overline{u'_j u'_i}) \quad (5.2)$$

where ρ and μ are fluid density and dynamic viscosity, t is time, U_i ($i=1,2$) and u_i ($i=1,2$) are time-averaged and instantaneous velocity components in x_i ($i=1,2$) directions, P is

time-averaged pressure. S_{ij} is the strain-rate tensor defined as:

$$S_{ij} = \frac{1}{2} \left(\frac{\partial U_i}{\partial x_j} + \frac{\partial U_j}{\partial x_i} \right) \quad (5.3)$$

The Reynolds stresses are related to the mean strain rates by:

$$\tau_{ij} = -\overline{u'_j u'_i} = \nu_t (2S_{ij}) - \frac{2}{3} \delta_{ij} k \quad (5.4)$$

where ν_t (or μ_t/ρ) is the kinematic eddy viscosity, δ_{ij} is the Kronecker delta, and k is turbulent kinetic energy. We adopt the k - ω turbulence closure scheme [Wilcox, 1991] since it has been demonstrated to work exceptionally well for separated flows with adverse pressure gradients, including flow over dunes where there is a pronounced eddy [Yoon and Patel, 1996; Cardenas and Wilson, 2006]. The eddy viscosity in this closure scheme is:

$$\nu_t = \frac{k}{\omega} \quad (5.5)$$

where ω is the ratio of the turbulence dissipation rate ε to k :

$$\omega = \frac{\varepsilon}{\beta^* k} \quad (5.6)$$

and β^* is a closure coefficient. The steady-state transport equations for k and ω are:

$$\rho \frac{\partial(U_j k)}{\partial x_j} = \rho \tau_{ij} \frac{\partial U_i}{\partial x_j} - \beta^* \rho \omega k + \frac{\partial}{\partial x_j} \left[(\mu + \mu_t \sigma_k) \frac{\partial k}{\partial x_j} \right] \quad (5.7)$$

$$\rho \frac{\partial(U_j \omega)}{\partial x_j} = \alpha \frac{\rho \omega}{k} \tau_{ij} \frac{\partial U_i}{\partial x_j} - \beta \rho \omega^2 + \frac{\partial}{\partial x_j} \left[(\mu + \mu_t \sigma_\omega) \frac{\partial \omega}{\partial x_j} \right] \quad (5.8)$$

The closure coefficients are defined as $\alpha=5/9$, $\beta=3/40$, $\beta^*=9/100$, and $\sigma_k=\sigma_\omega=0.5$. In all simulations, spatially periodic pressure boundaries are prescribed for the left and right boundaries of the domain (Figure 5.1a). This enables modeling turbulent flow with minimal a priori information regarding the turbulence and flow parameters.

The boundary conditions for k and ω at the interface, which is treated as a no-slip wall boundary are:

$$k(y=0)=0 \text{ and } \omega(y = \eta) = \frac{\mu}{\rho y^2} \quad (5.9)$$

where y is the normal distance from the wall (interface), and η is the normal distance between the wall and center of the computational cell adjacent to the wall. This formulation for wall boundaries is convenient since it does not necessitate prescribing wall functions, which are not well-described for cases of turbulent separated flow over dunes. Consideration of a wall boundary at the bottom of the water column, periodic boundaries for the lateral boundaries, and a symmetry boundary for the top of the domain

allows us to solve the complete and well-posed problem for turbulent flow while ignoring the presence of a porous media below the water column. The periodic left and right boundaries have a prescribed pressure drop dP , so that our domain approximates an infinite domain in the horizontal direction with flow from left to right.

RANS modeling, from pre-processing (including structured grid generation) through the solution to post-processing, is conducted using CFD-ACE+, a commercially available multiphysics modeling software, and its associated programs. CFD-ACE+ solves the finite-volume formulation of the coupled equations (5.2), (5.6) and (5.7). In the various simulations the number of structured grid nodes varies from ~16000 to more than 80000 (Figure 5.1a), with more densely spaced nodes near the bottom wall boundary.

5.2.1.2. Validation for turbulent flow

We validate our RANS formulation by simulating and comparing with the flume experiments of *van Mierlo and de Ruiter* [1988] where they investigated detached or recirculating turbulent flow over a fixed dune with an impermeable surface. The observed eddy detached at or near the crest and reattached on the stoss side of the downstream dune. Modeled properties of water correspond to reported values. The periodic pressure drop between the “upstream” and “downstream” boundaries is varied until the average velocity at the upstream inlet matched the reported value. *Yoon and Patel* [1996] previously used the same experiments to validate the $k-\omega$ model solved by their research code and found remarkable agreement between modeled and experimental values for flow and turbulence quantities. The reader is referred to *Yoon and Patel* [1996] for a detailed description of the flume experiments and of the nondimensionalization of velocity profiles. Our simulated dimensionless velocity profiles agree very well with

observed values (Figure 5.2). Note that we are able to simulate recirculating flow in the eddy from flow detachment to reattachment (profiles 2-6 in Figure 5.2). Our solutions for turbulence quantities k and v_t are comparable to those in *Yoon and Patel* [1996]. These are available in the Appendix.

5.2.2. Linking the two-domains: pressure along the interface

The RANS solution provides the averaged bottom pressures at the sediment-water interface (SWI), which is a no-slip wall in the turbulent flow model. This pressure solution is imposed as a Dirichlet boundary at the top boundary of the underlying domain representing the permeable sediments (Figure 5.1c). This results in sequential coupling with no feedback and emphasizes the need for accurate RANS pressure solutions along the SWI.

We validate the RANS bottom pressures by simulating the flume experiments of *Fehlman* [1985], in which they installed pressure taps on the surface of an artificial dune with an impermeable surface. *Fehlman* [1985] presented the spatial distribution of the differences between pressures (ΔP) measured at the pressure tap locations with respect to pressure at the crest of the dune. There were no pressure taps at the crest and this reference pressure was linearly interpolated between the measured values at pressure taps immediately surrounding the crest. This biases the pressure differences since the actual pressure at the crest does not necessarily fall between the measured values from the adjacent taps that are used for interpolation. An additional source of error is our consideration of a symmetry boundary for the top of the RANS domain when it is actually a free surface. Despite these factors, our simulated pressure profiles agree reasonably well with the experiments (Figure 5.3). Numerical solution difficulties also

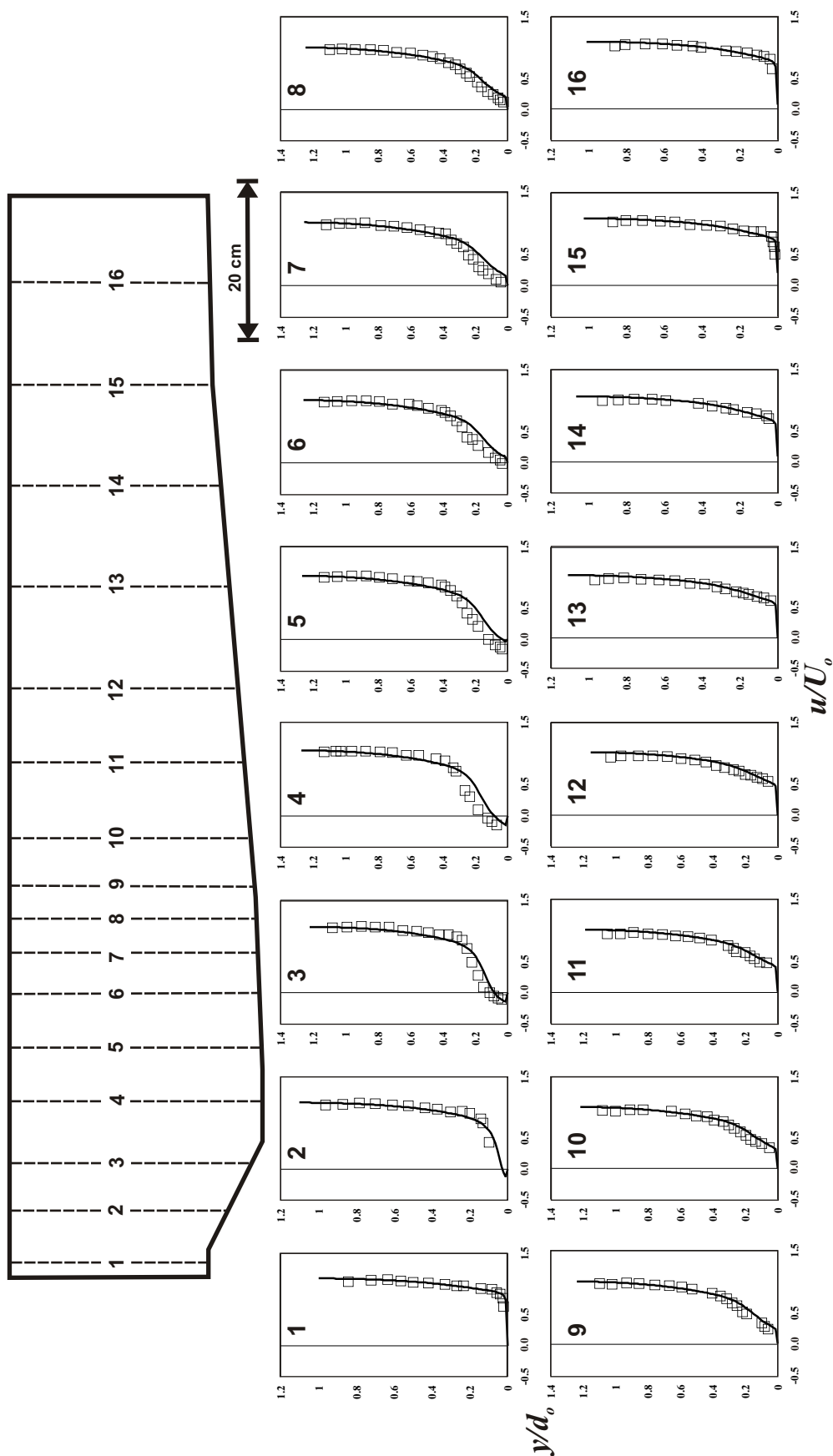


Figure 5.2. Comparison of experimental dimensionless water-column velocity profiles from van Mierlo and de Ruiter [1988] to simulated velocity profiles. Flow is from left to right. Profile numbers in the top locate the velocity profiles shown below. Note that both axes of the velocity profiles are nondimensional. The inlet average velocity is $U_0=0.63$ m/s and the inlet depth is $d_0=0.29$ m; these values are used for normalization.

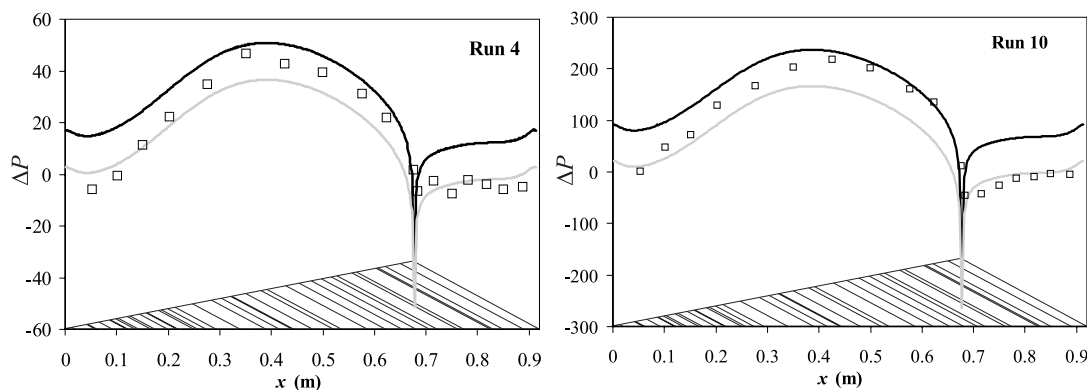


Figure 5.3. Comparison of measured pressure profiles along an impermeable dune surface (hollow squares) with simulated pressure profiles (gray and black curves). Flow in the water column is from left to right. The Run numbers correspond to original numbering scheme in *Fehlman* [1985]. Two simulated curves are presented. *Fehlman* defines the pressure change (ΔP) as the difference between the interpolated pressure at the crest and the pressure at other measurement points. The black curve corresponds to ΔP 's calculated based on the original definition. The gray curve corresponds to the simulated pressure difference referenced to a point just upstream of and not exactly at the crest. The geometry of the experimental dune is illustrated. Calculated average velocities taken at the crest are 0.43 m/s and 0.86 m/s, for Runs 4 and 10 respectively. Flow depth at the crest is 0.15 m for both runs.

contribute to the less than perfect agreement. The crest of the dune is a singularity, and most flows detach along this area. We expect an adverse pressure gradient at this point in order for separation to occur and from Bernoulli's Law. Although it appears that this dip in pressure may be exaggerated in our numerical solutions (Figure 5.3), the pressure at a separation or detachment point or an abrupt corner is extremely difficult to measure numerically or experimentally and a direct comparison is impossible. To partially get around this, pressure profiles referenced to a pressure value for a node just upstream of the crest are also presented (Figure 5.3). Both pressure profiles along the dune, one referenced to the simulated pressure at the crest (black curve) and one referenced to a simulated pressure just upstream of the crest (gray curve), reasonably reproduce the measured values. Although the simulated pressure dip near the crest appears exaggerated,

it is nevertheless consistent with observations from other flume experiments showing an adverse pressure gradient, and where the eddy detachment occurs near the pressure dip (e.g., *Huettel and Gust* [1992] and *Raudkivi* [1963]).

5.2.3.1. Sequentially coupled simulation for porous media flow

The porous media domain is governed by the combination of Darcy's Law and the continuity equation for incompressible flow in a non-deformable media, i. e., the groundwater flow equation:

$$\frac{\partial q_i}{\partial x_i} = 0 \quad (5.10)$$

$$q_i = -\frac{k_p}{\mu} \frac{\partial P}{\partial x_i} \quad (5.11)$$

where q_i ($i=1,2$) is the specific discharge (i.e. Darcy flux) and k_p is intrinsic permeability.

The top boundary of the porous domain (e.g., Figure 5.1c), the SWI, is a Dirichlet boundary which takes on the pressure from the RANS simulations. The lateral boundaries are periodic boundaries with an imposed pressure drop, dP , consistent with that for the RANS domain with which the porous domain is coupled. This formulation results in a continuous pressure distribution across the two domains (Figures 5.1b and 5.1d). It also results in what is commonly referred to as “underflow”, and is present in all or most simulations. Underflow is the ambient horizontal flow in the deeper parts of the porous domain which is unaffected by the irregular pressure boundary along the SWI (Figure 5.1d). Underflow is a direct result of the prescribed pressure drop between the lateral boundaries. The bottom boundary of the porous domain is a no-flow boundary. It may impact the flow field when it is too close to the top boundary. In order to approximate a semi-infinite vertical domain solution, where the bottom boundary no

longer has an effect on the flow field near the SWI, we follow criteria in *Cardenas and Wilson* [submitted]. Intrinsic permeability is $1 \times 10^{-10} \text{ m}^2$ for all simulations except for the validation experiment discussed below, where we use the reported value for k_p . Model generation, solution and post-processing for the porous media domain is implemented through the generic finite-element analysis code Comsol Multiphysics. The number of second-order triangular elements range from ~15000 to ~30000 (Figure 5.1c).

Figure 5.1d illustrates a typical solution for the porous domain. The pressure distribution along the SWI, which by definition is continuous across the two domains, sets-up two flow cells in the porous domain. The streamlines delineating and dividing these flow cells are determined by the location of the maximum and minimum pressures along the SWI. Illustrated in Figure 5.1d is the IEZ, separated by dividing streamlines from the area below which is dominated by underflow.

5.2.3.2. Sequentially coupled simulation validation

There are few laboratory experiments that allow for validation of coupled simulations of current-topography driven flow. The experiments by *Elliott and Brooks* [1997a] are a rare example, and we use their “Run 9” (see *Elliott* [1990] for a more detailed description of the flume experiments) for validation. Rather than a dune, they examined smaller bedforms- ripples. Fluid and sediment properties in the simulation are the reported values. The simulated SWI bedform topography, water column depth, and depth of the impermeable bottom boundary for the porous media domain (the floor of the flume) follows those published. However, there are two major differences between our simulations and the experiments. First, we do not consider the top of the water column as a free surface. This does not have a substantial effect on the flow field since the Froude

Numbers are below unity. Second, *Elliott and Brooks* [1997a] did not impose underflow in their Run 9 experiment; underflow is present in our simulation. They imposed underflow in subsequent experiments using an ad hoc method of having a separate fluid recirculating system for the sediments (see discussion in *Elliott* [1990] and Figure 1 of *Elliott and Brooks* [1997a]). As we shall see later, underflow is a natural consequence in flumes with many bedforms and there may be no need to introduce it artificially. In our validation exercise, no parameters were calibrated. The only parameter that varies is the prescribed pressure drop for periodic boundaries, dP , which was modified to match the reported mass flux of water recirculated through the flume.

The only water column experimental flow parameters (pressure, velocity and turbulence quantities) measured by *Elliott and Brooks* [1997a] were the free surface profile, interface topography and amount of water being recirculated through the flume. By focusing on the circulation through the porous media, this experiment is a rigorous test for our sequential coupled formulation. Can we reproduce the flow field in the sediments by matching only to the mass flux circulating through the flume? To observe this flow field, *Elliott and Brooks* [1997a] released dye from discrete ports within the sediments. Since flow is steady, the visually-mapped dye streaks effectively mapped streamlines in the sediments. Figure 5.4a superposes our simulated streamlines (gray dashed lines) with the observed dye streaks (black lines). Our formulation is able to reproduce the directions of flow accurately.

Elliott and Brooks [1997a] also introduced dye into the water column. The penetration front of the dye through the sediments was mapped through time. In order to further test our solutions to the porous flow problem, we coupled it with a solute

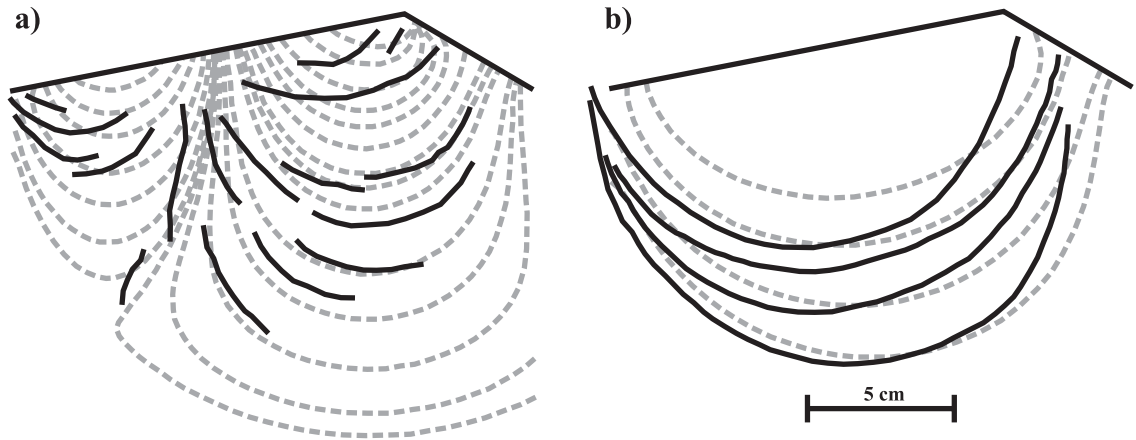


Figure 5.4. a) Comparison of dye streaks (black curves) from *Elliott's* [1990] Run 9 with simulated streamlines (dashed gray curves); b) comparison of dye penetration fronts (black lines) mapped at 75, 150, 320, and 650 minutes to simulated advective solute fronts (dashed gray curves) for the same run. Flow in the overlying water column (not shown) is from left to right.

transport simulation. Solute transport is governed by the classical advection-dispersion equation. The solute is released at $t=0$ from the SWI (top boundary of the porous domain) and its initial concentration is zero everywhere. The dispersion coefficient is set close to zero so that the mid-concentration line (i.e., $C/C_0=0.5$) represents the advective front. The simulated advective fronts are compared to the mapped dye fronts. Note that it was not reported how the experimental dye fronts were mapped. There is some subjectivity as to how a diffuse front is mapped by the human eye and it is difficult to tell if the dye fronts were mapped at the very edge of the plume where there is no discernible color change (e.g., $C/C_0 < 0.1$), at the plume interior zones where the color corresponds to pure dyed liquid (e.g., $C/C_0 > 0.9$), or at somewhere in between (e.g., $C/C_0 \sim 0.5$). Another immeasurable complicating factor is the potential effect of flow channeling along the walls of the flumes; of course this is where the fronts are mapped. The above factors introduce some uncertainty in our comparisons. Despite these concerns, the simulated

and mapped fronts agree well (Figure 5.4b). Our numerical model formulation reproduces aspects of both the turbulent flow in the water column (Figures 5.2 and 5.3) and the underlying Darcy flow in the sediments (Figure 5.4).

The results, where a simulation with underflow agrees with experiments and there is no artificially induced underflow, suggest that underflow may be occurring as a natural consequence in flume configurations where the lateral ends are impermeable boundaries. We surmise that this underflow results because of the configuration of the first bedform in the series of repeating bedforms. The very first bedform cannot have two flow cells as in Figure 5.1d since it is bounded by the impermeable flume end. The fluids that are introduced through the first bedform that cannot be returned to the SWI via the “upstream” circulating flow cell will have to move downstream via underflow and eventually return to the SWI.

5.3. Dynamical relationships between turbulent flow and porous media flow, and its effects on interfacial exchange

The relationship between features of the turbulent and porous media flow fields are discussed in this section. First, salient aspects of how the two domains are linked are discussed with particular emphasis on the dynamics of the turbulent eddy and the pressure distribution along the SWI, and how these influence flow in the porous media. Second, results of sensitivity analysis are presented, focusing on the sensitivity of the exchange process to the dune geometry (steepness and asymmetry) and to the flow dynamics in the water column as indicated by the Reynolds Number.

In the ensuing discussions, the length of the dune is $L=1.0$ m and the depth of water above the trough is $d_{wat}=0.5$ m. The dune height H and the horizontal distance

between the crest and the upstream trough L_c were varied to effectively change the dune steepness and asymmetry (Figure 5.1). These dune geometries, particularly the steepness, are typical of subaqueous dunes [Yalin, 1979]. As stated earlier, $k_p=10^{-10} \text{ m}^2$. The Reynolds Number Re is defined as [Cardenas and Wilson, submitted a; Cardenas and Wilson, submitted b]:

$$Re = \frac{U_{ave} H}{\nu} \quad (5.12)$$

where U_{ave} is the average horizontal ensemble velocity U taken directly above the crest, and ν is kinematic viscosity of the fluid. Refer to Figure 5.1 for schematic definition of geometric parameters.

5.3.1. Eddy and dune geometry, bottom pressure distribution and the interfacial exchange zone

The pressure distribution along the SWI drives the flow in the underlying porous media and determines the configuration of the resulting porous flow field. The SWI pressure distribution is represented by the pressures and locations of a pressure minimum and a pressure maximum, which are somewhat analogous to a dipole field. The minimum pressure, which represents a “sink” from the view of the porous media, is invariably located at or near the crest of dunes and almost always coincides with the eddy detachment point (Figure 5.1d). The pressure maximum, a “source”, is typically found near where the eddy reattaches (Figure 5.1b,d). As is true with most dipole potential fields (note that this is only an analogy and the field is not a true dipole field), its zone of influence is related to the distance between the two poles. (Huettel *et al.* [1996] used this

concept to model current-mound induced flow in sediments with a sink-source potential flow model). We have previously presented these aspects of the coupled systems for laminar flow conditions (see Figures 2-4 of *Cardenas and Wilson* [submitted b]) where we showed that the growth of the eddy, which is driven by increases in Re , controls the growth of the interfacial exchange zone. We define the interfacial exchange zone (IEZ) as the area adjacent to the SWI receiving water from above the SWI. This zone is delineated by the streamline which bounds all streamlines originating and ending at the SWI (see illustration in Figure 5.1d). Fluvial ecologists and hydrologists commonly refer to the IEZ as the “hyporheic zone”.

Before focusing on the dynamics of the IEZ, we discuss the dynamics of the eddy in the water column since it ultimately controls the pressure distribution along the SWI and therefore the processes in the IEZ. In laminar cases, where IEZ development tracks eddy growth [*Cardenas and Wilson*, submitted b], the eddy length, L_e , is also a measure of the distance between the pressure minimum and maximum since the eddy detaches and reattaches near these points [*Cardenas and Wilson*, submitted b]. However, eddies more or less stay the same length for fully-developed steady-state turbulent flows across a broad range of Res . This behavior was observed by *Armaly et al.* [1983] for turbulent flow past a backward-facing step. *Armaly et al.*'s [1983] flume experiments suggested that the length of the separation zone grows abruptly under laminar flow conditions, decreases through the transitional flow regime and eventually increases again to an asymptotic length when fully developed turbulence is attained (Figure 5.5a). The fully turbulent eddy length is smaller than the maximum length achieved under laminar conditions but larger than the minimum length attained during transition flows. These

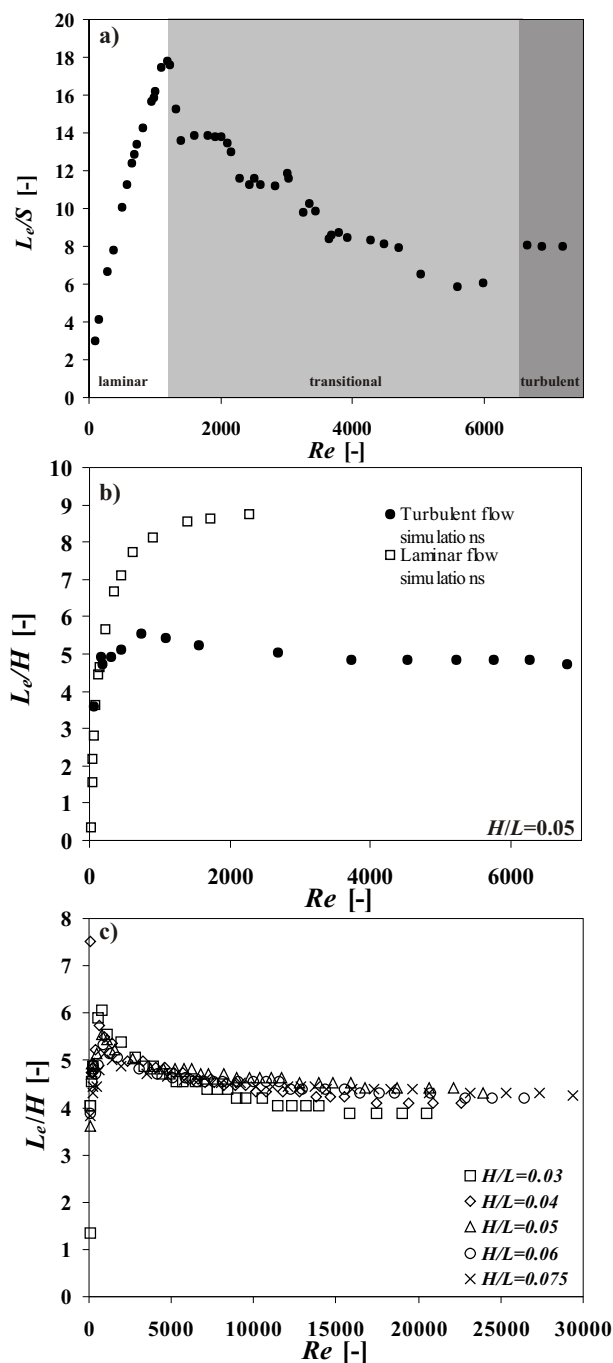


Figure 5.5. Dimensionless eddy length (L_e/S or L_e/H , S =back-step height) as a function of Reynolds Number (Re). The data in (a) are from experiments for flow past a backward-facing step by *Armaly et al.* [1983], while those in (b) and (c) are from our numerical simulations for dunes. Note that dimensionless eddy lengths and Re 's are computed differently in *Armaly et al.* [1983]. *Armaly et al.* [1983], based on the behavior of the eddy length, suggest that their experiments covered the three flow domains labeled in (a) and indicated by different shades. Data shown in (b) include results from laminar flow simulations (hollow squares) and turbulent flow simulations (solid circles). Results in (c) are from turbulent flow simulations representing different dune steepness (H/L); $L=1.0$ m and $L_c/L=0.9$ in all cases.

aspects of eddy behavior under evolving flow conditions (increasing Re) have been reproduced in our earlier simulations of laminar [*Cardenas and Wilson*, submitted a; *Cardenas and Wilson*, submitted b] and turbulent flow over dunes [*Cardenas and Wilson*, 2006]. Figure 5.5b plots results of both laminar and turbulent flow simulations. The results of laminar flow simulations were obtained following *Cardenas and Wilson* [submitted b]. The simulated dynamics of eddies over dunes from laminar through turbulent flow, shown in Figure 5.5b but without the transitional regime, is similar to those observed by *Armaly et al.* [1983] for flow over a step. Note that the RANS simulations are incorrect at low Res while the laminar flow simulations based on the classical Navier-Stokes equations are incorrect at high Res .

The invariance of the length of eddies over dunes for high Re turbulent flow has been observed previously in flume experiments but no experiments have examined flow over dunes from laminar to transitional flow. *Engel* [1981], and the references therein, show that for fully developed turbulent flow the ratio of eddy length to subaqueous dune height (L_e/H) varies within a narrow range of 4-6. We have previously verified this behavior with a few simulations [*Cardenas and Wilson*, 2006]. In this study, a suite of simulations representing different dune shapes and flows across a broad range of Res are presented. Two measures are used for dune geometry: the dune steepness or height-to-length ratio (H/L) and dune asymmetry (L_c/L), which is the location of the crest relative to the length of the dune (see Figure 5.1 for illustration of geometric parameters). The eddy length L_e is the horizontal distance between the detachment and reattachment points of the eddy. These points are determined by picking the points at which the horizontal-velocity changes directions along a profile of the computational cells that are located

adjacent to the wall boundary. Dimensionless eddy lengths (L_e/H) for five different dune steepnesses, covering the typical range for subaqueous dunes, are presented in Figure 5.5c. At low Re s, the results of these simulations may be incorrect since flow may be transitional or laminar. These low Re results are presented since a critical Re where flow becomes transitional or turbulent for flow over a variety of dune geometries has not been documented. At higher Re s where we might expect turbulent flow, all the values for L_e/H fall within the narrow experimental range reported by *Engel* [1981].

If eddy length is initially considered as a surrogate for the relative locations of the pressure minimum and maximum that drive flow through the IEZ, the spatial extent of IEZs for turbulent open channel flow conditions should be more or less constant and confined to a narrow range. Figure 5.1 suggests, however, that the eddy reattachment point does not exactly correspond to the maximum pressure point and is slightly upstream of it. This is similar to the simulated results of *Yoon and Patel* [1996]. In these turbulent cases, the eddy length is an indirect measure of the locations of the critical pressure points relative to each other. For laminar cases, the co-location of the reattachment point with the maximum pressure is more pronounced although not perfect [*Cardenas and Wilson*, submitted b].

Simulated IEZ depths, d_z , for laminar and turbulent flow conditions are superposed in Figure 5.6a. d_z is taken as the vertical distance between the trough and the deepest portion of the dividing streamline that envelopes all porous flow originating from the SWI (Figure 5.1d). The simulated d_z behavior tracks the behavior of the eddy in the water column. When the eddy length is still increasing under laminar water column conditions, so does the IEZ depth. When the eddy stabilizes to a shorter length under

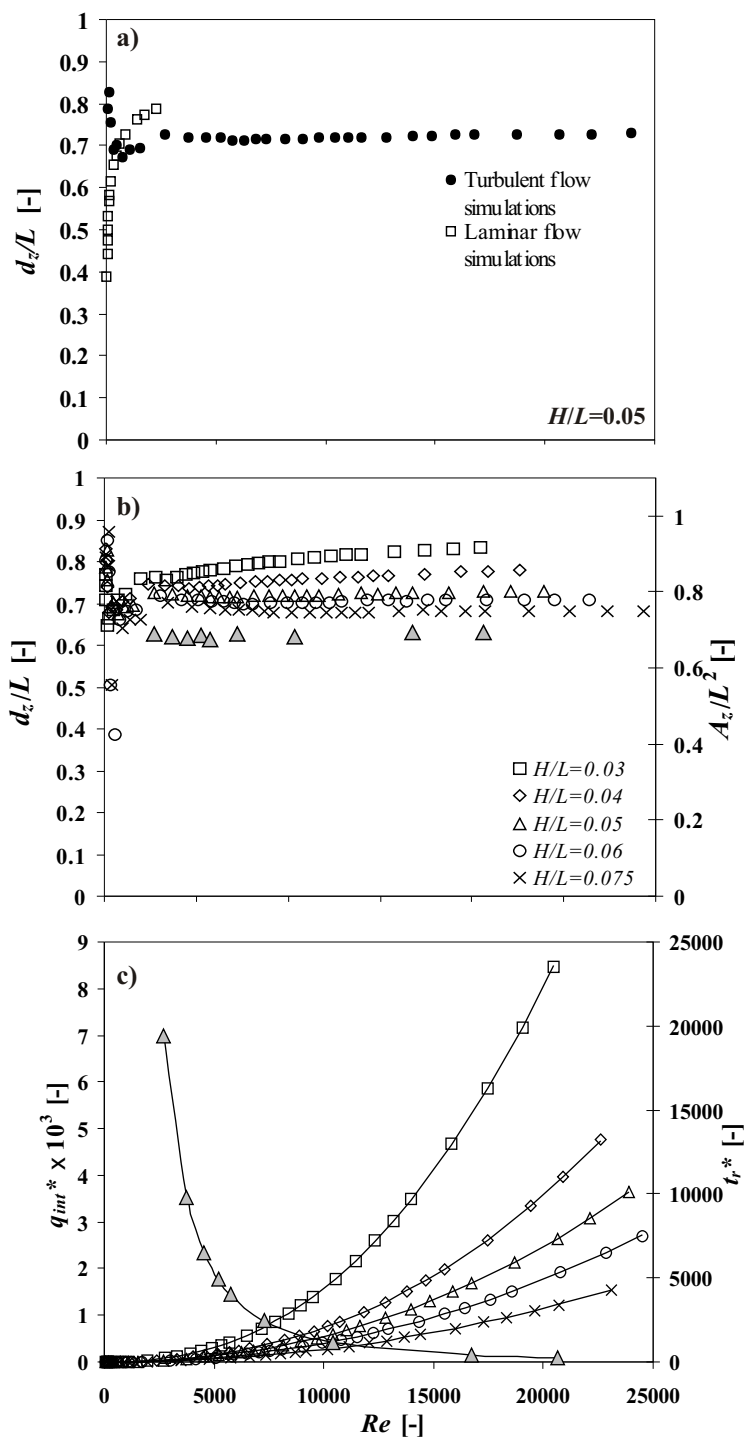


Figure 5.6. Part a) shows dimensionless interfacial exchange zone depth (d_z/L) as a function of Reynolds Number (Re) for laminar and turbulent flow simulations; $H/L=0.05$, $L_c/L=0.9$. Part b) shows simulated d_z/L for turbulent flow over different dune steepnesses (H/L ; $L=1.0$ m and $L_c/L=0.9$ in all cases). Also presented in (b) is the dimensionless area of the IEZ (A_z/L^2) for the case where $H/L=0.05$, indicated by gray-filled triangles. Shown in (c) are the dimensionless interfacial fluxes (q_{int}^*) corresponding to the same cases in (b). Gray-filled triangles in (c) correspond to the dimensionless residence times (t_r^*) for $H/L=0.05$. Curves in (c) are all fitted power models with $R^2 > 0.99$ in all cases.

fully-developed turbulent conditions, the IEZ similarly stabilizes to a shallower depth. At higher Res where turbulent flow is expected, the d_z remains essentially constant.

Figure 5.6b shows that steeper dunes (higher H/L) have shallower IEZs. This behavior is visualized in Figure 5.7a and explained by Figure 5.8a, which shows the normalized pressure distribution for simulations with different dune steepness. It illustrates that, with increasing dune steepness, the pressure maximum on the stoss (upstream) side of the dune moves downstream, closer to the pressure minimum near the crest. The locations of these critical pressure points along the SWI are indicated by the streamlines dividing the IEZ into distinct flow cells (Figure 5.7a). Figure 5.8b plots the locations of the critical pressure points for different dune steepness. The results are consistent with a “dipole” analogy- the farther apart the “poles” are, the larger the zone of influence (i.e., the IEZ and d_z are larger). This interpretation is limited only to cases where there is a pronounced eddy that detaches at or near the crest.

The behavior of the IEZ is different when a pronounced eddy is absent. Consider the case of simulations for dunes with different asymmetry ratios (L_c/L). In these simulations, $H/L=0.05$ and flow is always from left to right (Figure 5.7b). When $L_c/L>0.75$, which is more typical of dunes in unidirectional currents, the eddies detach at the crest and reattach further up the downstream stoss face. When $L_c/L < 0.75$, the eddies are extremely small and are confined to the trough region (Figure 5.8d); these eddies are not visible at the scale of the images in Figure 5.7b. This results in minor but important differences in the pressure along the SWI (Figure 5.8c). For smaller L_c/L 's, the pressure distribution is dictated primarily by Bernoulli's Law- the lowest pressure is at the most constricted area (the crest) and the highest pressure is close to the widest area (the

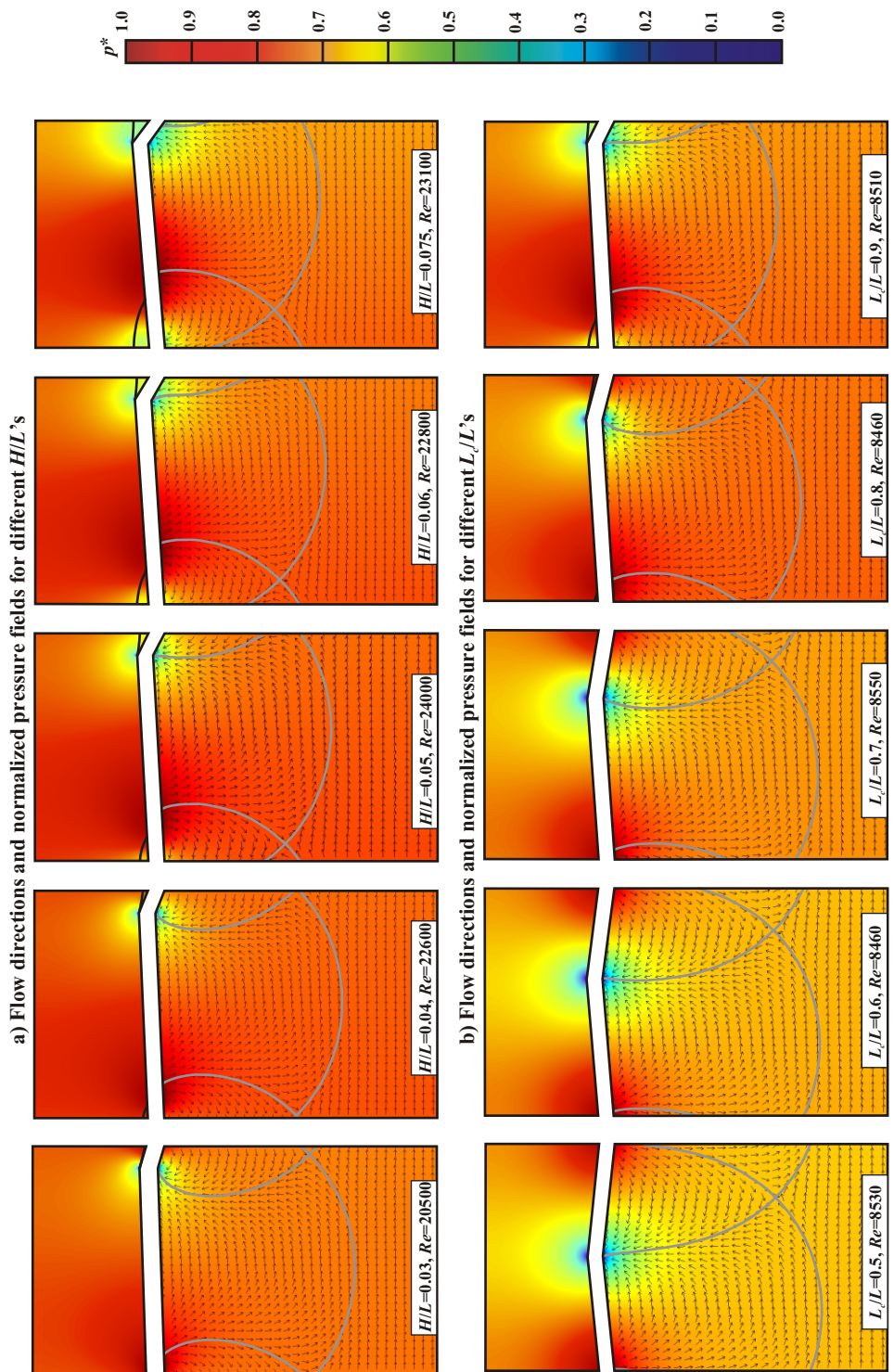


Figure 5.7. Flow and pressure fields for simulations with different H/L 's and L_c/L 's with $H/L=0.05$ (a) and different L_c/L 's with $H/L=0.9$ (b). Gray lines delineate the interfacial exchange zone and two flow cells within it. Pressure is normalized as $p^*=(p-p_{min}) / (p_{max} - p_{min})$, where p is the pressure, and p_{min} and p_{max} are, respectively, the minimum and maximum for each simulation. p_{min} and p_{max} are located near where the streamlines originate from at the top boundary. Illustrated in both panels are streamlines in the water column which delineate the eddy.

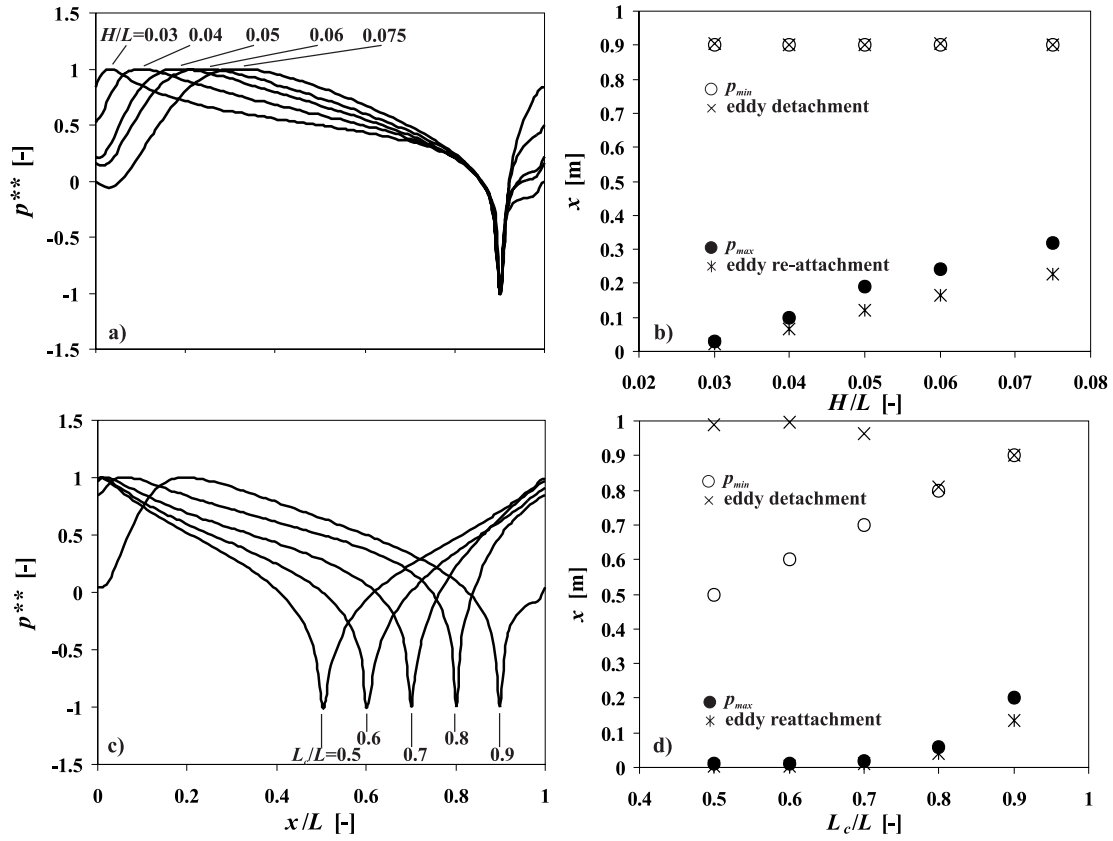


Figure 5.8. (a) and (c) are dimensionless pressure profiles taken along the sediment-water interface for the different-dune-shape simulations presented in Figure 7a and 7b, respectively. Pressure is normalized as $p^{**}=(p-p_{mid}) / (p_{max} - p_{min})$, where p_{mid} is the midpoint between the maximum and minimum pressures, p_{max} and p_{min} . The ambient pressure gradient has been removed in these profiles. (b) and (d) show the x -locations of the critical pressure points and eddy detachment and reattachment points for the same simulations in (a) and (c). The troughs are located at $x=0$ and 1 m for all figures. In (b) the crest is at $x=0.9$ m for all 5 cases; in (d) the crest location increases from $x=0.5$ to 0.9 m in increments of 0.1 m (consistent with the depicted range in L_c/L).

trough). This pressure configuration is favorable for forming deeper IEZs (see Figure 5.7b). For higher L_c/L 's, the detachment point becomes co-located with the pressure minimum at the crest and the pressure maximum location moves upstream along the stoss face favoring a shallower IEZ.

5.3.2. Fluxes and mean residence times

In addition to characterizing the spatial behavior of the IEZ, we investigate how

fluxes through the IEZ change across dynamical settings. Flux through the IEZ is computed by integrating the magnitude of normal fluxes along the SWI resulting in the volumetric discharge through the IEZ per unit area of SWI. The result is divided by twice the wavelength of the bedform since the integration does not discriminate between inward and outward flow which are presumably equal. The final number is therefore an effective flux density based on the bedform length. We normalize the effective flux density by the hydraulic conductivity of the porous media ($K=k_p\rho g/\mu$, K is the hydraulic conductivity) and express it as q_{int}^* . The IEZ flux increases with the water column Re via power functions (Figure 5.6c), with the steeper dunes resulting in less flux for a given Re . The flux is linearly related to the maximum pressure gradient along the SWI. This behavior is depicted in Figure 5.9, where the difference between the minimum and maximum pressure (p_{int}) along the interface is the independent variable ($h_{int} = p_{int}/\rho g$; pressure is converted to head). It is a natural consequence of Darcy's Law (equation 5.10). For lower Res , where flow is laminar, this relationship is not exactly linear due to

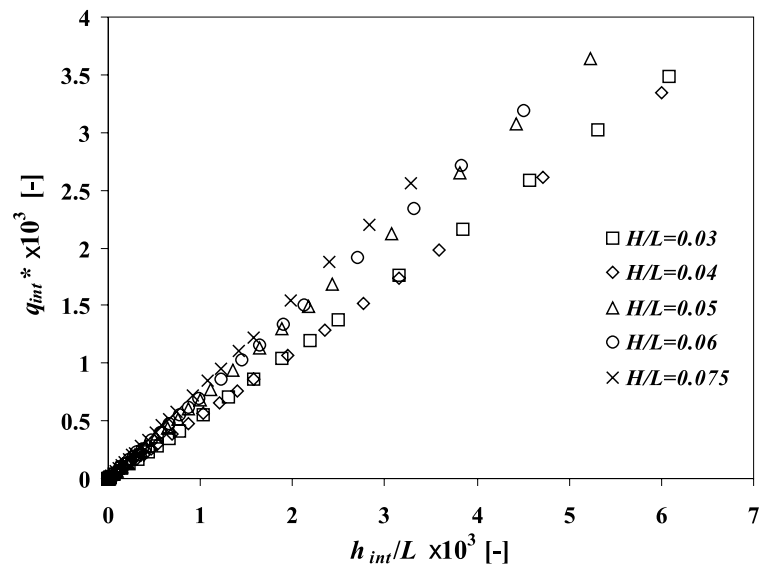


Figure 5.9. Normalized interfacial exchange zone flux density as a function of the head gradient along the sediment-water interface due to current-dune interactions, $L_c/L=0.9$.

the changing depth and area of the IEZ [Cardenas and Wilson, submitted b]. For turbulent flow regimes, where both the eddy and the IEZ no longer grow spatially, the q_{int}^* vs. (h_{int}/L) curve is linear. The slope of this curve is not equal to K , as a one-dimensional Darcy's Law would predict, since the flow is two-dimensional and the slope also integrates a geometric factor.

The volume of the IEZ is represented by its area (A_z) in these two-dimensional simulations. The area is defined by the SWI and streamlines which separate the IEZ from deeper parts of the porous media dominated by underflow (Figure 5.1d). Figure 5.6b shows that, like d_z , A_z is relatively constant for fully turbulent flow. Mean residence times of fluids flowing through the IEZ can be readily computed from the flux and area:

$$t_r = \frac{A_z}{q_{int} L_{int}} \quad (5.13)$$

where t_r is the mean residence time and L_{int} is the length along the SWI. We express t_r in dimensionless form, t_r^* , by dividing dimensionless area (A_z/L^2) by q_{int}^* . Since flux follows a power-law dependence with Re (Figure 5.6b), we expect the inverse behavior for t_r since A_z is more or less constant (Figure 5.6b). Figure 5.6c (gray-filled triangles) depicts this and indicates a sharp decrease in residence time with an increase in Re .

5.3.3. Predictive relationships

It would be ideal for applications if simple predictive relationships were available for determining both the rough spatial configuration of the IEZ and material fluxes through it based on easily measurable parameters. Examples of such parameters are the dune geometry and the Reynolds Number in the fluid column. In the absence of detailed

velocity profiles for turbulent flow in the fluid column, the free-stream velocity can be used as surrogate for average velocity keeping in mind that this will result in a slightly higher Re . Simple predictive models are developed and presented here.

The IEZ depths for cases where the water column flow is laminar fall under one curve when it is normalized by L [Cardenas and Wilson, submitted b]. IEZ fluxes can also be described by a universal curve [Cardenas and Wilson, submitted b]. This is not the case for turbulent scenarios (Figures 5.6b and 5.6c) even when normalized similarly. Therefore, the data presented in Figure 5.6 need additional scaling such that the data collapse into a single curve, or at least a more narrow range, so curve-fitting a single predictive model becomes tenable. It is intuitive to scale the wide-spread values with a variable describing the major differences between the simulations- a geometric parameter. We scaled both d_z/L and q_{int}^* by the dune steepness raised by a scaling power, $(H/L)^c$. We manually varied the power c until the spread in the data was minimized. The optimal parameter c for scaling d_z/L is 0.218. The scaled results and fitted equations are presented in Figure 5.10. Figure 5.10a includes a horizontal line that is determined by simply averaging the d_z/L values for cases where $Re > 5000$. The constant value,

$$d_z^{**} = (d_z/L) (H/L)^c = 0.379, \quad (5.14)$$

for this line can be used for approximating d_z given information about dune geometry and flow conditions. However, this is developed only for the case where $L_c/L=0.9$ (typical of angle-of-repose for subaqueous dunes); different constants may be appropriate for bedforms whose asymmetry ratio is very different from 0.9 (such as in ripples).

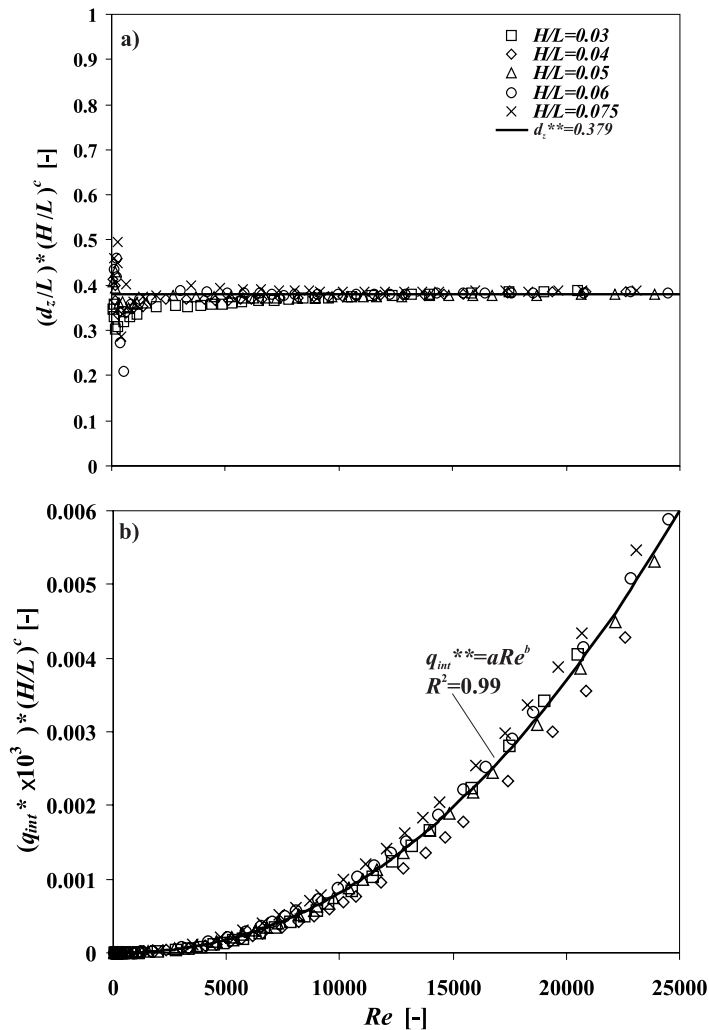


Figure 5.10. (a) Dimensionless exchange zone depths scaled by H/L raised to a power $c=0.218$. (b) Dimensionless flux similarly scaled with $(H/L)^c$ with $c=2.18$. The lone fitting parameter for the power-function in (b) is $a=1.53 \times 10^{-12}$; b is fixed as 2.18 and is equal to c . $L_c/L=0.9$ in all simulations.

Similar scaling of q_{int}^* with $(H/L)^c$ also results in $c=2.18$. We then fit a power-function to the scaled data (Figure 5.10b). The power of this function (b) is also close to 2.18. Fixing b at 2.18 only slightly changes the R^2 ($=0.99$) for the regression and leads to a simple predictive model for IEZ fluxes:

$$q_{int}^* = a + b Re_L^c \quad (5.15)$$

where $a=1.1 \times 10^{-5}$, $b=1.45 \times 10^{-15}$, $c = 2.18$, and Re_L is a new Reynolds Number based on dune length:

$$Re_L = \frac{Re}{H/L} = \frac{U_{ave} L}{\nu} \quad (5.16)$$

The characteristic length scale for fluxes changes from H to L . Equation (5.15) can be used in the prediction for IEZ fluxes, at least for dunes with shapes similar or close to those considered in the sensitivity analysis ($H/L=0.03$ to 0.075 and $L_c/L=0.9$). Of course, this is only valid for fully turbulent flow.

5.3.4. Towards fully coupled models and determining the nature of coupling

Our simulations are coupled sequentially. The full or simultaneous coupling between free fluid flow and porous media flow is an active field of research. There have been major advances regarding our knowledge of how such systems can be simultaneously coupled but severe limitations have been noted. Typical simultaneous coupling schemes for laminar free fluid flow and porous media flow involve a Brinkman-type equation and modifications thereof [*Brinkman*, 1947; *Durlofsky and Brady*, 1987; *Shavit et al.*, 2002], or different versions of the Beavers-Joseph-type equations [*Beavers and Joseph*, 1976]. Recently, it has been shown that the coupled problem based on the Beavers-Joseph formulation can be solved through non-coupled steps [*Layton et al.*,

2002]. Most Brinkman-type equations have been shown to be valid only for porous media with very high porosity [Durlafsky and Brady, 1987] and, to our knowledge, virtually no models have been presented for coupled detached turbulent flow-porous media flow. Modifications to the governing equations need be considered, especially for near-boundary effects along the interface. For example, the logarithmic law for velocity along a flat wall is modified by bed suction or injection [Cheng and Chiew, 1998; Chen and Chiew, 2004] and the area within the porous bed and adjacent to the SWI should consider higher-order momentum loss terms (e.g. Darcy-Brinkman-Forcheimer equations) [Zhou and Mendoza, 1993]. This has been investigated both theoretically and in laboratory experiments for simple flow conditions, that is, flat beds and no eddies.

For the case of turbulent recirculatory flow, our sequential coupling of a robust two-equation turbulence model ($k-\omega$ model) is a useful tool for investigating the macroscopic behavior of the coupled domains. Although the numerical algorithms we use allow full coupling of the equations governing the two domains, the physics may not be amenable to this especially since the equations solved are not modified to address the complicated and poorly understood fluid physics at the interface. We ran fully coupled simulations but were not able to generate eddies in the free-flowing fluid. Ideally there should be feedback between the free fluid and the porous media which is missing in our sequentially coupled simulations. This feedback, however, is limited for the systems on which we focus and for other scenarios where the permeability and porosity are small enough such that porous flow becomes Darcian at distances very close to the interface, there is no or minimal penetration of turbulent flow into the porous media, and the flux of fluid across the interface is small compared to the total flux in the free-flowing fluid.

A consequence of a sequential formulation is suggested by Figures 5.4, 5.7 and 5.8. Figure 5.4a shows that *Elliott and Brook's* [1997a] observed streamlines diverge from a point which is slightly upstream of the simulated divergence point. Figures 5.7 and 5.8 show that the eddy reattachment and maximum pressure points do not coincide; the reattachment point is located upstream of the maximum pressure point on the stoss side of the dune. This is expected for turbulent flow over impermeable surfaces, with the eddy reattachment and maximum pressure points becoming more separated with increasing skin roughness (i.e., larger grains) [*Yoon and Patel*, 1996]. This presents a paradox. When the porous media consists of larger grains, say gravel instead of sand, the turbulent flow in the free-flowing fluid is more likely to penetrate into the porous bed (e.g., *Packman et al.* [2004]) and feedback becomes more important. However, for the case of an impermeable rough bed such as in a flume where the impermeable bed is coated with a layer of gravel, one would expect a shorter eddy reattaching further upstream of the maximum pressure, and closer to the trough. On the other hand, for a porous and permeable gravel bed, one would expect the main in-flow point to the IEZ where streamlines diverge from to occur right where the eddy is reattaching since velocity normal to the wall is largest there. Since the eddy is expected to reattach at the in-flow point through the SWI, will the maximum pressure be co-located at the same point? Will the eddy reattachment point move downstream along the stoss side and/or the pressure maximum move upstream so that these two points coincide? The answers may contradict what one would expect for the case where the gravelly surface is impermeable and the reattachment and maximum pressure points are separated [*Yoon and Patel*, 1996]. To our knowledge, no laboratory experiments have been implemented to answer these

questions; nor is our methodology optimal for addressing these issues. From a numerical modeling perspective, solving the Navier-Stokes equations via direct numerical simulations of a continuum domain where the solid matrix of the porous media are explicitly represented seems to be the only available fully-coupled method that can be used for parametric studies. Currently available computing resources may not be able to handle such simulations for domains of a meter scale or even tens of centimeters. A Lattice-Boltzmann approach may make computation easier. Until alternative robust computational methods which appropriately honor the underlying physics are presented and optimally designed laboratory experiments for validation are implemented, our sequential approach provides a useful tool for investigating coupled turbulent fluid flow and underlying porous media flow in natural systems.

5.4. Summary

Fluid flow along and across interfaces between a column of fluid and an underlying porous media are ubiquitous in nature and play a determining role in the thermal, chemical and biological dynamics of such systems. However, much is left to be learned about these coupled physical processes. We present a sequential numerical simulation methodology that accurately reproduces both the turbulent flow in the fluid column and the porous media flow where the interface between these two domains is composed of dunes (triangular roughness elements). Using this approach, we are able to investigate the fundamental dynamics of such processes and develop some simple predictive relationships. This study builds on previous work for laminar free-flowing fluid conditions [*Cardenas and Wilson*, submitted a; *Cardenas and Wilson*, submitted b].

A salient feature of flow over asymmetric triangular topography is an eddy

detaching at or near the crest and reattaching on the stoss side of the succeeding dune. This recirculatory flow modifies the pressures along the interface between the free-flowing fluid and the porous media. Bernoulli's Law predicts a pressure minimum at the crest and a maximum at the trough. This is replicated for cases where there is no pronounced eddy, such as flow over more symmetric dunes or dunes with a small height-to-length ratio. When a large eddy is present, it detaches at or near the pressure minimum at the crest and reattaches just downstream of the pressure maximum. In these cases, the pressure maximum is no longer located close to the trough but migrates upwards along the stoss side of the following dune. The pressure distribution along the interface, which is tied to the eddy, is mainly determined by the location of the pressure maxima and minima. These pressures dominantly drive flow through the porous media and determine both the spatial configuration of the interfacial exchange zone and mass flux through the zone. Generally, the farther apart these points are relative to each other, the deeper and larger is the exchange zone. Flux through the zone is linearly related to the gradient between these two points, consistent with Darcy's Law. The pressure or head gradient in turn is related to the Reynolds Number of the turbulent flow via a power function.

Eddies scale with the height of the bedform, with the eddy length being ~4-6 times the height of the dune, for fully turbulent flow across a range of Reynolds Numbers. This has consequences for the dynamics of the interfacial exchange zone since the critical pressure points are related to the eddy; the interfacial exchange zone depths and volumes are similarly confined to a narrow range. Steeper dunes (larger height-to-length ratios) generally result in longer eddies which result in shallower exchange zones. The exchange zone depths therefore are sensitive to and vary with dune steepness. We were able to

finding a simple predictive expression (5.13) for exchange zone depth by scaling the depth by the dune steepness raised to a power.

Flux through the exchange zone is dependent on Reynolds Number via a power function. For Reynolds Numbers with dune height as the characteristic length, each dune shape results in a unique flux-Reynolds Number power relationship with steeper dunes having smaller flux for a given Reynolds Number. Scaled instead by a Reynolds Number with dune length as the characteristic length condenses all of the data to a single power function, permitting prediction of exchange zone fluxes (5.14) from dune length, free-flowing fluid velocity, porous media permeability, and fluid viscosity.

The exchange zone volume, or area in the case of our two-dimensional simulations, is directly related to the depth of the exchange zone and for turbulent flow also remains constant across a broad range of Reynolds Numbers. The mean residence or turnover times for fluids flowing through the exchange zones (volume/volumetric flux) is therefore just an inverted form of the flux-Reynolds Number relationship with residence time initially decreasing dramatically with an increase in Reynolds Number and eventually behaving asymptotically at higher Reynolds Number.

This study focuses on the coupled system where the fluid is water and the underlying porous media are sandy sediments, but the results are directly transferable to other natural environments that are geometrically and dynamically similar with our studied system.

References

- Albert, M. R., and R. Hawley, Seasonal changes in surface roughness characteristics at Summit, Greenland: Implications for air-snow transfer processes, *Ann. Glaciol.*, 35, 510-514, 2002.
- Albert, M. R., and E. F. Shultz, Snow and firn properties and air-snow transport processes at Summit, Greenland, *Atmos. Environ.*, 36, 2789-2797, 2002.
- Armaly, B. F., F. Durst, J.C.F Pereira, and B. Schonung, Experimental and theoretical investigation of backward-facing step flow, *J. Fluid Mech.*, 127, 473-496, 1983.
- Beavers, G. S., and D. D. Joseph, Boundary conditions at a naturally permeable wall, *J. Fluid Mech.*, 30, 197-207, 1976.
- Brinkman, H. C., A calculation of the viscous force exerted by a flowing fluid on a dense swarm of particles, *Appl. Sci. Res.*, 1, 27-34, 1947.
- Cardenas, M. B., J.L. Wilson, and V.A. Zlotnik, Impact of heterogeneity, bed form configuration, and channel curvature on hyporheic exchange, *Water Resour. Res.*, 40, W08307, doi:10.1029/2004WR003008, 2004.
- Cardenas, M. B., and J.L. Wilson, The influence of ambient groundwater discharge on hyporheic zones induced by current-bedform interactions, submitted to *J. Hydrol.*
- Cardenas, M. B., and J.L. Wilson, Hydrodynamics of coupled flow above and below a sediment-water interface with triangular bedforms, submitted to *Adv. Water Res.*
- Cardenas, M. B., and J.L. Wilson, Comment on "Flow resistance and bed form geometry in a wide alluvial channel" by Yang, Tan and Lim, *Water Resour. Res.*, in press.
- Chen, X., and Y.-M. Chiew, Velocity distribution of turbulent open-channel flow with bed suction, *J. Hydraul. Eng.*, 130, 140-148, 2004.
- Cheng, N. S., and Y.-M. Chiew, Modified logarithmic law for velocity distribution subjected to upward seepage, *J. Hydraul. Eng.*, 124, 1235-1241, 1998.
- Colbeck, S. C., Air movement in snow due to wind pumping, *J. Glaciol.*, 35, 209-213, 1989.
- Cunningham, J. C., and E.D. Waddington, Air flow and dry deposition of non-sea salt sulfate in polar firn: Paleoclimatic implications, *Atmos. Environ.*, 27, 2943-2956, 1993.
- Durllofsky, L., and J.F. Brady, Analysis of the Brinkman equation as a model for flow in porous media, *Phys. Fluids*, 30, 3329-3441, 1987.

- Elliott, A. H., Transfer of solutes into and out of streambeds, Ph.D. thesis, Rep KH-R-52, WM Keck Lab of Hydraul. and Water Resour., California Institute of Technology, Pasadena, 1990.
- Elliott A. H., and N.H. Brooks, Transfer of nonsorbing solutes to a streambed with bed forms: Laboratory experiments, *Water Resour. Res.*, 33, 137-1151, 1997a.
- Elliott, A. H., and N.H. Brooks, Transfer of nonsorbing solutes to a streambed with bed forms: Theory, *Water Resour. Res.*, 33, 123-136, 1997b.
- Engel, P., Length of flow separation over dunes, *J. Hydraul. Div. ASCE*, 107, 1133-1143, 1981.
- Fehlman, H. M., Resistance components and velocity distributions of open channel flows over bedforms, M. S. Thesis, Colorado State University, Fort Collins, CO, 1985.
- Findlay, S., Importance of surface-subsurface exchange in stream ecosystems: The hyporheic zone, *Limnol. Oceanogr.*, 40, 159-164, 1995.
- Goto, S., M. Yamano, and M. Kinoshita, Thermal response of sediment with vertical fluid flow to periodic temperature variation at the surface, *J. Geophys. Res.*, 110, B01106, doi:10.1029/2004JB003419, 2006.
- Harris, R. N., G. Garven, J. Geoghen, M.K. McNutt, and R.P. Von Herzen, Submarine hydrogeology of the Hawaiian archipelagic apron, Part 2, Numerical simulations of coupled heat transport and fluid flow, *J. Geophys. Res.*, 105, 371-385, 2000.
- Harvey, J. W., and C.W. Fuller, Effect of enhanced manganese oxidation in the hyporheic zone on basin-scale geochemical mass balance, *Water Resour. Res.*, 34, 623-636, 1998.
- Huettel M., and I.T. Webster, Porewater flow in permeable sediments, in: B.P. Boudreau, B.B. Jorgensen (Eds.), *The Benthic Boundary Layer: Transport Processes and Biogeochemistry*, Oxford University Press, pp. 144-179, 2001.
- Huettel, M., W. Ziebis, S. Forster, and G.W. Luther III, Advective transport affecting metal and nutrient distributions and interfacial fluxes in permeable sediments, *Geochim. Cosmochim. Acta*, 62, 613-631, 1998.
- Huettel, M., W. Ziebis, and S. Forster, Flow-induced uptake of particulate matter in permeable sediments, *Limnol. Oceanogr.*, 41, 309-322, 1996.
- Huettel, M., and G. Gust, Impact of bioroughness on interfacial solute exchange in permeable sediments, *Mar. Ecol. Prog. Ser.*, 89, 253-267, 1992.

- Jahnke, R. A., J.R. Nelson, R.L. Marinelli, and J.E. Eckman, Benthic flux of biogenic elements on the Southeastern US continental shelf: influence of pore water advective transport and benthic microalgae, *Cont. Shelf Res.*, 20, 109-127, 2000.
- Jorgensen, B. B., and B.P. Boudreau, Diagenesis and sediment-water exchange, in: B.P. Boudreau, B.B. Jorgensen (Eds.), *The Benthic Boundary Layer: Transport Processes and Biogeochemistry*, Oxford University Press, pp. 211-244, 2001.
- Layton, W. J., F. Schiewick, and I. Yotov, Coupling fluid flow with porous media flow, *SIAM J. Numer. Anal.*, 40, 2195-2218, 2002.
- Massmann, J., and D. F. Farrier, Effects of atmospheric pressures on gas transport in the vadose zone, *Water Resour. Res.*, 28, 777-791, 1992.
- Packman, A. I. M. Salehin, M. Zaramella, Hyporheic exchange with gravel beds: basic hydrodynamic interactions and bedform-induced advective flows, *J. Hydraul. Eng.* 130, 647-656, 2004.
- Raudkivi, A. J., Study of sediment ripple formation, *J. Hydr. Div. ASCE*, 89, 15-33, 1963.
- Rutherford, J. C., J.D. Boyle, A.H. Elliott, T.V.J. Hatherell, and T.W. Chiu, Modeling benthic oxygen uptake by pumping, *J. Environ. Eng.*, 121, 84-95, 1995.
- Salehin, M., A.I. Packman, and M. Paradis, Hyporheic exchange with heterogeneous streambeds: Laboratory experiments and modeling, *Water Resour. Res.*, 40, W11504, doi:10.1029/2003WR002567, 2004.
- Savant, S. A., D.D. Reible, and L.J. Thibodeaux, Convective transport within stable river sediments, *Water Resour. Res.*, 23, 1763-1768, 1987.
- Severinghaus, J. P., R. F. Keeling, B. R. Miller, R. F. Weiss, B. Deck, and W. S. Broecker, Feasibility of using sand dunes as archives of old air, *J. Geophys. Res.*, 102, 10.1029/97JD00525, 1997.
- Shavit, U., G. Bar-Yosef, R. Rosenzweig, and S. Assouline, Modified Brinkman equation for a free flow problem at the interface of porous surfaces: The Cantor-Taylor brush configuration case, *Water Resour. Res.*, 38, 1320, doi:10.1029/2001WR001142, 2002.
- Thibodeaux, L. J., and J.D. Boyle, Bed form-generated convective-transport in bottom sediments, *Nature*, 325, 341-343, 1987.
- Thorstenson, D. C., E. P. Weeks, H. Haas, E. Busenberg, L. N. Plummer, and C. A. Peters, Chemistry of unsaturated zone gases sampled in open boreholes at the crest of Yucca Mountain, Nevada: Data and basic concepts of chemical and physical

- processes in the mountain, *Water Resour. Res.*, 34, 1507-1529, 1998.
- Triska, F. J., V.C. Kennedy, R.J. Avanzino, G.W. Zellweger, and K.E. Bencala, Retention and transport of nutrients in third-order stream in Northwestern California: Hyporheic processes, *Ecology*, 70, 1893-1905, 1989.
- van Mierlo, M.C.L.M., and J.C.C. de Ruiter, Turbulence measurements above artificial dunes, Delft Hydraulics Laboratory, Delft, Netherlands, 1988.
- Webb, J. E., J. Theodor, Irrigation of submerged marine sands through wave action. *Nature*, 220, 1968.
- Wilcox, D. C., A half century historical review of the k- ω model, *AIAA Paper*, 91-0615, 1991.
- Worman, A., A.I. Packman, H. Johansson, and K. Jonsson, Effect of flow-induced exchange in hyporheic zones on longitudinal transport of solutes in streams and rivers, *Water Resour. Res.*, 38, doi:10.1029/2001WR000769, 2002.
- Yoon, J. Y., and V.C. Patel, Numerical model of turbulent flow over sand dune, *J Hydr. Eng. ASCE*, 122, 10-18, 1996.
- Yalin, M. S., Steepness of sedimentary dunes, *J. Hydr. Div. ASCE*, 105, 381-392, 1979.
- Zhou, D., and C. Mendoza, Flow through porous bed of turbulent stream, *J. Eng. Mech. ASCE* 119, 365-383, 1993.

CHAPTER 6

EXCHANGE ACROSS A SEDIMENT-WATER INTERFACE WITH AMBIENT GROUNDWATER DISCHARGE

6.1. Introduction

Biogeochemical processes occurring along sediment-water interfaces (SWIs) have measurable impacts on the distribution of ecologically and environmentally important substances, up to the watershed scale in the case of rivers [*Harvey and Fuller, 1998*] and lakes, and up to the global scale in the case of estuaries [*Webster et al., 1996*] and oceans [*Riedl et al., 1972*]. Transport of chemical and thermal energy along and across these interfaces is generated by several mechanisms including wave and tidal pumping [*Riedl et al., 1972; Shum, 1993*], flushing due to flow over irregular surfaces such as bedforms and obstacles [*Thibodeaux and Boyle, 1987; Huettel and Gust, 1992; Elliott and Brooks, 1997; Cardenas and Wilson, 2006a,c*], and biological processes [*Aller, 1982*]. This paper focuses on the second of these. Water-column currents interact with bedform topography to induce eddies and pressure variations along the interface. When the sediments are permeable enough these bottom-pressure variations drive advective transport through the permeable sediments below the interface. Advection dominates diffusion, and biogeochemical processes are strongly controlled by and/or

coupled to hydrodynamical processes [*Jones and Mulholland, 2000; Burnett et al., 2003; Huettel et al., 2003*].

Advective exchange between a flowing water column and an underlying sediment has been studied extensively in laboratory settings (e.g., *Huettel and Gust [1992], Elliott and Brooks [1997], Ren and Packman [2005]*, plus many others). Unfortunately, much is left to be understood regarding the fluid physics along and across SWIs. Flume experiments have advanced our basic understanding of coupled sediment-water column systems but they have also been limited in terms of the dynamical settings. High-fidelity multiphysics computational fluid dynamics (CFD) simulations allow for detailed investigations across a broad suite of dynamical settings which can lead to predictive relations with a strong mechanistic basis [*Cardenas and Wilson, 2006a,c*].

The case where the upward or downward flow of deep groundwater influences and further complicates the physics and biogeochemistry of both interstitial water and benthic water [*Burnett et al., 2003*] has received little to no attention in the past. Groundwater discharges into and/or from almost all freshwater rivers and lakes. Depending on the direction of net groundwater flow these are referred to as ‘gaining’ and ‘losing’ bodies [*Winter et al., 1998*]. It is also widely accepted that groundwater from coastal confined and unconfined aquifers is discharged along ocean coastlines and even deeper parts of the continental shelf up to as much as 80 km away from the coast [*Simmons, 1992; Moore, 1996; Moore and Shaw, 1998; Burnett et al., 2003*]. Our already restricted understanding of coupled fluid flow in the water column and underlying sediments is further limited for these systems with ambient groundwater discharge (AGD).

Our aim is to use multiphysics CFD to examine the current-bedform fluid dynamics along SWIs where there is AGD. This is an extension of our previous numerical experiments. The reader is referred to *Cardenas and Wilson* [2006c] for discussions regarding the base case where there is turbulent flow in the water column but no AGD. For cases where the flow in the water column is laminar, refer to *Cardenas and Wilson* [2006a,b].

6.2. Methodology

Our goal is addressed by numerically modeling the flow along SWIs in two-dimensions and at steady-state (Figure 6.1). The procedure and system formulation follows that of *Cardenas and Wilson* [2006c] where the turbulent water column is governed by the Reynolds-averaged Navier-Stokes (RANS) equations coupled with the k - ω closure scheme [Wilcox, 1991], and the interstitial flow within the sediments is assumed to be Darcian and described by the groundwater flow equation. Briefly, we solve the RANS equations first (using the CFD-ACE+ code) while considering the bottom of the water column (the SWI) to be a no-slip wall and then impose the RANS-based bottom-pressure solution along the wall as a Dirichlet boundary to the top of the groundwater flow model representing the sediments (solved via the Comsol Multiphysics code). The lateral boundaries for both domains (water column and sediments) are spatially periodic with a given pressure drop resulting in mean flow from left to right. This mean flow in the sediments is typically referred to as “underflow”. Details and validation of the methodology have been presented in *Cardenas and Wilson* [2006c] and are not repeated here. The main difference between our previous work and this study is that we impose a prescribed flux boundary at the lower boundary of the sediments

(compare to Figure 1c in *Cardenas and Wilson [2006c]*). At this boundary we consider prescribed flux both into and out of the domain representing, respectively, ‘gaining’ and ‘losing’ water columns. Fluid properties are those of fresh water at 20°C and isothermal conditions are assumed. The sediment, assumed to be a sand, is assigned a permeability (k) of 10^{-10} m^2 in all simulations.

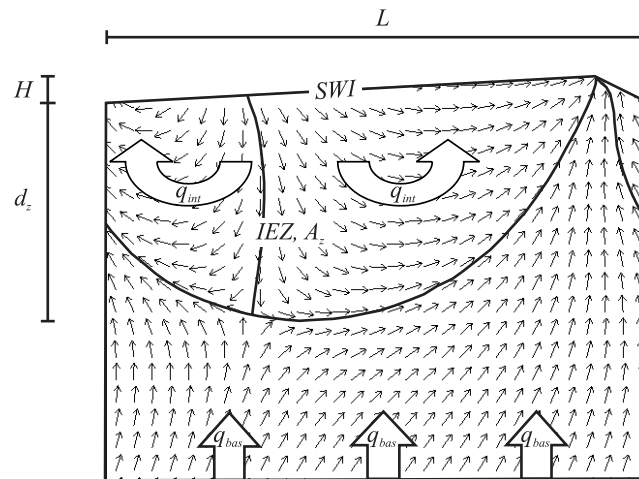


Figure 6.1. Schematic representation of the periodic flow domain, depicting geometric parameters- height (H) and length (L)- and fluxes- basal (q_{bas}) and interfacial (q_{int}). The depth of the interfacial exchange zone (IEZ), d_z , is the vertical distance from the trough to the deepest portion of the streamline enveloping the region wherein water flows from and then back into the water column. Small arrows correspond to flow directions.

Sensitivity analysis is performed via multiple CFD simulations by varying parameter values. We vary the water-column current, measured by a Reynolds numbers (Re), the bedform height (H), and effectively the bedform steepness (height-to-length ratio, H/L), as well as the prescribed ambient groundwater flux at the base of the groundwater flow domain, q_{bas} , which we refer to as “basal flux” to differentiate it from other flux terms (Figure 6.1). The bedform length, L , is fixed at 1.0 m and the crest is

invariantly located at $0.9L$, typical of subaqueous dunes. The Reynolds number of the flowing water column is varied by imposing different horizontal pressure drops across the domain which also effectively changes the average velocity in the water column, U_{ave} .

6.3. Results and Discussion

We limit our discussion to the results of simulations for flow through the sediments. By virtue of our sequential coupling, the turbulent flow fields in the water column are similar to those in *Cardenas and Wilson* [2006c].

The area within the permeable sediments that is physically influenced by fluid exchange across the SWI is the interfacial exchange zone (IEZ); this is the zone characterized by streamlines that originate and end at the SWI. Fluvial ecologists and hydrologists commonly refer to this as the “hyporheic zone” (Figure 6.1). The depth of the IEZ, d_z , is taken as the distance between the deepest portion of the streamline which envelopes all streamlines originating from and returning to the SWI, and the trough of the bedform. The IEZ flux density through the SWI is computed as follows: i) first, total volumetric flux through the SWI per bedform is computed by integration of the magnitude of the normal flux along the bedform surface; ii) then, we subtract from this total volumetric flux the prescribed volumetric basal flux (basal flux multiplied by the bedform length) resulting in the total volumetric interfacial flux that is induced solely by current-bedform interactions; iii) the resulting quantity is divided by the twice the length of the bedform because the integration does not discriminate between induced flux going in and out of the bed, which are approximately equal. The final value, q_{int} , is a flux density based on bedform length; the total IEZ flux is given by the product $q_{int} L$ and takes place only for that portion of the SWI subjected to current-induced flushing (bounded by the dividing

streamline discussed above and illustrated in Figure 6.1). The basal and interfacial flux densities, which are schematically represented in Figure 6.1, are nondimensionalized as follows:

$$q^* = \frac{q}{K} \quad (6.1)$$

where q^* is the dimensionless flux density, $K=kg/\nu$ is the hydraulic conductivity of the sediments, ν is kinematic viscosity, and g is the gravity.

We examine how the water column Reynolds number (Re) affects d_z and q_{int}^* .

We define Re as:

$$Re = \frac{U_{ave} H}{\nu} \quad (6.2)$$

where U_{ave} is the characteristic velocity considered as the average velocity along a vertical-section in the water column, taken above the crest of the bedform, and H , the height of the bedform, is the characteristic length scale.

Flow fields for scenarios with different Re and q_{bas}^* are presented in Figure 6.2. The first important observation from Figure 6.2 is that IEZs form even under conditions with AGD. Secondly, the flow fields within and outside the IEZ are a result of the competitive interaction between current-bedform induced flow and ambient groundwater flow. The results for both gaining and losing conditions are elaborated below.

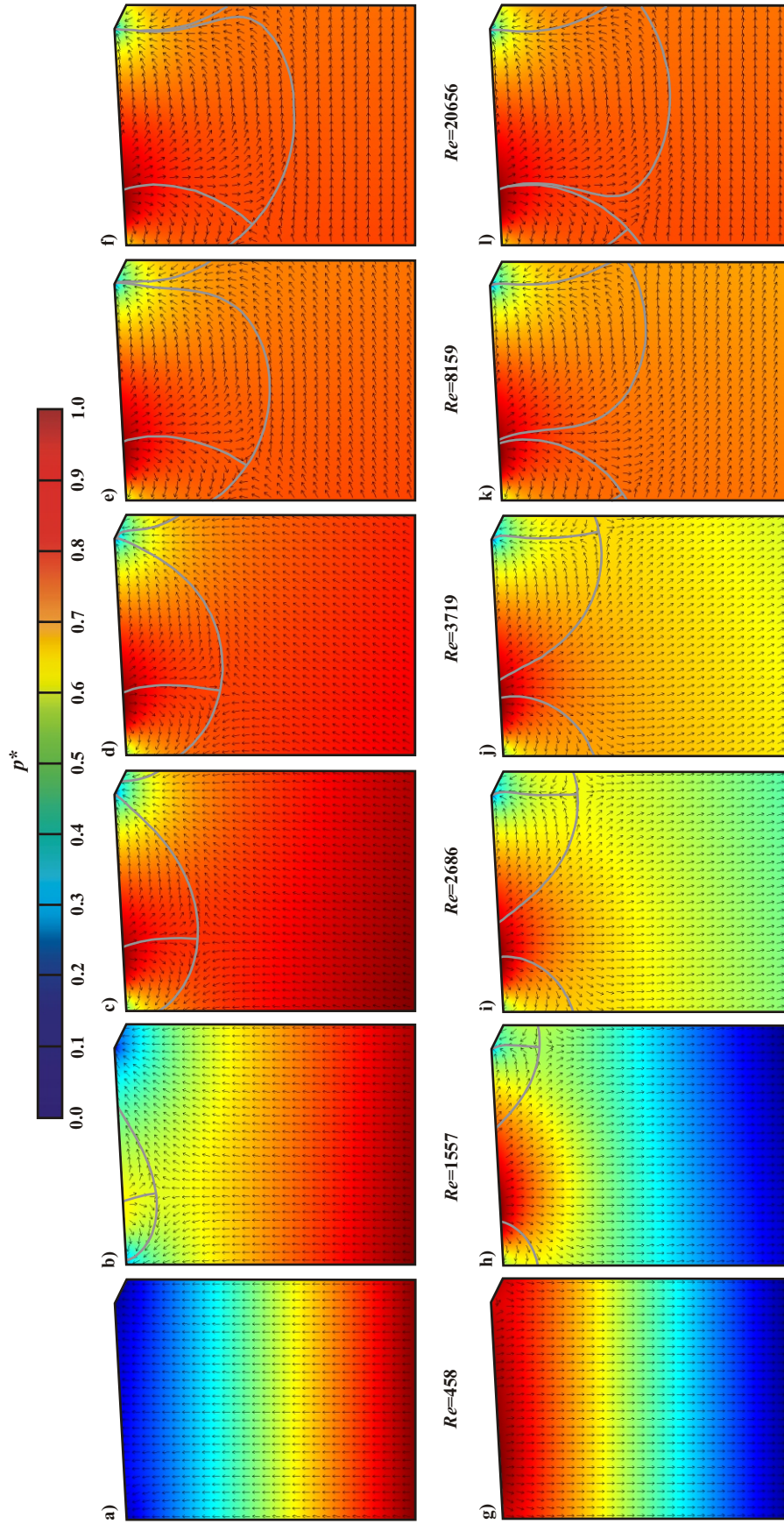


Figure 6.2. The top row shows pressure fields (color) and flow directions (arrows) for gaining conditions ($q_{bas}^* = 9.8 \times 10^{-2}$) at different Reynolds number (Re). The bottom row shows the same for losing conditions ($q_{bas}^* = -9.8 \times 10^{-2}$). Pressure is normalized as follows: $p^* = (p - p_{min}) / (p_{max} - p_{min})$ where p^* is normalized pressure, p_{max} and p_{min} are the maximum and minimum pressures for each simulation, respectively. The gray streamlines delineate the IEZs. $H/L = 0.05$ and $L = 1.0$ m for all cases.

6.3.1. IEZ spatial configuration and fluxes: gaining conditions

The ‘gaining’ cases are discussed first. The prescribed AGD flux at the lower sediment boundary is upwards. The IEZ, when it is present, is centered around the bottom-pressure maximum along the stoss face of the dune (Figure 6.2a-f). This maximum pressure point is located approximately where the eddy in the water column reattaches (see discussion in *Cardenas and Wilson* [2006c]). There are two flow cells in the sediments, similar to cases without AGD [*Cardenas and Wilson*, 2006c]. For lower Re , the IEZ terminates at points along the SWI that are between the location of the bottom-pressure maximum and the pressure minimum, which is located at the crest (e.g., Figure 6.2b). These termination points move closer to the crest as the Re increases, with the AGD becoming more focused towards the crest. These points eventually coalesce where the IEZ becomes similar to the case without AGD (compare to Figure 7 in *Cardenas and Wilson* [c]), but with a thin streamtube connecting the AGD to the pressure minimum near the crest. The implications of this behavior for biogeochemical processes are discussed later.

Steeper bedforms (larger H/L) that are subjected to the same dimensionless current and AGD, that is, the same Re and q_{bas}^* , result in shallower IEZs (Figure 6.3, left column). This trend is consistent with the cases involving no AGD [*Cardenas and Wilson*, 2006c]. The IEZ depths, d_z , for the base no-AGD case are indicated by the gray lines in Figure 6.3 (left column). In the absence of AGD, d_z stabilizes at these more or less constant values upon the onset of fully-developed turbulence [*Cardenas and Wilson*, 2006c]. When deep groundwater is flowing upwards towards the SWI, the d_z increases abruptly at low Re and behaves asymptotically at higher Re . The sharp growth in d_z/L is

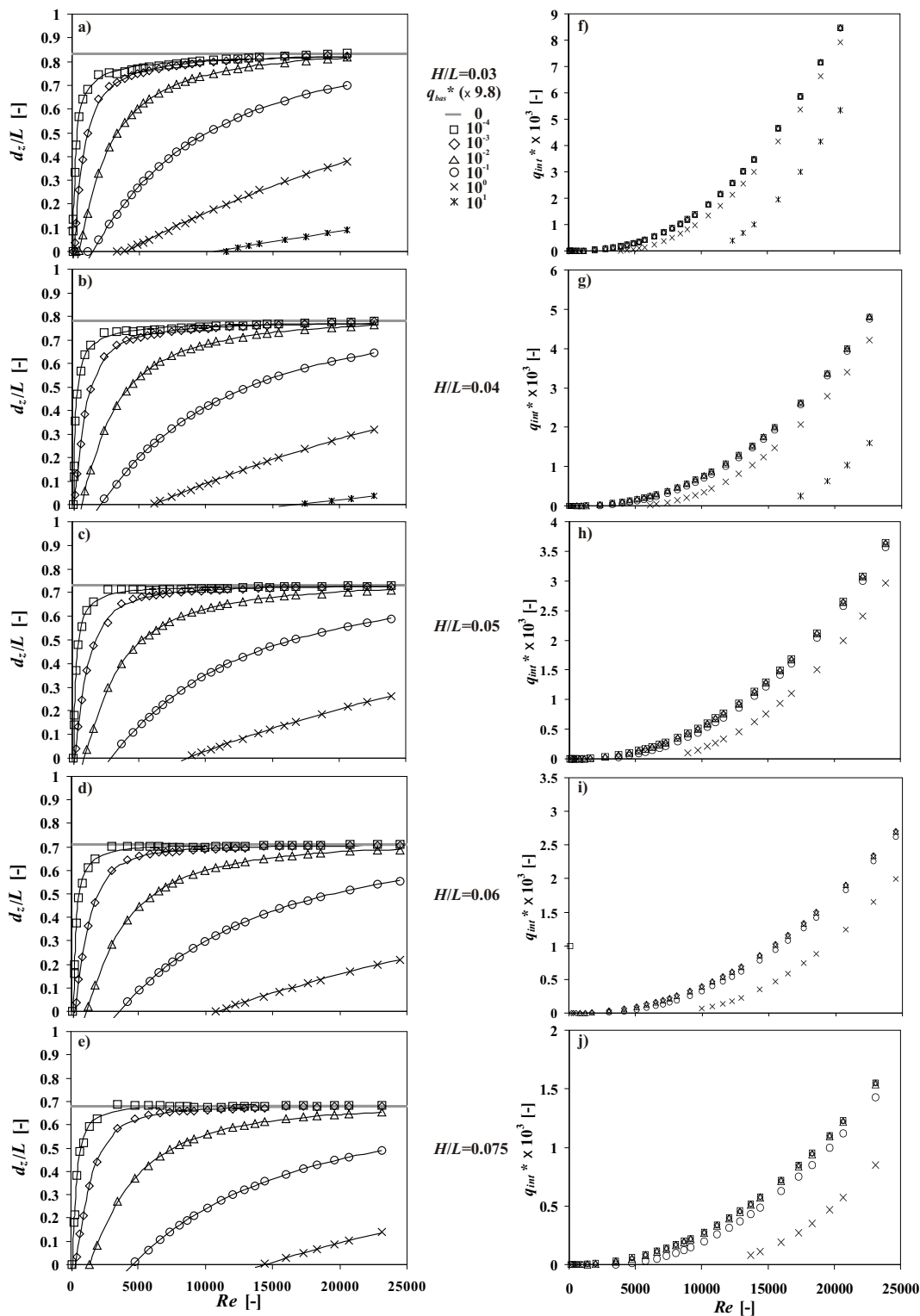


Figure 6.3. Gaining conditions. Dimensionless IEZ depths (d_z/L) and interfacial fluxes (q_{int}^*) for bedforms with different bedform steepness (H/L) and subjected to different upward AGD. The horizontal gray lines in the left column indicate the IEZ depth for the base case without AGD [Cardenas and Wilson, 2006c]. The solid curves in this column are MMF (6.3) fits to the simulation data.

subdued for larger q_{bas}^* (Figure 6.3, left column), and does not reach non-AGD values for typical water column Res .

Figures 6.2 and 6.3 also illustrate the presence of a threshold or critical Reynolds number, Re_{crit} , below which there is no IEZ, and the sediments are completely filled with discharging deep groundwater (Figure 6.2a). The existence of such a threshold was previously identified for the case when flow in the water column is laminar [Cardenas and Wilson, 2006b]. Below Re_{crit} , the dominant vertical pressure gradients result in essentially one-dimensional flow upwards.

Following Cardenas and Wilson [b], a curve-fitting algorithm was used to find an optimal functional form for the $d_z(Re)$ data from several candidate functional models. The Morgan-Mercer-Flodin (MMF) model [Morgan et al., 1975] consistently provided good fits to the data from simulations with varying combinations of q_{bas} and H/L . Other functions were not as consistent. The MMF model was originally developed to describe the nutritional response of higher organisms, and is defined as:

$$(d_z / L) = \frac{(ab + cRe^d)}{(b + Re^d)} \quad (6.3)$$

The x -intercept of the fitted MMF models represents Re_{crit} . Below the Re_{crit} , the current-bedform induced pressure gradient is overpowered by the ambient pressure gradient associated with AGD thereby preventing the development of an IEZ. Fitted MMF curves are presented in Figure 6.3 (left column); $R^2 > 0.99$ for all cases. Figure 6.4a illustrates the dependence of Re_{crit} on q_{bas}^* for the gaining cases. Re_{crit} initially increases sharply (note logarithmic scale) and then its rate of increase with q_{bas}^* becomes gradual at larger basal

fluxes. When subjected to the same q_{bas}^* , steeper bedforms have a larger Re_{crit} .

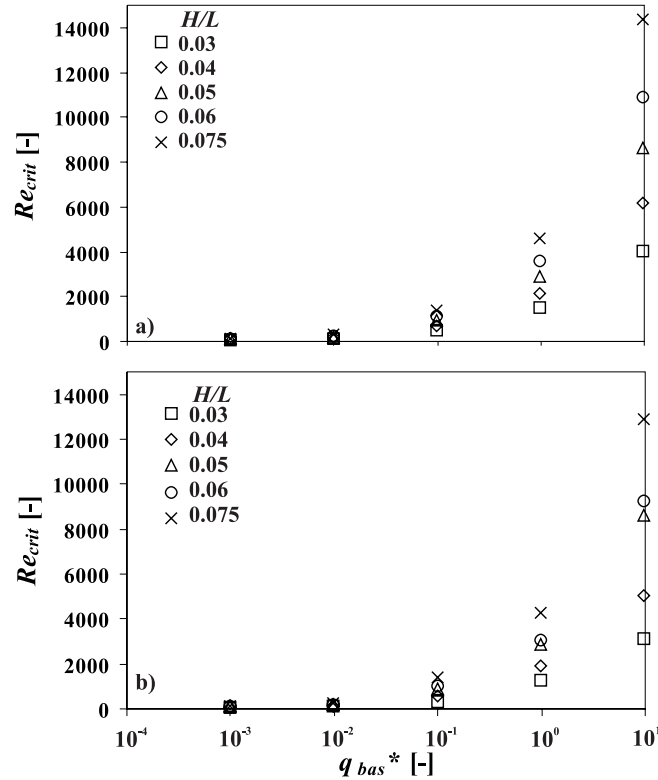


Figure 6.4. Critical Reynolds numbers, Re_{crit} , for bedforms with different bedform steepness (H/L) and subjected to different AGD (q_{bas}^*). (a) shows results for gaining conditions and (b) shows results for losing conditions.

Unlike d_z which follows a saturation growth curve-type model (MMF), the normal flux per unit length through the IEZ, q_{int}^* , continually increases with Re (Figure 6.3, right column). q_{int}^* is dependent on Re via a power model, similar to the model fit for the no-AGD relationship [Cardenas and Wilson, 2006c]. $R^2 > 0.99$ for all fitted power models but these are not displayed in the graphs for clarity. For a given Re and q_{bas}^* , steeper bedforms have a smaller q_{int}^* (note the differences in scale of the y-axis in the right column of Figure 6.3), again consistent with the no-AGD behavior (see Figure 6c of

Cardenas and Wilson [2006c]). Increasing q_{bas}^* does not significantly affect the q_{ini}^* except when q_{bas}^* is very large. For example, the topmost panel of the right column in Figure 6.3 ($H/L=0.03$) suggests that across five orders of magnitude of AGD, q_{ini}^* barely changes for the same Re .

6.3.2. IEZ spatial configuration and fluxes: losing conditions

When AGD is downwards along the bottom boundary, the water column is losing water. Looking only at d_z as a measure of the IEZ spatial configuration, there is hardly a discernable difference between losing (Figure 6.5, left column) and gaining (Figure 6.3, left column) conditions across varying H/L and q_{bas}^* . The differences, however, are apparent when viewing the whole flow field, as in Figure 6.2. Under losing conditions, the IEZ is centered around the bottom-pressure minimum at the crest (Figure 6.2, bottom row), whereas it is centered around the pressure maximum for gaining conditions (Figure 6.2, top row). The termination points of the IEZ along the SWI are areas where water is flowing down into the IEZ for the losing scenario; these are areas where water is flowing up into the water column for the gaining case. These termination points get closer to each other with increasing Re until, for the losing case, they eventually coalesce at the location of the bottom-pressure maximum and the IEZ again looks similar to the non-AGD case. Consequently, water loss from the overlying water column is focused into a narrow streamtube that originates around the pressure maximum at the SWI.

There is also a threshold Re_{crit} for losing conditions. When the downward AGD is dominant, there is no return flow to the SWI (Figure 6.2g). All water infiltrating from the water column flows towards deeper portions of the sediments. As Re increases, the lateral pressure gradient along the SWI becomes sufficiently large such that some of the water

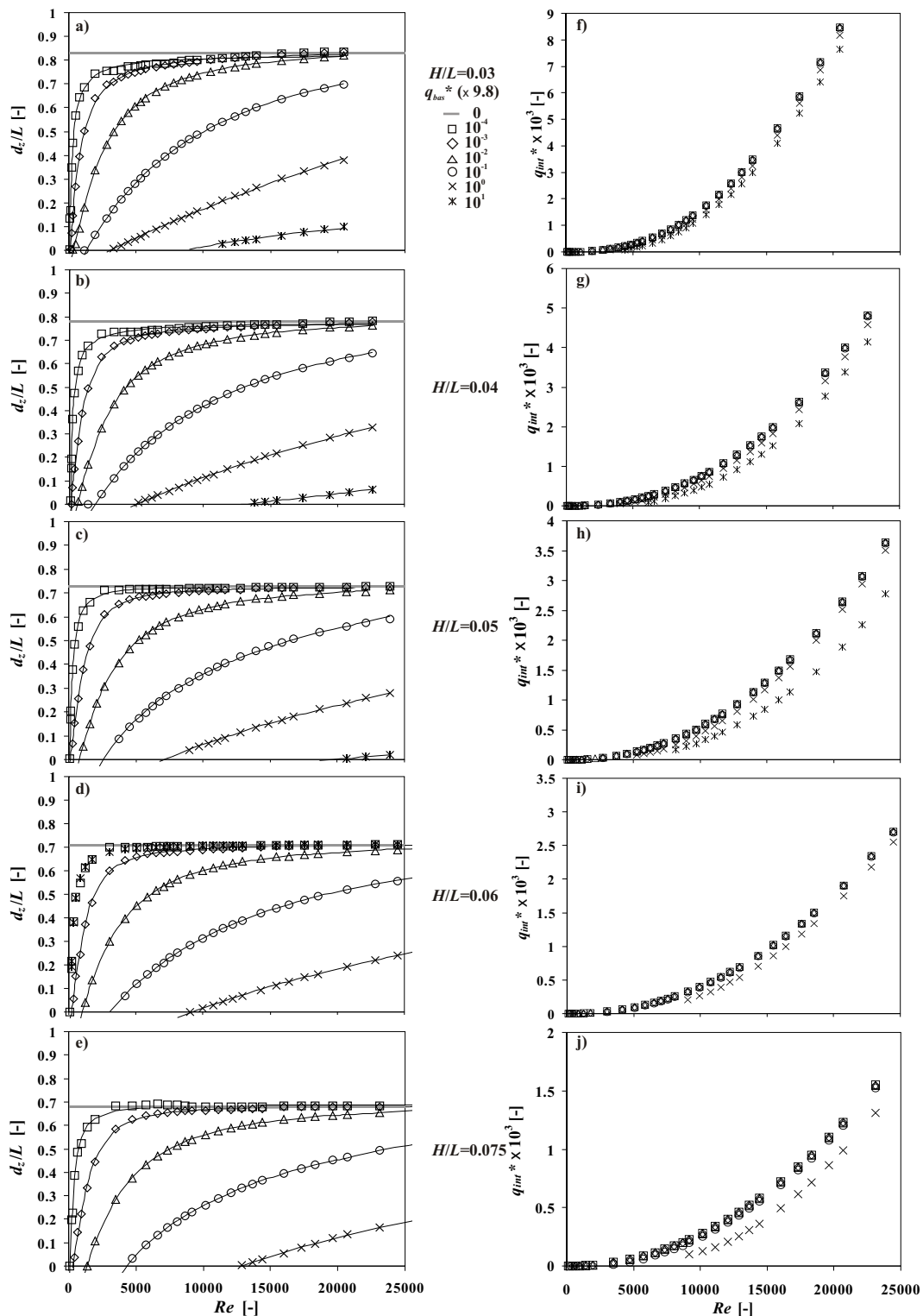


Figure 6.5. Losing conditions. Dimensionless IEZ depths (d_z/L) and interfacial fluxes (q_{int}^*) for bedforms with different bedform steepness (H/L) and subjected to different downward AGD. The horizontal gray lines in the left column indicate the IEZ depth for the base case without AGD [Cardenas and Wilson, 2006c]. The solid curves in this column are MMF (6.3) fits to the simulation data.

infiltrating near the bottom-pressure maximum is influenced by the pressure minimum and flows towards it, returning to the SWI and creating an IEZ, instead of following the ambient downward flow. Values for Re_{crit} can be derived from MMF model (3) fits, which describe the $d_z(Re)$ behavior for the losing conditions. The regressed MMF models ($R^2 > 0.99$ for all cases) are presented in Figure 6.5 (left column). Re_{crit} for losing conditions are similar to those for gaining conditions (Figure 6.4b).

The dependence of IEZ flux density q_{int}^* on Re for various H/L and q_{bas}^* conditions is likewise similar between gaining and losing conditions (compare right columns of Figures 6.5 and 6.3). Recall that for gaining conditions the $q_{int}^*(Re)$ results fall under a narrow range, except when q_{bas}^* is large. For losing conditions q_{int}^* is even less sensitive to q_{bas}^* . Consider, for example, the cases where $H/L=0.03$. For the gaining case, the curve defined by simulation results for $q_{bas}^*=9.8 \times 10^1$ fall outside the narrow range defined by the other simulation results on this chart (Figure 6.3f). For the corresponding losing case (Figure 6.5f), there is less variation.

6.3.3. Exchange zone areas and residence times for both cases

The area of the IEZ, A_z , is defined by the SWI and the bounding streamlines that surround all water originating from and returning to the SWI (Figure 6.1). IEZ depth, d_z , and area, A_z , are strongly related, as illustrated in Figure 6.6a,b, where the IEZs for both gaining and losing conditions, and for different q_{bas}^* , are superposed with each other and with the base case (i.e., $q_{bas}^*=0$). Figure 6.6c,d, shows fitted power models describing the relation between d_z and A_z , where A_z is normalized by L^2 . (The points in Figure 6.6c,d correspond to the respective plots in Figure 6.6a,b.) There is no noticeable difference in the area-depth relationships for gaining and losing conditions, although the actual IEZ

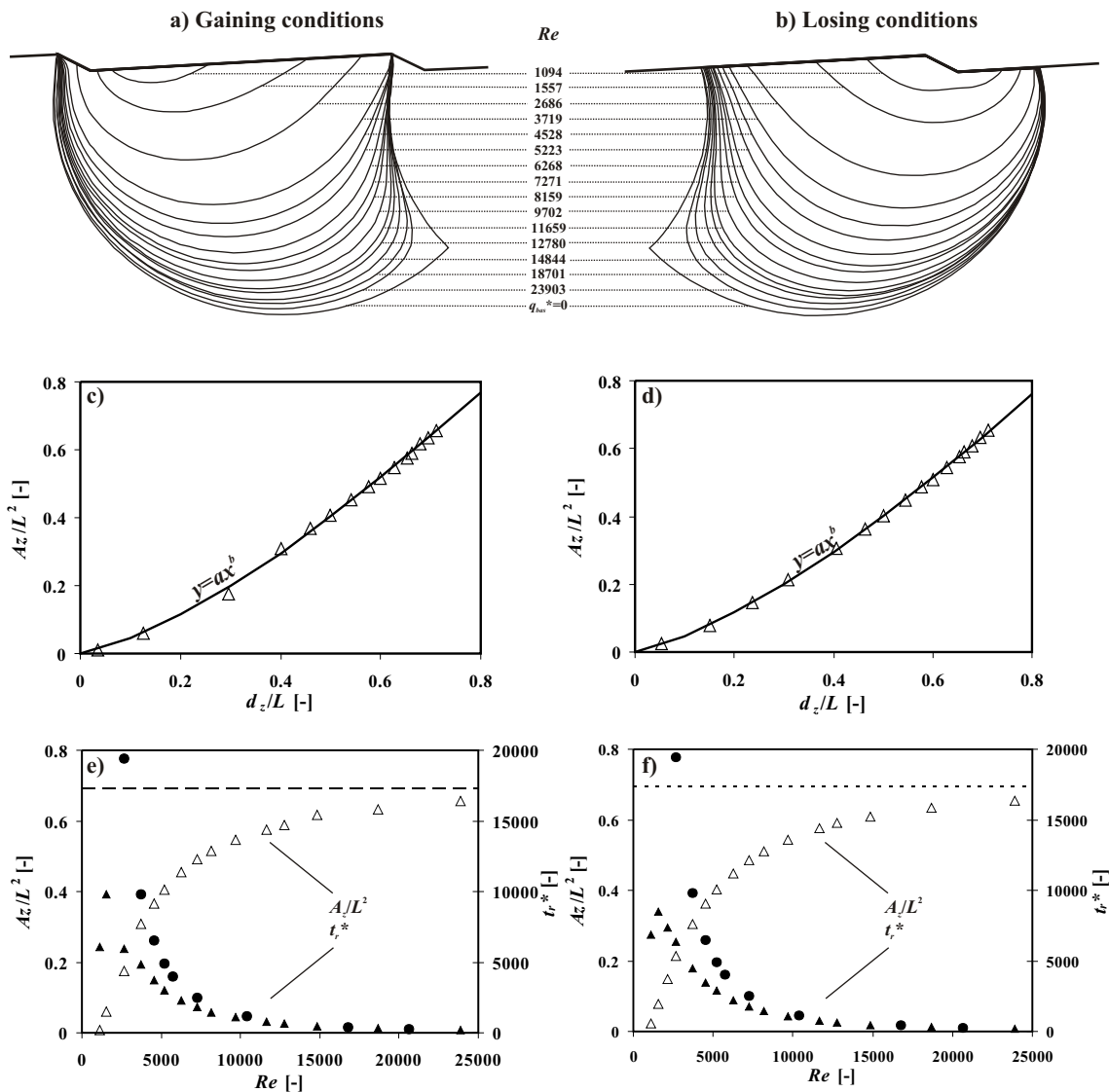


Figure 6.6. The left and right columns show results for gaining and losing conditions, respectively, with AGD magnitude $|q_{bas}^*|=9.8 \times 10^{-2}$. In all cases $H/L=0.5$, $L=1.0$ m. (a) and (b) illustrate the extent of the IEZs for different Re s (labels). (c) and (d) show the power relationships (solid lines) between dimensionless IEZ area (A_z/L^2) and depth (d_z/L) for the gaining and losing cases in (a) and (b). The coefficients for the power models in (c) are $a=1.046$ and $b=1.377$, while in (d) they are $a=1.029$ and $b=1.358$; $R^2>0.99$ in both cases. (e) and (f) show the dimensionless IEZ areas (hollow triangles) and residence times (t_r^* ; solid triangles, $q_{bas}^*=9.8 \times 10^{-2}$; solid circles, $q_{bas}^*=0$) as a function of Re . MMF models (6.3) (solid lines) are fitted to the $A_z/L^2(Re)$ data; $R^2>0.99$ for both cases. The dashed line in (e) and (f) represent A_z/L^2 for the base case without AGD ($q_{bas}^*=0$) [Cardenas and Wilson, 2006c].

spatial configuration and location are quite dissimilar. The relationship between IEZ depth and area is also manifested in the dependence of A_z on Re which is very similar to the $d_z(Re)$ curves (Figures 6.6e,f; compare to Figures 6.3c and 6.5c, respectively); once again, MMF curves (3) fit the $A_z(Re)$ data well ($R^2 > 0.99$ in both cases).

Mean or characteristic residence times of fluids flowing through the IEZ can be readily computed from the flux and porous area (see *Cardenas and Wilson* [2006a,b]):

$$t_r = \frac{nA_z}{q_{int}L} \quad (6.4)$$

where t_r is the mean residence time, and n is porosity. We express mean residence time in dimensionless form, t_r^* , by dividing dimensionless area (A_z/L^2) by q_{int}^* . Figure 6.6f shows t_r^* as a function of Re for gaining and losing cases (both solid triangles) as well as the no AGD cases (solid circles). Residence time t_r^* is large at low Re s and decreases rapidly with Re . Even though the IEZs are smaller in extent at low Re , the fluxes are so small that it takes a long time for fluids to circulate through these small zones. AGD decreases the residence time, with a larger decrease for lower Re . At the lowest Re ($=1094$, leftmost triangles in Figures 6.6e,f) the decrease is exceptionally large. At this Re , the flow may be transitional or even laminar, and the turbulent flow model may be inaccurate. We also know that t_r^* eventually approaches 0 as the Re approaches its critical value, when there is no current-bedform induced exchange and the IEZ shrinks to zero (Figure 6.2a,g).

6.3.4. On the similarity of gaining and losing IEZ metrics

Although the IEZ patterns are very different for gaining and losing conditions

(Figures 6.2 and 6.6a,b), their depths, areas, fluxes and residence times are remarkably similar (Figures 6.3-6.6). Why? We believe that this behavior is driven by the competition between two different pressure gradients. The first is the upwards or downwards ambient or basal-pressure gradient at the lower boundary of the sediments (dP_{bas}), resulting from the prescribed basal AGD. The second is the current-bedform induced pressure gradients along the SWI ($dP_{swi} = (p_{max}-p_{min})/L$, where p_{max} and p_{min} are the maximum and minimum bottom pressures along the SWI, respectively). Also related to dP_{swi} is a third gradient, which drives both the current and the underflow. This is the prescribed horizontal pressure gradient between the lateral periodic boundaries of the domain (dP_{und}). When the basal gradient, dP_{bas} , is large and dominant, the resulting pressure field is characterized by a largely vertical gradient, and the current-bedform induced pressure gradients is negligible (Figure 6.2a,g). In order for exchange flow to occur, the magnitude of the gradient due to current-bedform interaction, dP_{swi} , needs to be larger than dP_{bas} .

For the gaining cases, where the AGD is upwards, the bottom-pressure gradients along the SWI need to overpower the negative basal gradient, dP_{bas} (Figure 6.2b). Near the SWI, the largest vertical pressure gradients occur in the vicinity of the bottom-pressure maximum and minimum (see Figure 8 in *Cardenas and Wilson* [2006c] for bottom-pressure profiles). Therefore, downwards flow from the SWI occurs near the pressure maximum since the presence of a pressure peak allows for a positive gradient. Near the crest, where the pressure minimum is located, more vigorous upwards flow is favored due to the enhancement of negative pressure gradients. As the Re in the water column increases, so does the pressure gradient along the SWI resulting in more

significant bottom-pressure peaks and dips [Cardenas and Wilson, 2006c]. Ultimately, the bottom-pressure variation dominates, resulting in a flow field similar to the no-AGD case (Figure 6.2f). The final result of this competition between the bottom-pressure gradient along the SWI and the negative gradient driving the upward discharge of deep groundwater is the MMF-type (3) behavior of IEZ deepening and spatial development (Figure 6.3 and 6.6) with increasing Re .

For the losing cases, where ambient flow is downwards, an IEZ requires a dominant bottom-pressure minimum along the SWI such that it can promote return flow towards the water column, overcoming the predominant downwards flow (Figure 6.2h-l). In this case, the area near the bottom-pressure peak has an amplified positive gradient and downward movement of water. However, as Re increases, the bottom-pressure dip near the crest also becomes pronounced (Figure 6.2h), enhancing return flow towards the SWI. Similar to the gaining case, the negative gradient near the crest is tied to the Re in the water column. Eventually, at high Re , the bottom-pressure variation along the SWI dominates and the negative basal gradient is negligible (Figure 6.2l). This competition results in an MMF-type behavior for the IEZ metrics.

The discussion above is illustrated by plotting and comparing the different pressure gradients across the range of Re (Figure 6.7) corresponding to simulations in Figure 6.2. dP_{bas} is constant; this is a result of prescribing the normal basal flux, assuming homogeneous hydraulic properties of the sediments, and Darcy's Law. The bottom-pressure gradient, dP_{swi} , grows with Re . (It also mimics dP_{und} , illustrating that it is the periodic boundary condition that drives both the current and the underflow.) Comparing Figures 6.2-6.6 to the plots in Figure 6.7 suggests that IEZs form when,

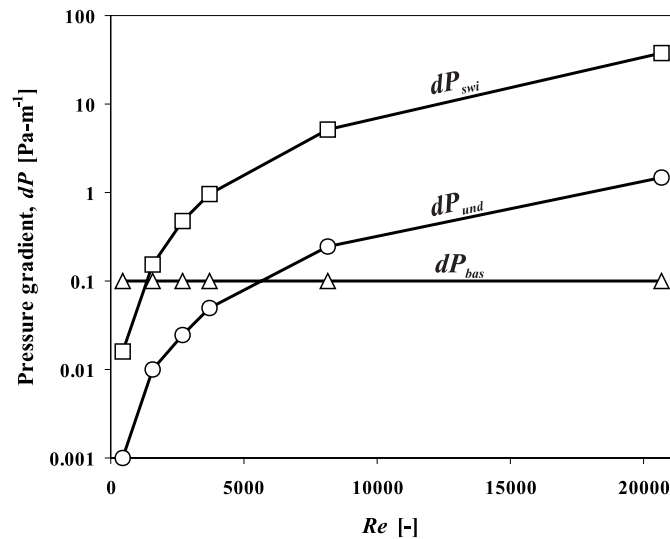


Figure 6.7. Superposed plot of pressure gradients, as a function of Re , along the SWI (dP_{swi}), between the lateral spatially periodic boundaries which drives underflow (dP_{und}) and the current in the water column, and the vertical gradient (dP_{bas}) along the bottom of the sediments due to the prescribed basal flux. Results plotted correspond to the simulations in Figure 6.2 (gaining conditions only, but with a sign change for dP_{bas} the pressure gradients for losing conditions are exactly the same).

roughly, $dP_{swi} > dP_{bas}$. When $dP_{swi} > dP_{bas} > dP_{und}$, the IEZ grows rapidly; this stage in IEZ development corresponds to the steep portions of the MMF model (6.3) and is illustrated by Figures 6.2b-6.2d and 6.2h-6.2j. At higher Re , when $dP_{swi} > dP_{und} > dP_{bas}$, the spatial development of the IEZ becomes subdued and starts to become asymptotic to the base no-AGD case. Figures 6.2 and 6.6a,b suggest that this corresponds to the conditions where the IEZs below two neighboring bedforms begin to coalesce (e.g. Figures 6.2e, 6.2f, 6.2k and 6.2l) and where the streamtube through which AGD exits or enters the IEZ becomes narrow. The similarities between the gaining and losing conditions can therefore be explained by forces which drive flow in the water column; these are essentially the same in both cases, despite the asymmetry in dune shape and eddy formation.

6.3.5. Predicting the presence of an IEZ

Using the concept of a critical Reynolds number, Figures 6.3 to 6.5 provide a basis for predicting the presence of an IEZ under AGD conditions. (However, note that Figure 6.4 is based on a single value for AGD). We believe that a more useful criterion would be based on pressure gradients instead of on Re_{crit} . By measuring the magnitude of AGD or its associated pressure gradient, dP_{bas} , and the bottom-pressure gradient, dP_{swi} , one would be able to predict whether a substantial IEZ is present. In the field dP_{bas} and/or q_{bas} can be estimated readily with piezometers, potentiomanometers and other related instrumentation. Unfortunately, dP_{swi} is difficult if not impossible to measure under most field conditions. It can, however, be predicted on the basis of the Re which itself can be readily quantified by taking an average velocity and observing the geometry of the bedforms. *Cardenas and Wilson* [2006c] present details of the turbulent flow simulations; these details are supplemented by Figure 6.8 which presents a power-law that relates the bottom-pressure gradient, dP_{swi} , with Re , which has been rescaled by bedform steepness (H/L). This effectively changes the Reynolds number characteristic length to the bedform length, L , instead of bedform height, and allows all of our simulation results to plot along the same curve in Figure 6.8. (Note that our simulations are based on bedforms where the crest is located at $0.9L$; the results in Figure 6.8 may not be appropriate to predict dP_{swi} when the crest is located differently.) Using field measurements to quantify dP_{bas} and Re , the power law in Figure 6.8 to estimate dP_{swi} , and the criterion that $dP_{swi} > dP_{bas}$, one can predict the existence of an IEZ under conditions of ambient groundwater discharge.

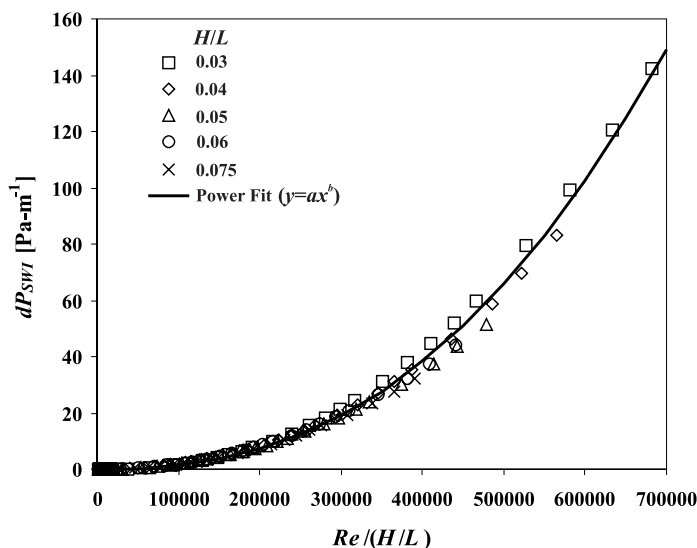


Figure 6.8. Pressure gradient along the SWI, dP_{swi} , as a function of Re scaled by bedform steepness, H/L . The fitted power model ($R^2 > 0.99$) has coefficients $a = 1.028 \times 10^{-12}$ and $b = 2.423$.

6.3.6. Implications for biogeochemical and thermal processes

To date, few studies, if any, have addressed the existence IEZs when the water column is gaining or losing water, let alone the dynamics of the exchange processes under these unique conditions. This modeling study illustrates that IEZs are present even under AGD conditions. It elucidates physical dynamics that have implications for biogeochemical and thermal processes occurring within IEZs. For example, under gaining conditions, discharging groundwater may have a different biogeochemical and thermal make-up compared to the overlying water column. Steep chemical and thermal energy gradients will form along the interface of the IEZ and deeper groundwater, i.e., the gray lines in Figure 6.2. These zones can be biogeochemical and ecological ‘hot spots’ [Huettel *et al.*, 1998]. Biological communities that depend on entrained gases and dissolved solutes abundant in the overlying water column will preferentially be located in

the IEZs, just underneath the maximum bottom-pressures along stoss side of the dune.

There may be different biogeochemical areas along the SWI under losing conditions as well. Typically, one might assume that the biogeochemistry directly underneath a losing water column and along the SWI is close to uniform since the same water (assuming the water column is reasonably well-mixed) is infiltrating through the SWI everywhere. However, given the occurrence of myriad biogeochemical reactions occurring within IEZs (a drastic change in redox conditions with depth or along a flowpath for example), water flowing out of the IEZ back to the water column might have a different chemistry compared to when it first entered the IEZ. *Huettel et al.* [1998] suggested that redox zones develop due to current-bedform driven advection under 'neutral' conditions where the water column is neither gaining nor losing water primarily. The different redox conditions arise primarily from return flow to the SWI. We show that there is return flow to the SWI even under losing conditions. Therefore, formation of zones with distinct redox conditions under losing conditions can be expected.

6.4. Summary

The biogeochemistry of areas along a sediment-water interface (SWI) is mediated by the movement of fluids along and across the SWI. This is particularly true in cases where chemical transport is dominated by advection. Currents interact with bedform topography to drive interfacial exchange across the SWI; the area influenced by interfacial exchange characterized by streamlines originating and ending at the SWI is the interfacial exchange zone (IEZ). Current-bedform driven advection of water through the sediments is further complicated by the presence of ambient groundwater discharge (AGD), the upward or downward ambient movement of groundwater. To date, the effects

of AGD on interfacial exchange processes has not been studied either in the field, laboratory or through computational fluids dynamics simulations. The biogeochemical and ecological processes occurring along SWIs cannot be fully understood without first understanding the physical template. We investigated the dynamics of IEZs both under the influence of current-bedform driven exchange and AGD through high-fidelity multiphysics numerical models wherein we simulate turbulent flow above the SWI and Darcy flow below the SWI.

The simulations show that an IEZ forms in the presence of AGD, under both ‘gaining’ and ‘losing’ conditions, provided that the forcing due to current-bedform interaction is at least equal in magnitude as that due to AGD. The competition between current-bedform interaction forcing and AGD forcing controls the IEZ shape, depth, area, fluxes, and residence time. Lateral bottom-pressure gradients along the SWI resulting from current-bedform interaction, which drives interfacial exchange, must be at least as important as the vertical pressure gradient associated with the AGD in order for an IEZ to be present. Otherwise, fluid flow within the sediments is dominated by AGD and flow essentially becomes one-dimensional upwards or downwards. The bottom-pressure gradient along the SWI increases systematically with the water-column Reynolds number (Re), thereby allowing for prediction of the presence of an IEZ on the basis of Re and measurements of water column mean velocity, bedform geometry, and vertical pressure gradients deeper in the sediments. The IEZ forms when the Reynolds number exceeds a critical value.

Our simulations show that the IEZ spatial extent (depth and area) is diminished by ambient groundwater discharge (AGD), for both gaining and losing conditions,

compared to the case where the water column is under ‘neutral’ conditions. In both conditions, the IEZ spatial extent increases with Re . As Re increases, the IEZ depth, area and shape become asymptotic to the neutral conditions without AGD. The relationship of IEZ depth and area to Re are described by Morgan-Mercer-Flodin functional models. Under gaining conditions, the IEZ is centered around the bottom-pressure maximum, which is located on the stoss face of dunes, near where the eddy in the water column reattaches. The deep groundwater discharges near the bottom-pressure minimum which is located at the crest. Under losing conditions, the IEZ forms around the pressure minimum at the crest. Water infiltrating from the water column near the bottom-pressure maximum infiltrates deeper into the sediments and does not return to the SWI.

The flux through the IEZ is dependent on Re via power models. The mean residence time of water through the IEZ is large when Re is low and becomes smaller with increasing Re . The mean residence times for both gaining and losing cases are less than the corresponding mean residence times for the case without AGD, with the difference decreasing as Re gets larger.

Our study based on high-fidelity multiphysics numerical models shows that current-bedform driven exchange interacts and competes with ambient groundwater discharge to control physical processes occurring along sediment-water interfaces. The understanding of these physical processes opens pathways towards an integrated physical-biological-chemical perspective of sediment-water interfaces with bedforms.

References

- Aller, R. C., The effects of macrobenthos on chemical properties of marine sediment and overlying water, in McCall, P. L. and M. J. S., Tevesz, *Animal-Sediment Relations*, Plenum Press, NY, 53-96, 1982.
- Burnett, W. C., H. Bokuniewicz, M. Huettel, W. S. Moore, and M. Taniguchi, Groundwater and pore water inputs to the coastal zone, *Biogeochemistry*, 66, 3-33, 2003.
- Cardenas, M. B., and J. L. Wilson, Hydrodynamics of coupled flow above and below a sediment-water interface with triangular bed forms: underflow case, submitted to *Adv. Water Resour.*, 2006a.
- Cardenas, M. B., and J. L. Wilson, Hydrodynamics of coupled flow above and below a sediment-water interface with triangular bed forms and ambient groundwater discharge, *J. Hydrol.*, in press.
- Cardenas, M. B., and J. L. Wilson, Dunes, turbulent eddies, and interfacial exchange with porous media, submitted to *J. Geophys. Res.*, 2006c.
- Elliott, A. H., and N. H. Brooks, Transfer of nonsorbing solutes to a streambed with bed forms: Theory, *Water Resour. Res.*, 33(1), 123-136, 1997.
- Fehlman, H. M., Resistance components and velocity distributions of open channel flows over bedforms, M. S. Thesis, Colo. State Univ., Fort Collins, CO, 1985.
- Harvey, J. W, and C. W. Fuller, Effect of enhanced manganese oxidation in the hyporheic zone on basin-scale geochemical mass balance, *Water Resour. Res.*, 34(4), 623-636, 1998.
- Huettel, M., and G. Gust, Impact of bioroughness on interfacial solute exchange in permeable sediments, *Mar. Ecol. Prog. Ser.*, 89, 253-267, 1992.
- Huettel, M., W. Ziebis, S. Forster, and G. W. Luther III, Advective transport affecting metal and nutrient distributions and interfacial fluxes in permeable sediments, *Geochim. Cosmochim. Acta*, 62(4), 613-631.
- Huettel, M., H. Roy, E. Precht, and S. Ehrenhauss, Hydrodynamical impact of biogeochemical processes in aquatic sediments, *Hydrobiologia*, 494, 231-236, 2003.
- Jones. J. B., and P. J. Mulholland, *Streams and Ground Waters*, Academic Press, San Diego, 2000.
- Moore, W. S., Large groundwater inputs to coastal waters revealed by ^{226}Ra enrichments,

- Nature*, 380, 612-614, 1996.
- Moore, W. S., and T. J. Shaw, Chemical signals from submarine fluid advection onto the continental shelf, *J. Geophys. Res.*, 103(C10), 21,543-21,552, 1998.
- Morgan, P. H., L. P. Mercer, N. W. Flodin, General model for nutritional responses of higher order mechanisms, *Proc. Nat. Acad. Sci. USA*, 72(11), 4327-4331, 1975.
- Ren, J., and A. I. Packman, Coupled stream-subsurface exchange of colloidal hematite and dissolved zinc, copper, and phosphate, *Environ. Sci. Technol.*, 39, 6387-6394, 2005.
- Riedl, R. J., N. Huang, and R. Machan, The subtidal pump: A mechanism of interstitial water exchange by wave action, *Mar. Biol.*, 13, 210-221, 1972.
- Shum, K. T., The effects of wave-induced pore water circulation on the transport of reactive solutes below a rippled water-sediment interface, *J. Geophys. Res.*, 98C, 10289-10301, 1993.
- Simmons, G. M., Jr., Importance of submarine groundwater discharge (SGWD) and seawater cycling to material flux across sediment/ water interfaces in marine environments, *Mar. Ecol. Prog. Ser.*, 84, 173-184, 1992.
- Thibodeaux, L. J., and J. D. Boyle, Bedform-generated convective-transport in bottom sediments, *Nature*, 325, 341-343, 1987.
- Webster, I. T., S. J. Norquay, F. C. Ross, and R. A. Wooding, Solute exchange by convection within estuarine sediments, *Estuar. Coast. Shelf Sci.*, 42, 171-183, 1996.
- Wilcox, D. C., A half century historical review of the k- ω model, *AIAA Paper* 91-0615, 1991.
- Winter, T. C., J. W. Harvey, O. L. Franke, and W. M. Alley, *Ground Water and Surface Water: A Single Resource*, USGS Circ 1139, Denver, CO, 1998.

CHAPTER 7

THE EFFECTS OF CURRENT-BEDFORM INDUCED FLUID FLOW ON THE THERMAL REGIME OF SEDIMENTS

7.1. Introduction

Permeable sediments are hosts to ecological and biogeochemical reactions in fluvial [*Stanford and Ward, 1988; Boulton et al., 1998; Hancock et al., 2005*], lacustrine, estuarine [*Webster et al., 1996*] and marine settings [*Huettel et al., 1998; Burnett et al., 2003*]. The physical processes, and ecological and biogeochemical reactions occurring in sediments and the overlying water column are often sensitive to temperature [*Ward, 1985; Westrich and Berner, 1988; Constantz et al., 1994; Allen, 1995; Evans et al., 1998; Johnson, 2004*]. Heat is transported through sediments via conduction, mechanical dispersion and advection by fluid flow. Fluid flow through sediments is driven by hydraulic head gradients over different scales. Locally, these head gradients are set up by the interactions of currents in the water column with bed topography such as dunes [e.g., *Thibodeaux and Boyle, 1987; Elliott and Brooks, 1997; Cardenas and Wilson, 2006a*]. The groundwater advection of heat has been used to trace flow and to characterize aquifer hydraulic properties from meter to kilometer scales [*Anderson, 2005*]. Temperature measurements are now typically used for quantifying groundwater discharge or recharge between rivers and alluvial aquifers [*Stonestrom and Constantz,*

2003; *Conant*, 2004], lakes and lake sediments [*Andrews and Anderson*, 1979; *Lee*, 1985], and oceans and coastal sediments [*Moore et al.*, 2002, *Taniguchi et al.*, 2003]. It is common to assume that groundwater flow within the sediments is vertically one-dimensional. This assumption is violated when the sediment-water interface (SWI) is not flat. Bedforms, such as ripples or dunes, or other obstacles result in pressure head variations at the SWI that cause two- and three-dimensional circulation of water within the sediments. Moreover, the spatial variability in the hydraulic properties within the sediments also influences groundwater flow [e.g., *Cardenas et al.*, 2004] and with it heat advection. Examples of spatially and temporally variable streambed temperatures are presented in *White* [1993], *Evans and Petts* [1997], *Clark et al.* [1999], and *Conant* [2004]. *Evans and Petts* [1997] suggested that temperatures measured at the heads of riffles in streams were closer to the river temperature while the temperatures at the tails of riffles near pools were more typical of groundwater. This configuration was explained as due to the downwelling of river water at the heads of riffles and upwelling of groundwater at the tails. This flow configuration is typical in pool-riffle sequences. Such areas within sediments that receive water from and transmit water back to the SWI are typically referred to as “hyporheic zones”. In this paper, we use the general term “interfacial exchange zone” (IEZ) to include similar lacustrine, estuarine and marine counterparts.

To our knowledge, excluding the field-based study by *Evans and Petts* [1997], the impacts of current-topography-induced flow on the thermal regime of sediments has not been studied in detail. Current-topography-induced flow also interacts with ambient groundwater discharge (AGD), such as in coastal areas subjected to submarine

groundwater discharge and in gaining and losing lakes and rivers, resulting in a more complicated hydrodynamic scenario [Cardenas and Wilson, 2006b]. Our goal is to investigate the thermal regime of sediments within and below dunes through coupled numerical simulation of turbulent flow in the water column and Darcy flow and heat transport in the sediments. Cases where the water column is neutral (neither gaining nor losing), and gaining and losing net water are considered.

7.2. Methodology

We achieve our goal through virtual experiments with numerical simulations. Details of the methodology for fluid flow simulation are described in *Cardenas and Wilson* [2006a], and here are presented schematically in Figure 7.1. Briefly, mean unidirectional turbulent flow in the water column over subaqueous two-dimensional dunes is simulated by solving the Reynolds-averaged Navier-Stokes (RANS) equations with the $k-\omega$ closure scheme. The RANS-derived pressure along the SWI, which is considered a no-slip wall for the water column, is prescribed as a Dirichlet boundary for the groundwater flow domain resulting in sequential coupling of flow in the water column and in the underlying sediments. The bottom boundary for the sediments is prescribed a basal flux, q_{bas} (see Figure 7.1) representing ambient groundwater discharge, where the flux may be zero (no-flow), upwards or downwards. Lateral boundaries are considered spatially periodic with the same prescribed pressure drop for both the water column and the sediments. The pressure drop, dP , results in mean flow from left to right of the domain. The RANS derived solution for the water column is shown in *Cardenas and Wilson* [2006a].

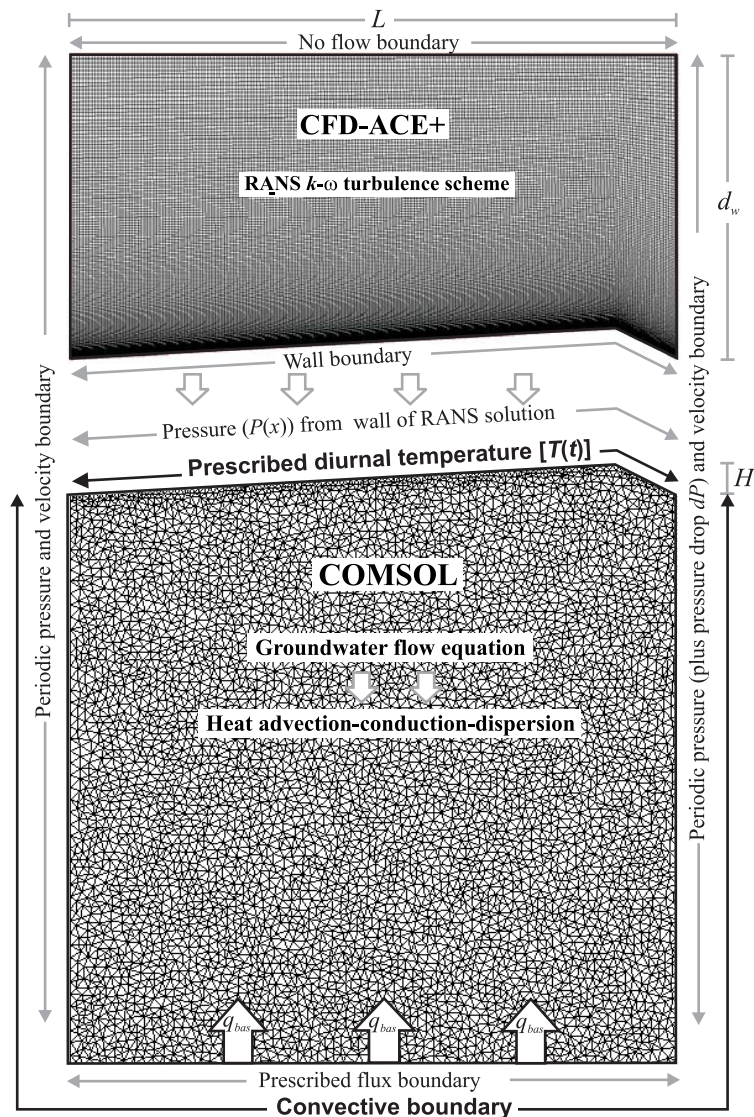


Figure 7.1. Numerical modeling formulation and sample grids. The gray lines bounding the domains illustrate boundary conditions for the fluid flow (turbulent and Darcy) models while the black lines and bold labels represent boundaries for the heat transport model. q_{bas} , the prescribed basal flux represented by arrows at the bottom of the sediment domain suggesting upward flux, is zero and downwards in some simulations. The governing equations are usually solved sequentially in the following order: 1) RANS- $k-\omega$, 2) groundwater flow equation, and 3) heat advection-conduction-dispersion. $L=1.0$ m, $H=0.05$ m, $d_{wat}=0.5$ m and the crest is at $0.9L$ in all simulations.

The groundwater flow equations (7.1, 7.2) and heat advection-conduction-dispersion equation are solved to yield fluid pressures, velocities, and temperatures in the sediments:

$$\frac{\partial q_i}{\partial x_i} = 0 \quad (7.1)$$

$$q_i = -\frac{k_p}{\mu} \frac{\partial P}{\partial x_i} \quad (7.2)$$

$$\frac{\partial T}{\partial t} = \frac{\partial}{\partial x_i} \left(D_{ij}^* \frac{\partial C}{\partial x_i} \right) - \frac{u_i}{\rho c} \frac{\partial T}{\partial x_i} \quad (7.3)$$

where q_i is the specific discharge (i.e. Darcy flux), k_p is intrinsic permeability, P is pressure, μ is fluid viscosity, T is temperature, D_{ij}^* is effective thermal diffusivity, u_i is the pore velocity (q_i/ϕ , ϕ =porosity), ρ and c are the effective density and effective specific heat capacity of the saturated sediments, respectively. Index $i, j=1, 2$. The effective or bulk density of the sediment-water composite is computed based on a weighted average:

$$\rho = \phi \rho_w + (1-\phi) \rho_s \quad (7.4)$$

where ρ_w is the density of water (1000 kg/m³) and ρ_s is the density of the sediment grains (2650 kg/m³). The effective heat capacity of the composite is similarly computed from:

$$C = \phi C_w + (1 - \phi) C_s \quad (7.5)$$

where the volumetric heat capacity of water, C_w , is $4.2 \times 10^6 \text{ J/m}^3 \cdot ^\circ\text{C}$ and the volumetric heat capacity of the sand grains, C_s , is $1.9 \times 10^6 \text{ J/m}^3 \cdot ^\circ\text{C}$. The effective specific heat capacity in equation (7.3) is $c = C/\rho$. D^* has thermal conduction and thermomechanical dispersion components:

$$D^*_{ij} = \left(\frac{K_T}{\rho c} + D^m_{ij} \right) \quad (7.6)$$

where K_T is effective thermal conductivity. D^m , the mechanical dispersion coefficient, is defined following *Bear* [1972]:

$$D^m_{ij} = \alpha_T U \delta_{ij} + (\alpha_L - \alpha_T) u_i u_j / U \quad (7.7)$$

where α_T and α_L are transverse and longitudinal dispersivities, U is the pore velocity magnitude, and δ_{ij} is the Dirac delta function. Mechanical dispersion of heat energy, assumed equivalent to solute dispersion [*de Marsily*, 1986], is often neglected in porous media due to large values of K_T . We account for it. α_L is set to 1 cm, equivalent to several grain diameters, which is typical for the scale of our experiments [e.g., *de Marsily*, 1986; *Schulze-Makuch*, 2005], and α_T is considered to be 1/10 of α_L . Unless otherwise stated, the hydraulic and thermal properties of the sediments are those presented in Table 7.1 and are typical of unconsolidated saturated medium sand to gravel.

Table 7.1. Parameters used in the simulations

Parameters	Symbol	Value/ Range	Units
intrinsic permeability	k_p	10^{-10} - 10^{-9}	m^2
viscosity of water ¹	μ	0.001	Pa-s
porosity	n	0.3	-
effective thermal conductivity ²	K_T	1.8	W/m-°C
effective density	ρ	2155	Kg/m ³
effective heat capacity	c	1200	J/Kg-°C
longitudinal dispersivity	α_L	0.01	m
water column depth	d_w	0.5	m
bedform height	H	0.05	m
bedform length	L	1.0	m

¹Described by equation (7.13) in some simulations

²Value from midpoint of range presented in *Niswonger and Prudic* [2003] for saturated sediments

For the thermal energy balance (7.3), the top of the sediments (the SWI) is a Dirichlet boundary with temperature varying through time but not in space, i.e., the water column is well-mixed. The transient temperature follows a model representing a prescribed diurnal cycle of temperature in the water column:

$$T(t) = T_{ave} + T_{amp}[(\sin(2\pi\tau/t))] \quad (7.8)$$

where T is the temperature, T_{ave} is the average temperature about which the temperature fluctuates, T_{amp} is the amplitude of the temperature fluctuations, τ is the period of the fluctuations, and t is time. $\tau=24$ hours in all simulations (Figure 7.2).

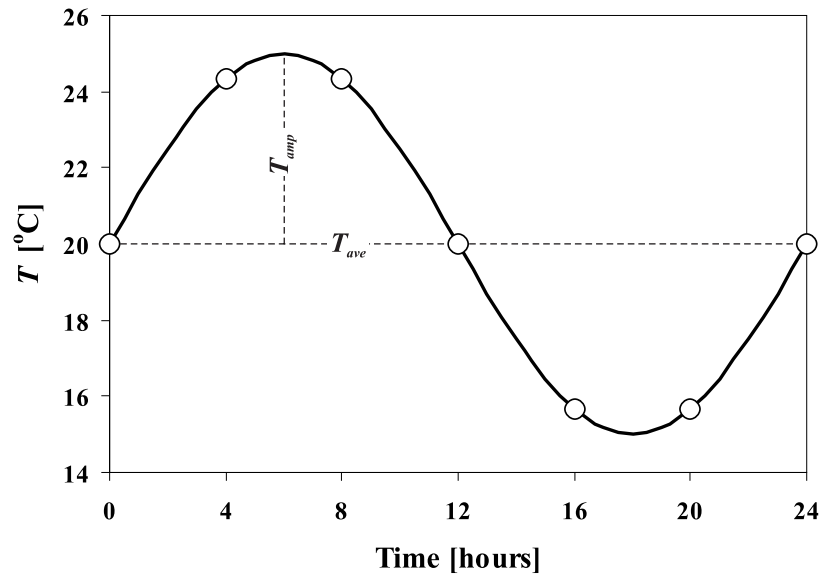


Figure 7.2. Typical prescribed temperature, $T(t)$, as described by equation (7.8), used as a Dirichlet top boundary for the sediment domain and representing the sediment-water interface. The timing is similar for all simulations, i.e., no phase shift, but the temperature amplitude (T_{amp}) and average (T_{ave}) vary in some simulations. The circles correspond to the timing of the simulation results presented in Figures 7.3, 7.7, and 7.8.

The initial temperature is considered equal to T_{ave} :

$$T(t=0)=T_{ave} \text{ for all } x, y \quad (7.9)$$

The bottom boundary for (3) is a convective or zero-gradient boundary described by:

$$\frac{\partial T}{\partial n} = 0 \quad (7.10)$$

where n is the direction normal to the boundary. The zero-gradient boundary is typically assumed for shallow sediments underlying water bodies [e.g., *Hondzo and Stefan*, 1994; *Fang and Stefan*, 1998; and *Ronan et al.*, 1998] although other studies, including some at the regional scale, assume a constant temperature at the bottom boundary [e.g., *Silliman et al.*, 1995; *Constantz et al.*, 2002; *Becker et al.*, 2004; and *Goto et al.*, 2005]. An alternative is to prescribe a total heat flux at the bottom boundary. Implementing a heat flux boundary at the bottom boundary based on representative continental heat flux values, when the water column is neither gaining nor losing net water, did not result in noticeable differences in the thermal regime compared to a zero-gradient boundary (7.10). When there is ambient downward or upward groundwater flow through the bottom boundary, the advective heat flux is many times larger than a typical continental heat flux value (30 mW/m^2). Therefore, we ignore the effects of regional heat flux in all simulations. The sides are spatially periodic boundaries. Heat transport simulations are run for 5 days allowing for several days of “spin-up”; results analyzed and presented correspond to the last diurnal cycle.

The RANS equations are numerically solved using the finite-volume approach as implemented in the commercial code CFD-ACE+. The groundwater flow and heat transport equations are solved using the finite-element method implemented in the commercial code COMSOL Multiphysics. Lagrange-Quadratic triangular elements are used in COMSOL Multiphysics with node spacing less than 2 cm. The governing equations are sequentially solved in the following order: 1) RANS- $k-\omega$, 2) groundwater flow equation, 3) heat transport equation. In all simulations, the bedform length $L=1.0$ m, the bedform height $H=0.05$ m, the depth of the sediments below the trough is >1.5 m, and

the water column depth along the trough $d_w=0.5$ m. The Reynolds number (Re) in the water column, following the definition in *Cardenas and Wilson* [2006a], is 10,395 and corresponds to an average horizontal velocity above the crest of 20.8 cm/s. Except for permeability k_p and basal flux q_{bas} , everything is the same for all simulations (boundaries and thermal and fluid properties) including $T_{ave}=20^\circ\text{C}$ and $T_{amp}=5^\circ\text{C}$. In the case where we investigate viscosity effects (i.e., § 7.3.2.), the groundwater flow and heat transport equations are solved simultaneously and we explore sensitivity to mean and amplitude of the temperature fluctuations. Except for this fully coupled case, the models (7.1)-(7.3) are linear.

7.3. Results

7.3.1. The impact of dunes and comparison to pure conduction case

Heat transport considering current-bedform driven flow may significantly differ from the case where only heat conduction is considered. For cases where the water column is neither gaining nor losing net water, one would typically assume, since there is presumably no movement of water across the sediment-water interface, that heat transport is dominated by or is exclusively through conduction. Figure 7.3, which shows the temperature distribution at 6 different times (timing shown in Figure 7.2), illustrates the differences between cases where current-bedform driven flow is considered and where it is not. In addition to time-snapshots, comparisons of temperature variation through time and space between different cases are facilitated through definition of a dimensionless temperature amplitude:

$$T^*(x, y) = \frac{T_{max} - T_{min}}{2T_{amp}} \quad (7.11)$$

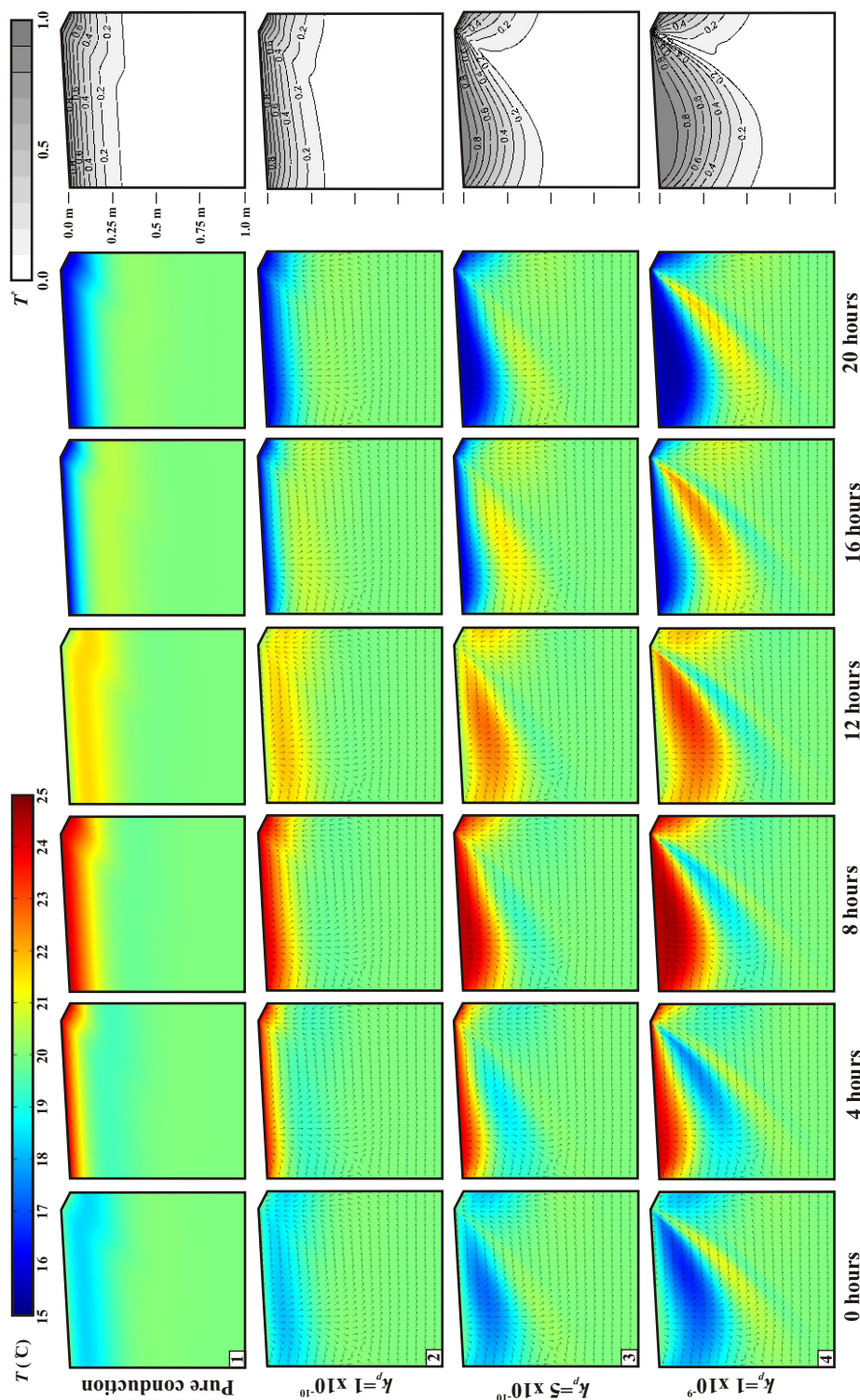


Figure 7.3. Temperature fields through time for cases where the water column is neither gaining nor losing net water, i.e., the bottom boundary is a no-flow boundary and $q_{bas}=0$. Results are shown for simulations with different permeability values (second to fourth rows) as well as a reference simulation where fluid advection due to current-bedform effects is ignored (the pure conduction case). The rightmost column shows plots of normalized temperature amplitude, T^* , described by equation (7.11). Small arrows indicate flow directions and not magnitude.

where T_{max} and T_{min} are the temperature maximum and minimum, respectively, observed at a given point within the sediments across a 24-hour period. A point with $T^*=1$ means that the entire diurnal temperature range is observed at that given point, e.g., points along the Dirichlet boundary. Consequently, a point with $T^*\sim 0$ is not sensitive to the diurnal temperature fluctuations at the SWI.

The importance of current-bedform driven flow depends on the magnitude of the flow. Figure 7.3 presents $T(x, y, t)$ and $T^*(x, y)$ for four simulations. The topmost row illustrates the pure conduction case where fluid flow is ignored (or essentially permeability $k_p=0$) while the results in the lower rows correspond to increasing k_p . When k_p is low (or when Re is low thereby resulting in smaller pressure gradients along the SWI which is linearly related to the flow velocities by Darcy's Law; see *Cardenas and Wilson* [2006a]), conduction dominates- i.e., the Peclet numbers (Pe) for heat transport decrease. The pure conduction case and the low k_p case expectedly look similar when Pe is small. As k_p (or Re) increases, advection dominates (i.e., Pe is larger) and a larger area of the sediments experiences diurnal temperature fluctuations (Figure 7.3). As expected the temperature fluctuations become damped downstream along a flow path (Figure 7.3, T^* plots). Depths of penetration of temperature fluctuations increase with the period of the fluctuations (not shown), τ , and T^* is not sensitive to the magnitude of fluctuations, T_{amp} , because the model is linear [e.g., *Carslaw and Jaeger*, 1959; *Goto et al.*, 2005]. There are, therefore, no differences in T^* distribution between the cases of $T_{amp}=7^\circ\text{C}$ and $T_{amp}=1.5^\circ\text{C}$ for the pure conduction and two other k_p scenarios (Figure 7.4). There is no reason for us to consider longer than diurnal fluctuations as the next larger time scale to

consider would be seasonal which is irrelevant for the spatial scale considered here. Seasonal temperature changes may be pertinent for much larger dunes ($L \sim 100$'s of meters) such as submarine dunes in the continental shelf or perhaps in eolian systems.

Figures 7.3 and 7.4 both show that when current-bedform advection is important, T^* can be quite heterogeneous within a small area underneath the bedform. A larger portion of the fluctuation is observed near the in-flow point of water at the stoss side of the dune, while a small area just below the crest where water is returning to the SWI is secluded from the diurnal fluctuations. This pattern is consistent with temperature observations by *Evans and Petts* [1997] within riffles where stream temperature fluctuations appeared to be propagated along interpreted flow paths within the riffle. Large fluctuations were observed in downwelling areas near the head of the riffle while

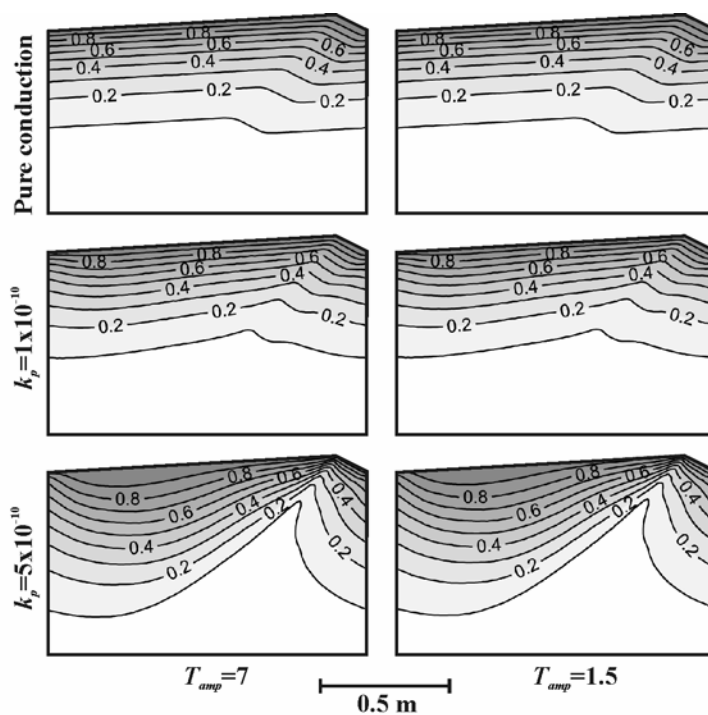


Figure 7.4. T^* , normalized temperature amplitude variation (7.11), plots for cases with varying permeability k_p and boundary amplitude T_{amp} .

hardly any fluctuations were observed underneath the downstream pool (see Figures 2 and 3 of *Evans and Petts* [1997]).

7.3.2. Effect of temperature-dependent viscosity on interfacial flux and effect of dispersion on temperature distribution

The viscosity and density of water is sensitive to temperature thereby affecting the hydraulic conductivity of porous media [*Bear*, 1972] via:

$$K = \frac{k_p \rho_w(T) g}{\mu(T)} \quad (7.12)$$

where K is the hydraulic conductivity and g is the gravitational acceleration constant. Under typical atmospheric conditions, the effects of temperature on ρ_w is negligible and we ignore this in our analysis. However, this is not the case for viscosity. The change in K with temperature, due to changes in μ , results in variation in infiltration from reservoirs with periodically varying temperature [*Jaynes*, 1990; *Constantz*, 1998]. We investigated the effects of temperature-dependent viscosity on fluxes through the interfacial exchange zone by simultaneously solving equations (7.1)-(7.3) while ignoring mechanical dispersion ($D^m_{ij}=0$). The viscosity dependence on temperature can be described by the polynomial function:

$$\mu(T) = a - bT + cT^2 - dT^3 + eT^4 \quad (7.13)$$

which was fitted through the data in *Schmidt* [1979] in the range $T=0^\circ\text{C}$ to 50°C and

where μ is in Pa-s and T is in $^{\circ}\text{C}$ (Figure 7.5a). $a=0.00179$, $b=5.94245 \times 10^{-5}$, $c=1.2863336 \times 10^{-6}$, $d=1.6239483 \times 10^{-8}$, and $e=8.6656672 \times 10^{-11}$ in equation (7.13). Three simulations corresponding to three scenarios were conducted. The first or “cold” scenario, with $T_{ave}=6^{\circ}\text{C}$ and $T_{amp}=5^{\circ}\text{C}$, represents a small exposed stream in cold climates or alpine areas (e.g., Constantz [1998], Cozetto *et al.* [2006]) while the second “warm” scenario, with $T_{ave}=15^{\circ}\text{C}$ and $T_{amp}=3^{\circ}\text{C}$, is for a small stream in a temperate climate

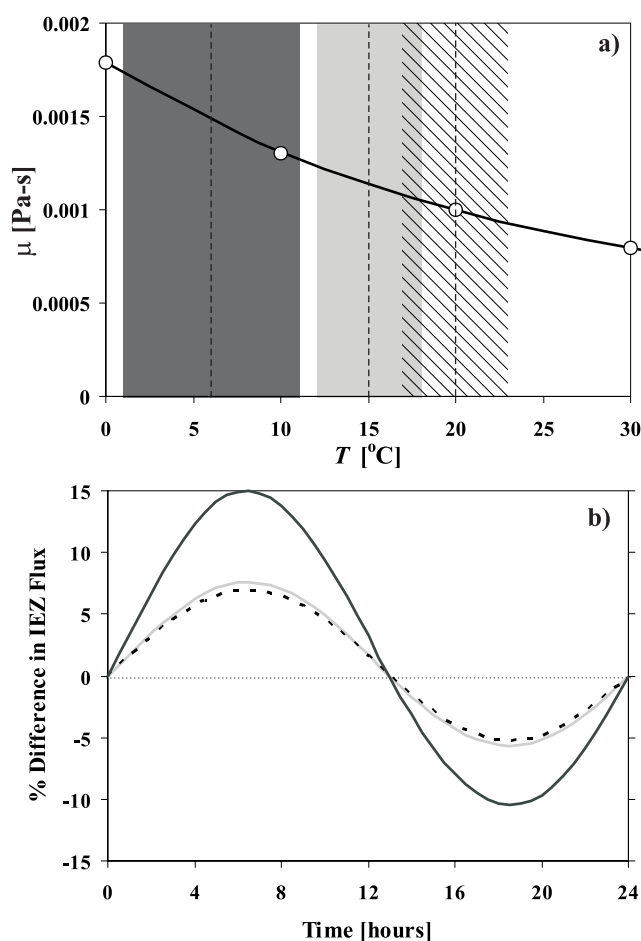


Figure 7.5. Fitted polynomial function, equation (7.13), to define the viscosity-temperature relationship used in simulations for testing sensitivity of flux through the interfacial exchange zone to viscosity (a). The shaded and hatched areas indicate the ranges in temperature, and the dashed line indicates the average temperature, used in the sensitivity simulations. Relative change in interfacial exchange zone flux through a diurnal period for three scenarios (b) whose temperature range correspond to the similarly colored temperature regions in (a); the dashed line corresponds to the hatched region (a).

during autumn (see *Ward* [1985] for examples). The third scenario, with $T_{ave}=20^{\circ}\text{C}$ and $T_{amp}=3^{\circ}\text{C}$, is conducted to isolate and investigate the impacts of T_{ave} as the T_{amp} is similar to the “warm” scenario but T_{ave} is higher. The flux through the IEZ is calculated following *Cardenas and Wilson* [2006a]. Fluxes across a diurnal cycle are calculated and normalized versus the flux for isothermal conditions. Figure 7.5b shows the relative change in flux through time which is the % difference between the IEZ flux at a given time with respect to IEZ flux for constant viscosity ($\mu(T_{ave})$).

IEZ fluxes are very sensitive to temperature when the stream temperature is low and the fluctuations are relatively large (Figure 7.5b). Sensitivity decreases as temperature increases even if the fluctuations are the same (Figure 7.5b). This behavior is entirely driven by the temperature dependence of K and μ (7.12, 7.13). Naturally, flux is higher when temperature is higher and vice versa. Since $\mu(T)$ is non-linear, with increasing slope at lower temperatures and a flattening at higher temperatures, the maximum increase in flux for the “cold” scenario occurs during its the warm phase and is larger than the decrease experienced during its cool phase. This asymmetry is less pronounced for the “warm” scenario, as the temperature dependence of μ is changing less drastically for the higher temperature range.

Our results further emphasize *Constantz'* [1998] suggestion that seepage flux measurements from streams may be biased as most measurements are conducted during the day when it is warmer. Although the bias may be small (up to ~15% in the case of small cold streams), these overestimated values may translate to substantial errors when used in calculation of regional-scale water budgets.

Plots of dimensionless amplitude T^* for cases with and without viscosity effects do not show a measurable difference (compare Figure 7.6a and 7.6b). Comparison of similar plots for the “cold” and “warm” scenarios also does not show any differences (not shown). The T^* plots suggests that the integrated variation in temperature is little affected by viscosity. Viscosity is therefore held constant in other simulations.

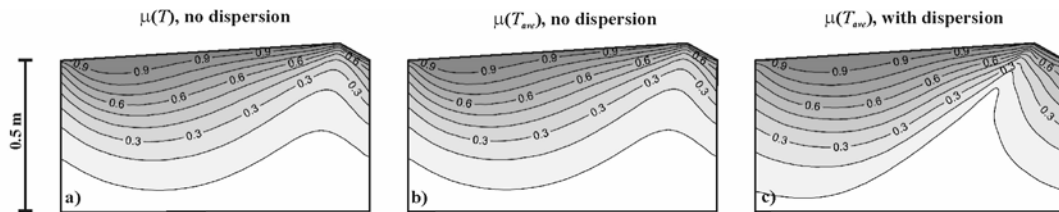


Figure 7.6. T^* , normalized temperature amplitude variation (7.11), plots for cases considering viscosity effects but ignoring mechanical dispersion (a), ignoring both viscosity effects and mechanical dispersion (b), and ignoring viscosity effects while considering mechanical dispersion (c). $k_p=5 \times 10^{-10} \text{ m}^2$, $T_{ave}=20^\circ\text{C}$, and $T_{amp}=3^\circ\text{C}$ for all cases.

Mechanical dispersion, on the other hand, has a measurable impact on the transport of heat. Figure 7.6b is based on a case with neither viscosity nor dispersion are considered. Figure 7.6c, which considers dispersion, illustrates the effects of an anisotropic dispersion tensor, where longitudinal dispersion is larger than transverse dispersion. Flow is focused and accelerates towards the crest near the upwelling region. This results in preferential dispersion of heat in the longitudinal direction towards the crest resulting, in limited transport in the transverse direction. Dispersion is considered in all simulations except in the cases above where temperature dependent viscosity is assumed.

7.3.3. Gaining and losing conditions

We investigated the impacts of losing and gaining conditions on the thermal regime of sediments by imposing various values for q_{bas} . A discussion of the hydrodynamics under ambient groundwater discharge can be found in *Cardenas and Wilson* [2006b] where the prescribed basal flux was expressed in dimensionless form as:

$$q_{bas}^* = q_{bas}/K \quad (7.14)$$

We apply the same nondimensionalization here to facilitate cross-comparison with the previous hydrodynamic study.

The transfer the diurnal temperature signal from the water column into the sediment is modulated by the ambient groundwater discharge. When it is losing net water, $q_{bas} < 0$, and simultaneously experiencing the effects of current-bedform induced flow, there is a complex temperature pattern through time and space (Figure 7.7). When q_{bas} is small enough, the effects of the downward ambient discharge is negligible and the temperature distribution is similar to the neutral case (compare Figure 7.3 row 3 to Figure 7.7 row 1; k_p in Figure 7.3 row 3 is the same as that in Figures 7.6 and 7.7). As the q_{bas} increases (Figure 7.7, row 2), the penetration of the temperature fluctuations increases while forming a narrow but vertically extensive channel beneath the crest where temperature fluctuations are minimal. The effects of current-bedform interaction induced advection are still evident even when q_{bas} is large (Figure 7.6, row 3) but still allows some of the infiltrating water to return to the SWI near the crest. The effect of interfacial

Figure 7.7 (following page). Temperature fields through time for ambient groundwater discharge where the water column is losing net water, i.e., the bottom boundary is prescribed a normal downward flux, q_{bas}^* (7.13). Results are shown for simulations with different basal flux values (first to third rows). The rightmost column shows plots of normalized temperature amplitude, T^* (7.11). The two bottom rows have similar q_{bas}^* . Like the rows above, the third row considers current-bedform effects (i.e., the pressure at the top is taken from the turbulent flow model) while the bottom row is based on a top boundary with a uniform pressure distribution. $k_p=5 \times 10^{-10} \text{ m}^2$ in all simulations. Small arrows indicate flow

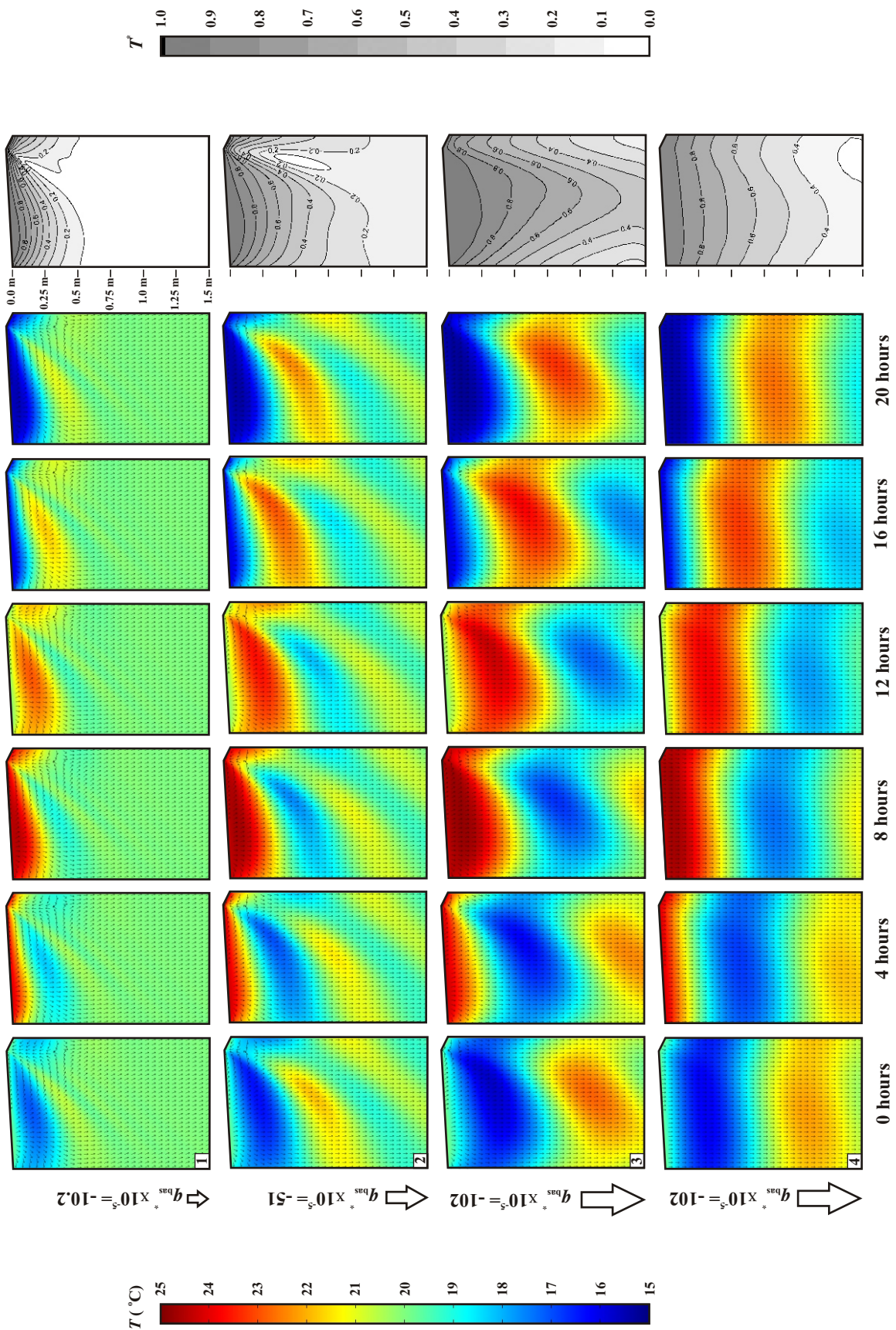
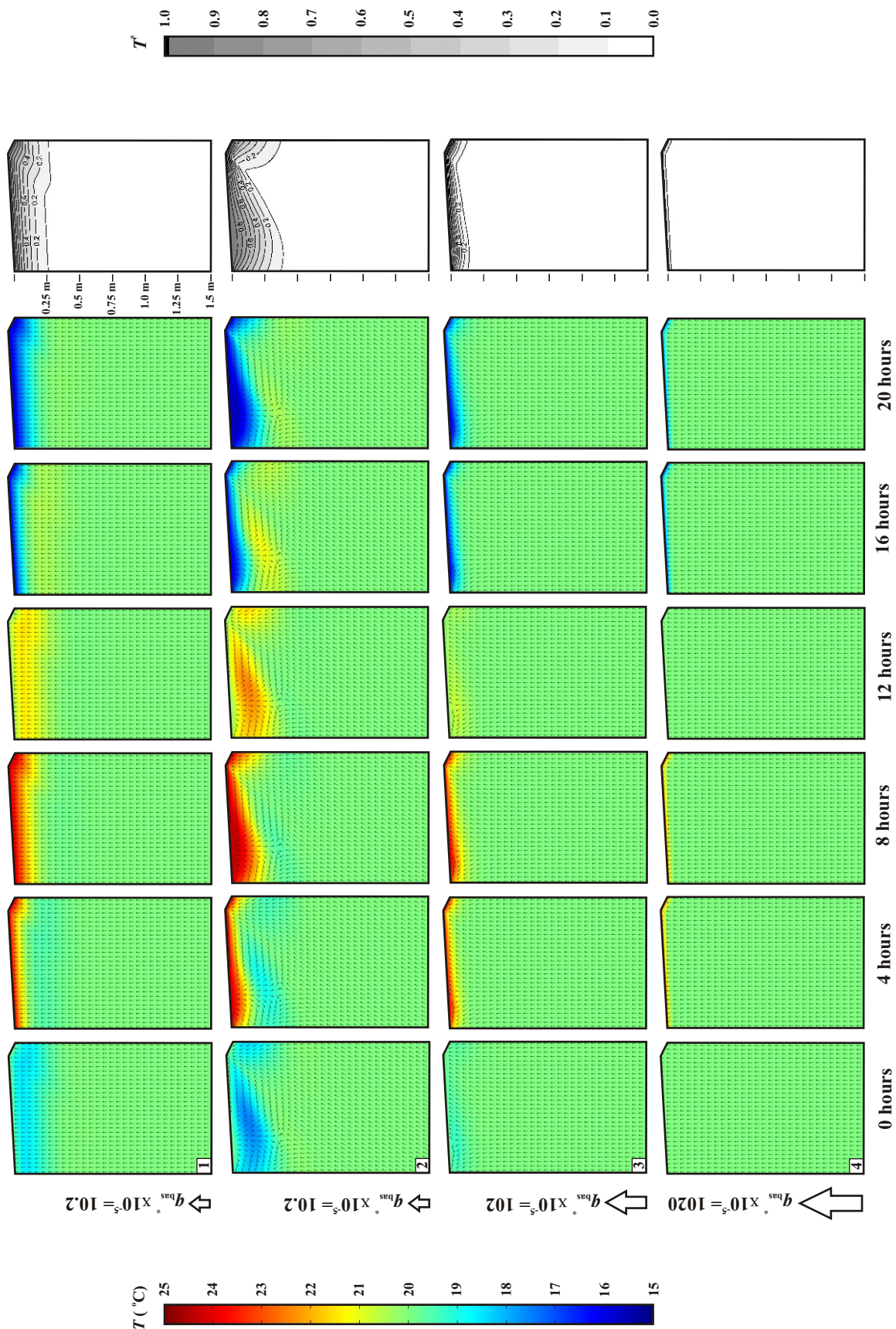


Figure 7.8 (following page). Temperature fields through time for ambient groundwater discharge where the water column is gaining net water, i.e., the bottom boundary is prescribed a normal upward flux, q_{bas}^* (7.13). Results are shown for simulations with different basal flux values. The rightmost column shows plots of normalized temperature amplitude, T^* (7.11). The top two rows have similar q_{bas}^* . The second row (and rows below) considers current-bedform effects (i.e., the pressure at the top is taken from the turbulent flow model) while the top row is based on a top boundary with a uniform pressure distribution. $k_p=5 \times 10^{-10} \text{ m}^2$ in all simulations. Small arrows indicate flow directions and not magnitude.



exchange on the thermal regime at high q_{bas} is illustrated by comparing rows 3 and 4 of Figure 7.7. The bottom row corresponds to the case where the SWI boundary is a constant-in-space pressure boundary as opposed to the spatially-variable pressure imposed in the cases above it (row 3), where the pressure is taken from the turbulent flow model. Ultimately, at high q_{bas} the fluid flow and heat transport through the sediments becomes essentially vertically one-dimensional.

The effects of an upward ambient groundwater discharge under gaining water column conditions are somewhat less complicated compared to the losing case (Figure 7.8). A relatively small magnitude of imposed basal flux ($q_{bas}^*=10.2$) results in an observable difference in the temperature variation for the gaining case when compared to the neutral case (compare Figure 7.3 row 3 to Figure 7.8 row 2). Further increases in q_{bas} collapses the IEZ [Cardenas and Wilson, 2006b] resulting in practically no transmission of the temperature fluctuations from the water column to the sediments (Figure 7.8, rows 3 and 4).

7.4. Ecological and biogeochemical implications

Since temperature is a primary variable for many physical, chemical and biological processes occurring in streams, lakes, estuaries and oceans and in their bottom sediments [Ward, 1985; Allen, 1995; Evans *et al.*, 1998; Johnson, 2003], the ramifications of our simulation results on ecological and biogeochemical processes are briefly discussed here.

Closing the energy budgets in any of these environments is challenging [e.g., Evans *et al.*, 1998; Cozetto *et al.*, 2006]. Processes within the sediments contribute significant uncertainty to the energy budgets as the sediment hydraulic and thermal

properties vary in space and time resulting in complex and time-varying flow paths [e.g., *Poole and Berman, 2001*]. Our simulations offer a method of predicting the spatial distribution of flow and temperature in permeable sediments when the flow is due to current-bedform interaction.

Most studies of gaining or upwelling systems assume no interfacial exchange in sediments. These gaining systems are used as thermal refugia by some organisms and affect fish spawning [e.g., *Alexander and Caissie, 2003*]. Our results suggest that, depending on the relative magnitude of current-bedform induced interfacial exchange and the ambient groundwater discharge, there may be interfacial flow-driven advection of heat through sediments in gaining, as well as losing systems (Figure 7.8). Therefore, fish may preferentially spawn in certain areas of a dune depending on which thermal regime is favorable for survival.

Biogeochemical processes occurring in permeable sediments that affect both the water column and porewater chemistry can be temperature sensitive [*Westrich and Berner, 1998; Nimick et al., 2003*]. Biogeochemical cycles are typically strongly correlated to diel cycles in temperature. For example, *Kaplan and Bott [1989]* showed through experiments that activity of bacteria attached to sediments is more sensitive to changes in temperature than to changes in water chemistry. Sensitivity to temperature can be attributed to myriad factors and correlation to temperature is not necessarily indicative of a causal relationship. However, in certain instances, diel fluctuations in trace metal concentrations in streams have been postulated to be primarily driven by temperature-sensitive sorption/ desorption processes occurring in sediments [*Nimick et al., 2003*]. The magnitude of the variation in sorption/desorption effects in stream and groundwater

chemistry is directly controlled by the volume of sediments undergoing temperature shifts. Our simulations provide an approach of determining both the volume of the sediments subjected to the temperature shifts as well as the magnitude of the temperature fluctuations.

Brick and Moore [1996] suggested that diel trace metal cycles in streams may be the result of variations in influx of groundwater to a stream as a result of evapotranspiration. Another possible explanation for *Brick and Moore's* [1996] suggestion of differential influx variation due to evapotranspiration is found in § 7.3.2 where it is shown that, even without evapotranspiration or changes in head gradients due to fluctuations in river stage (e.g. *Constantz* [1998]), changes in viscosity result in significant increases and decreases in interfacial flux. Our simulations illustrate the extent to which diurnal warming and cooling of surface water affects the sediments, for neutral, gaining and losing conditions, and provide a physical basis for chemical phenomenon observed previously.

7.5. Summary

Many ecological and biogeochemical reactions in coupled water column and sediment systems bodies are temperature sensitive. However, the dynamics of thermal energy in permeable sediments with dune topography underlying moving waters has not been investigated. We conducted coupled numerical simulations in order to illustrate the hydrodynamical and thermal processes occurring in these permeable sediments. Turbulent flow over dunes is simulated by solving the Reynolds-averaged Navier-Stokes (RANS) equations. The RANS-derived pressure solution along the sediment-water interface (SWI) is imposed as a Dirichlet boundary for the Darcy flow model of the

sediments. Heat advection, conduction, and dispersion through the sediments are simulated based on the Darcy flow solution. The overlying water column is assumed thermally well-mixed and is represented by a spatially constant Dirichlet temperature boundary along the SWI in the sediment heat transport simulations. This temperature varies in time and in our simulations follows a sinusoidal diurnal pattern. Conditions representing neutral, gaining and losing conditions for the water column are presented. Gaining and losing conditions are considered by imposing ambient groundwater discharge (AGD) at the bottom boundary of the sediments.

Current-bedform interactions results in fluid circulation, i.e., interfacial exchange, within dunes. Our simulations show that two-dimensional current-bedform induced fluid flow results in a complicated but predictable transient temperature distribution within the sediments. When AGD is present, whether towards or away from the SWI, the influence of current-bedform induced advection becomes subdued until, at higher rates of AGD, fluid flow and heat transport becomes essentially vertically one-dimensional. Zones within the sediments experiencing strong diurnal temperature variations may be found horizontally adjacent to zones lacking any substantial temperature variations. These zones with weak temperature variations are found close to crests of dunes where pore water is upwelling from deeper areas of the sediments. Strong temperature variations are observed underneath areas where water is infiltrating into the sediments from the water column.

Temperature effects on viscosity, and therefore the hydraulic conductivity of the sediments, were also investigated. Simulations suggest that fluid flux through the

interfacial exchange zone may be substantially modified by viscosity changes due to varying temperature.

References

- Alexander, M. D., and D. Caissie, Variability and comparison of hyporheic water temperatures and seepage fluxes in a small Atlantic salmon stream, *Ground Water*, 41(1), 72-82, 2003.
- Allen, J. D., *Stream ecology: Structure and function of running waters*, Chapman and Hall, NY, 388 pp., 1995.
- Anderson, M. P., Heat as a ground water tracer, *Ground Water*, 43(6), 1-18, 2005.
- Andrews, C. B., and M. P. Anderson, Thermal alteration of groundwater caused by seepage from a cooling lake, *Water Resour. Res.*, 15(3), 595-602, 1979.
- Bear, J. C., *Dynamics of Fluids in Porous Media*, Dover Publications, Inc., New York, 1972.
- Becker, M. W., T. Georgian, H. Ambrose, J. Siniscalchi, and K. Fredrick, Estimating flow and flux of ground water discharge using water temperature and velocity, *J. Hydrol.*, 296, 221-233, 2004.
- Brick, C. M., and J. N. Moore, Diel variation of trace metals in the Upper Clark Fork Fiver, Montana, *Environ. Sci. Technol.*, 30, 1953-1960, 1996.
- Burnett, W. C., H. Bokuniewicz, M. Huettel, W. S. Moore, and M. Taniguchi, Groundwater and pore water inputs to the coastal zone, *Biogeochemistry*, 66, 3-33, 2003.
- Boulton, A. J., S. Findlay, P. Marmonier, E. H. Stanley, and H. M. Valett, The functional significance of the hyporheic zone in streams and rivers, *Annu. Rev. Ecol. Syst.*, 29, 59-81, 1998.
- Cardenas, M. B., J. L. Wilson, and V. A. Zlotnik, Impact of heterogeneity, bedforms, and channel curvature on hyporheic exchange, *Water Resour. Res.*, 40, W08307, doi:10.1029/2004WR003008, 2004.
- Cardenas, M. B., and J. L. Wilson, Dunes, turbulent eddies, and interfacial exchange, submitted to *J. Geophys. Res.*
- Cardenas, M. B., and J. L. Wilson, Exchange across a sediment-water interface with ambient groundwater discharge, under preparation.
- Carslaw, H. S., and J. C. Jaeger, *Conduction of Heat in Solids*, 2nd ed., Oxford University Press, New York, 1959.
- Clark, E., B. W. Webb, and M. Ladle, Microthermal gradients and ecological implications in Dorset rivers, *Hydrol. Proc.*, 13, 423-438, 1999.

- Conant, B. J., Delineating and quantifying ground water discharge zones using streambed temperature, *Ground Water*, 42(2), 243-257, 2004.
- Constantz, J., C. L. Thomas, G. Zellweger, Influence of diurnal variations in stream temperature on streamflow loss and groundwater recharge, *Water Resour. Res.*, 30(12), 3253-3264, 1994.
- Constantz, J., Interaction between stream temperature, streamflow, and groundwater exchanges in alpine streams, *Water Resour. Res.*, 34(7), 1609-1615, 1998.
- Constantz, J., A. E. Stewart, R. Niswonger, and L. Sarma, Analysis of temperature profiles for investigating stream losses beneath ephemeral channels, *Water Resour. Res.*, 38(12), 1316, doi:10.1029/2001WR001221, 2002.
- Cozzetto, K., D. M. McKnight, T. Nylen, and A. Fountain, Experimental investigations into processes controlling stream and hyporheic temperatures, Fryxell Basin, Antarctica, *Adv. Water Resour.*, 29(6), 130-153, 2006.
- de Marsily, G., *Quantitative hydrogeology : groundwater hydrology for engineers*, xix, 440 pp., Academic Press, Orlando, FL, 1986.
- Elliott, A. H., N. H. Brooks, Transfer of nonsorbing solutes to a streambed with bed forms: Theory, *Water Resour. Res.*, 33(1), 123-236, 1997.
- Evans, E. C., and G. E. Petts, Hyporheic temperature patterns within riffles, *Hydrol. Sci. J.*, 42, 199-213, 1997.
- Evans, E. C., G. R. McGregor, and G. E. Petts, River energy budgets with special reference to river bed processes, *Hydrol. Process.*, 12, 575-595, 1998.
- Fang, X., and H. G. Stefan, Temperature variability in lake sediments, *Water Resour. Res.*, 34(4), 717-729, 1998.
- Goto, S., M. Yamano, and M. Kinoshita, Thermal response of sediment with vertical fluid flow to periodic temperature variation at the surface, *J. Geophys. Res.*, 110, B01106, doi:10.1029/2004JB003419, 2005.
- Hondzo, M., and H. G. Stefan, Riverbed heat conduction prediction, *Water Resour. Res.*, 30(5), 1503-1513, 1994.
- Jaynes, D. B., Temperature variation effect on field-measured infiltration, *Soil Sci. Soc. Am. J.*, 54(2), 305-311, 1990.
- Johnson, S. L., Stream temperature: scaling of observations and issue for modeling, *Hydrol. Process.*, 17, 497-499, 2003.

- Johnson, S. L., Factors influencing stream temperatures in small streams: substrate effects and a shading experiment, *Can. J. Fish. Aquat. Sci.*, 61, 913-923, 2004.
- Hancock, P. J., A. J. Boulton, and W. F. Humphreys, Aquifers and hyporheic zones: towards an ecological understanding of groundwater, *Hydrogeol. J.*, 13, 98-111, 2005.
- Huettel, M., W. Ziebis, S. Forster, and G. Luther, Advective transport affecting metal and nutrient distribution and inter-facial fluxes in permeable sediments, *Geochim. Cosmochim. Acta*, 62, 613-631, 1998.
- Kaplan, L. A., and T. L. Bott, Diel fluctuations in bacterial activity on streambed substrata during vernal algal blooms: Effects of water temperature, water chemistry and habitat, *Limnol. Oceanog.*, 34(4), 718-733, 1989.
- Lee, D. R., Method for locating sediment anomalies in lake beds that can be caused by groundwater inflow, *J. Hydrol.*, 79, 187-193, 1985.
- Moore, W. S., J. Krest, G. Taylor, E. Roggenstein, S. Joye, and R. Lee, Thermal evidence of water exchange through a coastal aquifer: Implications for nutrient fluxes, *Geophys. Res. Lett.*, 29(14), 1704, 10.1029/2002GL014923, 2002.
- Nimick, D. A., C. H. Gammons, T. E. Cleasby, J. P. Madison, D. Skaar, and M. Brick, Diel cycles in dissolved metal concentration in streams: Occurrence and possible causes, *Water Resour. Res.*, 39(9), 1247, doi:10.1029/2002WR001571, 2003.
- Niswonger, R. G., and D. E. Prudic, Modeling heat as a tracer to estimate streambed seepage and hydraulic conductivity, In *Heat as a Tool for Studying the Movement of Ground Water Near Streams*, ed. D.A. Stonestrom and J. Constantz, 1-6. USGS Circular 1260. Reston, Virginia: USGS, 2003.
- Poole, G. C., and C. H. Berman, An ecological perspective of in-stream temperature: natural heat dynamics and mechanisms of human-caused thermal degradation, *Environmental Management*, 27, 787-802, 2001.
- Ronan, A. D., D. E. Prudic, C. E. Thodal, and J. Constantz, Field study and simulation of diurnal temperature effects on infiltration and variably saturated flow beneath an ephemeral stream, *Water Resour. Res.*, 34(9), 2137-2153, 1998.
- Schmidt, E., *Properties of Water and Steam in SI-Units*, Springer-Verlag, New York, 1979.
- Schulze-Makuch, D., Longitudinal dispersivity data and implications for scaling behavior, *Ground Water*, 43(3), 443-456, 2005.

- Silliman, S. E., J. Ramirez, and R. L. McCabe, Quantifying downflow through creek sediments using temperature time series: one-dimensional solution incorporating measured surface temperature, *J. Hydrol.*, 167, 99-119, 1995.
- Stanford, J. A., and J. V. Ward, The hyporheic habitat of river ecosystems, *Nature*, 335, 64-66, 1988.
- Stonestrom, D. A., and J. Constantz, *Heat as a tool for studying the movement of groundwater near streams*, USGS Circular 1260, USGS, 2003.
- Taniguchi, M., J. V. Turner, and A. J. Smith, Evaluations of groundwater discharge rates from subsurface temperature in Cockburn Sound, Western Australia, *Biogeochemistry*, 66, 111-124, 2003.
- Thibodeaux, L. J., and J. D. Boyle, Bedform-generated convective transport in bottom sediment, *Nature*, 325, 341-343, 1987.
- Ward, J. V., Thermal characteristics of running waters, *Hydrobiologia*, 125, 31-46, 1985.
- Webster, I. T., S. J. Norquay, F. C. Ross, and R. A. Wooding, Solute exchange by convection within estuarine sediments, *Estuar. Coast. Shelf Sci.*, 42, 171-183, 1996.
- Westrich, J. T., and R. A. Berner, The effect of temperature on rates of sulfate reduction in marine sediments, *Geomicrobiol. J.*, 6(2), 99-117, 1988.
- White, D. S., Perspectives on defining and delineating hyporheic zones, *J. N. Am. Benthol. Soc.*, 12(1), 61-69, 1993.

CHAPTER 8

CONCLUSIONS AND RECOMMENDATIONS

8.1. Epilogue

For this dissertation, I investigate the dynamics of physical processes occurring near sediment-water interfaces with a focus on interfacial (or hyporheic) exchange. The dynamical studies are based on numerical simulations of fluid, heat and solute transport. In the early part of this study (Chapter 2), I investigate the impacts of heterogeneity in permeability, bedforms, and channel curvature following a “groundwater” perspective. In later chapters (Chapters 3 to 6), the coupled dynamics of a water column and an underlying sediment are examined for water-column conditions ranging from laminar flow to fully-developed turbulent flow. Chapter 6 considers ambient groundwater flow to and from the water column, while Chapter 7 examines the effects of the flow processes on heat transport.

8.2. Synthesis

The interface between a water column and underlying sediments bounds a complex and poorly studied coupled system. Water movement along and across the sediment-water interface (SWI) dictates myriad ecological and biogeochemical processes. This study fills and addresses this knowledge gap by examining the physics of advective exchange. The results are synthesized below.

The dynamics of fluids, heat and solutes along the SWI has been analyzed observationally, experimentally and theoretically. Previous observational and experimental studies illustrated processes but did not elucidate the details of physics and biogeochemistry. Only a few specific situations were studied, and in any event the laboratory or field observations and experiments are tedious and resource-intensive. Theoretical analysis can potentially cover a broad range of dynamical conditions. Unfortunately, theoretical approaches are themselves limited by the complex physics, chemistry, and geometry of coupled sediment-water systems. The few theoretical formulations that provide valuable insight regarding processes are based on limiting but needed simplifying assumptions. A suitable alternative, but also fraught with its own limitations, is to numerically model the processes in a reductionist framework where simplifications of the physics, chemistry, geometry and other pertinent parameters, are minimized. This is possible through powerful, albeit commercially available, numerical modeling tools which are applied in this study.

The simulations in this study are designed to investigate both external and internal forcing of fluid exchange between a sediment and its overlying water column. It is widely known that obstacles or topography along a channel result in an irregular pressure distribution along the sides of the channel. This is also true for the SWI at the bottom of the channel, where mean unidirectional flow occurs over bedforms. The irregular topography creates variable bottom pressures along the SWI that drive fluid flow into and out of the sediments. This process is referred to as interfacial exchange and the zone defined by the path of infiltrating and exfiltrating water is referred to as the interfacial exchange zone (IEZ). Other external forcing of fluid flow in sediments below

a channel include head gradients set-up due to channel geomorphology (e.g., sinuosity) and regional head gradients.

The simulation results suggest that, for laminar flow conditions, the pressure distribution along the SWI which drives interfacial exchange is a consequence of both a Bernoulli effect due to channel constriction and expansion and the presence of an eddy. The eddy detaches at the pressure minimum located at the crest of the bedform and reattaches at a pressure maximum on the stoss slope of the succeeding bedform. These critical pressure points drive interfacial exchange and control the spatial configuration and depth of the IEZ. The infiltration is focused near the pressure maxima, along the stoss slope, while exfiltration is focused near the pressure minimum near the crest. Since the eddy grows with increasing water column flow Reynolds number (Re), so does the IEZ. A laminar flow eddy can only grow up to the length of the bedform where it becomes confined between two crests. The extent of the IEZ is therefore similarly limited by the bedform length. Increasing the Re also increases the pressure gradient for driving flow through the SWI, resulting in larger fluxes through the IEZ, even when the IEZ reaches an asymptotic size.

At higher Re , the laminar flow assumption no longer holds and the water column becomes turbulent. Simulations of turbulent flow over bedforms show that eddies are smaller compared to when flow is laminar. Eddy lengths are about 4-6 times the height of the bedform regardless of the Re . Eddy detachment points are still co-located with the pressure minimum at the crest. However, the pressure maximum at the stoss side is slightly upstream of where the eddy reattaches. Nonetheless, the locations of these two critical pressure points are more or less fixed in space, even with increasing Re . This

results in an IEZ whose depth is also insensitive to Re . However, increasing Re in the water column increases the difference in pressure between the two essentially fixed critical points. This translates to a linear increase in flux through the IEZ, with Re , owing to Darcy's Law.

Ambient groundwater discharge (AGD) from deeper parts of the sediments and towards the SWI, or towards deeper parts of the sediments from the SWI, interacts and competes with the current-topography induced pressure gradient driving interfacial exchange. When the gradient associated with AGD is significantly larger than the current-topography induced gradient along the SWI, flow within the sediments becomes essentially vertical and one-dimensional. Flow is upwards in the case of a gaining water column and downwards in the case of a losing one. When pressure gradient associated with the AGD is the same magnitude as, or is less than, the SWI gradient, an IEZ forms. Portions of the SWI are subjected to IEZ and the remainder to AGD, the proportions changing with the ratio of these two fluxes. Under gaining conditions, the IEZ is centered and develops around the pressure maximum associated with the eddy reattachment point. Deep groundwater moving upwards discharges near the pressure minimum at the crest. Under losing conditions, the IEZ is centered and develops around the pressure minimum at the crest. Water coming from the water column, which does not return to the SWI, but moves towards deeper portions of the sediments, originates at the pressure maximum along the SWI which is associated with the eddy reattachment point.

Interfacial exchange affects the thermal regime of sediments subjected to diurnal temperature changes along the SWI, particularly when the sediments are permeable and when heat advection becomes important. The distinct flow pattern within sediments, set-

up by current-bedform interactions, results in complex variations of temperature in space and time. Minor temperature variations are found close to crests of dunes where pore water is upwelling from deeper areas of the sediments, while strong temperature variations are observed underneath areas where water is infiltrating into the sediments from the water column. Simpler heat flow patterns arise when AGD is dominant and is approximated by one-dimensional flow.

The internal permeability structure of streambed sediments influences local scale exchange. Our simulations, using three-dimensional groundwater flow models with a flat boundary for the SWI but with spatially and sinusoidally varying pressure, show that heterogeneity in permeability is important in determining fluxes and the spatial configuration of the IEZ. The sinusoidal pressure fluctuations are a surrogate for the pressure distribution that develops due to current-bedform interactions. The importance of a heterogeneous permeability field becomes less important when the sinusoidal fluctuations, the external forcing, increase in amplitude and frequency. When fluctuation amplitude and frequency is large enough, the IEZ that forms within a heterogeneous permeability field looks similar to that for an equivalent homogeneous medium. This competition between external and internal forcing is described by a dimensionless number. Furthermore, head gradients are generated by open channel flow through curved channels. Along meanders, the elevation of the stream's water surface is higher on the outer cutbank compared to the inner bank adjacent to the point bar. Groundwater flow simulations show that this head gradient drives flow into the point bar and also interacts with local scale forcing by permeability variation.

This study has shown that interfacial exchange along sediment-water interfaces is

driven by several dynamic factors, both external and internal, which interact with each other. Deconvolution of the relative contributions of these individual factors and investigation of the detailed hydrodynamics and their consequence on thermal energy transport is made possible through the use of both of both simple and high-fidelity multiphysics numerical models. The culmination of the studies is the development of mechanistically based dimensionless ratios and equations that allow for prediction of which driving factor dominates as well as for prediction of the integrated effects of interfacial exchange.

8.3. Recommendations for Future Work

For this dissertation, I investigated the various *internal* (e.g., permeability structure) and *external* (current-bedform interactions and ambient groundwater discharge) factors that affect interfacial exchange. The external and internal forcing mechanisms were analyzed using modeling. The models of the competition between local control by permeability and external control by current-bedform interactions assumed a sinusoidal pressure distribution along the sediment-water interface. Future integrative studies should include heterogeneous permeability fields, synthetic or real, in coupled modeling formulations accounting explicitly for the dynamics of fluid flow in the water column.

There are two major limitations of the methods and results for topography-current induced exchange presented in Chapters 3-7. First, the models are based on a two-dimensional formulation of idealized bedform shapes. Second, the bedforms are fixed in space and time. This study should be extended to three dimensions and encompass actual data on bed topography (two- and three-dimensional). Moving bedforms should be

considered through moving meshes or through ad hoc methods.

That interfacial exchange processes have not received much research attention is primarily due to issues with the hydrodynamics. Even so, equally or more important fundamental issues with ecological and biogeochemical processes remain unstudied. The concepts and methods that I've presented bring us closer to tackling interdisciplinary studies of interfacial exchange. Although this study emphasized hydrodynamic processes, the robust numerical models allow for coupling of transport and biogeochemical processes. For example, solute transport simulations with multiple reacting and interacting species, coupled with the hydrodynamic and thermal models presented here, may allow for a holistic investigation of sediment-water interfaces. Nutrient and chemical uptake by organisms, and purely chemical processes such as sorption/desorption and biogeochemical processes such as reduction/oxidation reactions, can be represented in these reactive transport models. Future work on reactive transport should also include laboratory experiments or field observations that, when integrated with the modeling studies, will provide the process-based framework for interpreting the observations.

This dissertation presents some predictive equations (e.g., equations 5.14 and 5.15) and diagnostic dimensionless numbers (equation 2.4). Future work should test these in actual field or laboratory studies.

BIBLIOGRAPHY

- Advisory Committee for Environmental Research and Education, *Complex Environmental Systems: Pathways to the Future*, National Science Foundation, Washington, DC, 12pp., 2005.
- Albert, M. R., and R. Hawley, Seasonal changes in surface roughness characteristics at Summit, Greenland: Implications for air-snow transfer processes, *Ann. Glaciol.*, 35, 510-514, 2002.
- Albert, M. R., and E. F. Shultz, Snow and firn properties and air-snow transport processes at Summit, Greenland, *Atmos. Environ.*, 36, 2789-2797, 2002.
- Alexander, M. D., and D. Caissie, Variability and comparison of hyporheic water temperatures and seepage fluxes in a small Atlantic salmon stream, *Ground Water*, 41(1), 72-82, 2003.
- Allen. J. R. L., *Sedimentary Structures: Their Character and Physical Basis*, Volume I. Developments in Sedimentology 30, Elsevier Science Publishers, Amsterdam, 1982.
- Allen, J. D., *Stream ecology: Structure and function of running waters*, Chapman and Hall, NY, 388 pp., 1995.
- Aller, R. C., The effects of macrobenthos on chemical properties of marine sediment and overlying water, in McCall, P. L. and M. J. S., Tevesz, *Animal-Sediment Relations*, Plenum Press, NY, 53-96, 1982.
- Anderson, M. P., Heat as a ground water tracer, *Ground Water*, 43(6), 1-18, 2005.
- Andrews, C. B., and M. P. Anderson, Thermal alteration of groundwater caused by seepage from a cooling lake, *Water Resour. Res.*, 15(3), 595-602, 1979.
- Armaly B. F., F. Durst, J. C. F. Pereira, and B. Schonung, Experimental and theoretical investigation of backward-facing step flow, *J. Fluid Mech.*, 127, 473-496, 1983.
- Bear, J. C., *Dynamics of Fluids in Porous Media*, Dover Publications, Inc., New York, 1972.

- Beavers, G. S., and D. D. Joseph, Boundary conditions at a naturally permeable wall, *J. Fluid Mech.*, 30, 197-207, 1976.
- Becker, M. W., T. Georgian, H. Ambrose, J. Siniscalchi, and K. Fredrick, Estimating flow and flux of ground water discharge using water temperature and velocity, *J. Hydrol.*, 296, 221-233, 2004.
- Bencala, K. E., and R. A. Walters, Simulation of solute transport in a mountain pool-and-riffle stream: a transient storage model, *Water Resour. Res.*, 19(3), 718-724, 1983.
- Boudreau, B. P., Solute transport above the sediment-water interface, in *The Benthic Boundary Layer: Transport Processes and Biogeochemistry*, edited by B. P. Boudreau and B. B. Jorgensen, New York: Oxford University Press, 2001.
- Boulton, A. J., S. Findlay, P. Marmonier, E. H. Stanley, and H. M. Valett, The functional significance of the hyporheic zone in streams and rivers, *Annu. Rev. Ecol. Syst.*, 29, 59-81, 1998.
- Brick, C. M., and J. N. Moore, Diel variation of trace metals in the Upper Clark Fork Fiver, Montana, *Environ. Sci. Technol.*, 30, 1953-1960, 1996.
- Bridge, J. S., *Rivers and Floodplains: Forms, Processes, and Sedimentary Record*, Blackwell Publishing, UK, 491 pp., 2003.
- Bridge, J. S., A revised model for water flow, sediment transport, bed topography and grain size sorting in natural river bends, *Water Resour. Res.*, 28(4), 999-1013, 1992.
- Brinkman, H. C., A calculation of the viscous force exerted by a flowing fluid on a dense swarm of particles, *Appl. Sci. Res.*, 1, 27-34, 1947.
- Burnett W. C., H. Bokuniewicz, M. Huettel, W. S. Moore, and M. Taniguchi M., Groundwater and pore water inputs to the coastal zone, *Biogeochemistry*, 66, 3-33, 2003.
- Cardenas, M. B., J.L. Wilson, and V.A. Zlotnik, Impact of heterogeneity, bed form configuration, and channel curvature on hyporheic exchange, *Water Resour. Res.*, 40, W08307, doi:10.1029/2004WR003008, 2004.
- Cardenas, M. B., and J. L. Wilson, Dunes, turbulent eddies, and interfacial exchange with porous media, submitted to *J. Geophys. Res.*.
- Cardenas, M. B., and J. L. Wilson, Exchange across a sediment-water interface with ambient groundwater discharge, under preparation.
- Cardenas, M. B., and J.L. Wilson, The influence of ambient groundwater discharge on

- hyporheic zones induced by current-bedform interactions, *J. Hydrol*, in press.
- Cardenas, M. B., and J.L. Wilson, Hydrodynamics of coupled flow above and below a sediment-water interface with triangular bedforms, submitted to *Adv. Water Res.*
- Cardenas, M. B., and J.L. Wilson, Comment on “Flow resistance and bed form geometry in a wide alluvial channel” by Yang, Tan and Lim, *Water Resour. Res.*, in press.
- Cardenas, M. B., and V. A. Zlotnik, Three-dimensional model of modern channel bend deposits, *Water Resour. Res.*, 39(6), 1441, doi:10.1029/2002WR001383, 2003a.
- Cardenas, M. B., and V. A. Zlotnik, A simple constant-head injection test for streambed hydraulic conductivity estimation, *Ground Water*, 41(6), 867-871, 2003b.
- Carslaw, H. S., and J. C. Jaeger, *Conduction of Heat in Solids*, 2nd ed., Oxford University Press, New York, 1959.
- Chen, X., and Y.-M. Chiew, Velocity distribution of turbulent open-channel flow with bed suction, *J. Hydraul. Eng.*, 130, 140-148, 2004.
- Cheng, N. S., and Y.-M. Chiew, Modified logarithmic law for velocity distribution subjected to upward seepage, *J. Hydraul. Eng.*, 124, 1235-1241, 1998.
- Cheong, H. F., and H. Xue, Turbulence model for water flow over two-dimensional bed forms, *J. Hydraul. Eng.*, 123(5), 402-409, 1997.
- Choe, K. Y., G. A. Gill, R. D. Lehman, S. Han, W. A. Heim, and K. H. Coale, Sediment-water exchange of total mercury in the San Francisco Bay-Delta, *Limnol. Oceanogr.*, 49(5), 1512-1527, 2004.
- Choi, J., J. W. Harvey, and M. H. Conklin, Characterizing multiple scales of stream and storage zone interaction that affect solute fate and transport in streams, *Water Resour. Res.*, 36(6), 1511-1518, 2000.
- Chun, S., Y. Z. Liu, and H. J. Sung, Wall pressure fluctuations of a turbulent and reattaching flow affected by an unsteady wake, *Exp. Fluids*, 37, 531-546, 2004.
- Clark, E., B. W. Webb, and M. Ladle, Microthermal gradients and ecological implications in Dorset rivers, *Hydrol. Proc.*, 13, 423-438, 1999.
- Colbeck, S. C., Air movement in snow due to wind pumping, *J. Glaciol.*, 35, 209-213, 1989.
- Committee on Hydrologic Sciences, *Groundwater Fluxes Across Interfaces*, National Research Council, National Academies Press, Washington DC, 85 pp., 2004.

- Conant, B. J., Delineating and quantifying ground water discharge zones using streambed temperature, *Ground Water*, 42(2), 243-257, 2004.
- Constantz, J., C. L. Thomas, G. Zellweger, Influence of diurnal variations in stream temperature on streamflow loss and groundwater recharge, *Water Resour. Res.*, 30(12), 3253-3264, 1994.
- Constantz, J., Interaction between stream temperature, streamflow, and groundwater exchanges in alpine streams, *Water Resour. Res.*, 34(7), 1609-1615, 1998.
- Constantz, J., A. E. Stewart, R. Niswonger, and L. Sarma, Analysis of temperature profiles for investigating stream losses beneath ephemeral channels, *Water Resour. Res.*, 38(12), 1316, doi:10.1029/2001WR001221, 2002.
- Cozzetto, K., D. M. McKnight, T. Nysten, and A. Fountain, Experimental investigations into processes controlling stream and hyporheic temperatures, Fryxell Basin, Antarctica, *Adv. Water Resour.*, 29(6), 130-153, 2006.
- Cunningham, J. C., and E.D. Waddington, Air flow and dry deposition of non-sea salt sulfate in polar firn: Paleoclimatic implications, *Atmos. Environ.*, 27, 2943-2956, 1993.
- Davis, T. A., A column pre-ordering strategy for the unsymmetric-pattern multifrontal method, *ACM Trans. Math. Software*, 30(2), 165-195, 2004.
- de Marsily, G., *Quantitative hydrogeology : groundwater hydrology for engineers*, xix, 440 pp., Academic Press, Orlando, FL, 1986.
- Doyle, M. W., E. H. Stanley, and J. M. Harbor, Hydrogeomorphic controls on phosphorus retention in streams, *Water Resour. Res.*, 39(6), 1147, doi:10.1029/2003WR002038, 2003.
- Durlafsky, L., and J.F. Brady, Analysis of the Brinkman equation as a model for flow in porous media, *Phys. Fluids*, 30, 3329-3441, 1987.
- Elliott, A. H., Transfer of solutes into and out of streambeds, Ph.D. thesis, Rep KH-R-52, WM Keck Lab of Hydraul and Water Resour, Calif Inst of Technol, Pasadena, 1990.
- Elliott, A. H., and N. H. Brooks, Transfer of nonsorbing solutes to a streambed with bed forms: Theory, *Water Resour. Res.*, 33(1), 123-136, 1997a.
- Elliott, A. H., and N. H. Brooks, Transfer of nonsorbing solutes to a streambed with bed forms: Laboratory experiments, *Water Resour. Res.*, 33(1), 137-151, 1997b.
- Engel, P., Length of flow separation over dunes, *J. Hydraul. Div. ASCE*, 107, 1133-1143,

1981.

- Evans, E. C., and G. E. Petts, Hyporheic temperature patterns within riffles, *Hydrol. Sci. J.*, 42, 199-213, 1997.
- Evans, E. C., G. R. McGregor, and G. E. Petts, River energy budgets with special reference to river bed processes, *Hydrol. Process.*, 12, 575-595, 1998.
- Fehlman, H. M., Resistance components and velocity distributions of open channel flows over bedforms, M. S. Thesis, Colo State Univ, Fort Collins, CO, 1985.
- Fang, X., and H. G. Stefan, Temperature variability in lake sediments, *Water Resour. Res.*, 34(4), 717-729, 1998.
- Findlay, S., Importance of surface-subsurface exchange in stream ecosystems: The hyporheic zone, *Limnol. Oceanogr.*, 40(1), 159-164, 1995.
- Goto, S., M. Yamano, and M. Kinoshita, Thermal response of sediment with vertical fluid flow to periodic temperature variation at the surface, *J. Geophys. Res.*, 110, B01106, doi:10.1029/2004JB003419, 2006.
- Hancock, P. J., A. J. Boulton, and W. F. Humphreys, Aquifers and hyporheic zones: towards an ecological understanding of groundwater, *Hydrogeol. J.*, 13, 98-111, 2005.
- Harbaugh, A. W., *A Program for Calculating Subregional Water Budgets using Results from the U. S. Geological Survey's Modular Three-dimensional Finite-difference Ground-water Flow Model*, USGS Open File Report 90-392, Reston, VA, 27 pp., 1990.
- Harris, R. N., G. Garven, J. Georgen, M.K. McNutt, and R.P. Von Herzen, Submarine hydrogeology of the Hawaiian archipelagic apron, Part 2, Numerical simulations of coupled heat transport and fluid flow, *J. Geophys. Res.*, 105, 371-385, 2000.
- Harvey, J. W., and K. E. Bencala, The effect of streambed topography on surface-subsurface water exchange in mountain catchments, *Water Resour. Res.*, 29(1), 89-98, 1993.
- Harvey, J. W., and C. W. Fuller, Effect of enhanced manganese oxidation in the hyporheic zone on basin-scale geochemical mass balance, *Water Resour. Res.*, 34(4), 623-636, 1998.
- Harvey, J. W., and B. J. Wagner, Quantifying hydrologic interactions between streams and their subsurface hyporheic zones, in *Streams and Ground Waters*, edited by J. B. Jones and P. J. Mulholland, Academic Press, San Diego CA, 3-44, 2000.

- Harvey, J. W., B. J. Wagner, and K. E. Bencala, Evaluating the reliability of the stream tracer approach to characterize stream-subsurface water exchange, *Water Resour. Res.*, 32(8), 2441-2451, 1996.
- Ho, R. T., and L. W. Gelhar, Turbulent flow with wavy permeable boundaries, *J. Fluid Mech.*, 58(2), 403-414, 1973.
- Hondzo, M., and H. G. Stefan, Riverbed heat conduction prediction, *Water Resour. Res.*, 30(5), 1503-1513, 1994.
- Huettel, M., H. Roy, E. Precht, and S. Ehrenhauss, Hydrodynamical impact of biogeochemical processes in aquatic sediments, *Hydrobiologia*, 494, 231-236, 2003.
- Huettel, M., W. Ziebis, S. Forster, and G. W. Luther III, Advective transport affecting metal and nutrient distributions and interfacial fluxes in permeable sediments, *Geochim. Cosmochim. Acta* 1998;62(4): 613-631.
- Huettel, M., and I. T. Webster, Porewater flow in permeable sediments, in *The Benthic Boundary Layer: Transport Processes and Biogeochemistry*, edited by BP Boudreau and BB Jorgensen, New York: Oxford University Press, 2001.
- Huettel, M., W. Ziebis, and S. Forster, Flow-induced uptake of particulate matter in permeable sediments, *Limnol. Oceanogr.*, 41(2), 309-322, 1996.
- Huettel, M., and G. Gust, Impact of bioroughness on interfacial solute exchange in permeable sediments, *Mar. Ecol. Prog. Ser.*, 89, 253-267, 1992.
- Jahnke, R. A., J.R. Nelson, R.L. Marinelli, and J.E. Eckman, Benthic flux of biogenic elements on the Southeastern US continental shelf: influence of pore water advective transport and benthic microalgae, *Cont. Shelf Res.*, 20, 109-127, 2000.
- Jaynes, D. B., Temperature variation effect on field-measured infiltration, *Soil Sci. Soc. Am. J.*, 54(2), 305-311, 1990.
- Johnson, S. L., Stream temperature: scaling of observations and issue for modeling, *Hydrol. Process.*, 17, 497-499, 2003.
- Johnson, S. L., Factors influencing stream temperatures in small streams: substrate effects and a shading experiment, *Can. J. Fish. Aquat. Sci.*, 61, 913-923, 2004.
- Jones, J. B., and P. J. Mulholland, *Streams and Ground Waters*, Academic Press, San Diego, 2000.
- Jonsson, K., H. Johansson, and A. Worman, Hyporheic exchange of reactive and conservative solutes in streams- tracer methodology and model interpretation, *J.*

- Hydrology*, 278(1-4), 153-171, 2003.
- Jorgensen, B. B., and B. P. Boudreau, Diagenesis and sediment-water exchange, in *The Benthic Boundary Layer: Transport Processes and Biogeochemistry*, edited by BP Boudreau and B B Jorgensen, New York: Oxford University Press, 2001.
- Kasahara, T., and S. M. Wondzell, Geomorphic controls on hyporheic exchange flow in mountain streams, *Water Resour. Res.*, 39(1), 1005, doi:10.1029/2002WR001386, 2003.
- Larkin, R. G., and J. M. Sharp, Jr., On the relationship between river-basin geomorphology, aquifer hydraulics, and ground-water flow direction in alluvial aquifers, *Geol. Soc. America. Bull.*, 104, 1608-1620, 1992.
- Layton, W. J., F. Schiewick, and I. Yotov, Coupling fluid flow with porous media flow, *SIAM J. Numer. Anal.*, 40, 2195-2218, 2002.
- Lee, D. R., Method for locating sediment anomalies in lake beds that can be caused by groundwater inflow, *J. Hydrol.*, 79, 187-193, 1985.
- Marion, A., M. Bellinello, I. Guymer, and A. Packman, Effect of bed form geometry on the penetration of nonreactive solutes into a streambed, *Water Resour. Res.*, 38(10), 1209, doi:10.1029/2001WR000264, 2002.
- Massmann, J., and D. F. Farrier, Effects of atmospheric pressures on gas transport in the vadose zone, *Water Resour. Res.*, 28, 777-791, 1992.
- Matos, J.E.R., Welty, C., and Packman, A.I., Stream-groundwater interactions: The influence of aquifer heterogeneity and stream meandering on 2-D and 3-D hyporheic exchange flows, *Proceedings of MODFLOW and More 2003: Understanding through Modeling*, Golden, Colorado, Sept. 17-19, 2003.
- McDonald, M. G., and A. W. Harbaugh, *Programmer's Documentation for MODFLOW-96, an update to the U.S. Geological Survey Modular Finite-Difference Ground-Water Flow Model*, U.S. Geol. Surv. Open File Rep. 96-486, 220 pp., 1996.
- Mendoza, C., and H. W. Shen, Investigation of turbulent flow over dunes, *J. Hydr. Eng. ASCE*, 116(4), 459-477, 1990.
- Michaelis, L., and M. L. Menten, Die kinetik der invertinwirkung (The kinetics of invertase activity), *Biochem. Z.*, 49, 333-369, 1913.
- Moore, W.S., Large groundwater inputs to coastal waters revealed by ^{226}Ra enrichments. *Nature*, 380, 612-614, 1996.
- Moore, W.S., and T. J. Shaw, Chemical signals from submarine fluid advection onto the

- continental shelf, *J. Geophys. Res.*, 103(C10), 543-552, 1998.
- Moore, W. S., J. Krest, G. Taylor, E. Roggenstein, S. Joye, and R. Lee, Thermal evidence of water exchange through a coastal aquifer: Implications for nutrient fluxes, *Geophys. Res. Lett.*, 29(14), 1704, 10.1029/2002GL014923, 2002.
- Morgan, P. H., L. P. Mercer, and N. W. Flodin, General model for nutritional responses of higher order mechanisms, *Proc. Nat. Acad. Sci. USA*, 72(11), 4327-4331, 1975.
- Nelson, J. M., and J. D. Smith, Mechanics of flow over ripples and dunes, *J. Geophys. Res.*, 94(C6), 8146-8162, 1989
- Nield, D. A., The limitations of the Brinkman-Forcheimer equation in modeling flow in a saturated porous medium and at an interface, *Int. J. Heat and Fluid Flow*, 12(3), 269-272, 1991.
- Nimick, D. A., C. H. Gammons, T. E. Cleasby, J. P. Madison, D. Skaar, and M. Brick, Diel cycles in dissolved metal concentration in streams: Occurrence and possible causes, *Water Resour. Res.*, 39(9), 1247, doi:10.1029/2002WR001571, 2003.
- Niswonger, R. G., and D. E. Prudic, Modeling heat as a tracer to estimate streambed seepage and hydraulic conductivity, In *Heat as a Tool for Studying the Movement of Ground Water Near Streams*, ed. D.A. Stonestrom and J. Constantz, 1-6. USGS Circular 1260. Reston, Virginia: USGS, 2003.
- Packman, A. I., and K. E. Bencala, Modeling surface-subsurface hydrological interactions, in *Streams and Ground Waters*, edited by J. B. Jones and P. J. Mulholland, Academic Press, San Diego CA, 45-80, 2000.
- Packman, A. I., and N. H. Brooks, Hyporheic exchange of solutes and colloids with moving bed forms, *Water Resour. Res.*, 37(10), 2591-2605, 2001.
- Packman, A. I., M. Salehin, and M. Zaramella, Hyporheic exchange with gravel beds: basic hydrodynamic interactions and bedform-induced advective flows, *J. Hydraul. Eng.*, 130(7): 647-656, 2004.
- Poole, G. C., and C. H. Berman, An ecological perspective of in-stream temperature: natural heat dynamics and mechanisms of human-caused thermal degradation, *Environmental Management*, 27, 787-802, 2001.
- Pollock, D. W., *User's Guide for MODPATH/ MODPATH-PLOT, Version 3: A particle tracking post-processing package for MODFLOW, the U. S. Geological Survey finite-difference ground-water flow model*, U.S. Geol. Surv. Open File Rep. 94-464, 234 pp., 1994.
- Precht, E., and M. Huettel, Advective pore-water exchange driven by surface gravity

- waves and its ecological implications, *Limnol. Oceanogr.*, 48(4), 1674-1684, 2003.
- Raudkivi, A. J., Study of sediment ripple formation, *J. Hydr. Div. ASCE*, 89(6): 15-33, 1963.
- Ren, J., and A. I. Packman, Coupled stream-subsurface exchange of colloidal hematite and dissolved zinc, copper, and phosphate, *Environ. Sci. Technol.*, 39, 6387-6394, 2005.
- Richardson, C. P., and A. D. Parr, Modified Fickian model for solute uptake by runoff, *J. Environ. Eng.*, 114(4), 792-809, 1988.
- Riedl, R. J., H. Huang, and R. Machan, The subtidal pump: A mechanism of interstitial water exchange by wave action, *Mar. Biol.*, 13, 210-221, 1972.
- Ronan, A. D., D. E. Prudic, C. E. Thodal, and J. Constantz, Field study and simulation of diurnal temperature effects on infiltration and variably saturated flow beneath an ephemeral stream, *Water Resour. Res.*, 34(9), 2137-2153, 1998.
- Runkel, R. L., One dimensional transport with inflow and storage (OTIS): A solute transport model for streams and rivers, U.S. Geological Survey Water-Resources Investigation Report 98-4018, Denver: USGS, 1998.
- Runkel, R. L., D. M. McKnight, and H. Rajaram, Modeling hyporheic zone processes, *Adv. Water Resour.*, 26(9), 901-905, 2003.
- Rutherford, J. C., J. D. Boyle, A. H. Elliott, T. V. J. Hatherell, and T. W. Chiu, Modeling benthic oxygen uptake by pumping, *J. Environ. Eng.*, 121(1), 84-95, 1995.
- Salehin, M., A. I. Packman, and M. Paradis, Hyporheic exchange with heterogeneous streambeds: Laboratory experiments and modeling, *Water Resour. Res.*, 40: W11504, doi:10.1029/2003WR002567, 2004.
- Savant, S. A., D. D. Reible, and L. J. Thibodeaux, Convective transport within stable river sediments, *Water Resour. Res.*, 23(9), 1763-1768, 1987.
- Schmidt, E., *Properties of Water and Steam in SI-Units*, Springer-Verlag, New York, 1979.
- Schulze-Makuch, D., Longitudinal dispersivity data and implications for scaling behavior, *Ground Water*, 43(3), 443-456, 2005.
- Severinghaus, J. P., R. F. Keeling, B. R. Miller, R. F. Weiss, B. Deck, and W. S. Broecker, Feasibility of using sand dunes as archives of old air, *J. Geophys. Res.*, 102, 10.1029/97JD00525, 1997.

- Shavit, U., G. Bar-Yosef, R. Rosenzweig, and S. Assouline, Modified Brinkman equation for a free flow problem at the interface of porous surfaces: The Cantor-Taylor brush configuration case, *Water Resour. Res.*, 38, 1320, doi:10.1029/2001WR001142, 2002.
- Shen, H. W., H. M. Fehlmán, and C. Mendoza, Bedform resistances in open channel flows, *J. Hydraul. Eng. ASCE*, 116(6), 799-815, 1990.
- Shum, K. T., Wave-induced advective transport below a rippled water-sediment interface, *J. Geophys. Res.*, 97(C1), 798-808, 1992.
- Shum, K. T., The effects of wave-induced pore water circulation on the transport of reactive solutes below a rippled water-sediment interface, *J. Geophys. Res.*, 98C, 10289-10301, 1993.
- Silliman, S. E., J. Ramirez, and R. L. McCabe, Quantifying downflow through creek sediments using temperature time series: one-dimensional solution incorporating measured surface temperature, *J. Hydrol.*, 167, 99-119, 1995.
- Simmons, G. M., Jr., Importance of submarine groundwater discharge (SGWD) and seawater cycling to material flux across sediment/ water interfaces in marine environments, *Mar. Ecol. Prog. Ser.*, 84, 173-184, 1992.
- Smyth, R. L., and J. M. Gephart (eds), *Water: Challenges at the Intersection of Human and Natural Systems*, US Department of Energy, 50 pp., 2005.
- Sophocleous, M., Interactions between groundwater and surface water: the state of the science, *Hydrogeol. J.*, 10(1), 52-67. doi:10.1007/s10040-001-0170-8, 2002.
- Southard, J. B., and L. A. Boguchwal, Bed configurations in steady unidirectional flows. Part 2. Synthesis of flume data, *J. Sed. Pet.*, 60(5), 658-679, 1990.
- Stanford, J. A., and J. V. Ward, The hyporheic habitat of river ecosystems, *Nature*, 335, 64-66, 1988.
- Stonestrom, D. A., and J. Constantz, *Heat as a tool for studying the movement of groundwater near streams*, USGS Circular 1260, USGS, 2003.
- Storey, R. G., K. W. F. Howard, and D. D. Williams, Factors controlling riffle-scale hyporheic exchange and their seasonal changes in a gaining stream: A three-dimensional groundwater flow model, *Water Resour. Res.*, 39(2), 1034, doi:10.1029/2002WR001367, 2003.
- Tachie, M. F., D. F. James, and I. G. Currie, Velocity measurements of a shear flow penetrating a porous medium, *J. Fluid Mech.*, 493, 319-343, 2003.

- Taniguchi, M., J. V. Turner, and A. J. Smith, Evaluations of groundwater discharge rates from subsurface temperature in Cockburn Sound, Western Australia, *Biogeochemistry*, 66, 111-124, 2003.
- Thibodeaux, L. J., and J. D. Boyle, Bed form-generated convective-transport in bottom sediments, *Nature*, 325, 341-343, 1987.
- Thorstenson, D. C., E. P. Weeks, H. Haas, E. Busenberg, L. N. Plummer, and C. A. Peters, Chemistry of unsaturated zone gases sampled in open boreholes at the crest of Yucca Mountain, Nevada: Data and basic concepts of chemical and physical processes in the mountain, *Water Resour. Res.*, 34, 1507-1529, 1998.
- Tóth, J., A theoretical analysis of groundwater flow in small drainage basins, *Jour. Geophys. Res.*, 68(10), 4795-4812, 1963.
- Triska, F. J., V. C. Kennedy, R. J. Avanzino, G. W. Zellweger, and K. E. Bencala, Retention and transport of nutrients in third-order stream in Northwestern California: Hyporheic processes, *Ecology*, 70(6), 1893-1905, 1989.
- Triska, F. J., J. H. Duff, and R. J. Avanzino, The role of water exchange between a stream channel and its hyporheic zone in nitrogen cycling at the terrestrial-aquatic interface, *Hydrobiologia*, 251(1-3), 167-184, 1993.
- van Mierlo, M.C.L.M., and J.C.C. de Ruiter, Turbulence measurements above artificial dunes, Delft Hydraulics Laboratory, Delft, Netherlands, 1988.
- Vanoni, V. A., and L. S. Hwang, Relation between bed forms and friction in streams, *J. Hydr. Div. ASCE*, 93(3), 121-144, 1967.
- Vittal, N., K. G. Rangu Raju, and R. J. Garde, Resistance of two-dimensional triangular roughness, *J. Hydraul. Res.*, 15(1), 19-36, 1977.
- Wagner, F. H., and G. Bretschko, Interstitial flow through preferential flow paths in the hyporheic zone of the Oberer Seebach, Austria, *Aquat. Sci.*, 64(3), 307-316, 2002.
- Ward, J. V., Thermal characteristics of running waters, *Hydrobiologia*, 125, 31-46, 1985.
- Waterloo Hydrogeologic, Inc., *Visual MODFLOW v2.8.2 User's Manual*, 311 pp., 2000.
- Webb, J. E., and J. Theodor, Irrigation of submerged marine sands through wave action, *Nature*, 220, 682-685, 1968.
- Webster, I. T., S. J. Norquay, F. C. Ross, and R. A. Wooding, Solute exchange by convection within estuarine sediments, *Estuar. Coast. Shelf Sci.*, 42, 171-183, 1996.

- Westrich, J. T., and R. A. Berner, The effect of temperature on rates of sulfate reduction in marine sediments, *Geomicrobiol. J.*, 6(2), 99-117, 1988.
- White, D. S., Perspectives on defining and delineating hyporheic zones, *J. N. Am. Benthol. Soc.*, 12(1), 61-69, 1993.
- Wilcox, D. C., A half century historical review of the k- ω model, *AIAA Paper*, 91-0615, 1991.
- Winter, T.C., J. W. Harvey, O. L. Franke, and W. M. Alley, *Ground Water and Surface Water: A Single Resource*, United States Geological Survey Circular 1139, Denver: USGS, 1998.
- Woessner, W. W., Stream and fluvial plain ground water interactions: rescaling hydrogeologic thought, *Ground Water*, 38(3), 423-429, 2000.
- Wondzell, S. M., and F. J. Swanson, Floods, channel change, and the hyporheic zone, *Water Resour. Res.*, 35(2), 555-567, 1999.
- Wondzell, S. M., and F. J. Swanson, Seasonal and storm dynamics of the hyporheic zone of a 4th-order mountain stream. 1. Hydrologic processes, *J. N. Am. Benthol. Soc.*, 15(1), 3-19, 1996.
- Worman, A., Analytical solution and timescale for transport of reactive solutes in rivers and streams, *Water Resour. Res.*, 34(10), 2703-2716, 1998.
- Worman, A., A. I. Packman, H. Johansson, and K. Jonsson, Effect of flow-induced exchange in hyporheic zones on longitudinal transport of solutes in streams and rivers, *Water Resour. Res.*, 38(1), doi:10.1029/2001WR000769, 2002.
- Wroblicky, G. J., M. E. Campana, H. M. Valett, and C. N. Dahm, Seasonal variation in surface-subsurface water exchange and lateral hyporheic area of two stream-aquifer systems, *Water Resour. Res.*, 34(3), 317-328, 1998.
- Wurtsbaugh, W., J. Cole, D. McKnight, P. Brezonik, S. MacIntyre, and K. Potter (eds), *Report on the Workshop on Emerging Research Questions for Limnology: The Study of Inland Waters*, American Society of Limnology and Oceanography, Waco, Texas, 50 pp., 2003.
- Yalin, M. S., *Mechanics of Sediment Transport*, Oxford, Pergamon Press, 1977.
- Yalin, M. S., Steepness of sedimentary dunes, *J. Hydr. Div. ASCE*, 105, 381-392, 1979.
- Yoon, J. Y., and V. C. Patel, Numerical model of turbulent flow over sand dune, *J. Hydr. Eng. ASCE*, 122(1), 10-18, 1996.

Young, P. C., and S. G. Wallis, The aggregated dead zone (ADZ) model for dispersion in rivers, paper presented at International Conference on Water Quality Modeling in the Inland Natural Environment, Bournemouth, England, June 10-13, 1986.

Zheng, C., MT3DMS, A modular three-dimensional multi-species transport model for simulation of advection, dispersion and chemical reactions of contaminants in groundwater systems; documentation and user's guide, U.S. Army Engineer Research and Development Center Contract Report SERDP-99-1, Vicksburg, MS, 202 p., 1999.

Zhou, D., and C. Mendoza, Flow through porous bed of turbulent stream, *J. Eng. Mech. ASCE* 119, 365-383, 1993.

APPENDICES

APPENDIX I

Tabulation of Results from Chapter 3

Data for Results Presented in Figure 3.3.

Re	d_z/L	L_e/L	$q_{int}^* \times 10^6$	A_z/L^2	$(h_{max}-h_{min})/L \times 10^6$
6	0.299	0.000	0.002	0.275	0.001
30	0.423	0.029	0.011	0.389	0.009
59	0.482	0.096	0.028	0.446	0.022
174	0.572	0.232	0.130	0.539	0.100
288	0.616	0.297	0.268	0.579	0.203
569	0.666	0.402	0.750	0.631	0.525
1124	0.716	0.499	2.124	0.682	1.339
1674	0.742	0.554	3.903	0.709	2.313
2221	0.761	0.593	6.638	0.725	3.417
2766	0.773	0.620	9.247	0.738	4.620
3852	0.791	0.656	15.217	0.758	7.277

Data for Results Presented in Figure 3.7

$H/L=0.0385$			$H/L=0.0416$			$H/L=0.0454$		
Re	d_z/L	$q_{int}^* \times 10^6$	Re	d_z/L	$q_{int}^* \times 10^6$	Re	d_z/L	$q_{int}^* \times 10^6$
5	0.254	0.000	5	0.267	0.000	5	0.283	0.000
46	0.438	0.002	49	0.451	0.002	54	0.465	0.002
224	0.575	0.015	241	0.588	0.018	263	0.600	0.021
442	0.630	0.042	477	0.643	0.050	519	0.654	0.060
874	0.682	0.120	1404	0.721	0.262	1026	0.703	0.170
2150	0.745	0.477	2324	0.753	0.562	1529	0.731	0.313
4258	0.788	1.343	3704	0.784	1.140	3770	0.788	1.231
			4629	0.800	1.597	5007	0.805	1.886

$H/L=0.05$			$H/L=0.0555$		
Re	d_z/L	$q_{int}^* \times 10^6$	Re	d_z/L	$q_{int}^* \times 10^6$
6	0.299	0.000	7	0.318	0.000
59	0.482	0.003	65	0.498	0.003
569	0.666	0.081	630	0.678	0.093
1124	0.716	0.229	1245	0.727	0.258
2221	0.761	0.646	1856	0.752	0.471
2766	0.773	0.901	3084	0.784	1.021
3852	0.791	1.482	4319	0.804	1.694

Data for Results Presented in Figure 3.8

Re	500		1000		1500		3000	
	d_z/L	$q_{int}^* \times 10^5$						
0.1	0.683	0.339	0.724	0.958	0.742	1.662	0.764	4.519
0.2	0.683	0.242	0.725	0.697	0.742	1.183	0.759	3.210
0.3	0.685	0.200	0.724	0.585	0.736	0.973	0.75	2.617
0.4	0.683	0.176	0.718	0.509	0.728	0.842	0.729	1.973
0.5	0.676	0.159	0.709	0.428	0.719	0.740	0.73	1.978
0.6	0.669	0.144	0.701	0.380	0.713	0.662	0.729	1.804
0.7	0.661	0.128	0.694	0.348	0.712	0.629	0.737	1.768
0.8	0.655	0.121	0.696	0.340	0.72	0.624	0.757	1.794
0.9	0.655	0.123	0.705	0.352	0.733	0.647	0.778	1.840

APPENDIX II

Tabulation of Results from Chapter 4

Data for Results Presented in Figure 4.3a

$$q_{bas}^* \times 10^6 = 1.8$$

H/L	0.0385		0.0416		0.0454		0.05		0.0555
Re	d/L	Re	d/L	Re	d/L	Re	d/L	Re	d/L
787	0.00	430	0.00	696	0.00	512	0.00	566	0.00
979	0.02	850	0.02	924	0.06	1011	0.10	1120	0.14
1172	0.10	1059	0.08	1376	0.16	1506	0.20	1670	0.23
1554	0.18	1266	0.13	2275	0.29	2518	0.31	2767	0.34
1936	0.23	2094	0.26	3393	0.37	3518	0.39	3862	0.42
3832	0.38	3326	0.36	4506	0.43	4980	0.46		
5735	0.47	4144	0.41						
		4962	0.44						

$$q_{bas}^* \times 10^6 = 5.5$$

H/L	0.0385		0.0416		0.0454		0.05		0.0555
Re	d/L	Re	d/L	Re	d/L	Re	d/L	Re	d/L
398	0.00	1266	0.00	467	0.00	512	0.00	566	0.00
1935	0.06	2093	0.09	2275	0.12	1506	0.02	1670	0.07
2695	0.14	3326	0.19	3393	0.21	1998	0.10	2766	0.18
3831	0.22	4144	0.24	4506	0.27	2518	0.15	3862	0.25
		4961	0.28			3517	0.22		
						4979	0.30		

$$q_{bas}^* \times 10^6 = 9.1$$

H/L	0.0385		0.0416		0.0454		0.05		0.0555
Re	d/L	Re	d/L	Re	d/L	Re	d/L	Re	d/L
1935	0.00	2092	0.00	467	0.00	512	0.00	566	0.00
2694	0.05	3325	0.12	2275	0.05	2517	0.08	2766	0.11
3831	0.14	4143	0.17	3393	0.13	3517	0.15	3861	0.18
		4960	0.21	4507	0.19	4978	0.22		

$q_{bas}^* \times 10^6 = 15$

H/L	0.0385	0.0416	0.0454	0.05	0.0555
Re	d/z	Re	d/z	Re	d/z
2694	0.00	2092	0.00	2275	0.00
3830	0.08	3324	0.05	3393	0.07
		4142	0.10	4506	0.13
		4959	0.14	4977	0.16
				3860	0.12

 $q_{bas}^* \times 10^6 = 18$

H/L	0.0385	0.0416	0.0454	0.05	0.0555
Re	d/z	Re	d/z	Re	d/z
1934	0.00	2092	0.00	2275	0.00
3829	0.05	3323	0.02	3393	0.04
		4141	0.07	4506	0.10
		4958	0.11	4975	0.13
				2764	0.00
				3859	0.09

Data for Results Presented in Figure 4.3b

$q_{bas} * x10^6$		0		1.8		5.5	
Re	$q_{int} * x10^5$	Re	$q_{int} * x10^5$	Re	$q_{int} * x10^5$	Re	$q_{int} * x10^5$
4.6	0.0001	849	0.0000	1505	0.0000		
5.0	0.0001	923	0.0152	1670	0.0650		
5.5	0.0001	979	0.0128	1935	0.0544		
6	0.0002	1011	0.0460	1998	0.1552		
7	0.0002	1059	0.0372	2093	0.1288		
46	0.0015	1120	0.0961	2275	0.2345		
49	0.0018	1172	0.0559	2518	0.3956		
54	0.0023	1266	0.0941	2695	0.3380		
59	0.0030	1376	0.1451	2766	0.5877		
65	0.0035	1506	0.2134	3326	0.6895		
224	0.0150	1554	0.1705	3393	0.7930		
241	0.0179	1670	0.3109	3517	0.9434		
263	0.0213	1936	0.3068	3831	0.8952		
442	0.0422	2094	0.3960	3862	1.2618		
477	0.0499	2275	0.5088	4144	1.1436		
519	0.0596	2518	0.6726	4506	1.4617		
569	0.0810	2767	0.8622	4961	1.6443		
630	0.0932	3326	0.9775	4979	1.8832		
874	0.1203	3393	1.0756				
1026	0.1697	3518	1.2209				
1124	0.2291	3832	1.1850				
1245	0.2578	3862	1.5311				
1404	0.2623	4144	1.4291				
1529	0.3129	4506	1.7376				
1856	0.4715	4962	1.9245				
2150	0.4769	4980	2.1508				
2221	0.6464						
2324	0.5622						
2766	0.9005						
3084	1.0210						
3704	1.1399						
3770	1.2315						
3852	1.4819						
4258	1.3425						
4319	1.6944						
4629	1.5966						
5007	1.8861						

Data for Results Presented in Figure 4.3b (cont.)

$q_{bas} * 10^6$	9.1		15		18	
	Re	$q_{int} * 10^5$	Re	$q_{int} * 10^5$	Re	$q_{int} * 10^5$
2092	0.0000		2693	0.0000	2764	0.0000
2274	0.0406		2764	0.0816	3323	0.0125
2517	0.1732		3323	0.1434	3392	0.0780
2694	0.1180		3393	0.2336	3515	0.1969
2766	0.3527		3516	0.3727	3859	0.4843
3325	0.4400		3830	0.3106	4141	0.3458
3393	0.5433		3860	0.6806	4506	0.6470
3517	0.6940		4142	0.5412	4958	0.8065
3831	0.6372		4506	0.8558	4975	1.0646
3861	1.0142		4959	1.0239		
4143	0.8838		4977	1.2808		
4507	1.2051					
4960	1.3830					
4978	1.6315					

Data for Results Presented in Figure 4.4

$q_{bas} *$	$Re_{crit} (d/L)$	$Re_{crit} (q_{int} *)$
0	0.00	0
1.8×10^{-8}	41	234
1.8×10^{-7}	182	404
1.8×10^{-6}	786	1078
5.5×10^{-6}	1325	1805
9.1×10^{-6}	1777	2309
1.5×10^{-5}	2516	2872
1.8×10^{-5}	2855	3217

Data for Results Presented in Figure 4.5a and 4.5b

$q_{bas} * 10^7$	$t^* \times 10^{-6}$	$q_{int} * 10^7$	A^*
0.00	2.72	3.68	1.000
0.18	2.58	3.57	0.921
0.55	1.94	3.36	0.653
0.92	1.64	3.16	0.519
1.28	1.48	2.96	0.439
1.83	1.29	2.67	0.344

APPENDIX III

Discussion of CFD-ACE+ k - ω model and Tabulation of Results from Chapter 5

Discussion CFD-ACE+ k - ω model

The k - ω closure scheme for the Reynolds-averaged Navier-Stokes equations has had many variants since its inception. The equations implemented and numerically solved in CFD-ACE+, the software used in this dissertation, are compared with the “standard” version presented in *Wilcox* [1991].

CFD-ACE+:

$$\frac{\partial(\rho k)}{\partial t} + \frac{\partial(\rho u_j k)}{\partial x_j} = \rho P^* - \rho \omega k + \frac{\partial}{\partial x_j} \left[\left(\mu + \frac{\mu_t}{\sigma_k} \right) \frac{\partial k}{\partial x_j} \right]$$

$$\frac{\partial(\rho \omega)}{\partial t} + \frac{\partial(\rho u_j \omega)}{\partial x_j} = C_{\omega 1} \frac{\rho P \omega^*}{k} - C_{\omega 2} \rho \omega^2 + \frac{\partial}{\partial x_j} \left[\left(\mu + \frac{\mu_t}{\sigma_\omega} \right) \frac{\partial \omega}{\partial x_j} \right]$$

where

$$P^* = \nu_i \left(\frac{\partial u_i}{\partial x_j} + \frac{\partial u_j}{\partial x_i} + \frac{2}{3} \frac{\partial u_m}{\partial x_m} \delta_{ij} \right) \frac{\partial u_i}{\partial x_j} - \frac{2}{3} k \frac{\partial u_m}{\partial x_m}$$

$$C_{\mu}=9/100, C_{\omega 1}=5/9, C_{\omega 2}=0.833, \sigma_k=\sigma_\omega=2.0$$

Wilcox:

$$\frac{\partial(\rho k)}{\partial t} + \rho \frac{\partial(u_j k)}{\partial x_j} = \rho \tau_{ij} \frac{\partial u_i}{\partial x_j} - \beta^* \rho \omega k + \frac{\partial}{\partial x_j} \left[(\mu + \mu_t \sigma^*) \frac{\partial k}{\partial x_j} \right]$$

$$\frac{\partial(\rho\omega)}{\partial t} + \rho \frac{\partial(u_j\omega)}{\partial x_j} = \alpha \frac{\omega}{k} \tau_{ij} \frac{\partial u_i}{\partial x_j} - \beta \rho \omega^2 + \frac{\partial}{\partial x_j} \left[\left(\mu + \mu_t \sigma \right) \frac{\partial \omega}{\partial x_j} \right]$$

where

$$\tau_{ij} = -\overline{\rho u'_j u'_i} = \nu_t (2S_{ij}) - \frac{2}{3} \rho \delta_{ij} k = \nu_t \left(\frac{\partial u_i}{\partial x_j} + \frac{\partial u_j}{\partial x_i} \right) - \frac{2}{3} \rho k \delta_{ij}$$

$$\alpha=5/9, \beta=3/40, \beta^*=9/100, \sigma=\sigma^*=0.5$$

Comparing the ACE+ implementation with the Wilcox model in the reference, all the closure coefficients are the same except β when compared to $C_{\omega 2}$

$$C_{\omega 2}=0.833 \text{ and } \beta=3/40$$

In the ACE+ model, the second term on the RHS of k equation is: $\rho\omega k$

while in the Wilcox model, this term is replaced with: $\beta^* \rho \omega k$

From this we can find that: $\omega=\beta^* \varpi$

Substituting the equation into the ω equation of ACE+ and divide all terms with β^* , we have:

$$\frac{\partial(\rho\varpi)}{\partial t} + \frac{\partial(\rho u_j \varpi)}{\partial x_j} = C_{\omega 1} \frac{\rho P^* \varpi^*}{k} - C_{\omega 2} \beta^* \rho \varpi^2 + \frac{\partial}{\partial x_j} \left[\left(\mu + \frac{\mu_t}{\sigma_\omega} \right) \frac{\partial \varpi}{\partial x_j} \right]$$

Comparing with the ω equation of Wilcox, it can be easily found that:

$$\beta = C_{\omega 2} \beta^*$$

The output ω from CFD-ACE+ needs to be scaled by β^* , as the output is actually ϖ . All other quantities of turbulence and the flow field are unchanged.

Results of model validation with the experiments of van Mierlo and de Ruiter [1988].

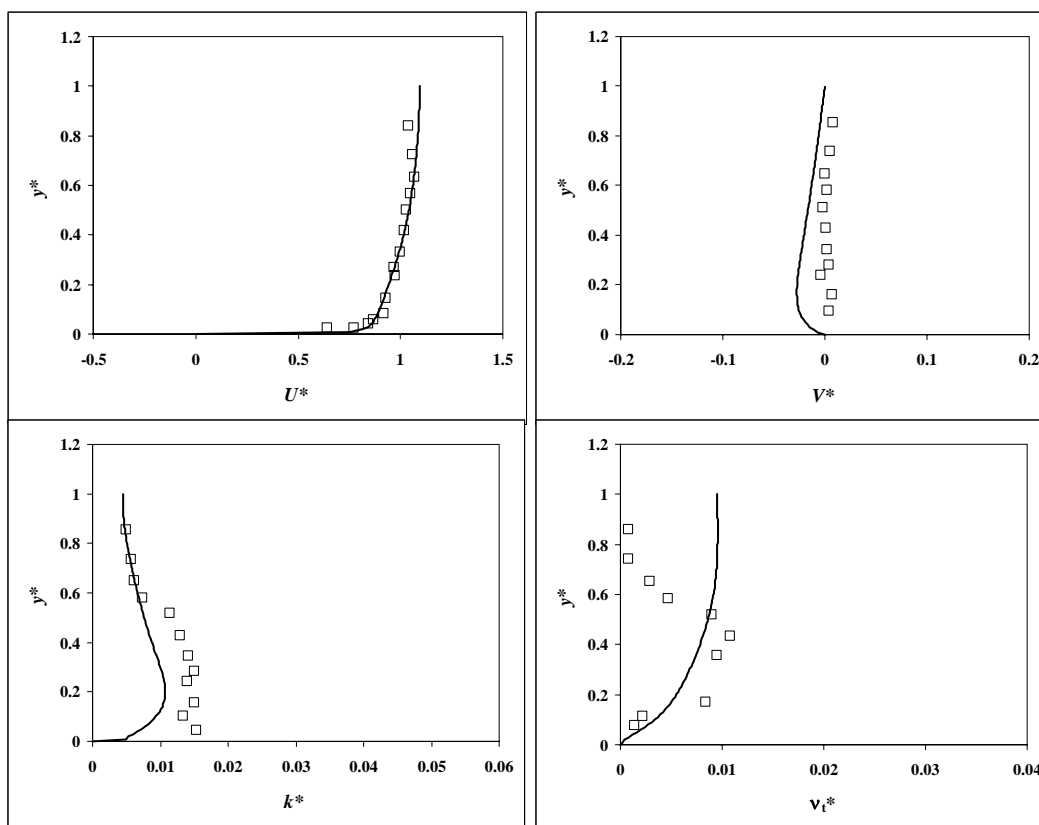
Nondimensionalization follows that of van Mierlo and de Ruiter [1988]. Dimensionless horizontal velocities, as well as station locations, are also presented in Figure 5.2.

Key to symbols (* denotes dimensionless)

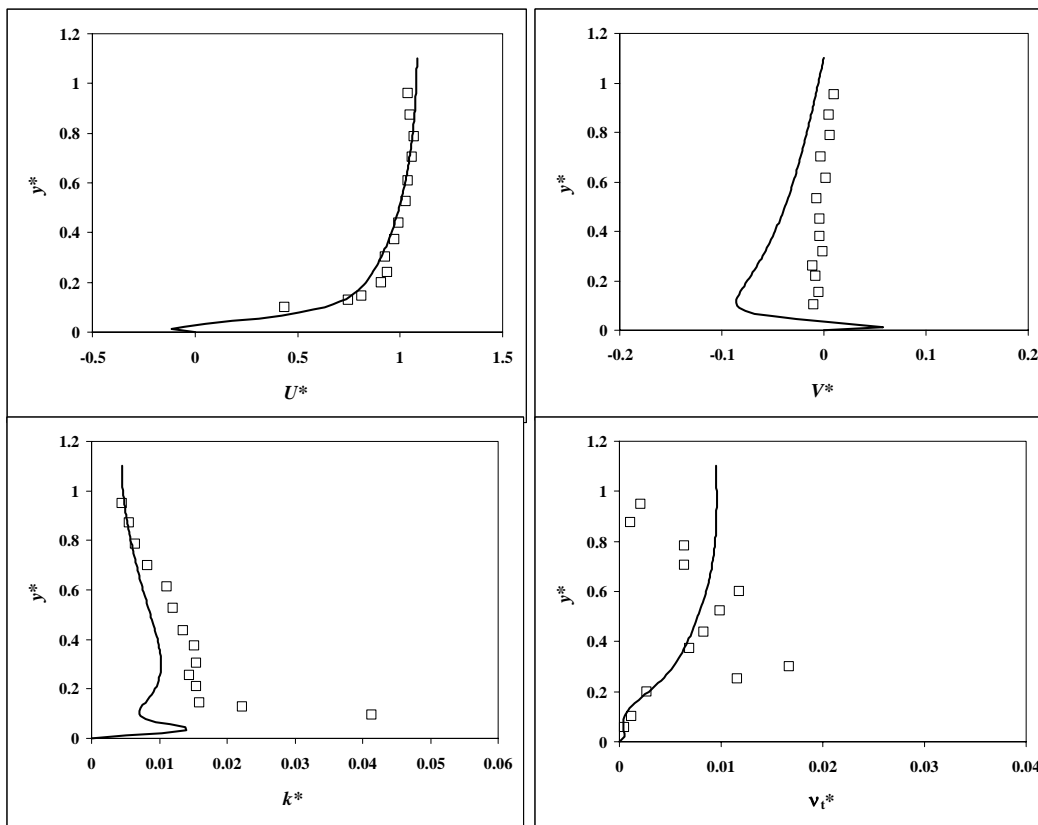
U^* = average horizontal velocity V^* = average horizontal velocity

k^* = turbulent kinetic energy ν_t^* = eddy viscosity

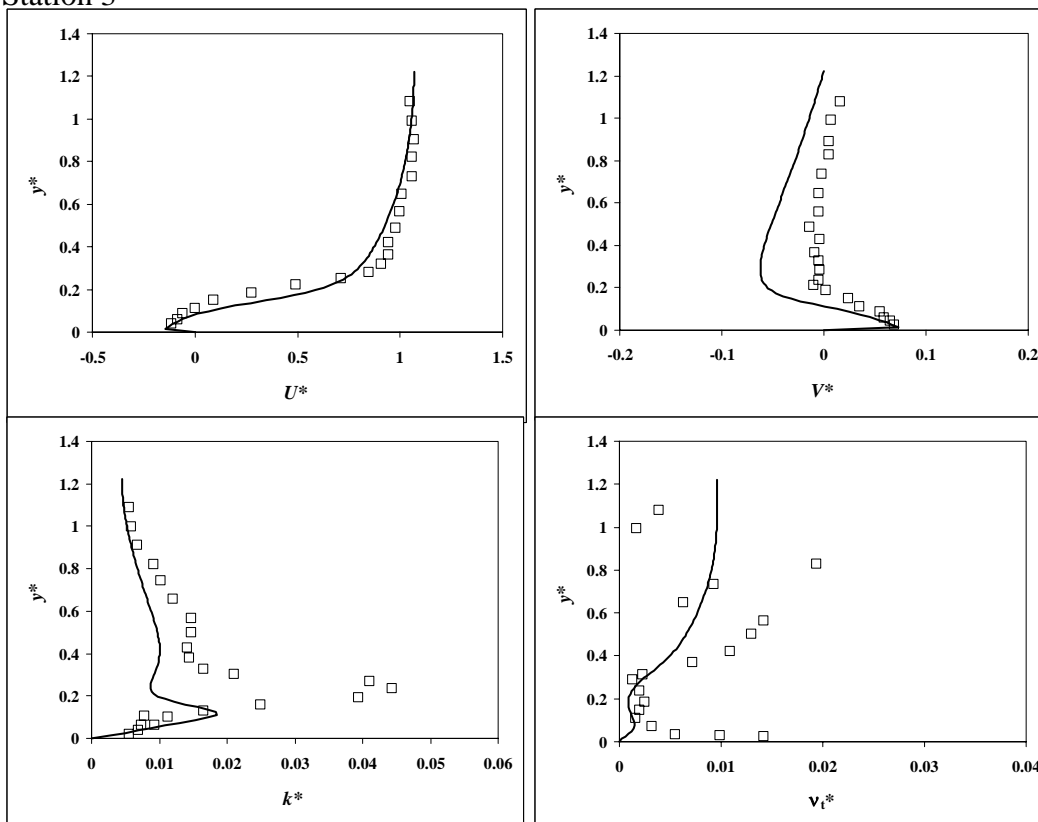
Station 1



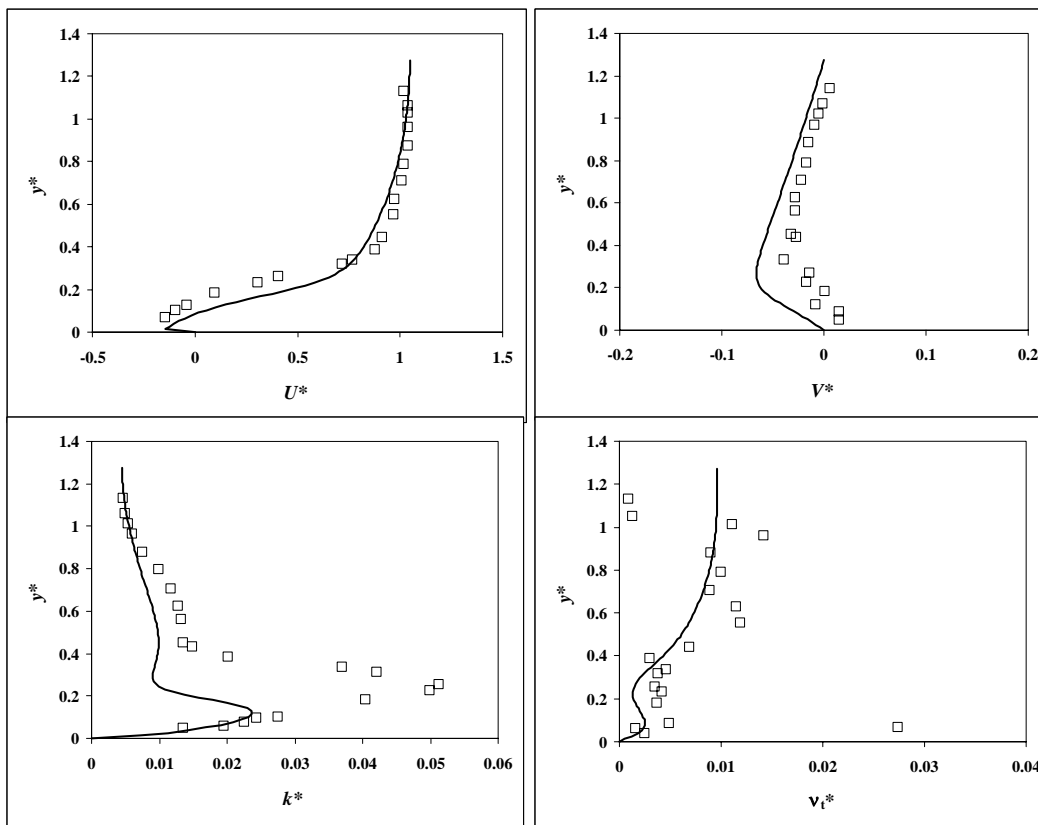
Station 2



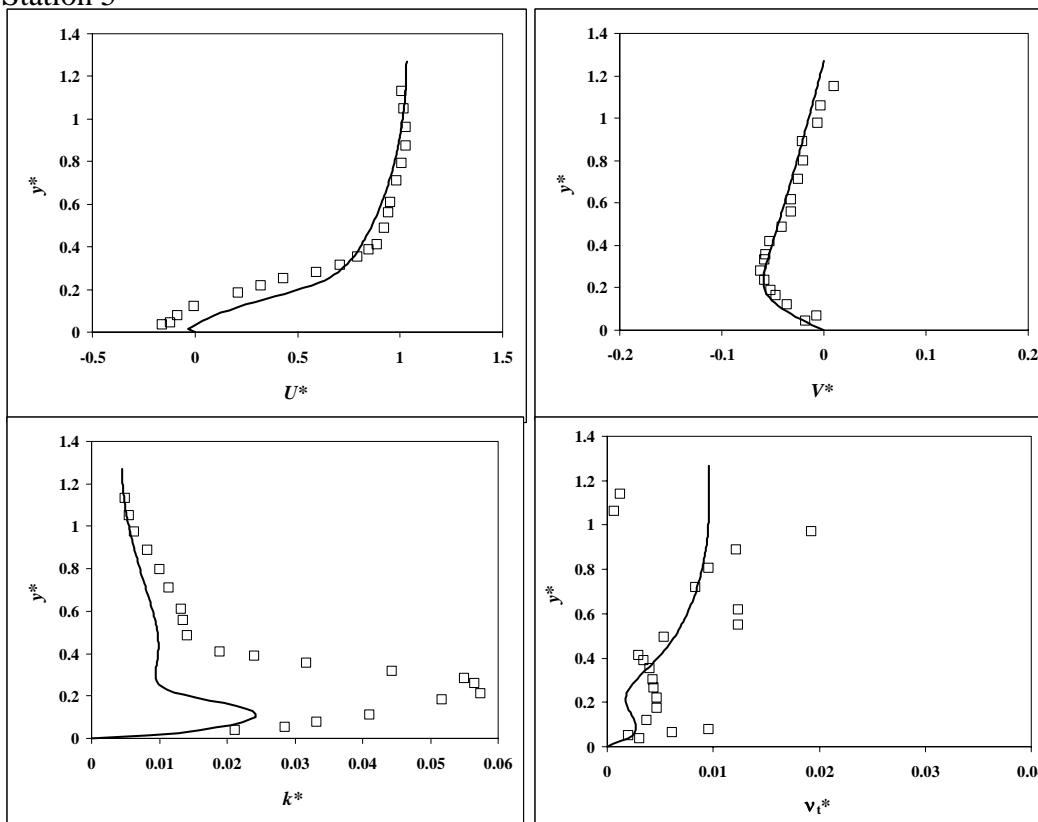
Station 3



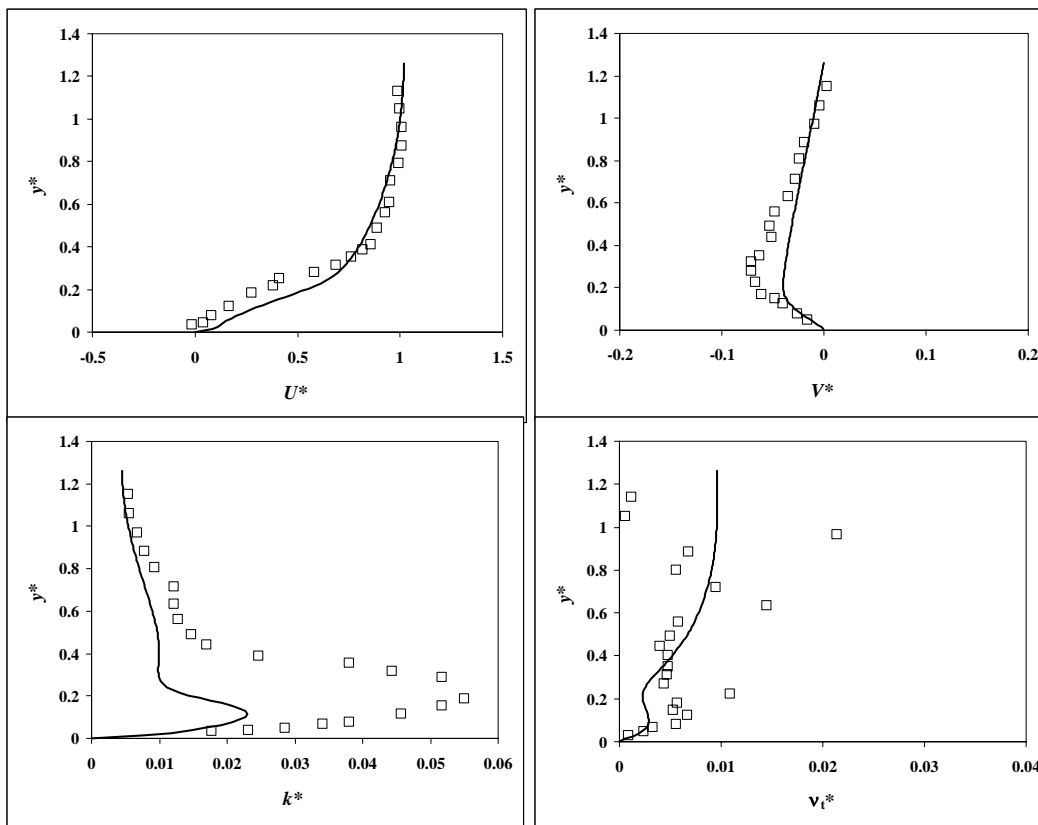
Station 4



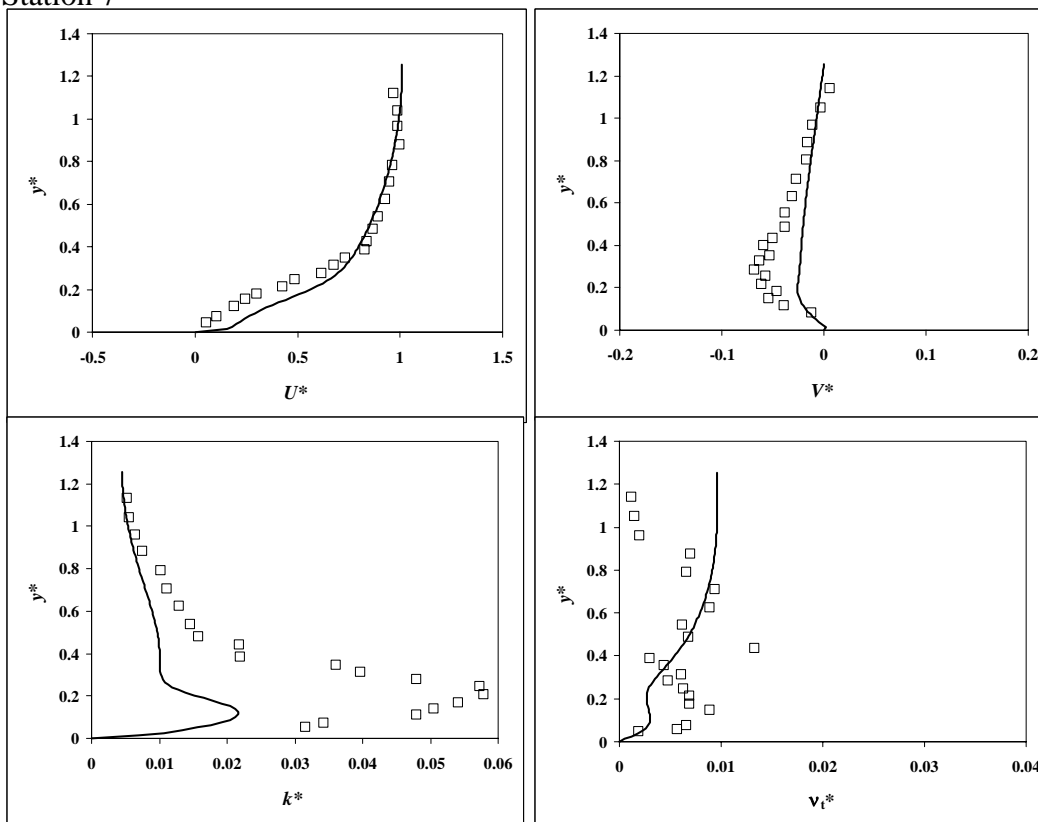
Station 5



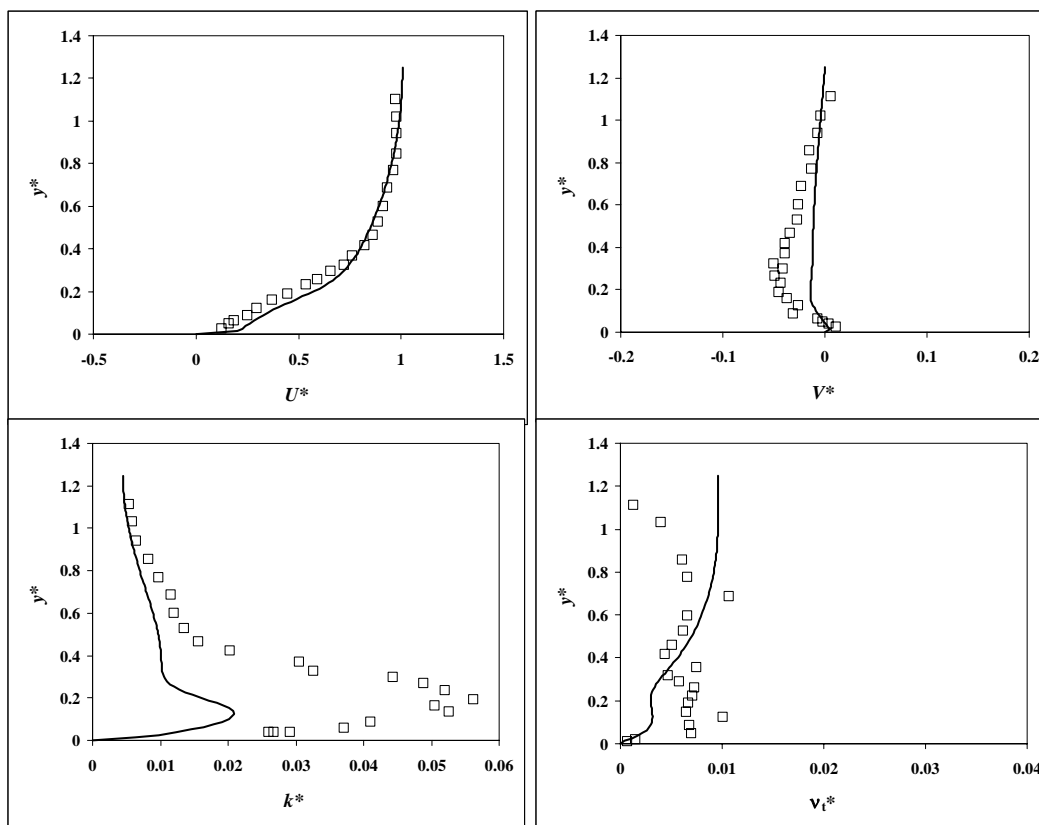
Station 6



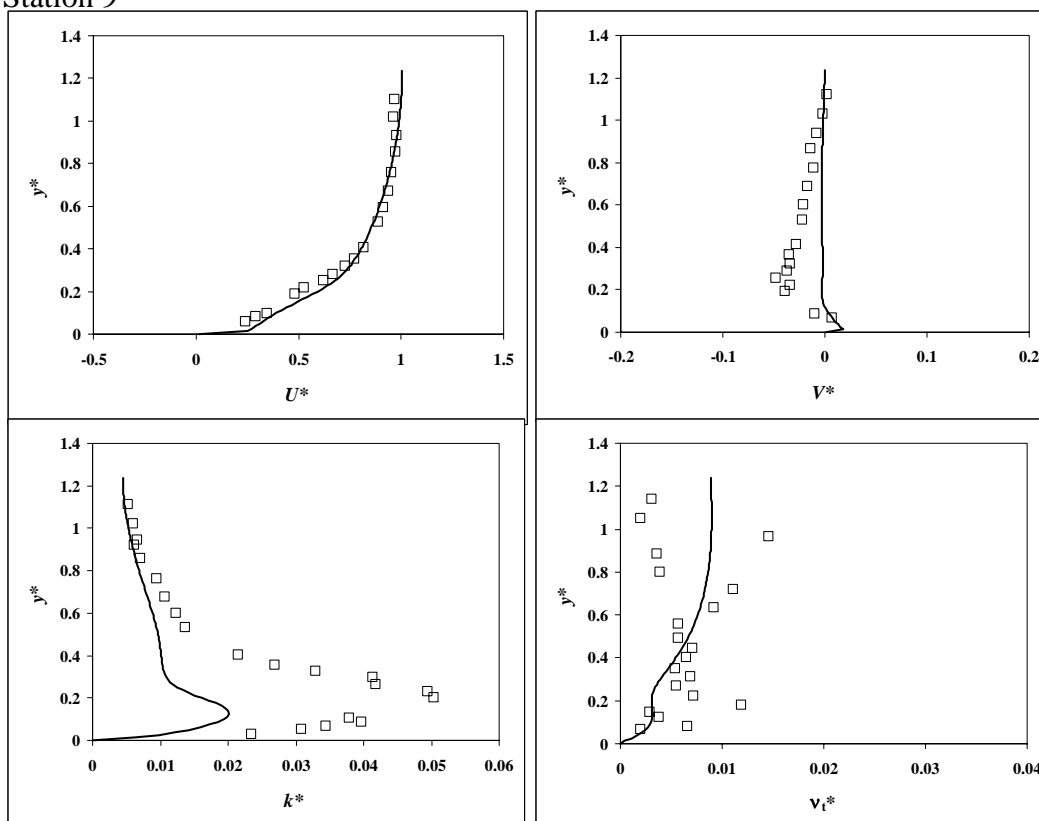
Station 7



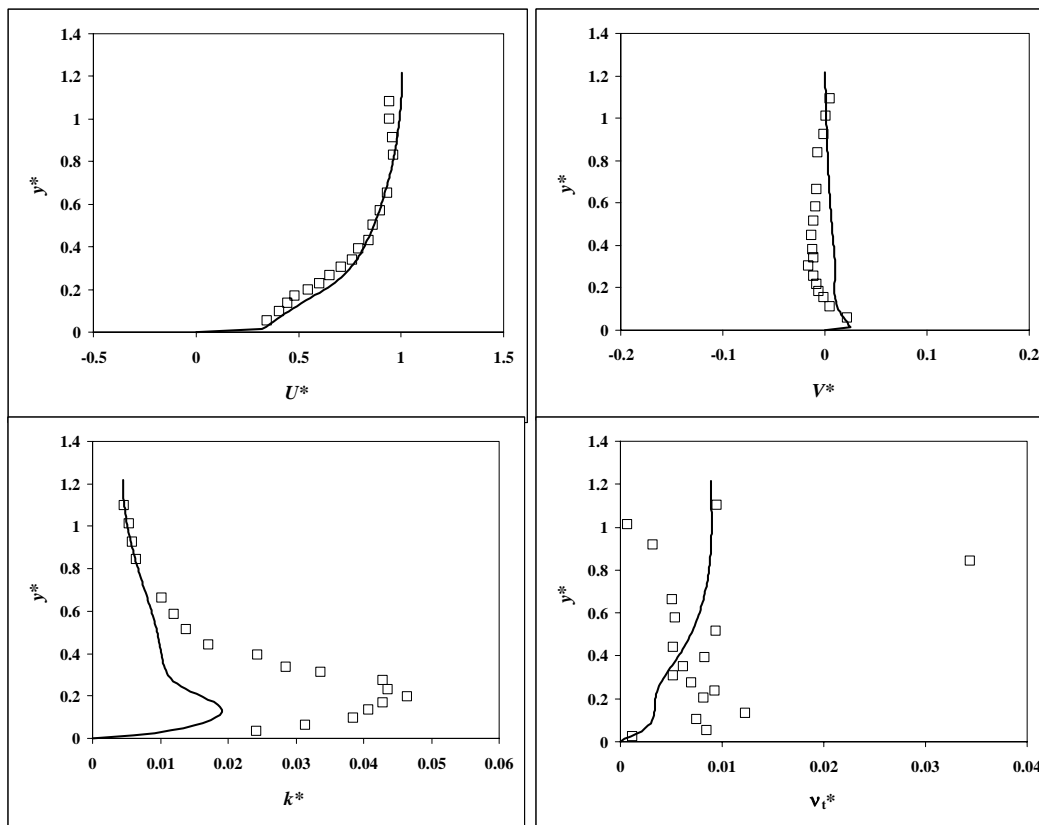
Station 8



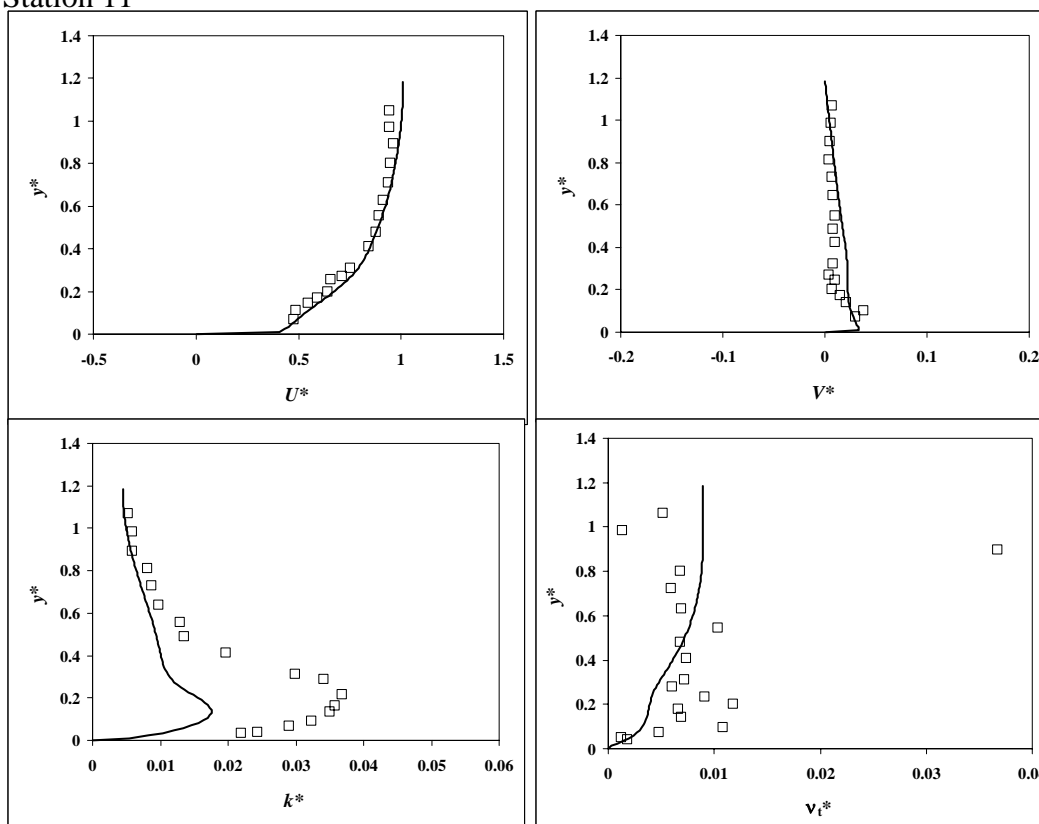
Station 9



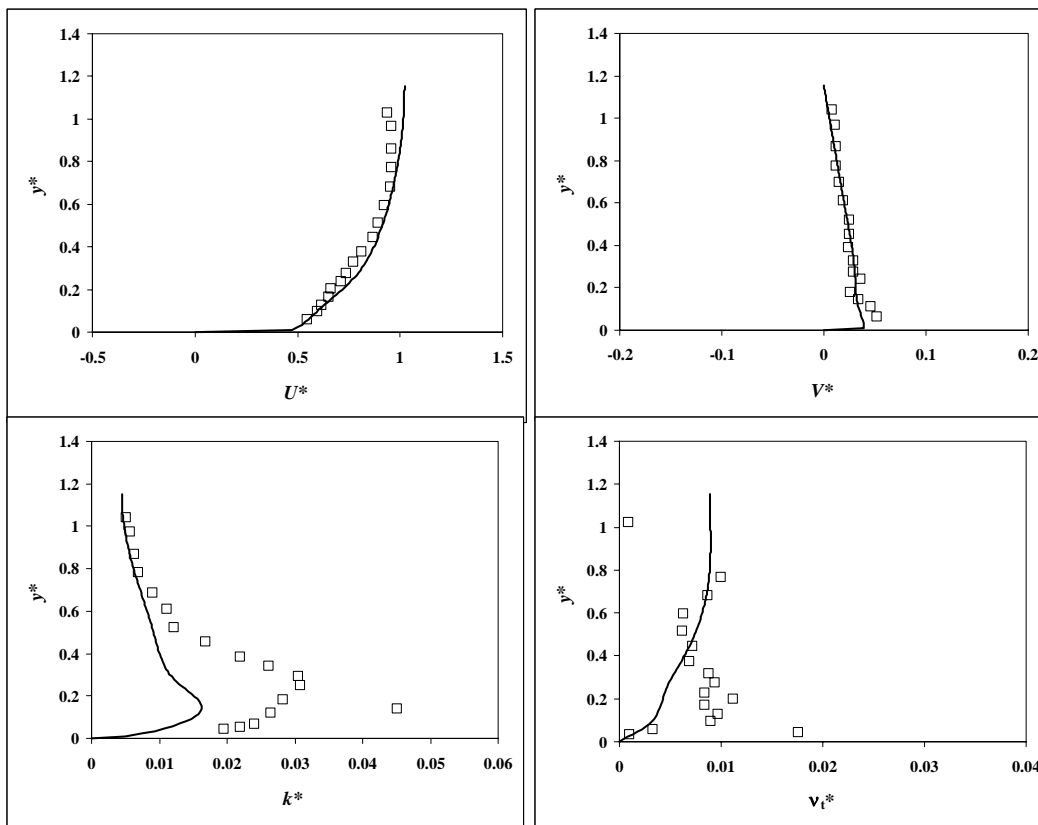
Station 10



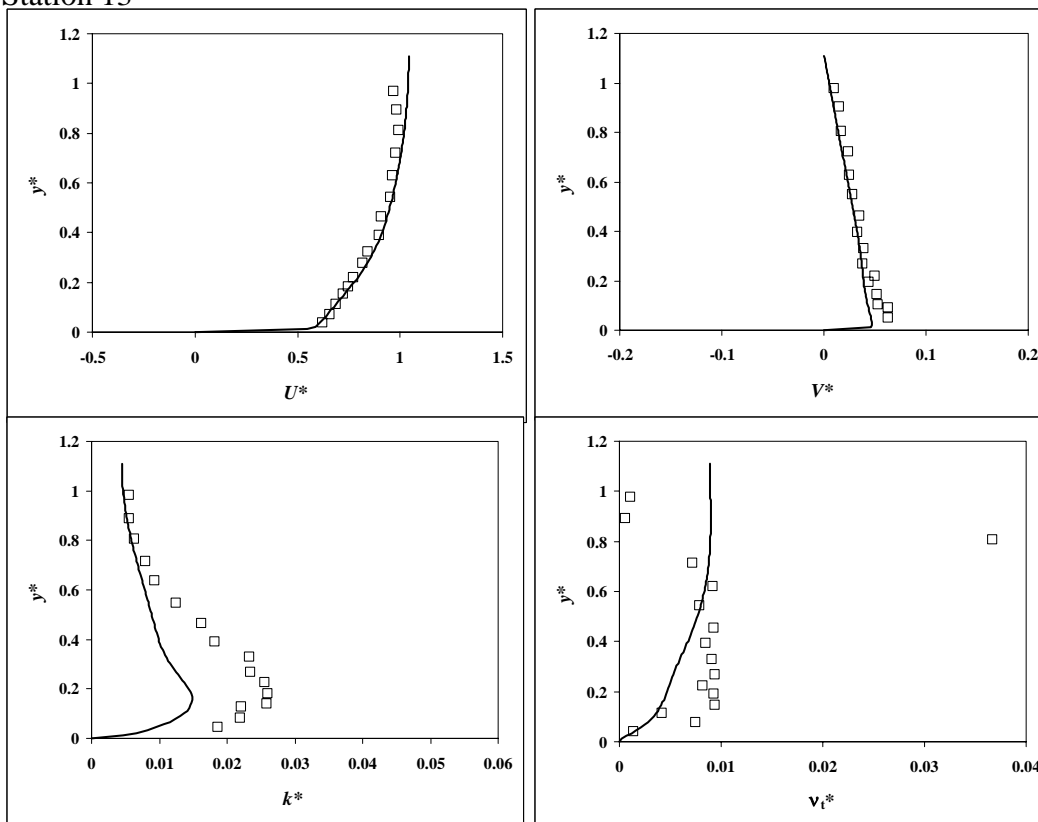
Station 11



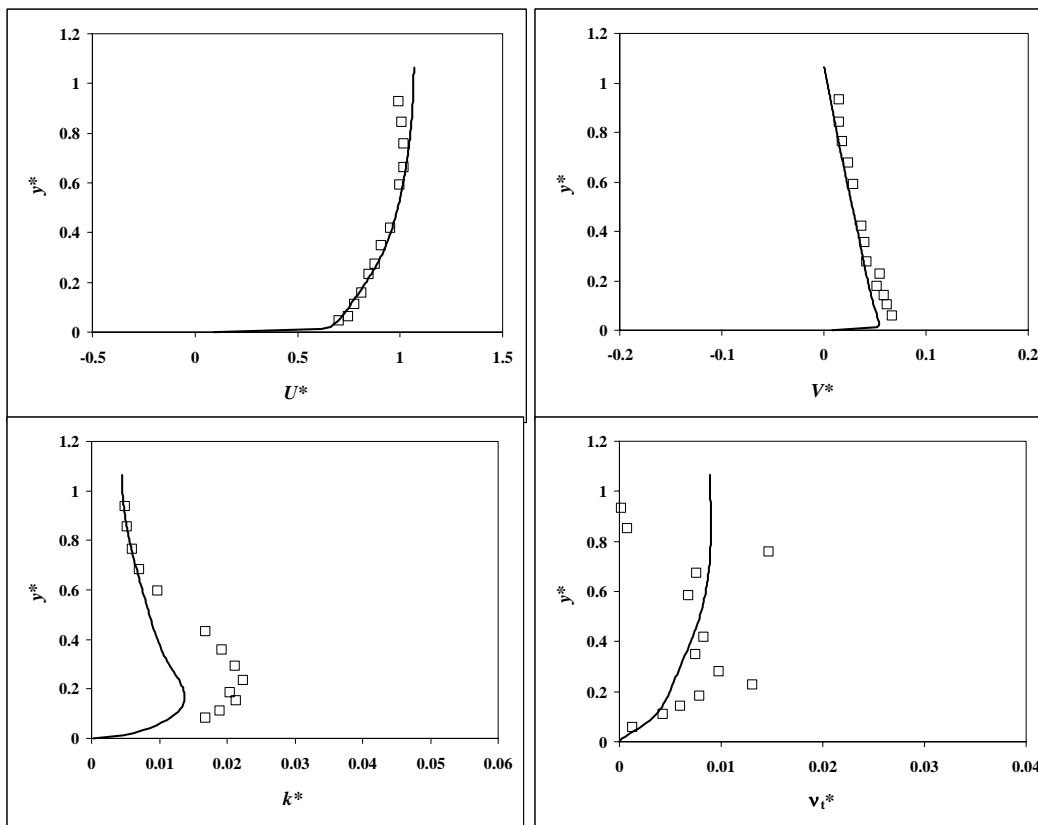
Station 12



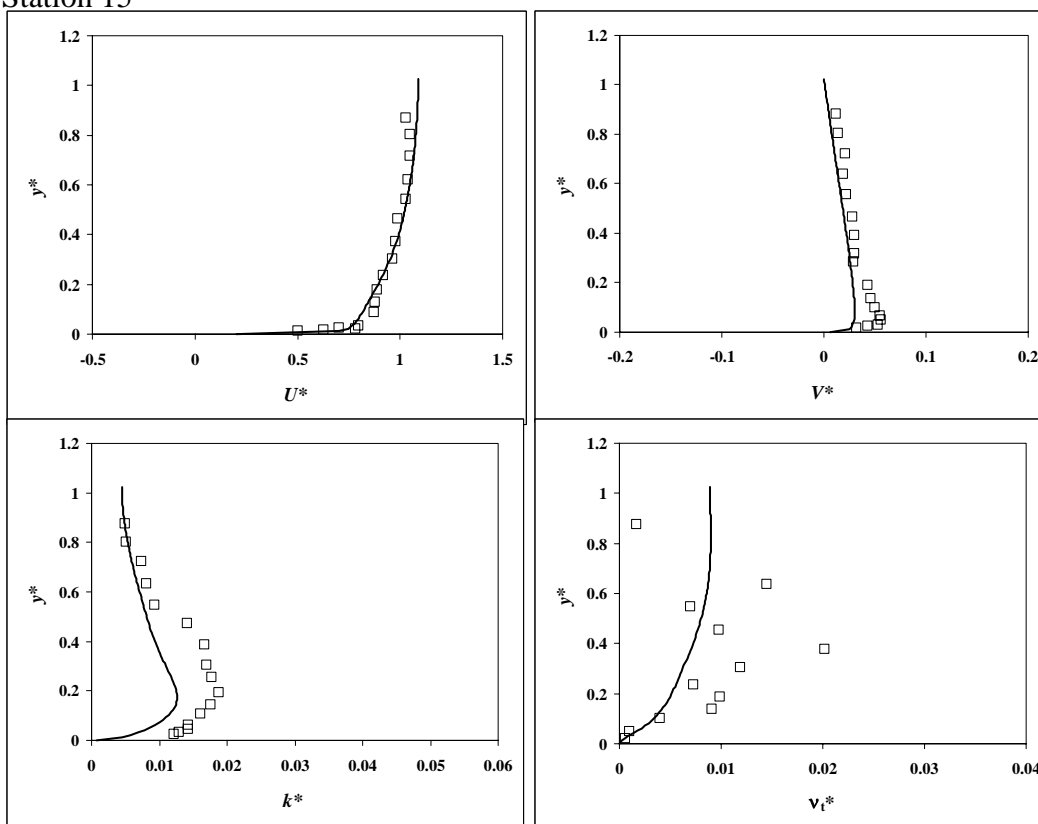
Station 13



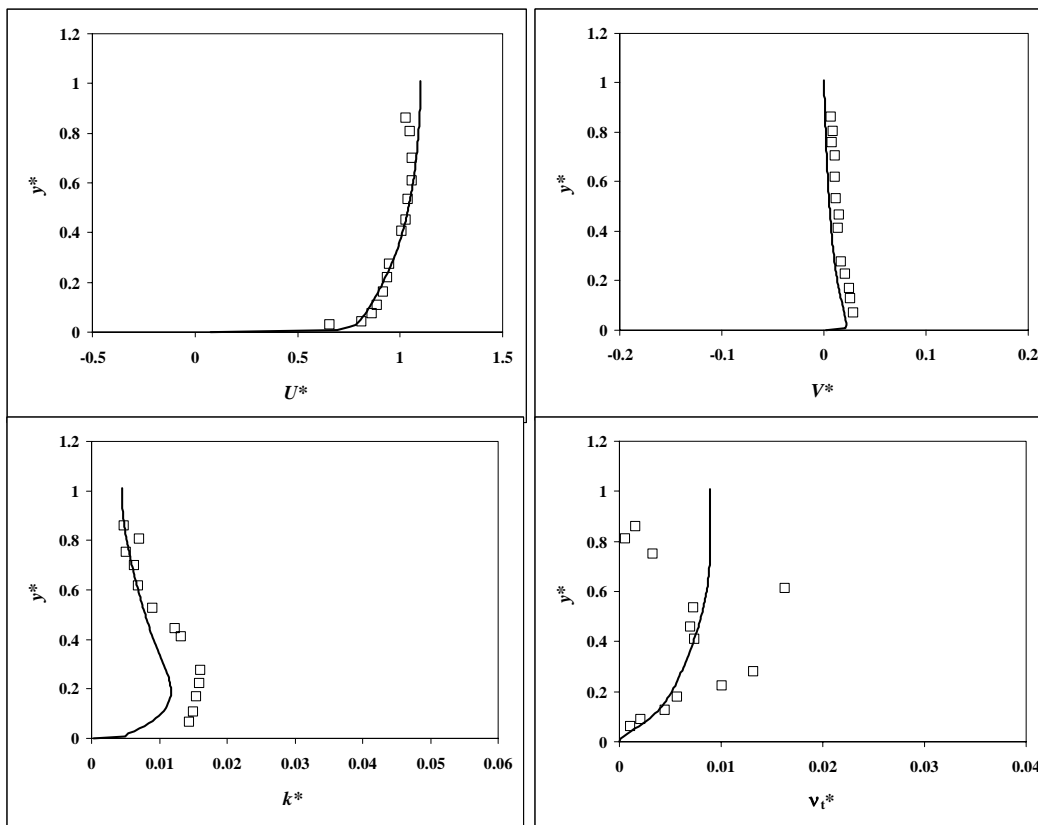
Station 14



Station 15



Station 16



Data for Results Presented in Figure 5.5c

$H/L = 0.03$		$H/L = 0.04$		$H/L = 0.05$		$H/L = 0.06$		$H/L = 0.075$	
Re	L_c/H	Re	L_c/H	Re	L_c/H	Re	L_c/H	Re	L_c/H
42	1.353	51	7.516	68	3.606	81	3.873	97	3.830
99	4.047	133	4.729	164	4.930	202	4.896	244	4.450
109	4.047	145	4.729	178	4.726	217	4.811	260	4.312
184	4.552	248	4.729	309	4.930	363	4.726	445	4.450
272	4.888	371	5.236	458	5.134	541	4.896	660	4.794
521	5.898	645	5.743	744	5.541	836	5.323	947	5.139
777	6.067	954	5.489	1094	5.439	1229	5.152	1400	5.001
1127	5.562	1368	5.362	1557	5.235	1743	5.067	1976	4.863
1964	5.393	2365	4.982	2686	5.032	3026	4.811	3492	4.725
2784	5.057	3308	4.982	3719	4.828	4166	4.726	4757	4.657
3337	4.888	4054	4.856	4528	4.828	5061	4.640	5748	4.588
3905	4.888	4579	4.856	5223	4.828	5824	4.640	6594	4.588
4418	4.720	5146	4.729	5750	4.828	6510	4.555	7347	4.519
4885	4.720	5670	4.729	6268	4.828	7045	4.555	8038	4.519
5319	4.552	6155	4.602	6786	4.726	7550	4.555	8672	4.519
5727	4.552	6607	4.602	7271	4.726	8076	4.555	9166	4.519
6479	4.552	7437	4.602	8159	4.726	9055	4.555	10168	4.450
7168	4.383	8192	4.476	8963	4.624	9942	4.555	11140	4.450
7808	4.383	8890	4.476	9702	4.624	10760	4.555	12045	4.450
8409	4.383	9542	4.476	10395	4.624	11522	4.555	12889	4.450
8974	4.215	10158	4.349	11044	4.624	12238	4.384	13677	4.450
9511	4.215	10741	4.349	11659	4.624	12916	4.384	14424	4.381
10514	4.215	11803	4.349	12780	4.522	14317	4.384	16001	4.381
11448	4.047	12800	4.349	13972	4.522	15480	4.384	17304	4.381
12335	4.047	13787	4.222	14844	4.522	16425	4.299	18310	4.381
13166	4.047	14631	4.222	15885	4.522	17590	4.299	19632	4.381
13965	4.047	15476	4.222	16758	4.420	18548	4.299	20686	4.312
15816	3.878	17441	4.095	18701	4.420	20758	4.299	23118	4.312
17460	3.878	19405	4.095	20656	4.420	22842	4.214	25323	4.312
19027	3.878	20893	4.095	22144	4.420	24492	4.214	27355	4.312
20479	3.878	22602	4.095	23903	4.318	26399	4.214	29345	4.243

Data for Results Presented in Figure 5.6b

$H/L = 0.03$		$H/L = 0.04$		$H/L = 0.05$		$H/L = 0.06$		$H/L = 0.075$	
Re	d_z/L	Re	d_z/L	Re	d_z/L	Re	d_z/L	Re	d_z/L
42	0.743	51	0.831	68	0.786	81	0.802	97	0.811
99	0.769	133	0.805	164	0.828	202	0.851	244	0.870
109	0.708	145	0.739	178	0.757	217	0.775	260	0.789
184	0.648	248	0.677	309	0.692	363	0.699	445	0.506
272	0.665	371	0.691	458	0.701	541	0.705	660	0.706
521	0.685	645	0.684	744	0.674	836	0.662	947	0.641
777	0.708	954	0.704	1094	0.691	1229	0.68	1400	0.660
1127	0.721	1368	0.712	1557	0.696	1743	0.684	1976	0.662
1964	0.758	2365	0.745	2686	0.727	3026	0.717	3492	0.703
2784	0.762	3308	0.743	3719	0.721	4166	0.710	4757	0.691
3337	0.756	4054	0.744	4528	0.72	5061	0.707	5748	0.687
3905	0.763	4579	0.737	5223	0.718	5824	0.706	6594	0.686
4418	0.768	5146	0.74	5750	0.714	6510	0.706	7347	0.684
4885	0.772	5670	0.742	6268	0.714	7045	0.701	8038	0.684
5319	0.775	6155	0.744	6786	0.715	7550	0.699	8672	0.682
5727	0.779	6607	0.746	7271	0.716	8076	0.700	9166	0.679
6479	0.784	7437	0.749	8159	0.717	9055	0.701	10168	0.677
7168	0.789	8192	0.751	8963	0.717	9942	0.702	11140	0.678
7808	0.792	8890	0.753	9702	0.719	10760	0.702	12045	0.678
8409	0.796	9542	0.755	10395	0.719	11522	0.703	12889	0.679
8974	0.799	10158	0.757	11044	0.72	12238	0.703	13677	0.679
9511	0.801	10741	0.758	11659	0.72	12916	0.704	14424	0.679
10514	0.806	11803	0.76	12780	0.721	14317	0.707	16001	0.683
11448	0.809	12800	0.762	13972	0.724	15480	0.708	17304	0.684
12335	0.813	13787	0.764	14844	0.723	16425	0.706	18310	0.680
13166	0.816	14631	0.765	15885	0.725	17590	0.709	19632	0.683
13965	0.818	15476	0.767	16758	0.726	18548	0.709	20686	0.683
15816	0.824	17441	0.771	18701	0.726	20758	0.709	23118	0.683
17460	0.827	19405	0.777	20656	0.728	22842	0.710	25323	0.683
19027	0.831	20893	0.777	22144	0.728	24492	0.708	27355	0.683
20479	0.834	22602	0.78	23903	0.730	26399	0.710	29345	0.683

Data for Results Presented in Figure 5.6c

$H/L = 0.03$		$H/L = 0.04$		$H/L = 0.05$		$H/L = 0.06$		$H/L = 0.075$	
Re	q_{int}^* $\times 10^3$	Re	q_{int}^* $\times 10^3$						
42	1.2E-05	51	1.9E-05	68	2.0E-05	81	2.2E-05	97	2.4E-05
99	6.9E-05	133	8.5E-05	164	1.2E-04	202	1.4E-04	244	1.7E-04
109	9.5E-05	145	1.1E-04	178	1.5E-04	217	1.8E-04	260	2.1E-04
184	3.7E-04	248	4.2E-04	309	5.5E-04	363	5.8E-04	445	6.1E-04
272	0.001	371	0.001	458	0.001	541	0.001	660	0.001
521	0.002	645	0.002	744	0.002	836	0.002	947	0.002
777	0.006	954	0.005	1094	0.005	1229	0.005	1400	0.005
1127	0.013	1368	0.011	1557	0.011	1743	0.011	1976	0.009
1964	0.041	2365	0.036	2686	0.036	3026	0.035	3492	0.031
2784	0.084	3308	0.071	3719	0.071	4166	0.067	4757	0.059
3337	0.123	4054	0.106	4528	0.106	5061	0.100	5748	0.087
3905	0.174	4579	0.135	5223	0.142	5824	0.133	6594	0.116
4418	0.229	5146	0.172	5750	0.171	6510	0.167	7347	0.145
4885	0.287	5670	0.211	6268	0.205	7045	0.195	8038	0.173
5319	0.350	6155	0.252	6786	0.242	7550	0.226	8672	0.200
5727	0.416	6607	0.293	7271	0.279	8076	0.261	9166	0.224
6479	0.556	7437	0.380	8159	0.357	9055	0.331	10168	0.280
7168	0.705	8192	0.470	8963	0.433	9942	0.402	11140	0.339
7808	0.863	8890	0.564	9702	0.510	10760	0.474	12045	0.400
8409	1.037	9542	0.661	10395	0.604	11522	0.547	12889	0.459
8974	1.200	10158	0.760	11044	0.686	12238	0.621	13677	0.519
9511	1.382	10741	0.862	11659	0.770	12916	0.696	14424	0.579
10514	1.762	11803	1.066	12780	0.935	14317	0.865	16001	0.720
11448	2.165	12800	1.282	13972	1.135	15480	1.023	17304	0.847
12335	2.591	13787	1.519	14844	1.293	16425	1.159	18310	0.951
13166	3.028	14631	1.738	15885	1.498	17590	1.343	19632	1.101
13965	3.483	15476	1.979	16758	1.681	18548	1.503	20686	1.228
15816	4.668	17441	2.605	18701	2.122	20758	1.911	23118	1.549
17460	5.872	19405	3.339	20656	2.647	22842	2.345	25323	1.874
19027	7.160	20893	3.964	22144	3.078	24492	2.709	27355	2.204
20479	8.470	22602	4.769	23903	3.643	26399	3.193	29345	2.556

Data for Simulation Results for $H/L=0.05$

Re	d_z/L	$q_{int}^* \times 10^3$	A_z/L^2	t_r^*
2686	0.727	0.036	0.690	19443
3719	0.721	0.071	0.683	9802
4528	0.72	0.106	0.680	6509
5223	0.718	0.142	0.684	4896
5750	0.714	0.171	0.675	4009
7271	0.716	0.279	0.688	2499
10395	0.719	0.604	0.682	1144
16758	0.726	1.681	0.694	418
20656	0.728	2.647	0.694	265

Data for Results Presented in Figure 5.9a

$H/L = 0.03$		$H/L = 0.04$		$H/L = 0.05$		$H/L = 0.06$		$H/L = 0.075$	
Re	$h_{int}/L \times 10^3$	Re	$h_{int}/L \times 10^3$						
42	1.9E-05	51	3.5E-05	68	2.8E-05	81	3.2E-05	97	3.5E-05
99	1.1E-04	133	1.4E-04	164	1.8E-04	202	2.1E-04	244	2.3E-04
109	1.6E-04	145	1.9E-04	178	2.3E-04	217	2.6E-04	260	2.8E-04
184	0.001	248	0.001	309	0.001	363	0.001	445	0.001
272	0.002	371	0.002	458	0.002	541	0.002	660	0.002
521	0.004	645	0.003	744	0.003	836	0.003	947	0.003
777	0.009	954	0.008	1094	0.007	1229	0.007	1400	0.006
1127	0.020	1368	0.017	1557	0.016	1743	0.014	1976	0.012
1964	0.069	2365	0.057	2686	0.049	3026	0.046	3492	0.039
2784	0.150	3308	0.118	3719	0.098	4166	0.090	4757	0.075
3337	0.225	4054	0.184	4528	0.149	5061	0.135	5748	0.111
3905	0.323	4579	0.239	5223	0.201	5824	0.182	6594	0.147
4418	0.427	5146	0.310	5750	0.245	6510	0.229	7347	0.184
4885	0.537	5670	0.384	6268	0.297	7045	0.269	8038	0.221
5319	0.653	6155	0.460	6786	0.352	7550	0.313	8672	0.255
5727	0.773	6607	0.538	7271	0.408	8076	0.363	9166	0.286
6479	1.027	7437	0.699	8159	0.521	9055	0.462	10168	0.357
7168	1.297	8192	0.866	8963	0.637	9942	0.564	11140	0.433
7808	1.582	8890	1.038	9702	0.754	10760	0.666	12045	0.509
8409	1.878	9542	1.215	10395	0.874	11522	0.770	12889	0.586
8974	2.184	10158	1.396	11044	0.995	12238	0.876	13677	0.663
9511	2.500	10741	1.582	11659	1.117	12916	0.982	14424	0.741
10514	3.155	11803	1.953	12780	1.357	14317	1.220	16001	0.920
11448	3.844	12800	2.342	13972	1.646	15480	1.444	17304	1.083
12335	4.569	13787	2.768	14844	1.875	16425	1.638	18310	1.217
13166	5.311	14631	3.162	15885	2.170	17590	1.896	19632	1.409
13965	6.082	15476	3.592	16758	2.434	18548	2.123	20686	1.572
15816	8.090	17441	4.707	18701	3.067	20758	2.698	23118	1.985
17460	10.127	19405	6.004	20656	3.817	22842	3.308	25323	2.405
19027	12.304	20893	7.105	22144	4.433	24492	3.823	27355	2.830
20479	14.515	22602	8.508	23903	5.231	26399	4.501	29345	3.286

APPENDIX IV

Tabulation of Results from Chapter 6

Data for Results Presented in Figure 6.3 (depths)

 $H/L = 0.03$

$q_{bas}^* \times 9.8$	10^{-4}	10^{-3}	10^{-2}	10^{-1}	10^0	10^1
Re	d_z/L	d_z/L	d_z/L	d_z/L	d_z/L	d_z/L
42	-	-	-	-	-	-
99	0.087	-	-	-	-	-
109	0.135	-	-	-	-	-
184	0.332	0.038	-	-	-	-
272	0.448	0.120	-	-	-	-
521	0.567	0.258	0.003	-	-	-
777	0.642	0.388	0.072	-	-	-
1127	0.685	0.500	0.162	-	-	-
1964	0.743	0.640	0.331	0.048	-	-
2784	0.754	0.695	0.442	0.114	-	-
3337	0.751	0.710	0.496	0.158	-	-
3905	0.759	0.727	0.542	0.201	0.004	-
4418	0.765	0.739	0.576	0.238	0.016	-
4885	0.77	0.748	0.602	0.269	0.027	-
5319	0.774	0.755	0.624	0.296	0.038	-
5727	0.777	0.76	0.641	0.319	0.049	-
6479	0.783	0.769	0.667	0.359	0.069	-
7168	0.788	0.777	0.688	0.392	0.088	-
7808	0.792	0.782	0.704	0.419	0.105	-
8409	0.795	0.787	0.716	0.444	0.121	-
8974	0.798	0.791	0.727	0.465	0.136	-
9511	0.801	0.794	0.736	0.483	0.151	-
10514	0.805	0.799	0.75	0.515	0.176	-
11448	0.809	0.804	0.761	0.541	0.199	-
12335	0.812	0.808	0.77	0.564	0.221	0.018
13166	0.815	0.811	0.778	0.583	0.240	0.025
13965	0.818	0.815	0.784	0.601	0.258	0.032
15816	0.824	0.821	0.796	0.635	0.296	0.048
17460	0.827	0.825	0.804	0.661	0.327	0.063
19027	0.831	0.829	0.811	0.682	0.355	0.077
20479	0.834	0.823	0.817	0.699	0.378	0.090

Data for Results Presented in Figure 6.3 (depths, cont.)

 $H/L = 0.04$

$q_{bas}^* \times 9.8$	10^{-4}	10^{-3}	10^{-2}	10^{-1}	10^0	10^1
Re	d_z/L	d_z/L	d_z/L	d_z/L	d_z/L	d_z/L
51	-	-	-	-	-	-
133	0.118	-	-	-	-	-
145	0.162	-	-	-	-	-
248	0.354	0.041	-	-	-	-
371	0.47	0.129	-	-	-	-
645	0.567	0.256	-	-	-	-
954	0.637	0.383	0.057	-	-	-
1368	0.676	0.491	0.147	-	-	-
2365	0.729	0.627	0.316	0.024	-	-
3308	0.735	0.676	0.422	0.087	-	-
4054	0.739	0.697	0.483	0.137	-	-
4579	0.733	0.701	0.516	0.171	-	-
5146	0.737	0.711	0.548	0.205	-	-
5670	0.740	0.718	0.572	0.235	-	-
6155	0.742	0.723	0.592	0.262	0.006	-
6607	0.744	0.727	0.607	0.283	0.015	-
7437	0.748	0.734	0.632	0.321	0.032	-
8192	0.750	0.739	0.65	0.352	0.047	-
8890	0.753	0.742	0.663	0.378	0.062	-
9542	0.755	0.746	0.675	0.401	0.076	-
10158	0.756	0.748	0.684	0.420	0.090	-
10741	0.758	0.751	0.692	0.438	0.102	-
11803	0.759	0.754	0.703	0.467	0.126	-
12800	0.761	0.756	0.712	0.491	0.147	-
13787	0.765	0.760	0.721	0.514	0.167	-
14631	0.766	0.761	0.726	0.531	0.184	-
15476	0.767	0.764	0.731	0.547	0.200	-
17441	0.771	0.768	0.742	0.579	0.237	0.004
19405	0.777	0.774	0.753	0.607	0.270	0.016
20893	0.777	0.775	0.756	0.624	0.295	0.026
22602	0.780	0.780	0.763	0.643	0.319	0.037

Data for Results Presented in Figure 6.3 (depths, cont.)

 $H/L = 0.05$

$q_{bas}^* \times 9.8$	10^{-4}	10^{-3}	10^{-2}	10^{-1}	10^0	10^1
Re	d_z/L	d_z/L	d_z/L	d_z/L	d_z/L	d_z/L
68	-	-	-	-	-	-
164	0.14	-	-	-	-	-
178	0.18	-	-	-	-	-
309	0.37	0.041	-	-	-	-
458	0.48	0.129	-	-	-	-
744	0.556	0.256	-	-	-	-
1094	0.624	0.383	0.035	-	-	-
1557	0.66	0.491	0.126	-	-	-
2686	0.712	0.627	0.297	-	-	-
3719	0.714	0.676	0.4	0.059	-	-
4528	0.715	0.697	0.459	0.107	-	-
5223	0.715	0.701	0.498	0.147	-	-
5750	0.71	0.711	0.521	0.175	-	-
6268	0.711	0.718	0.542	0.202	-	-
6786	0.712	0.723	0.561	0.227	-	-
7271	0.713	0.727	0.576	0.249	-	-
8159	0.715	0.734	0.599	0.286	-	-
8963	0.716	0.739	0.616	0.316	0.011	-
9702	0.717	0.742	0.628	0.341	0.024	-
10395	0.718	0.746	0.639	0.362	0.037	-
11044	0.719	0.748	0.647	0.381	0.049	-
11659	0.719	0.751	0.653	0.398	0.06	-
12780	0.72	0.754	0.663	0.426	0.082	-
13972	0.724	0.756	0.675	0.453	0.104	-
14844	0.722	0.76	0.679	0.47	0.12	-
15885	0.725	0.761	0.686	0.49	0.139	-
16758	0.725	0.764	0.69	0.504	0.154	-
18701	0.725	0.768	0.695	0.532	0.186	-
20656	0.728	0.774	0.703	0.558	0.217	-
22144	0.727	0.775	0.705	0.572	0.239	-
23903	0.729	0.78	0.711	0.59	0.263	-

Data for Results Presented in Figure 6.3 (depths, cont.)

 $H/L = 0.06$

$q_{bas}^* \times 9.8$	10^{-4}	10^{-3}	10^{-2}	10^{-1}	10^0	10^1
Re	d_z/L	d_z/L	d_z/L	d_z/L	d_z/L	d_z/L
81	-	-	-	-	-	-
202	0.163	-	-	-	-	-
217	0.198	-	-	-	-	-
363	0.376	0.039	-	-	-	-
541	0.485	0.135	-	-	-	-
836	0.545	0.232	-	-	-	-
1229	0.613	0.365	0.019	-	-	-
1743	0.648	0.463	0.110	-	-	-
3026	0.702	0.600	0.286	-	-	-
4166	0.702	0.643	0.387	0.040	-	-
5061	0.702	0.660	0.446	0.090	-	-
5824	0.702	0.670	0.484	0.130	-	-
6510	0.702	0.677	0.513	0.164	-	-
7045	0.698	0.676	0.53	0.188	-	-
7550	0.697	0.678	0.546	0.210	-	-
8076	0.698	0.681	0.561	0.233	-	-
9055	0.699	0.686	0.583	0.269	-	-
9942	0.700	0.689	0.600	0.299	-	-
10760	0.701	0.691	0.612	0.324	0.002	-
11522	0.702	0.693	0.622	0.346	0.014	-
12238	0.703	0.695	0.630	0.365	0.027	-
12916	0.704	0.696	0.637	0.381	0.038	-
14317	0.707	0.701	0.650	0.412	0.062	-
15480	0.707	0.702	0.658	0.436	0.083	-
16425	0.705	0.701	0.662	0.453	0.099	-
17590	0.708	0.704	0.669	0.472	0.118	-
18548	0.708	0.705	0.673	0.487	0.134	-
20758	0.709	0.706	0.68	0.516	0.168	-
22842	0.710	0.708	0.686	0.540	0.199	-
24492	0.709	0.706	0.687	0.555	0.221	-
26399	0.711	0.709	0.692	0.572	0.245	-

Data for Results Presented in Figure 6.3 (depths, cont.)

 $H/L = 0.075$

$q_{bas}^* \times 9.8$	10^{-4}	10^{-3}	10^{-2}	10^{-1}	10^0	10^1
Re	d_z/L	d_z/L	d_z/L	d_z/L	d_z/L	d_z/L
97	-	-	-	-	-	-
244	0.183	-	-	-	-	-
260	0.212	-	-	-	-	-
445	0.383	0.032	-	-	-	-
660	0.485	0.13	-	-	-	-
947	0.524	0.21	-	-	-	-
1400	0.593	0.338	0.001	-	-	-
1976	0.626	0.441	0.084	-	-	-
3492	0.688	0.585	0.271	-	-	-
4757	0.685	0.625	0.369	0.012	-	-
5748	0.682	0.641	0.425	0.063	-	-
6594	0.682	0.649	0.464	0.105	-	-
7347	0.681	0.655	0.492	0.139	-	-
8038	0.681	0.659	0.513	0.169	-	-
8672	0.68	0.66	0.528	0.191	-	-
9166	0.676	0.66	0.539	0.208	-	-
10168	0.676	0.661	0.559	0.244	-	-
11140	0.676	0.665	0.576	0.274	-	-
12045	0.677	0.667	0.588	0.299	-	-
12889	0.678	0.669	0.598	0.321	-	-
13677	0.678	0.67	0.605	0.339	0.001	-
14424	0.678	0.671	0.612	0.356	0.003	-
16001	0.682	0.677	0.626	0.388	0.028	-
17304	0.683	0.678	0.634	0.412	0.05	-
18310	0.679	0.675	0.636	0.427	0.066	-
19632	0.683	0.679	0.644	0.447	0.086	-
20686	0.683	0.679	0.647	0.461	0.102	-
23118	0.682	0.68	0.654	0.49	0.138	-
25323	0.683	0.68	0.658	0.512	0.167	-
27355	0.683	0.681	0.661	0.529	0.193	-
29345	0.684	0.682	0.665	0.545	0.216	-

Data for Results Presented in Figure 6.3 (fluxes, cont.)

 $H/L = 0.03$

$q_{bas}^* \times 9.8$	10^{-4}	10^{-3}	10^{-2}	10^{-1}	10^0	10^1
Re	$q_{int}^* \times 10^3$					
42	-	-	-	-	-	-
99	2.3E-05	-	-	-	-	-
109	4.5E-05	-	-	-	-	-
184	3.1E-04	8.7E-05	1.7E-06	-	-	-
272	0.001	4.7E-04	7.4E-06	-	-	-
521	0.002	0.002	1.0E-04	-	-	-
777	0.005	0.005	0.002	-	-	-
1127	0.012	0.012	0.008	-	-	-
1964	0.041	0.040	0.035	0.064	-	-
2784	0.084	0.083	0.078	0.099	-	-
3337	0.123	0.122	0.117	0.132	-	-
3905	0.174	0.173	0.167	0.178	0.011	-
4418	0.229	0.228	0.222	0.229	0.035	-
4885	0.287	0.287	0.281	0.286	0.065	-
5319	0.350	0.349	0.343	0.347	0.100	-
5727	0.416	0.415	0.409	0.411	0.137	-
6479	0.556	0.555	0.549	0.549	0.238	-
7168	0.705	0.704	0.699	0.698	0.363	-
7808	0.863	0.863	0.857	0.855	0.503	-
8409	1.037	1.036	1.031	1.032	0.657	-
8974	1.200	1.200	1.194	1.191	0.811	-
9511	1.382	1.381	1.376	1.371	0.977	-
10514	1.762	1.762	1.756	1.751	1.330	-
11448	2.165	2.164	2.158	2.153	1.716	-
12335	2.590	2.590	2.584	2.579	2.128	0.385
13166	3.028	3.027	3.021	3.017	2.555	0.672
13965	3.483	3.483	3.477	3.472	3.001	1.007
15816	4.668	4.667	4.662	4.657	4.169	1.951
17460	5.871	5.871	5.865	5.860	5.359	2.999
19027	7.160	7.159	7.154	7.149	6.630	4.149
20479	8.470	8.469	8.464	8.459	7.933	5.335

Data for Results Presented in Figure 6.3 (fluxes, cont.)

$H/L = 0.04$

$q_{bas}^* \times 9.8$	10^{-4}	10^{-3}	10^{-2}	10^{-1}	10^0	10^1
Re	$q_{int}^* \times 10^3$					
51	-	-	-	-	-	-
133	3.6E-05	-	-	-	-	-
145	6.2E-05	-	-	-	-	-
248	0.000	9.8E-05	-	-	-	-
371	0.001	5.0E-04	-	-	-	-
645	0.002	0.002	-	-	-	-
954	0.005	0.005	0.002	-	-	-
1368	0.011	0.011	0.007	-	-	-
2365	0.036	0.035	0.030	0.006	-	-
3308	0.071	0.071	0.065	0.032	-	-
4054	0.107	0.107	0.101	0.062	-	-
4579	0.137	0.136	0.130	0.089	-	-
5146	0.174	0.173	0.167	0.123	-	-
5670	0.213	0.213	0.206	0.159	-	-
6155	0.254	0.253	0.247	0.196	0.022	-
6607	0.296	0.295	0.289	0.236	0.040	-
7437	0.384	0.383	0.377	0.321	0.086	-
8192	0.475	0.474	0.468	0.411	0.140	-
8890	0.569	0.569	0.562	0.504	0.200	-
9542	0.667	0.667	0.660	0.602	0.272	-
10158	0.768	0.767	0.761	0.702	0.351	-
10741	0.870	0.870	0.863	0.804	0.436	-
11803	1.077	1.076	1.070	1.010	0.616	-
12800	1.295	1.294	1.288	1.227	0.811	-
13787	1.534	1.533	1.527	1.466	1.030	-
14631	1.756	1.755	1.749	1.687	1.236	-
15476	1.998	1.998	1.991	1.930	1.466	-
17441	2.631	2.630	2.624	2.562	2.070	0.243
19405	3.372	3.371	3.365	3.303	2.790	0.630
20893	4.004	4.003	3.997	3.935	3.407	1.029
22602	4.817	4.816	4.810	4.747	4.208	1.603

Data for Results Presented in Figure 6.3 (fluxes, cont.)

 $H/L = 0.05$

$q_{bas}^* \times 9.8$	10^{-4}	10^{-3}	10^{-2}	10^{-1}	10^0	10^1
Re	$q_{int}^* \times 10^3$					
51	-	-	-	-	-	-
133	3.6E-05	-	-	-	-	-
145	6.2E-05	-	-	-	-	-
248	0.000	9.8E-05	-	-	-	-
371	0.001	5.0E-04	-	-	-	-
645	0.002	0.002	-	-	-	-
954	0.005	0.005	0.002	-	-	-
1368	0.011	0.011	0.007	-	-	-
2365	0.036	0.035	0.030	0.006	-	-
3308	0.071	0.071	0.065	0.032	-	-
4054	0.107	0.107	0.101	0.062	-	-
4579	0.137	0.136	0.130	0.089	-	-
5146	0.174	0.173	0.167	0.123	-	-
5670	0.213	0.213	0.206	0.159	-	-
6155	0.254	0.253	0.247	0.196	0.022	-
6607	0.296	0.295	0.289	0.236	0.040	-
7437	0.384	0.383	0.377	0.321	0.086	-
8192	0.475	0.474	0.468	0.411	0.140	-
8890	0.569	0.569	0.562	0.504	0.200	-
9542	0.667	0.667	0.660	0.602	0.272	-
10158	0.768	0.767	0.761	0.702	0.351	-
10741	0.870	0.870	0.863	0.804	0.436	-
11803	1.077	1.076	1.070	1.010	0.616	-
12800	1.295	1.294	1.288	1.227	0.811	-
13787	1.534	1.533	1.527	1.466	1.030	-
14631	1.756	1.755	1.749	1.687	1.236	-
15476	1.998	1.998	1.991	1.930	1.466	-
17441	2.631	2.630	2.624	2.562	2.070	0.243
19405	3.372	3.371	3.365	3.303	2.790	0.630
20893	4.004	4.003	3.997	3.935	3.407	1.029
22602	4.817	4.816	4.810	4.747	4.208	1.603

Data for Results Presented in Figure 6.3 (fluxes, cont.)

 $H/L = 0.06$

$q_{bas}^* \times 9.8$	10^{-4}	10^{-3}	10^{-2}	10^{-1}	10^0	10^1
Re	$q_{int}^* \times 10^3$					
81	-	-	-	-	-	-
202	8.4E-05	-	-	-	-	-
217	1.2E-04	2.1E-05	-	-	-	-
363	0.001	1.7E-04	-	-	-	-
541	0.001	0.001	9.9E-05	-	-	-
836	0.002	0.002	1.9E-04	-	-	-
1229	0.005	0.004	0.001	-	-	-
1743	0.010	0.010	0.005	-	-	-
3026	0.035	0.035	0.029	0.006	-	-
4166	0.067	0.066	0.059	0.021	-	-
5061	0.100	0.099	0.092	0.045	-	-
5824	0.133	0.132	0.125	0.073	-	-
6510	0.167	0.166	0.159	0.103	-	-
7045	0.194	0.194	0.186	0.128	-	-
7550	0.226	0.225	0.218	0.158	-	-
8076	0.261	0.260	0.253	0.190	-	-
9055	0.331	0.330	0.323	0.257	-	-
9942	0.402	0.401	0.394	0.326	0.066	-
10760	0.474	0.473	0.466	0.396	0.095	-
11522	0.547	0.547	0.539	0.468	0.134	-
12238	0.621	0.621	0.613	0.541	0.179	-
12916	0.696	0.695	0.688	0.615	0.229	-
14317	0.865	0.864	0.856	0.782	0.350	-
15480	1.023	1.022	1.015	0.939	0.474	-
16425	1.159	1.159	1.151	1.075	0.585	-
17590	1.343	1.342	1.334	1.258	0.741	-
18548	1.503	1.502	1.495	1.419	0.880	-
20758	1.911	1.910	1.902	1.826	1.246	0.164
22842	2.345	2.344	2.336	2.260	1.648	0.261
24492	2.708	2.708	2.700	2.623	1.992	0.345
26399	3.193	3.193	3.185	3.108	2.456	0.474

Data for Results Presented in Figure 6.3 (fluxes, cont.)

 $H/L = 0.075$

$q_{bas}^* \times 9.8$	10^{-4}	10^{-3}	10^{-2}	10^{-1}	10^0	10^1
Re	$q_{int}^* \times 10^3$					
97	-	-	-	-	-	-
244	1.1E-04	-	-	-	-	-
260	1.4E-04	-	-	-	-	-
445	0.001	1.5E-04	-	-	-	-
660	0.001	0.001	-	-	-	-
947	0.002	0.001	-	-	-	-
1400	0.005	0.004	0.001	-	-	-
1976	0.009	0.009	0.004	-	-	-
3492	0.031	0.031	0.024	-	-	-
4757	0.059	0.058	0.052	0.010	-	-
5748	0.087	0.087	0.080	0.028	-	-
6594	0.116	0.115	0.108	0.050	-	-
7347	0.144	0.144	0.137	0.073	-	-
8038	0.173	0.173	0.166	0.098	-	-
8672	0.200	0.200	0.193	0.122	-	-
9166	0.224	0.224	0.217	0.145	-	-
10168	0.280	0.279	0.273	0.199	-	-
11140	0.339	0.338	0.332	0.256	-	-
12045	0.400	0.400	0.393	0.317	-	-
12889	0.459	0.458	0.451	0.372	-	-
13677	0.519	0.518	0.511	0.430	0.082	-
14424	0.579	0.579	0.572	0.489	0.109	-
16001	0.720	0.719	0.712	0.625	0.189	-
17304	0.847	0.846	0.840	0.749	0.273	-
18310	0.951	0.950	0.944	0.850	0.350	-
19632	1.101	1.101	1.094	0.996	0.469	-
20686	1.228	1.227	1.220	1.119	0.573	-
23118	1.549	1.548	1.541	1.430	0.851	0.164
25323	1.874	1.873	1.867	1.747	1.146	0.261
27355	2.204	2.203	2.196	2.067	1.454	0.345
29345	2.556	2.556	2.549	2.410	1.795	0.474

Data for Results Presented in Figure 6.4a

H/L	0.03	0.04	0.05	0.06	0.075
$q_{bas}^* \times 9.8$	Re_{crit}	Re_{crit}	Re_{crit}	Re_{crit}	Re_{crit}
10^{-4}	80	103	112	134	128
10^{-3}	141	180	218	242	317
10^{-2}	518	723	922	1125	1402
10^{-1}	1515	2131	2900	3572	4580
10^0	4047	6190	8646	10876	14372
10^1	10344	16851	-	-	-

Data for Results Presented in Figure 6.4b

H/L	0.03	0.04	0.05	0.06	0.075
$q_{bas}^* \times 9.8$	Re_{crit}	Re_{crit}	Re_{crit}	Re_{crit}	Re_{crit}
10^{-4}	46	90	68	118	113
10^{-3}	100	114	111	198	285
10^{-2}	337	600	820	1004	1376
10^{-1}	1305	1885	2602	3037	4306
10^0	3102	5054	7110	9242	12915
10^1	8471	13010	19667	-	-

Data for Results Presented in Figure 6.5 (depths)

 $H/L = 0.03$

$q_{bas}^* \times 9.8$	10^{-4}	10^{-3}	10^{-2}	10^{-1}	10^0	10^1
Re	d_z/L	d_z/L	d_z/L	d_z/L	d_z/L	d_z/L
42	0.004	-	-	-	-	-
99	0.133	0.002	-	-	-	-
109	0.17	0.004	-	-	-	-
184	0.35	0.072	-	-	-	-
272	0.452	0.146	0.004	-	-	-
521	0.568	0.27	0.026	-	-	-
777	0.642	0.394	0.092	-	-	-
1127	0.685	0.502	0.179	-	-	-
1964	0.743	0.641	0.338	0.066	-	-
2784	0.754	0.696	0.446	0.133	0.005	-
3337	0.754	0.71	0.499	0.174	0.007	-
3905	0.759	0.727	0.544	0.215	0.02	-
4418	0.773	0.739	0.578	0.249	0.033	-
4885	0.775	0.748	0.604	0.279	0.046	-
5319	0.778	0.755	0.624	0.303	0.058	-
5727	0.782	0.761	0.641	0.326	0.068	-
6479	0.785	0.77	0.668	0.364	0.087	-
7168	0.786	0.777	0.688	0.396	0.105	-
7808	0.791	0.782	0.704	0.423	0.121	-
8409	0.796	0.787	0.716	0.447	0.136	0.003
8974	0.799	0.791	0.727	0.467	0.15	0.007
9511	0.802	0.795	0.736	0.485	0.163	0.012
10514	0.806	0.8	0.75	0.517	0.187	0.02
11448	0.81	0.805	0.761	0.542	0.209	0.027
12335	0.813	0.809	0.771	0.565	0.229	0.035
13166	0.817	0.813	0.778	0.584	0.247	0.041
13965	0.82	0.816	0.785	0.601	0.264	0.047
15816	0.826	0.823	0.797	0.635	0.301	0.063
17460	0.83	0.827	0.806	0.661	0.332	0.076
19027	0.834	0.832	0.813	0.682	0.357	0.089
20479	0.837	0.835	0.819	0.699	0.381	0.101

Data for Results Presented in Figure 6.5 (depths, cont.)

 $H/L = 0.04$

$q_{bas}^* \times 9.8$	10^{-4}	10^{-3}	10^{-2}	10^{-1}	10^0	10^1
Re	d_z/L	d_z/L	d_z/L	d_z/L	d_z/L	d_z/L
51	0.015	-	-	-	-	-
133	0.156	-	-	-	-	-
145	0.192	-	-	-	-	-
248	0.364	0.071	-	-	-	-
371	0.473	0.151	-	-	-	-
645	0.568	0.267	0.012	-	-	-
954	0.638	0.389	0.077	-	-	-
1368	0.676	0.493	0.168	-	-	-
2365	0.729	0.628	0.326	0.045	-	-
3308	0.735	0.677	0.427	0.112	-	-
4054	0.737	0.697	0.487	0.161	-	-
4579	0.737	0.701	0.518	0.192	-	-
5146	0.737	0.711	0.55	0.224	0.009	-
5670	0.74	0.718	0.574	0.251	0.019	-
6155	0.742	0.723	0.593	0.274	0.029	-
6607	0.745	0.728	0.609	0.295	0.039	-
7437	0.748	0.734	0.633	0.331	0.057	-
8192	0.75	0.739	0.65	0.36	0.073	-
8890	0.753	0.743	0.665	0.385	0.089	-
9542	0.756	0.746	0.676	0.407	0.103	-
10158	0.758	0.748	0.685	0.426	0.116	-
10741	0.759	0.751	0.692	0.443	0.128	-
11803	0.761	0.754	0.703	0.471	0.149	-
12800	0.762	0.756	0.713	0.495	0.169	-
13787	0.766	0.76	0.721	0.516	0.188	0.006
14631	0.766	0.762	0.726	0.533	0.204	0.011
15476	0.768	0.763	0.732	0.549	0.219	0.015
17441	0.771	0.768	0.742	0.581	0.252	0.028
19405	0.777	0.774	0.753	0.609	0.283	0.041
20893	0.777	0.775	0.756	0.625	0.305	0.051
22602	0.782	0.779	0.763	0.644	0.329	0.063

Data for Results Presented in Figure 6.5 (depths, cont.)

 $H/L = 0.05$

$q_{bas}^* \times 9.8$	10^{-4}	10^{-3}	10^{-2}	10^{-1}	10^0	10^1
Re	d_z/L	d_z/L	d_z/L	d_z/L	d_z/L	d_z/L
68	0.003	-	-	-	-	-
164	0.170	-	-	-	-	-
178	0.204	-	-	-	-	-
309	0.377	0.065	-	-	-	-
458	0.483	0.154	-	-	-	-
744	0.558	0.257	-	-	-	-
1094	0.625	0.376	0.054	-	-	-
1557	0.660	0.478	0.151	-	-	-
2686	0.712	0.611	0.309	0.019	-	-
3719	0.714	0.655	0.406	0.088	-	-
4528	0.715	0.674	0.463	0.137	-	-
5223	0.715	0.684	0.502	0.174	-	-
5750	0.716	0.686	0.524	0.198	-	-
6268	0.716	0.689	0.545	0.225	-	-
6786	0.716	0.693	0.563	0.246	0.001	-
7271	0.717	0.697	0.578	0.267	0.007	-
8159	0.718	0.702	0.600	0.300	0.025	-
8963	0.719	0.704	0.617	0.328	0.039	-
9702	0.720	0.708	0.629	0.352	0.054	-
10395	0.720	0.710	0.639	0.372	0.067	-
11044	0.720	0.711	0.647	0.389	0.080	-
11659	0.721	0.713	0.654	0.406	0.092	-
12780	0.721	0.714	0.664	0.432	0.113	-
13972	0.725	0.719	0.676	0.458	0.135	-
14844	0.723	0.719	0.679	0.475	0.150	-
15885	0.726	0.721	0.687	0.494	0.167	-
16758	0.726	0.721	0.691	0.508	0.182	-
18701	0.726	0.722	0.696	0.535	0.211	-
20656	0.726	0.724	0.704	0.560	0.238	0.005
22144	0.729	0.724	0.705	0.575	0.258	0.012
23903	0.729	0.726	0.711	0.590	0.280	0.021

Data for Results Presented in Figure 6.5 (depths, cont.)

 $H/L = 0.06$

$q_{bas}^* \times 9.8$	10^{-4}	10^{-3}	10^{-2}	10^{-1}	10^0	10^1
Re	d_z/L	d_z/L	d_z/L	d_z/L	d_z/L	d_z/L
81	-	-	-	-	-	-
202	0.185	-	-	-	-	-
217	0.217	-	-	-	-	-
363	0.383	0.056	-	-	-	-
541	0.488	0.153	-	-	-	-
836	0.547	0.245	-	-	-	-
1229	0.614	0.371	0.039	-	-	-
1743	0.648	0.466	0.135	-	-	-
3026	0.702	0.601	0.299	0.001	-	-
4166	0.702	0.644	0.395	0.067	-	-
5061	0.702	0.661	0.451	0.12	-	-
5824	0.702	0.671	0.489	0.159	-	-
6510	0.703	0.677	0.516	0.189	-	-
7045	0.703	0.677	0.533	0.21	-	-
7550	0.703	0.679	0.548	0.231	-	-
8076	0.703	0.681	0.563	0.251	-	-
9055	0.703	0.686	0.585	0.284	0.002	-
9942	0.703	0.689	0.601	0.312	0.016	-
10760	0.704	0.692	0.614	0.335	0.03	-
11522	0.704	0.693	0.623	0.356	0.043	-
12238	0.704	0.695	0.632	0.373	0.056	-
12916	0.705	0.696	0.639	0.389	0.068	-
14317	0.708	0.701	0.651	0.42	0.094	-
15480	0.708	0.703	0.659	0.442	0.114	-
16425	0.708	0.703	0.662	0.458	0.13	-
17590	0.709	0.705	0.67	0.477	0.148	-
18548	0.709	0.705	0.673	0.491	0.162	-
20758	0.71	0.706	0.68	0.519	0.193	-
22842	0.711	0.709	0.686	0.543	0.22	-
24492	0.711	0.71	0.687	0.557	0.239	-
26399	0.711	0.711	0.692	0.574	0.262	-

Data for Results Presented in Figure 6.5 (depths, cont.)

 $H/L = 0.075$

$q_{bas}^* \times 9.8$	10^{-4}	10^{-3}	10^{-2}	10^{-1}	10^0	10^1
Re	d_z/L	d_z/L	d_z/L	d_z/L	d_z/L	d_z/L
97	-	-	-	-	-	-
244	0.199	-	-	-	-	-
260	0.228	-	-	-	-	-
445	0.388	0.038	-	-	-	-
660	0.487	0.143	-	-	-	-
947	0.524	0.221	-	-	-	-
1400	0.593	0.334	0.001	-	-	-
1976	0.627	0.445	0.106	-	-	-
3492	0.682	0.586	0.283	-	-	-
4757	0.685	0.625	0.376	0.031	-	-
5748	0.687	0.641	0.431	0.091	-	-
6594	0.690	0.650	0.468	0.133	-	-
7347	0.688	0.655	0.495	0.166	-	-
8038	0.687	0.659	0.516	0.191	-	-
8672	0.685	0.661	0.531	0.212	-	-
9166	0.680	0.661	0.541	0.229	-	-
10168	0.679	0.662	0.561	0.260	-	-
11140	0.679	0.665	0.577	0.288	-	-
12045	0.679	0.668	0.589	0.311	-	-
12889	0.679	0.669	0.599	0.332	0.005	-
13677	0.680	0.670	0.606	0.349	0.015	-
14424	0.680	0.671	0.613	0.365	0.027	-
16001	0.684	0.677	0.627	0.395	0.054	-
17304	0.684	0.678	0.634	0.417	0.078	-
18310	0.684	0.677	0.636	0.432	0.096	-
19632	0.684	0.679	0.644	0.452	0.118	-
20686	0.684	0.679	0.648	0.466	0.134	-
23118	0.684	0.680	0.655	0.494	0.165	-
25323	0.684	0.680	0.658	0.515	0.191	-
27355	0.684	0.680	0.662	0.532	0.214	-
29345	0.684	0.682	0.665	0.547	0.235	-

Data for Results Presented in Figure 6.5 (fluxes)

 $H/L = 0.03$

$q_{bas}^* \times 9.8$	10^{-4}	10^{-3}	10^{-2}	10^{-1}	10^0	10^1
Re	$q_{int}^* \times 10^3$					
42	-	-	-	-	-	-
99	4.9E-05	2.1E-05	-	-	-	-
109	7.4E-05	3.6E-05	-	-	-	-
184	3.5E-04	2.5E-04	-	-	-	-
272	0.001	0.001	3.9E-04	-	-	-
521	0.002	0.002	0.001	-	-	-
777	0.006	0.005	0.004	-	-	-
1127	0.013	0.012	0.010	-	-	-
1964	0.041	0.040	0.037	0.028	0.015	-
2784	0.084	0.083	0.080	0.066	0.046	-
3337	0.123	0.122	0.119	0.103	0.078	0.010
3905	0.174	0.173	0.170	0.152	0.121	0.042
4418	0.229	0.228	0.225	0.206	0.169	0.080
4885	0.287	0.287	0.284	0.263	0.220	0.125
5319	0.350	0.349	0.346	0.324	0.274	0.174
5727	0.416	0.415	0.412	0.389	0.331	0.226
6479	0.556	0.555	0.552	0.527	0.455	0.336
7168	0.705	0.705	0.701	0.675	0.592	0.462
7808	0.863	0.863	0.860	0.832	0.739	0.604
8409	1.037	1.036	1.033	1.001	0.894	0.753
8974	1.200	1.200	1.197	1.168	1.058	0.909
9511	1.382	1.382	1.378	1.349	1.229	1.072
10514	1.762	1.762	1.759	1.729	1.589	1.413
11448	2.165	2.164	2.161	2.130	1.974	1.777
12335	2.590	2.590	2.587	2.555	2.383	2.170
13166	3.028	3.027	3.024	2.992	2.806	2.574
13965	3.483	3.483	3.480	3.447	3.248	2.996
15816	4.668	4.668	4.664	4.630	4.407	4.099
17460	5.871	5.871	5.868	5.834	5.595	5.222
19027	7.160	7.160	7.156	7.122	6.866	6.421
20479	8.470	8.469	8.466	8.431	8.162	7.643

Data for Results Presented in Figure 6.5 (fluxes, cont.)

 $H/L = 0.04$

$q_{bas}^* \times 9.8$	10^{-4}	10^{-3}	10^{-2}	10^{-1}	10^0	10^1
Re	$q_{int}^* \times 10^3$					
51	1.0E-05	2.4E-06	-	-	-	-
133	6.4E-05	3.4E-05	-	-	-	-
145	9.2E-05	5.2E-05	-	-	-	-
248	4.0E-04	2.8E-04	1.4E-04	-	-	-
371	0.001	0.001	3.9E-04	-	-	-
645	0.002	0.002	0.001	2.5E-04	-	-
954	0.005	0.005	0.003	0.002	-	-
1368	0.011	0.011	0.009	0.005	-	-
2365	0.036	0.036	0.033	0.022	0.011	-
3308	0.071	0.071	0.068	0.054	0.032	-
4054	0.107	0.107	0.104	0.088	0.055	-
4579	0.137	0.136	0.133	0.116	0.075	0.013
5146	0.174	0.174	0.171	0.154	0.104	0.035
5670	0.213	0.213	0.210	0.192	0.138	0.060
6155	0.254	0.254	0.251	0.232	0.174	0.087
6607	0.296	0.296	0.293	0.273	0.211	0.117
7437	0.384	0.383	0.381	0.359	0.290	0.180
8192	0.475	0.474	0.472	0.449	0.374	0.246
8890	0.569	0.569	0.566	0.543	0.462	0.316
9542	0.667	0.667	0.664	0.640	0.553	0.389
10158	0.768	0.767	0.765	0.740	0.647	0.466
10741	0.870	0.870	0.867	0.843	0.745	0.549
11803	1.077	1.077	1.074	1.049	0.941	0.722
12800	1.295	1.295	1.292	1.266	1.147	0.907
13787	1.534	1.534	1.531	1.505	1.375	1.112
14631	1.756	1.755	1.753	1.726	1.586	1.304
15476	1.998	1.998	1.995	1.968	1.818	1.517
17441	2.631	2.631	2.628	2.601	2.429	2.086
19405	3.372	3.372	3.369	3.341	3.154	2.779
20893	4.004	4.003	4.000	3.973	3.777	3.375
22602	4.817	4.816	4.814	4.786	4.581	4.148

Data for Results Presented in Figure 6.5 (fluxes, cont.)

 $H/L = 0.05$

$q_{bas}^* \times 9.8$	10^{-4}	10^{-3}	10^{-2}	10^{-1}	10^0	10^1
Re	$q_{int}^* \times 10^3$					
68	1.3E-05	4.6E-06	-	-	-	-
164	9.7E-05	6.4E-05	9.1E-06	-	-	-
178	1.3E-04	8.8E-05	2.6E-05	-	-	-
309	0.001	3.8E-04	2.4E-04	-	-	-
458	0.001	0.001	0.001	8.5E-05	-	-
744	0.002	0.002	0.001	0.001	-	-
1094	0.005	0.005	0.003	0.002	-	-
1557	0.011	0.011	0.009	0.005	0.001	-
2686	0.036	0.036	0.034	0.022	4.589	-
3719	0.071	0.070	0.068	0.053	0.034	-
4528	0.106	0.106	0.104	0.088	0.056	0.010
5223	0.142	0.141	0.139	0.124	0.078	0.029
5750	0.171	0.170	0.168	0.153	0.096	0.044
6268	0.205	0.205	0.203	0.188	0.119	0.067
6786	0.242	0.242	0.240	0.224	0.146	0.091
7271	0.279	0.279	0.277	0.261	0.176	0.116
8159	0.357	0.356	0.354	0.339	0.244	0.167
8963	0.433	0.433	0.431	0.415	0.316	0.219
9702	0.510	0.510	0.508	0.492	0.392	0.273
10395	0.602	0.602	0.600	0.586	0.484	0.338
11044	0.686	0.686	0.684	0.670	0.567	0.397
11659	0.770	0.770	0.768	0.754	0.650	0.458
12780	0.935	0.934	0.933	0.918	0.813	0.579
13972	1.135	1.135	1.133	1.118	1.012	0.727
14844	1.293	1.292	1.291	1.276	1.169	0.845
15885	1.498	1.497	1.495	1.480	1.373	0.999
16758	1.681	1.681	1.679	1.663	1.556	1.138
18701	2.122	2.121	2.119	2.102	1.995	1.473
20656	2.647	2.647	2.645	2.628	2.519	1.888
22144	3.078	3.078	3.076	3.058	2.948	2.261
23903	3.642	3.642	3.640	3.622	3.510	2.777

Data for Results Presented in Figure 6.5 (fluxes, cont.)

 $H/L = 0.06$

$q_{bas}^* \times 9.8$	10^{-4}	10^{-3}	10^{-2}	10^{-1}	10^0	10^1
Re	$q_{int}^* \times 10^3$					
81	1.4E-05	6.4E-06	-	-	-	-
202	1.1E-04	7.2E-05	2.1E-05	-	-	-
217	1.5E-04	9.3E-05	4.1E-05	-	-	-
363	0.001	3.9E-04	2.5E-04	-	-	-
541	0.001	0.001	0.001	9.4E-05	-	-
836	0.002	0.002	0.001	0.001	-	-
1229	0.005	0.005	0.003	0.002	-	-
1743	0.010	0.010	0.008	0.005	2.5E-04	-
3026	0.035	0.035	0.033	0.019	0.013	-
4166	0.067	0.066	0.064	0.048	0.031	-
5061	0.100	0.099	0.098	0.080	0.050	-
5824	0.133	0.133	0.131	0.113	0.070	-
6510	0.167	0.167	0.165	0.147	0.090	-
7045	0.195	0.194	0.192	0.174	0.106	-
7550	0.226	0.226	0.224	0.206	0.125	-
8076	0.261	0.261	0.259	0.241	0.148	-
9055	0.331	0.331	0.329	0.311	0.201	-
9942	0.402	0.402	0.400	0.383	0.260	-
10760	0.474	0.474	0.472	0.455	0.326	-
11522	0.547	0.547	0.545	0.529	0.395	-
12238	0.621	0.621	0.619	0.603	0.467	-
12916	0.696	0.696	0.694	0.678	0.540	-
14317	0.865	0.865	0.863	0.847	0.706	-
15480	1.023	1.023	1.021	1.005	0.863	-
16425	1.159	1.159	1.158	1.142	0.999	-
17590	1.343	1.343	1.341	1.325	1.182	-
18548	1.503	1.503	1.501	1.486	1.342	-
20758	1.911	1.910	1.909	1.894	1.749	-
22842	2.345	2.345	2.343	2.328	2.184	-
24492	2.709	2.708	2.707	2.692	2.548	1.6E-06
26399	3.193	3.193	3.192	3.177	3.033	2.0E-06

Data for Results Presented in Figure 6.5 (fluxes, cont.)

$H/L = 0.075$

$q_{bas}^* \times 9.8$	10^{-4}	10^{-3}	10^{-2}	10^{-1}	10^0	10^1
Re	$q_{int}^* \times 10^3$					
81	1.4E-05	6.4E-06	-	-	-	-
202	1.1E-04	7.2E-05	2.1E-05	-	-	-
217	1.5E-04	9.3E-05	4.1E-05	-	-	-
363	0.001	3.9E-04	2.5E-04	-	-	-
541	0.001	0.001	0.001	9.4E-05	-	-
836	0.002	0.002	0.001	0.001	-	-
1229	0.005	0.005	0.003	0.002	-	-
1743	0.010	0.010	0.008	0.005	2.5E-04	-
3026	0.035	0.035	0.033	0.019	0.013	-
4166	0.067	0.066	0.064	0.048	0.031	-
5061	0.100	0.099	0.098	0.080	0.050	-
5824	0.133	0.133	0.131	0.113	0.070	-
6510	0.167	0.167	0.165	0.147	0.090	-
7045	0.195	0.194	0.192	0.174	0.106	-
7550	0.226	0.226	0.224	0.206	0.125	-
8076	0.261	0.261	0.259	0.241	0.148	-
9055	0.331	0.331	0.329	0.311	0.201	-
9942	0.402	0.402	0.400	0.383	0.260	-
10760	0.474	0.474	0.472	0.455	0.326	-
11522	0.547	0.547	0.545	0.529	0.395	-
12238	0.621	0.621	0.619	0.603	0.467	-
12916	0.696	0.696	0.694	0.678	0.540	-
14317	0.865	0.865	0.863	0.847	0.706	-
15480	1.023	1.023	1.021	1.005	0.863	-
16425	1.159	1.159	1.158	1.142	0.999	-
17590	1.343	1.343	1.341	1.325	1.182	-
18548	1.503	1.503	1.501	1.486	1.342	-
20758	1.911	1.910	1.909	1.894	1.749	-
22842	2.345	2.345	2.343	2.328	2.184	-
24492	2.709	2.708	2.707	2.692	2.548	1.6E-06
26399	3.193	3.193	3.192	3.177	3.033	2.0E-06

Data for Results Presented in Figure 6.6c and 6.6e

Re	d_z/L	$q_{int}^* \times 10^3$	A_z/L^2	t_r^*
1094	0.035	0.001	0.009	6103
1557	0.126	0.006	0.060	9783
2686	0.297	0.029	0.174	5924
3719	0.400	0.064	0.309	4867
4528	0.459	0.099	0.367	3722
5223	0.498	0.134	0.406	3027
6268	0.542	0.198	0.454	2291
7271	0.576	0.271	0.491	1807
8159	0.599	0.351	0.514	1463
9702	0.628	0.505	0.547	1084
11659	0.653	0.762	0.576	755
12780	0.663	0.927	0.589	636
14844	0.679	1.285	0.618	481
18701	0.695	2.114	0.634	300
23903	0.711	3.635	0.657	181

Data for Results Presented in Figure 6.6d and 6.6f

Re	d_z/L	$q_{int}^* \times 10^3$	A_z/L^2	t_r^*
1094	0.054	0.003	0.023	6835
1557	0.151	0.009	0.077	8482
2118	0.237	0.020	0.147	7339
2686	0.309	0.034	0.213	6333
3719	0.406	0.068	0.306	4481
4528	0.463	0.104	0.361	3489
5223	0.502	0.139	0.402	2886
6268	0.545	0.203	0.449	2210
7271	0.578	0.277	0.486	1756
8159	0.600	0.354	0.510	1440
9702	0.629	0.508	0.545	1073
11659	0.654	0.768	0.575	749
12780	0.664	0.933	0.591	633
14844	0.679	1.291	0.608	471
18701	0.696	2.119	0.633	299
23903	0.711	3.640	0.654	180

Data for Results Presented in Figure 6.7

Re	dP_{und}	dP_{swi}	dP_{bas}
458	0.001	0.016	0.1
1557	0.01	0.153	0.1
2686	0.025	0.485	0.1
3719	0.05	0.963	0.1
8159	0.25	5.107	0.1
20656	1.5	37.401	0.1

Data for Results Presented in Figure 6.8

Re	dP_{und}	dP_{swi}	dP_{bas}
458	0.001	0.016	0.1
1557	0.01	0.153	0.1
2686	0.025	0.485	0.1
3719	0.05	0.963	0.1
8159	0.25	5.107	0.1
20656	1.5	37.401	0.1

Data for Results Presented in Figure 6.9

$H/L = 0.03$		$H/L = 0.04$		$H/L = 0.05$		$H/L = 0.06$		$H/L = 0.075$	
Re	dP_{swi}	Re	dP_{swi}	Re	dP_{swi}	Re	dP_{swi}	Re	dP_{swi}
42	1.8E-04	51	3.4E-04	68	2.8E-04	81	3.1E-04	97	3.4E-04
99	0.001	133	0.001	164	0.002	202	0.002	244	0.002
109	0.002	145	0.002	178	0.002	217	0.003	260	0.003
184	0.007	248	0.007	309	0.008	363	0.008	445	0.008
272	0.015	371	0.015	458	0.016	541	0.016	660	0.015
521	0.036	645	0.033	744	0.032	836	0.030	947	0.025
777	0.087	954	0.078	1094	0.073	1229	0.067	1400	0.057
1127	0.197	1368	0.170	1557	0.153	1743	0.140	1976	0.117
1964	0.675	2365	0.557	2686	0.484	3026	0.450	3492	0.386
2784	1.472	3308	1.155	3719	0.963	4166	0.881	4757	0.733
3337	2.204	4054	1.798	4528	1.462	5061	1.327	5748	1.084
3905	3.161	4579	2.339	5223	1.974	5824	1.784	6594	1.439
4418	4.183	5146	3.038	5750	2.400	6510	2.248	7347	1.798
4885	5.264	5670	3.762	6268	2.909	7045	2.633	8038	2.161
5319	6.397	6155	4.506	6786	3.449	7550	3.072	8672	2.499
5727	7.577	6607	5.270	7271	3.996	8076	3.554	9166	2.804
6479	10.068	7437	6.849	8159	5.107	9055	4.530	10168	3.503
7168	12.714	8192	8.484	8963	6.241	9942	5.524	11140	4.244
7808	15.499	8890	10.171	9702	7.390	10760	6.531	12045	4.993
8409	18.406	9542	11.906	10395	8.563	11522	7.550	12889	5.747
8974	21.405	10158	13.683	11044	9.749	12238	8.582	13677	6.499
9511	24.498	10741	15.499	11659	10.949	12916	9.624	14424	7.258
10514	30.922	11803	19.136	12780	13.302	14317	11.959	16001	9.012
11448	37.670	12800	22.954	13972	16.134	15480	14.155	17304	10.611
12335	44.775	13787	27.128	14844	18.377	16425	16.053	18310	11.931
13166	52.048	14631	30.987	15885	21.263	17590	18.581	19632	13.812
13965	59.603	15476	35.202	16758	23.851	18548	20.803	20686	15.410
15816	79.282	17441	46.129	18701	30.055	20758	26.438	23118	19.455
17460	99.243	19405	58.843	20656	37.402	22842	32.420	25323	23.566
19027	120.575	20893	69.634	22144	43.441	24492	37.463	27355	27.735
20479	142.245	22602	83.375	23903	51.267	26399	44.107	29345	32.200

APPENDIX V

**TRACER TESTS USING SF₆ TO DETERMINE SEEPAGE FLUXES AND
HYDRAULIC PROPERTIES OF THE RIO GRANDE STREAMBED**



A 3-day tracer experiment (from 12/9/03 to 12/11/03) was conducted in the Rio Grande streambed along the Escondida Bridge just north of Socorro, NM. Sulfur hexafluoride (SF₆), an inert, nonflammable, odorless, colorless and environmentally benign gas, was injected into the streambed in order to determine seepage fluxes and hydraulic conductivity of the sediments.

A piezometer nest consisting of 1.25 inch PVC pipes and 1 stainless steel screened drivepoints with 10-cm long screens (from Johnson screens) was manually installed using a postdriver. The shallowest piezometer is screened about 0.5 m below the

the sediment-water interface. Three other piezometers are driven to and screened at greater depths in increments of 0.4 and 0.3 m (Figures 1 and 2).

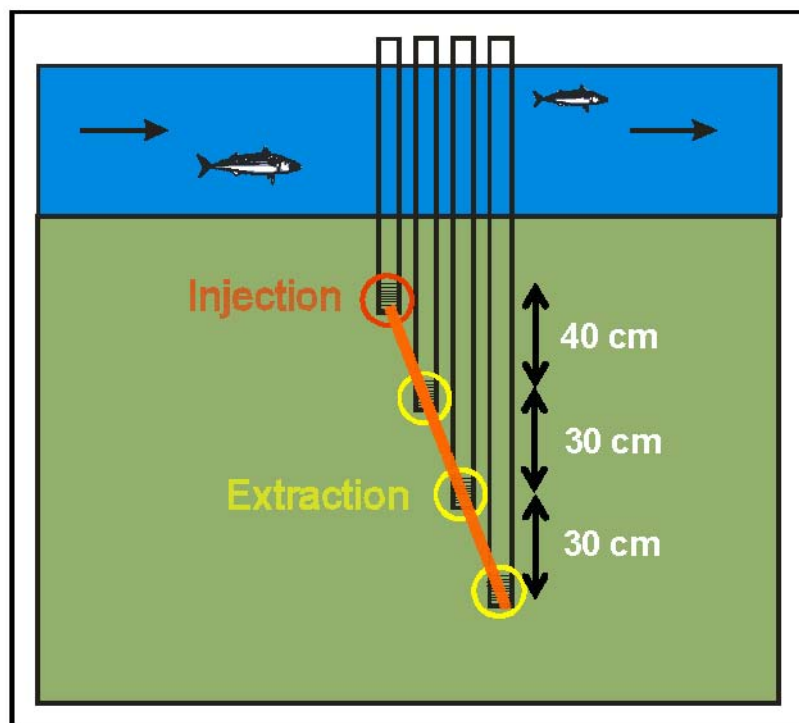


Figure 1. Schematic diagram of piezometer layout and location of injection and extraction ports.



Figure 2. Picture of piezometers (leftmost, with black hose, is used for injection, others are used for sampling).

SF₆ was released from a container equipped with valves and regulators. The SF₆ and fittings were supplied by Scott Gas. The container was connected by a hose to a diffusing stone (Figure 3) that was then placed in screened section of the injection piezometer. The test started at 10 PM on 12/9/03. Water samples were collected from the four piezometers right before the SF₆ was released. Samples were extracted using a peristaltic pump. The outlet hose was placed in a bucket that was first rinsed with the effluent water. After rinsing, water was allowed to fill part of the bucket until vacutainers (pre-evacuated vacuum containers) were completely submerged in water. The vacutainers were placed sideways at the bottom of the bucket with the septum facing the hose outlet. The septum was then punctured with a syringe needle and water allowed to fill the vacutainer (Figure 4). A new needle was used for each sample.



Figure 3. SF₆ bottle, valves, gauges, regulators, hose and diffusing stone.

The SF₆ was released overnight. By 7 AM the following morning (12/10/03), the SF₆ container was empty. The first sampling was conducted at this time. Additional samples were collected from the 3 extraction piezometers at time intervals that varied from 2 to 3.5 hours except at night. A total of 45 samples were collected. However, only

the samples from the injection piezometer and the shallowest extraction piezometer were sent off for analyses. The rest are stored in a refrigerator. The analysis was conducted by Dr. Jordan F. Clark in his laboratory at University of California- Santa Barbara. Since the headspace in the vacutainers was so small and the input concentrations were so high, gas extracted from the headspace had to be diluted first prior to injection to a gas chromatograph. This may have resulted in large errors in absolute concentration. However, the intent of this study was to determine tracer arrival times thus errors in the absolute concentration have little consequence in the analysis as long as the errors are systematic.

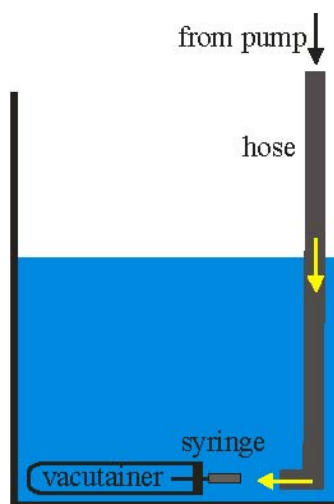


Figure 4. Diagram of water sample collection scheme for SF_6 analysis.

Background concentrations (based on samples collected prior to SF_6 release) were on the order of $1\text{e-}11$ to $1\text{e-}10$ mol/L. Figure 5 shows the breakthrough curve for the shallowest piezometer (distance from injection point= $z = 40$ cm). The maximum arrival time for the peak is 9 hours which gives a minimum pore velocity of 4.4 cm/hr. Assuming an effective porosity of 0.3, the minimum vertical seepage (Darcy) velocity is therefore 1.3 cm/hr. The head difference between the injection and extraction piezometer was manually measured (through visual inspection) to be 1-2 cm resulting in a gradient (dh/dz) of 0.025-0.05. Based on Darcy's law, the

vertical hydraulic conductivity of the sediments would therefore vary from 6.4 m/d to 12.8 m/d.

This range is consistent for those of medium sands found in the Rio Grande streambed.

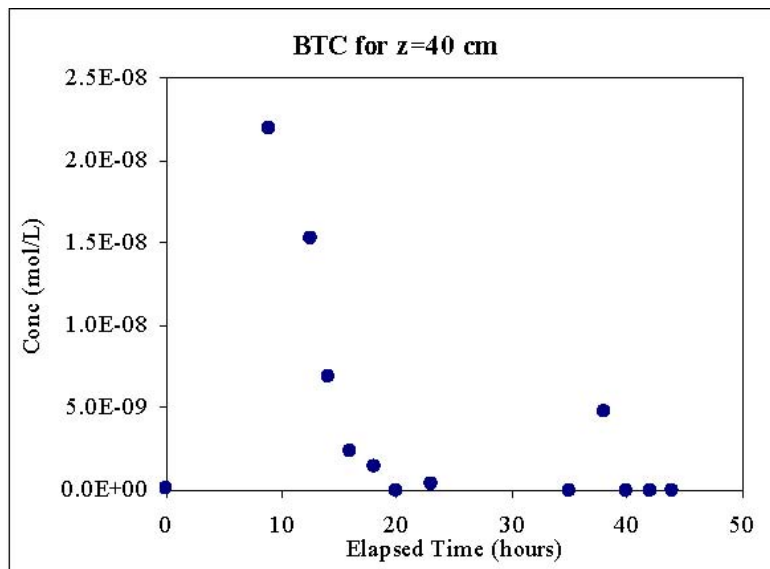


Figure 5. Breakthrough curve for SF₆ at the shallowest extraction piezometer.

APPENDIX VI

**COMMENT ON “FLOW RESISTANCE AND BED-FORM GEOMETRY
IN A WIDE ALLUVIAL A CHANNEL” BY SHU-QING YANG, SOON-KEAT
TAN AND SIOW-YONG LIM**

(This appendix has been accepted for publication as: Cardenas, M. B, and J. L. Wilson, Comment on “Flow resistance and bed form geometry in a wide alluvial channel” by Yang, Tan and Lim, *Water Resources Research*)

1. Introduction

Yang et al. [2005] present a paper which uses previously published data to explore the underlying mechanism of flow resistance in alluvial channels with bed forms. One of the major goals of their paper is to provide a method for estimation of the energy slope, S , and its components, for flow over bedforms using minimal and readily measurable information such as average velocity, average water depth, bedform geometry, grain size, and the hydraulic radius. Included in their analyses is a relationship between the length of the eddy separation zone (L'') and bedform height (δ) that we show here again (the reader is referred to Figure 1 of *Yang et al.*):

$$L'' = \alpha \delta \quad (1; 11 \text{ in the original paper})$$

α , a proportionality coefficient, was defined on the basis of its empirical relationships with the ratio of δ to the average water depth h . A fitted equation for ripples and dunes was presented as follows:

$$\alpha = \frac{45}{1 + 5\delta/h} \quad (2; 28a \text{ in the original paper})$$

Our parochial interest in this equation lies in the observation that the geometry of the eddy controls the biogeochemically important flow field in the underlying sediments (the hyporheic zone). This control has been demonstrated using coupled-process computational fluid dynamics (CFD) for laminar flow conditions (e.g., *Cardenas and Wilson* [2004]), and on-going CFD work suggests the same for turbulent flow cases. Application of the authors' equation (28a) would allow prediction of hyporheic zone structure based on readily acquired information. In the ensuing discussion, we use the original symbols and equation numbers of *Yang et al.* unless otherwise stated.

2. Discussion of reanalysis of the *Yang et al.* methodology

Equation (28a) suggests that α may vary from 12-45 (see Figure 4 in *Yang et al.*). We believe these values are too large. *Engel* [1981], and the references therein, show an α that varies from 4-6, which is much lower and less sensitive to the ratio of bedform height to depth than values suggested by (28a). Simple calculations demonstrate the potential error associated with predictive application of this equation. Consider a bedform with $\delta = 0.06$ m and length $L = 1$ m. Based on (20) in *Yang et al.*, $h = 0.16$ m. It follows from (28a) and (11) that $\alpha = 15.7$ and $L'' = 0.94$ m; the eddy reattaches almost at the crest

of the succeeding dune. This is practically impossible for separated turbulent flow over dunes. In fact for a bedform with a similar δ/L ($=0.06$), *Karahan and Peterson* [1980] found $\alpha \approx 5.33$. For this case, equation (28a) overestimates α by $\sim 300\%$. This led us to closely inspect the analysis by *Yang et al.*. We first review the procedure employed by *Yang et al.* to estimate α and S , facilitated by worksheets provided by the original authors, and resolve some of its ambiguities. We then revise the procedure for estimating S , mainly by using the lower range of prescribed α values consistent with those in *Engel* [1981]. We use this estimate of S and experimental data to create an *a posteriori* estimate of α , and compare to the range in *Engel* [1981]. Finally, we confirm that range of lower α values using CFD computations. Our inspection is based on the original data set of *Guy et al.* [1966] which was also used by *Yang et al.* in their analysis.

Consider the three flume experiments with measured or known parameters presented in our Table 1. Consistent with their goal of using minimal data, *Yang et al.* attempted to estimate S using calculated parameters when they could, rather than looking up experimental parameter values. Calculated parameters are labeled in this paper with the subscript c while the actual experimental values are labeled with the subscript a . Their procedure for computing the energy slope due to grain resistance, S' , the energy slope due to bed form resistance, S'' , and the total energy slope, S , appears to be as follows:

- (A) Compute the energy slope due to grain resistance, S' via (8) and by assuming that the equivalent roughness, k'_{s} , is equal to $2d_{50}$.

(B) Compute the energy slope due to bed-form resistance, S'' , via (13). The equivalent roughness related to the bedforms, k''_s , is determined by (16) and (14). In the application of (16), the authors use the experimental values δ_a and L_a . Note that (16) is not an approximation of (15) which had been previously presented. Instead, (16) is a new (and quite different) empirical relationship developed by the authors based on *Guy et al.*'s [1966] experimental data. We examined the difference if (15) were used in lieu of (16), but it is not large.

(C) The total energy slope, S_c , is finally computed from (12b) again using δ_a and L_a . However, α needs to be computed first or prescribed in order to use (12b).

It is not clear what value for α is used for calculation of S_c in step C. The sample calculations provided to us by Shu-Qing Yang fix $\alpha = 16$, much higher than *Engel*'s [1981] range, in the determination of S_c . Prescribing α circumvents part of the inconsistency elaborated below. However, Yang informed us that α was not fixed in the estimation for S_c presented in *Yang et al.*. Instead, it appears that α was computed based on substituting the equations for shear velocity (8, 13) into (12b). After manipulation of equation (12b), this approach gives α as:

$$(D) \quad \alpha = \left(\frac{L_c}{\delta_c} \right) \left(\frac{u_*^2 - u_*'^2}{u_*'^2 - u_*^2} \right) \quad (3)$$

Note that this equation uses computed, instead of experimental, values for δ and L . L_c is computed first through (19). Afterwards, δ_c is computed through (17) using the experimental water depth, h_a , as input. The shear velocity in this equation (3), u_* , is

computed using the experimental value, S_a , of the total energy slope. If the α used for computing S_c in step C is indeed determined through the approach just mentioned (step D), the analysis for S_c would have used the actual experimental values for h , δ , L , and, most inconsistently, S at some point.

In order to generate Figure 4 in *Yang et al.*, and consequently equation (28a), the α computed through step D was plotted versus the ratio of the computed δ_c over the experimental h_a , the same ratio used in their Figure 4. Our Figure 1 shows that using the experimental δ_a can significantly change the plot. Those labeled by circles are the original data points in Figure 4 of *Yang et al.* while the x's correspond to the same data set using δ_a (instead of δ_c computed through equation (17)). Just by re-evaluating δ/h using experimental data, and not changing α , we can see that some differences are already evident.

We re-evaluated S' , S'' , S , and α for the three cases in Table 1 using the measured parameters. This not only circumvents the problem of using inconsistent combinations of estimated and experimental values for the same parameters in the analysis, but is also a more direct test of the proposed methodology. Our computation goes as follows:

(E) Compute S' using equation (8) and V_a , R , and d_{50} as input values. This is essentially similar to step A, except that in step A, *Yang et al.* opted to re-estimate V by dividing Q_a by the measured cross-sectional area. This resulted in minor differences, including small round-off errors.

- (F) Compute S'' using (13), (14) and (16). This is again similar to (B) except in the calculation for V . Again we found small differences between our values and those of *Yang et al.*.
- (G) Important differences are present in the last step, the calculation for the total energy slope S . As in step C we calculated S through (12b), but instead of approximating the value of α as in step D, we use the (roughly) minimum and maximum values of 4 and 6 as suggested by *Engel* [1981] resulting in a range of estimated S_c .
- (H) An *a posteriori* estimate for α is computed from (12b) using the values for S' and S'' , derived through steps E and F, and the experimental values S_a , δ_a and L_a . Since the estimate for S'' in step F is already based on a range of α 's, we can only test consistency. Is this *a posteriori* estimate of α consistent with the range of 4 to 6?

Our step G leads to S_c values that are closer to the experimental values than those derived following step C, the *Yang et al.* procedure (compare our Tables 1 and 2). Step G results also show that using the entire but realistic range for α , suggested by *Engel* [1981], does not introduce much spread in the computed energy slope, S_c (Table 2). Our *a posteriori* estimates for α , computed from experimental data (step H), are different from those estimated using the analysis by *Yang et al.* (step D) based on calculated parameters (Table 2). Although our *a posteriori* estimates are smaller than the α values calculated by *Yang et al.*, they are still not consistent with the expected values of $\sim 4-6$. We even estimate an unrealistic negative α value for one of the flume experiments (the contribution of experimental error to this unrealistic value cannot be ruled out). A similar recalculation of all the data in Figure 4 of *Yang et al.* (even with negative values) might

show a regressed equation where α is closer to the range ~4-6, especially if all of *Guy et al.*'s [1966] flume data is included. For example, the points in the lower left corner of the inset graph in our Figure 1, circumscribed by the dotted ellipse, are absent from *Yang et al.*'s Figure 4. These points correspond to lower values of α and are somewhat more consistent with the range in *Engel* [1981].

To further test equation (28a) as a predictive model for eddy length L'' , we numerically simulated turbulent flow over dunes. Our CFD simulations, based on the Reynolds-averaged formulation of the Navier-Stokes equation with the $k-\omega$ closure scheme [Wilcox, 1993], essentially parallel those in *Yoon and Patel* [1996]. The CFD simulations were conducted via the commercial multiphysics CFD package CFD-ACE+. We used the same validation experiment reported in *Yoon and Patel* [1996] and got similarly good agreement between measured and simulated flow fields for separated flow over dunes. We can directly observe the eddy length in the simulation results. We ran five simulations (our Table 3) and found simulated values for α that range from 4.7-5.9 (squares in our Figure 1), consistent with *Engel's* [1981] experimental values, and providing further evidence questioning the validity of equation (28a).

In summary, *Yang et al.*, in the development of a method for estimating the energy slope of flow over bedforms, provide an empirical equation (28a) that predicts the length of the eddy zone in the lee side of a bedform. We show that their approach, used to define data points to which the equation is fitted (their Figure 4), is inconsistent with experimental and simulated values of eddy zone length. Although we did not try to fit a new equation based on a re-analysis of a portion of the data, we expect significant differences, with equation (28a) over predicting the eddy zone length. Inasmuch as this

model for eddy zone length plays an important role in the model for energy slope, equation (12b), the reanalysis should extend to the entire procedure.

Acknowledgement

Shu-Qing Yang graciously provided sample spreadsheets pertaining to some of their calculations. The authors benefited from and are grateful for discussions with him. Comments from AE Sean Bennett helped improve this manuscript. MBC is currently supported by the Kottowski Fellowship of the NM Bureau of Geology and Mineral Resources. This work is partially funded by a student grant from the NM Water Resources Research Institute and the AGU Horton Research Grant awarded to MBC.

References

- Cardenas, M. B., and J. L. Wilson (2004), Hydrodynamic interactions of free-flowing fluids and pore-fluids in triangular bed forms, Supplement to EOS Transactions, American Geophysical Union, 2004 AGU Fall Meeting, San Francisco, California, December.
- Engel, P. (1981), Length of flow separation over dunes, *J. Hydraul. Div., ASCE*, 107(10), 1133-1143.
- Guy, H. P., D. B. Simons, and E. V. Richardson (1966), Summary of alluvial channel data from flume experiments, 1956-1961, U. S. Geol. Surv. Prof. Pap., 462-1.
- Karahan, M. E., and A. W. Peterson (1980), Visualization of separation over sand waves, *J. Hydraul. Div., ASCE*, 106(8), 1345-1352.
- Yang, S. Q., S. K. Tan, and S. Y. Lim (2005), Flow resistance and bed form geometry in a wide alluvial channel, *Water Resour. Res.*, 41, W09419, doi:10.1029/2005WR004211.
- Yoon, J. Y., and V. C. Patel (1996), Numerical model of turbulent flow over sand dune, *J. Hydraul. Eng.*, 122(1), 10-18.

Table 1. Data for flume experiments with ripples (from Table 9 of *Guy et al.* [1966], $d_{50} = 0.33$ mm).

Run	δ_a (m)	h_a (m)	L_a (m)	R (m)	V_a (m/s)	Q (m ³ /s)	S_a
16	0.0061	0.15	0.13	0.1016	0.326	0.0297	0.00029
6	0.0091	0.16	0.15	0.1030	0.323	0.0300	0.00047
5	0.0152	0.16	0.09	0.1043	0.436	0.0413	0.00063

Table 2. Comparison of our calculations with those of *Yang et al.* [2005].

This work

Run	δ_a / h_a	S'	S''	S_c	α
16	0.040	0.00031	0.00054	0.00035-0.00038	-1.75
6	0.059	0.00030	0.00061	0.00037-0.00041	9.25
5	0.096	0.00053	0.00136	0.00111-0.00139	0.67

Yang et al [2005].

Run	δ_c / h_a	S'	S''	S_c	L_c (m)	α	δ_c (m)
16	0.037	0.00030	0.00054	0.00049	0.33	9.56	0.0056
6	0.070	0.00029	0.00061	0.00060	0.33	17.69	0.0108
5	0.049	0.00051	0.00142	0.00300	0.33	14.90	0.0078

Table 3. Parameters and results for turbulent CFD simulations ($L = 1$ m for all cases).

δ (m)	h (m)	V (m/s)	L'' (m)	α
0.03	0.485	0.26	0.151	5.03
0.04	0.480	0.25	0.216	5.40
0.05	0.475	0.21	0.293	5.86
0.06	0.470	0.18	0.345	5.75
0.075	0.463	0.14	0.350	4.67

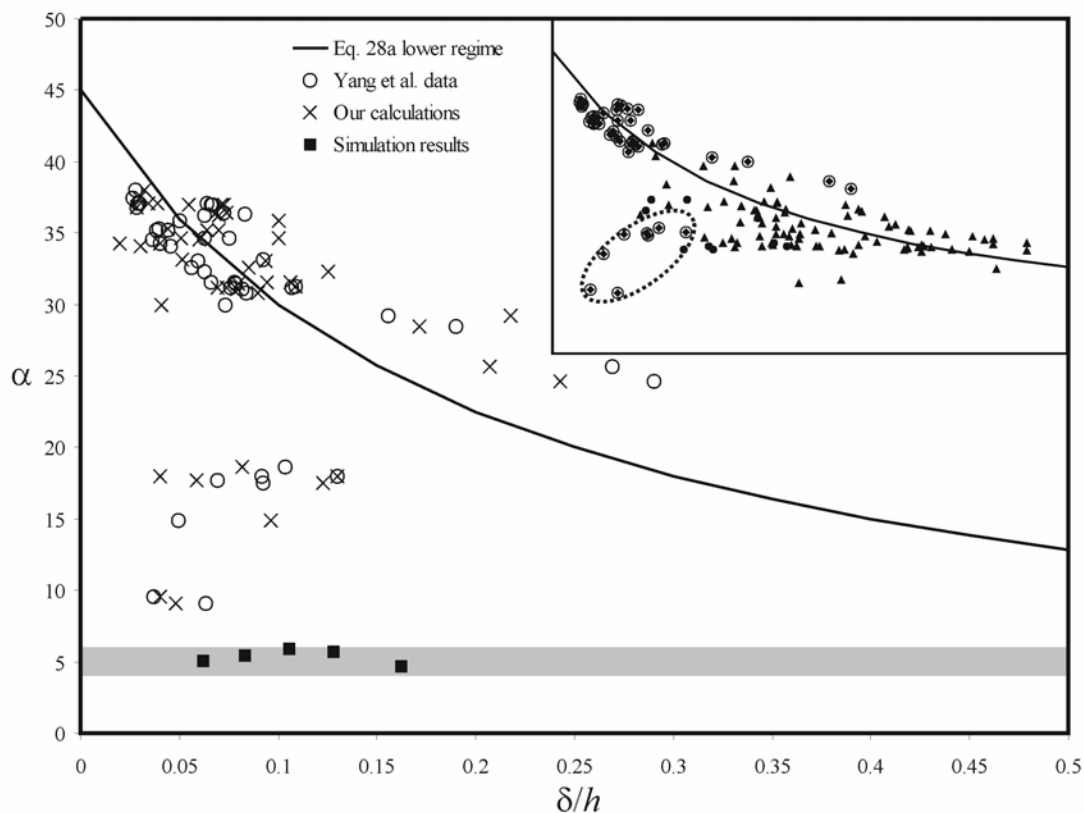


Figure 1. Plot of $\alpha(\delta/h)$ for Yang *et al.*'s [2005] original approach based on data in Guy *et al.* [1966] (circles), our re-calculations (x's) using measured data, CFD simulation results (squares), and equation (28a). The grayed region (horizontal bar) defines the expected range for α based on Engel [1981]. The inset graph corresponds to Figure 4 of Yang *et al.* [2005] with the data used here encircled. The points within the dotted ellipse are not presented in Yang *et al.* [2005] but are available from Guy *et al.* [1966]. Note that our re-calculations are for values of δ/h only, and we use the same values of α .